REPORT NO.
EERC 75-19
DECEMBER 1975

EARTHQUAKE ENGINEERING RESEARCH CENTER

THE SEISMIC BEHAVIOR OF CRITICAL REGIONS OF REINFORCED CONCRETE COMPONENTS AS INFLUENCED BY MOMENT, SHEAR AND AXIAL FORCE

by

MEHMET BILGIN ATALAY

JOSEPH PENZIEN

Report to the National Science Foundation

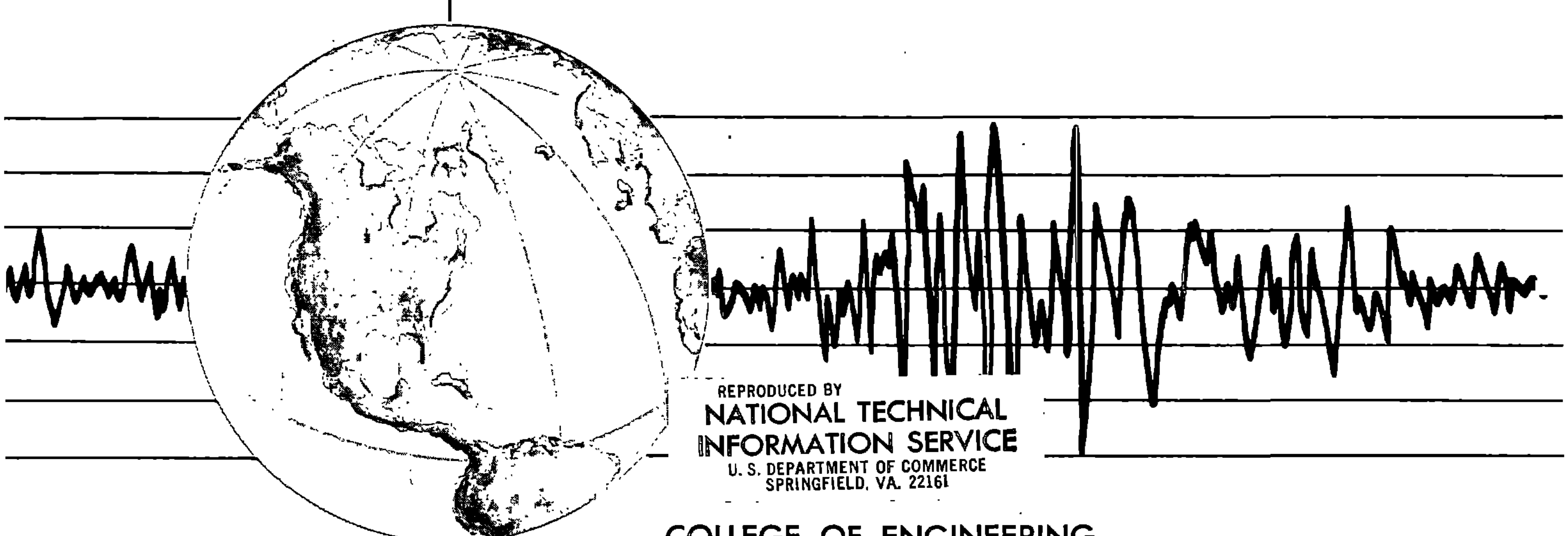

COLLEGE OF ENGINEERING

UNIVERSITY OF CALIFORNIA · Berkeley, California

For sale by the National Technical Information Service, U. S. Department of Commerce, Springfield, Virginia 2216̇.

See back of report for up to date listing of EERC reports.

BIBLIOGRAPHIC DATA SHEET	1. Report No. EERC 75-19	2.	3. Recipient's Accession No.
4. Title and Subtitle "The Seismic Behavior of Critical Regions of Reinforced Concrete Components as Influenced by Moment, Shear and Axial Force"			5. Report Date December 1975
			6.
7. Author(s) Mehmet Bilgin Atalay and Joseph Penzien			8. Performing Organization Rept. No. 75-19
9. Performing Organization Name and Address Earthquake Engineering Research Center University of California, Berkeley 1301 S. 46th Street Richmond, California			10. Project/Task/Work Unit No.
			11. Contract/Grant No. AEN73-07732 A02
12. Sponsoring Organization Name and Address National Science Foundation 1800 G Street Washington, D. C. 20550			13. Type of Report & Period Covered
			14.

15. Supplementary Notes

16. Abstracts

Building response caused by moderate to severe earthquake excitation is often in the inelastic range; thus, to enable reliable predictions of overall performance, the energy absorption and failure characteristics of individual components must be established. For reinforced concrete frame buildings, the critical or yielding regions may occur in either or both the girders and columns subjected to various combinations of bending, shear, and axial load.

To determine the characteristics and modes of failure of columns under excitations causing degradations in stiffness, strength, and energy absorption, a series of twelve members simulating a column between inflection points above and below a floor level were designed and tested dynamically. The variable parameters introduced were (1) magnitude of applied axial load chosen to represent lower, intermediate, and upper story columns, (2) lateral reinforcement percentage chosen to study the influence of confinement on ductility, and (3) history of controlled lateral displacement chosen to determine the effects of rate and sequence loading.

The results of these tests show that (1) increasing the applied axial load decreases the ultimate lateral displacement capacity, enhances the degrading mechanisms of strength, and stiffness, and, when the axial load is sufficiently high, causes changes in the failure modes from ductile flexure behavior to more brittle shear and buckling behavior, (2) decreasing the lateral reinforcement percentage decreases the ultimate lateral displacement capacity and enhances the degrading mechanisms. All experimental data from these tests have been analyzed and correlated to characterize the energy absorption, stiffness, and strength degradation mechanisms, the modes of failure, and the ductility capacities.

In addition to discussing the above described test program and its correlation studies, this report presents a mathematical model for reinforced concrete columns which predicts force-deformation characteristics under inelastic cyclic conditions. This model can serve as a sub-element in an overall mathematical model of a building.

17c. COSATI Field/Group

PRICES SUBJECT TO CHANGE

18. Availability Statement	19. Security Class (This Report)	21. No. of Pages
Release Unlimited	UNCLASSIFIED	250
	20. Security Class (This Page) UNCLASSIFIED	22. Price $8.00

FORM NTIS-35 (REV. 3-72) USCOMM-DC 14952-P72

INSTRUCTIONS FOR COMPLETING FORM NTIS-35 (10-70) (Bibliographic Data Sheet based on COSATI Guidelines to Format Standards for Scientific and Technical Reports Prepared by or for the Federal Government, PB-180 600).

1. **Report Number.** Each individually bound report shall carry a unique alphanumeric designation selected by the performing organization or provided by the sponsoring organization. Use uppercase letters and Arabic numerals only. Examples FASEB-NS-87 and FAA-RD-68-09.

2. Leave blank.

3. **Recipient's Accession Number.** Reserved for use by each report recipient.

4. **Title and Subtitle.** Title should indicate clearly and briefly the subject coverage of the report, and be displayed prominently. Set subtitle, if used, in smaller type or otherwise subordinate it to main title. When a report is prepared in more than one volume, repeat the primary title, add volume number and include subtitle for the specific volume.

5. **Report Date.** Each report shall carry a date indicating at least month and year. Indicate the basis on which it was selected (e.g., date of issue, date of approval, date of preparation.

6. **Performing Organization Code.** Leave blank.

7. **Author(s).** Give name(s) in conventional order (e.g., John R. Doe, or J.Robert Doe). List author's affiliation if it differs from the performing organization.

8. **Performing Organization Report Number.** Insert if performing organization wishes to assign this number.

9. **Performing Organization Name and Address.** Give name, street, city, state, and zip code. List no more than two levels of an organizational hierarchy. Display the name of the organization exactly as it should appear in Government indexes such as **USGRDR-I.**

10. **Project/Task/Work Unit Number.** Use the project, task and work unit numbers under which the report was prepared.

11. **Contract/Grant Number.** Insert contract or grant number under which report was prepared.

12. **Sponsoring Agency Name and Address.** Include zip code.

13. **Type of Report and Period Covered.** Indicate interim, final, etc., and, if applicable, dates covered.

14. **Sponsoring Agency Code.** Leave blank.

15. **Supplementary Notes.** Enter information not included elsewhere but useful, such as: Prepared in cooperation with . . . Translation of . . . Presented at conference of . . . To be published in . . . Supersedes . . . Supplements . . .

16. **Abstract.** Include a brief (200 words or less) factual summary of the most significant information contained in the report. If the report contains a significant bibliography or literature survey, mention it here.

17. **Key Words and Document Analysis. (a). Descriptors.** Select from the Thesaurus of Engineering and Scientific Terms the proper authorized terms that identify the major concept of the research and are sufficiently specific and precise to be used as index entries for cataloging.
(b). Identifiers and Open-Ended Terms. Use identifiers for project names, code names, equipment designators, etc. Use open-ended terms written in descriptor form for those subjects for which no descriptor exists.
(c). COSATI Field/Group. Field and Group assignments are to be taken from the 1965 COSATI Subject Category List. Since the majority of documents are multidisciplinary in nature, the primary Field/Group assignment(s) will be the specific discipline, area of human endeavor, or type of physical object. The application(s) will be cross-referenced with secondary Field/Group assignments that will follow the primary posting(s).

18. **Distribution Statement.** Denote releasability to the public or limitation for reasons other than security for example "Release unlimited". Cite any availability to the public, with address and price.

19 & 20. **Security Classification.** Do not submit classified reports to the National Technical

21. **Number of Pages.** Insert the total number of pages, including this one and unnumbered pages, but excluding distribution list, if any.

22. **Price.** Insert the price set by the National Technical Information Service or the Government Printing Office, if known.

THE SEISMIC BEHAVIOR OF CRITICAL REGIONS
OF REINFORCED CONCRETE COMPONENTS
AS INFLUENCED BY MOMENT, SHEAR AND AXIAL FORCE

by

MEHMET BILGIN ATALAY

JOSEPH PENZIEN

Report to

National Science Foundation

Report No. EERC 75-19
Earthquake Engineering Research Center
College of Engineering
University of California
Berkeley, California

December 1975

ABSTRACT

Building response caused by moderate to severe earthquake excitation is often in the inelastic range; thus, to enable reliable predictions of overall performance, the energy absorption and failure characteristics of individual components must be established. For reinforced concrete frame buildings, the critical or yielding regions may occur in either or both the girders and columns subjected to various combinations of bending, shear, and axial load.

To determine the characteristics and modes of failure of columns under excitations causing degradations in stiffness, strength, and energy absorption, a series of twelve members simulating a column between inflection points above and below a floor level were designed and tested dynamically. The variable parameters introduced were (1) magnitude of applied axial load chosen to represent lower, intermediate, and upper story columns, (2) lateral reinforcement percentage chosen to study the influence of confinement on ductility, and (3) history of controlled lateral displacement chosen to determine the effects of rate and sequence of loading.

The results of these tests show that (1) increasing the applied axial load decreases the ultimate lateral displacement capacity, enhances the degrading mechanisms of strength, and stiffness, and, when the axial load is sufficiently high, causes changes in the failure modes from ductile flexure behavior to more brittle shear and buckling behavior, (2) decreasing the lateral reinforcement percentage decreases the ultimate lateral displacement capacity and enhances the degrading mechanisms. All

experimental data from these tests have been analyzed and correlated to characterize the energy absorption, stiffness, and strength degradation mechanisms, the modes of failure, and the ductility capacities.

In addition to discussing the above described test program and its correlation studies, this report presents a mathematical model for reinforced concrete columns which predicts force-deformation characteristics under inelastic cyclic conditions. This model can serve as a subelement in an overall mathematical model of a building.

ACKNOWLEDGEMENTS

This report was written in partial satisfaction of the requirements for the degree of Doctor of Philosophy in Engineering by M. B. Atalay under the supervision of Professor J. Penzien. The valuable suggestions and assistance of Professor V. V. Bertero are gratefully acknowledged.

The assistance of the staff of the Structures Research Laboratory, Earthquake Engineering Research Center and the Division of Structural Engineering and Structural Mechanics, during the execution of the experimental investigation and the preparation of the final manuscript of this report is sincerely appreciated. The use of the facilities of the University of California Computer Center proved invaluable during the course of the research.

Financial support for this research was provided by the National Science Foundation under Grant No. AEN 73-07732 A02.

TABLE OF CONTENTS

Page

NOTATION

a	Length along the longitudinal axis
A	Area
A	Force quantity used as coefficient of trigonometric term
b	Width of compression face of cross-section of member
b	Transverse distance between instrumentation mounting points
B	Force quantity used as coefficient of trigonometric term
c	Distance from extreme compression fiber to neutral axis
C	Compressive force
d	Distance from extreme compression fiber
d	Differential operator
D	Total depth of cross-section
E	Modulus of elasticity
f	Stress in concrete or reinforcing steel
F	Lateral force
g_i	Distance between tension and compression reinforcement divided by total depth of cross-section
h	Transverse distance between instrumentation mounting points
I	Moment of inertia of cross-section
J	Inelastic half cycle number
k_u, k_p	Empirical constants
K	Stiffness
ℓ, L	Longitudinal distance
M	Bending moment
n	Ratio E_s/E_c
n	Number of ties crossed by an inclined crack
s	Spacing of transverse reinforcement

t	Time
T	Tensile force
V	Shear force
W	Work
x	Distance along the longitudinal axis
Z	Section modulus
α	Stiffness reduction factor
β	Empirical constant defined by Timoshenko and Goodier [32]
β	Parameter used in definition of loss of resistance
γ	Average shear deformation
δ	Lateral displacement
Δ	Finite difference operator
Δ	Relative displacement measured by instrumentation
ε	Strain
η_o	Axial compression index
μ	Ductility
ν	Poisson's ratio
ξ	Equivalent damping factor
ρ	Reinforcement ratio
ρ_w	Transverse reinforcement ratio, A_v/bs
ρ''	Ratio of volume of transverse reinforcement to volume of concrete core
ϕ	Average curvature
ϕ	Capacity reduction factor
Ω	Slope of the descending branch of stress-strain relationship for concrete

SUBSCRIPTS

b	Balanced capacity of cross-section
B	Bottom
c	Concrete
cr	Cracking
E	Elastic
f,flex.	Component due to flexural deformation
g	Gross
I	Initial
J	Inelastic half cycle number
M,max.	Maximum
N	Corresponding to initiation of loss of resistance
P	Due to "pinching" effect
PH	Component due to plastic hinge rotation
r	Return
rel.	Relative
s	Steel
S	Corresponding to the "skeleton" curve
S,shear	Component due to shear deformation
SH	Strain hardening
t	Tensile
tr	Transformed
T	Top
u	Ultimate force capacity of cross-section
ult	Ultimate deformation capacity of specimen
v,w	Transverse reinforcement
y	Yield
ys	Yield of transverse reinforcement

SUPERSCRIPTS

c	Cyclic
c	Stiffness degrading model
M	Maximum in absolute value
p	Present
us	Action or deformation when extreme compression fiber strain equals usable concrete strain
uℓt	Action or deformation when extreme compression fiber strain equals ultimate concrete strain
-	Corresponding to lateral loading in the negative direction
+	Corresponding to lateral loading in the positive direction
'	Compressive
"	Confined or pertaining to confinement
*	Forces adjusted by the "N-δ" effect

1. INTRODUCTION

1.1 GENERAL

In accordance with the recommendations of the Structural Engineers Association of California [1]† and the provisions of the Uniform Building Code [2], the construction of reinforced concrete moment resisting space frames of height more than 160 feet has been permitted, even in areas of high seismicity. The recognized philosophy governing the design of a building against severe earthquakes dictates that it not collapse even though considerable damage is permissible. To economically behave in this manner, the structure must be able to absorb and dissipate the earthquake energy input by undergoing numerous cycles of deformations into the inelastic range. Prediction of the inelastic response of buildings to strong ground motions having a wide range of frequencies and amplitudes is a complex problem since the post-elastic behavior is greatly influenced by the interaction of individual components such as beams, columns, shear walls, etc. Often, typically assumed [3,4,5] elasto-plastic hysteretic member behavior does not realistically model the behavior of reinforced concrete members. Therefore, better knowledge of the energy absorbtion and failure characteristics of individual structural components is essential for reliable predictions of overall building performance during an earthquake.

Inelastic deformations in a reinforced concrete multistory frame result from a superimposition of gravity and lateral forces and are concentrated around regions of peak internal forces. Considering a

---

†Numerals in brackets refer to the corresponding Reference numbers.

reinforced concrete frame as shown in Fig. 1.1, localized inelastic deformations occur at certain overstressed regions designated as critical regions. These critical regions can be classified according to the internal force components controlling their behavior as follows: (1) Moment - These regions have moment as the only important force component. They are usually located in the girders of the top stories of a building as indicated by regions Nos. 1, 2, and 3 in Fig. 1.1; however, they may also occur in the columns of the upper stories of a frame building. Region No. 1 can experience reversals of loading due to the vertical accelerations of ground motions. (2) Moment with High Shear - These regions, having high shear and moment, are located at the ends of short girders located in the lower stories of medium or high rise buildings; see regions Nos. 2 and 3 in Fig. 1.1 (3) Moment with High Shear and Axial Force - These regions have relatively high axial forces as well as moment and high shear and are usually located at the ends of columns as indicated by regions Nos. 4, 5, 6 and 7 in Fig. 1.1 (4) Axial Force and Shear - These regions are located within joints as indicated by regions Nos. 2 and 8 in Fig. 1.1.

As part of a comprehensive program conducted at the University of California at Berkeley, inelastic cyclic behavior of reinforced concrete members under various loading conditions has been studied. Results of this investigation have already been reported for critical regions under combined bending moment with low shear [6,7], and under combined bending with high shear [8]. Study of the inelastic cyclic behavior of reinforced concrete members under the combined action of bending moment, shear, and axial force forms the third phase of the general program of research and is the subject of this report.

Inelastic deformations under the combined actions of cyclic bending moment, shear, and axial force occur in the columns of a multistory frame when subjected to moderate to severe earthquake ground motions. Although, this behavior is contradictory with the recently suggested [3,9,10] strong column-weak girder design philosophy, present code regulations (Section 2630, UBC) fall short of preventing possible yielding in the columns of a multistory frame. Inherent in the present regulations are the assumptions that (1) structural response to earthquake excitation is primarily in the first mode, (2) points of inflection in columns are located near midheight, and (3) the earthquake lateral forces act along one of the two principal axes of the frame. These assumptions are, of course, not necessarily valid for all cases under generalized earthquake excitations. Yielding and large inelastic deformations can take place in columns of a reinforced concrete frame resulting in catastrophic, brittle failure of the member and collapse of the complete structure [11,12].

Inelastic cyclic behavior of reinforced concrete columns has been the subject of numerous investigations. Many Japanese researchers have reported experimental results and suggested empirical relations based on a statistical analysis of experimental data to describe the effect of various parameters on member behavior. Yamada [13] and Okamoto and Hirosawa [14] point out that the ratio of the moment arm, a, to the depth, D, is the most important factor affecting the deformation capacity of reinforced concrete columns. Ohno, et al. [15] suggest empirical values for ultimate shear resistance and deformability at shear failure for a column based on the results of some 378 tests conducted by various researchers. They also emphasize the effect of the a/D ratio. Ikeda [16], Yamada [13], and Umemura, et al. [17] point out that the axial compression force effects the ductility capacity and type of failure of columns, and that load resistance capacity decreases with successive cycles of loading to a fixed deflection amplitude and with successive cycles using increasing deflection amplitudes. Hisada, et al. [18] emphasize the effect of transverse reinforcement ratio and detailing on the shear strength and deformation capacities of reinforced concrete columns. Sugano and Koreishi [19] report empirical relations to calculate points on the skeleton force-deformation relationship. Higashi and Takeda [20] suggest several rules to develop hysteretic loops from such a skeleton relationship.

It is only recently that analytical prediction of the actual shape of the moment-curvature, and thus of the load-deflection response has been attempted. These theories have generally been based on an assumed linear strain profile down the depth of the section and idealized cyclic stress-strain curves for concrete and reinforcing steel. The moment-curvature loop has usually been obtained by calculating the moment and curvature corresponding to a range of strains in the extreme fiber of the section and taking into account the previous strain history of the materials. Having determined the curvature distribution along the member, classical moment-area relationships are then used to determine the load-deflection characteristics of the member. Park, et al. [21] have applied this method and concluded, in view of the considerable computer time required, that some simplifications were desirable. Muguruma, et al. [22] and Wight and Sozen [23] have compared experimentally observed response with the response predicted by such analytical methods and have concluded that the deformation characteristics of reinforce concrete columns cannot be estimated by considering only flexural deformations.

1.2 OBJECTIVES

This investigation is part of an ongoing research program aimed at evaluating the response of reinforced concrete structures and members subjected to seismic actions. The present investigation is an extension of earlier studies and its objectives are: (1) to experimentally investigate the performance and modes of failure of reinforced concrete columns under controlled deformation time-histories similar to those caused by earthquake excitations resulting in degradations of strength, stiffness, and energy dissipation capacity, and (2) with the guidance of experimental data, to analytically define the inelastic cyclic behaviors of the critical region, and overall member in terms of certain structural parameters.

1.3 SCOPE

To accomplish the above objectives, twelve specimens, each simulating a reinforced concrete column, were designed, manufactured and tested. All specimens had an identical length and section geometry, and therefore an identical moment arm-to-depth ratio which was high enough to prevent shear type failures. All specimens had identically the same main reinforcement percentage. No attempt was made to analyze the effect of the main reinforcement percentage on member behavior since it was felt that this effect had already been fairly well defined by the present state-of-the-art. Variable parameters in the experimental series were the amount of applied axial load, percentage of transverse reinforcement, and the time-history prescribed for lateral displacement. The series was designed such that the effect of each of the variable parameters on member behavior could be isolated. Range of applied axial loads was below the so-called "balanced-point" axial load for the cross-section. Transverse reinforcement percentage was varied to investigate its effects on the degradation characteristics of the member. Lateral displacements were prescribed not only to truly simulate earthquake type motions, but also to enable comparisons with the results of previous tests conducted in the overall experimental program.

Continuous time records of average curvatures, shear deformations in the critical regions, and longitudinal and transverse reinforcement strains, as well as applied loads and displacements were obtained. No direct measurement of slippage of longitudinal reinforcement bars was provided; however, this component of deformation could be calculated from available data.

Correlation studies to relate certain test variables to the degrading mechanisms and a method to analytically predict the hysteretic action-deformation relationships for the member are reported. In selecting the analytical method, emphasis was placed on reaching a balance between simplicity and accuracy, since the governing objective of developing an analytical model for the hysteretic behavior of a member is to later incorporate it in a general method of analysis for the inelastic cyclic response of a multistory frame.

2. EXPERIMENTAL PROGRAM

2.1 TEST SPECIMENS

The test specimen was designed to simulate that segment of a reinforced concrete column located between inflection points above and below a story level in a multistory frame when subjected to the action of a constant magnitude axial load and time varying lateral displacements at the story levels. Several alternatives for the shape of the test specimen simulating such behavior were considered. Although test specimens of the subassemblage type and simple specimens under double curvature (Fig. 2.1.b) would have been more realistic, their testing would have necessitated a complex assembly of equipment and reaction frames. Simple specimens under single curvature (Fig. 2.1.c) were selected as used in previous investigations [8,16,17,21]. This type of specimen offers practical advantages for studying the behavior of critical regions. Celebi and Penzien [8] studied the degree of interference from one side of the joint area to the other and concluded that the strain in the longitudinal reinforcement within the joint area does not reach values above yield until after member displacement ductility factors reach values around 4 or 5; therefore, the interference from one side to the other is small in the tests of specimens of this type. Care must be taken however to account for the deflection component due to slippage of the longitudinal reinforcement within the critical region of the specimen being tested. This deflection component would have been considerably larger had the specimen been under double curvature. However, omission of study of this effect does not result in a serious violation of the study of the behavior of the column critical region since, in reality occurance of inelastic deformations simultaneously above and below a floor level in a column of a reinforced concrete frame which has been designed according to the present ductile moment resisting frame philosophy is highly unlikely.

In determining the geometry and design of the test specimens, considerations were given to (1) the limitations of the testing equipment and the loading system, (2) the requirements needed to develop the desired behavior and (3) the desirability of permitting comparisons of results with previous experimental results obtained in the overall investigation. Considering these factors, a specimen was selected having a length of 11 feet and a cross section of 12 in. x 12 in. (Fig. 2.2). Its longitudinal reinforcement consisted of two #7 deformed bars at the top and two similar bars at the bottom continuously placed throughout the length of the specimen. These bars were welded to a 1 inch thick steel plate at each end of the specimen. These plates were specially manufactured to be bolted to the reaction frame. Transverse reinforcement consisted of #3 deformed bars placed according to the spacing requirements of the particular specimen. Concrete cover was nominally set at 1 1/4 inches. The simulated joint area at the center of each specimen had a length of 12 inches, and a cross-section of 12 in. x 24 in. To simplify the interpretation of results obtained, the joint was designed to suffer only minimal damage throughout testing with its deformations remaining small. Therefore, the joint area was enlarged and heavily reinforced.

Strengths of materials used, dimensions of the cross-section, and percentages and detailing of longitudinal reinforcement satisfied the requirements of the ACI Code '71 [24], Appendix A "Special Provisions for Seismic Design". While the transverse reinforcement was designed to resist the maximum shear force that could be developed, it did not satisfy the requirements for confinement of the concrete core (Sections A.5.9 and A.6.4 of [24])†. The effect of spacing of transverse reinforcement on member behavior was a factor to be studied in this investigation.

The manufacture of test specimens were carried out in the laboratory within close tolerance limits. The reinforcement cage was constructed and strain gages on transverse reinforcement were spot-welded at their proper locations. Protruding steel stubs, 1/2" x 1/2" x 1 5/8", were silver soldered at four prescribed locations on the top and bottom longitudinal reinforcement for later attachment of clip gages to measure average steel strains. The stubs were protected by plastic tubes to prevent interaction with the concrete cover. Two eye-bolts were attached to the cages to assist in later handling of the specimen.

Two forms, each made up of 15 inch wide steel channels on both sides, and another 15 inch wide channel at the bottom, were used in casting the specimens in pairs. Thus, Specimens 1 and 2, and Specimens 3 and 4, etc., were cast simultaneously. Prepared cages were placed in oiled formwork with their positions being secured by 1 5/8 inch plastic chairs. The concrete was placed in the forms and vibrated internally by a high frequency vibrator. Standard 6 x 12 inch control cylinders were cast from the same concrete mix according to ASTM Standard C-31, to be used later to determine the 7, 14, 28 and test day compressive strengths of concrete. After the initial set, surfaces were finished and the

---

†Number 3 ties at a spacing of 2 inches or No. 4 ties at 3 inches would have satisfied the quoted confinement requirements. Such stringent transverse reinforcement detailing would be necessary since the area of the confined core is relatively small (confined core area-to-gross area ratio = 0.63).

specimens were covered with wet burlap and plastic sheets. The side channels of the forms were removed after 24 hours and the specimens were covered with wet burlap and plastic sheets for 6 more days. After this time, the specimens were stored at room temperature until the time of testing.

2.2 MATERIAL PROPERTIES

2.2.1 Reinforcing Steel

Reinforcement used throughout the tests was Grade 40 deformed bars conforming to ASTM Designation A615. Transverse reinforcement was No. 3 bars and the longitudinal reinforcement was No. 7 bars. Coupon samples taken from the same bars used in constructing the specimens were tested to determine the average properties of the reinforcement. Unmachined coupons were subjected to quasi-static tensile tests, and their stress-strain relationships were obtained using a mechanical extensometer and an X-Y recorder. A typical record of such a stress-strain curve is given in Fig. 2.3 and the summary of results is given in Table 2.1. Mean values for yield stress f_y, yield strain, ε_y and Young's Modulus, E_s are 55.2 ksi., 0.00197 and 28500 ksi., respectively. Of primary interest from the point of view of inelastic cyclic behavior are (1) the values given for strain and tangent modulus at the onset of strain hardening, and the ultimate stress, and (2) the so-called "Bauschinger effect", noticeable in the unloading portions of the diagrams.

2.2.2 Concrete

Concrete used in the tests was designed to have an ultimate compressive strength of about 4000 psi. at 28 days. The mix, prepared at the laboratory, had weight proportions of 1 part Type II Cement to 0.39

parts fine sand (fineness modulus 1.54) to 2.12 parts coarse sand (fineness modulus 3.17) to 2.93 parts coarse gravel in sizes ranging from 1/4 inch to 3/4 inch (fineness modulus 6.70). The water-cement ratio of the fresh concrete was nominally set at 0.55 and the slump at around 4 inches.

To obtain the required information about the mechanical characteristics of concrete, fifteen 6 x 12 inch control cylinders were made for each pair of specimens cast. Control specimens were tested in sets of three at ages 7, 14 and 28 days and at the day of the test of the specimen. Average compressive strengths obtained as a result of these quasi-static tests are summarized in Table 2.2. Additionally, tests to determine the stress-strain relationship of concrete were conducted on the 6 x 12 inch control cylinders. These tests are summarized in Table 2.3 and a typical stress-strain relationship is given in Fig. 2.4. Mean values for ultimate stress, f_c', at test day, strain at ultimate stress, ε_o, and tangent modulus, E_c were found to be 4470 psi, 0.0028 and 3190 ksi, respectively. The mean usable value of strain, ε_c^{us}, (for unconfined concrete) defined as that strain corresponding to the strength after it dropped a value equal to 0.85 f_c' was found to be 0.0040. Although the tensile strength of the concrete, f_t, could be determined experimentally (through conventional splitting or modulus of rupture tests), for the purposes of this study an equally reliable means of obtaining values for this quantity was the use of empirically suggested relationships. The relationship used herein is $f_t = 6.8 \sqrt{f_c'}$ [19].

2.3 LOADING SYSTEM

The loading system (Figures 2.5 and 2.6) consisted of two-basic parts i.e., reaction blocks and a loading device which allowed the specimens to be tested in a horizontal plane. Reactions to forces generated by the loading device were transferred to the test floor by four heavy reinforced concrete blocks, each anchored to the floor by high strength prestressing rods.

One actuator with a piston area of 78.5 square inches and a capacity of 235 kips provided the constant magnitude axial load. It can be noted from Fig. 2.6.b that during the application of the lateral displacement time history, point B will move on line $\overline{AB}$, necessitating a control mechanism to maintain a constant magnitude of axial load. An electronic error signal, proportional to the difference between the constant command signal and the signal from the load cell which continuously measured the actual force was used for this purpose. It controlled a servo-value which, in turn, directed the flow of hydraulic oil from a main supply to one side of the actuator piston to achieve the correct load cell signal.

The force required to generate the prescribed lateral displacement time histories was provided by another hydraulic actuator. This double-acting actuator was attached to the specimen at its midlength by a special loading yoke. The actuator had a piston area of 25.4 square inches, a maximum static load capacity of 76.2 kips, and a maximum stroke of $\pm$ 6 inches. It had a pedestal base and a swivel head. The flow of hydraulic oil to the actuator was again controlled electronically through the use of a command signal and a servo-valve. The command signal used represented actuator displacement as generated by an anolog computer. The difference between this signal and the signal from a linear variable differential transformer (LVDT) incorporated into the actuator assembly controlled a 200 gallons-per-minute servo-valve which directed the flow of hydraulic oil from the main supply to the side of the actuator. The electronic systems controlling the functioning of both actuators were manufactured by MTS Systems Inc.

The specimen was supported on low friction teflon bearing pads at points A and B. A rigid link between points B and C, with hinged connections to the reinforced concrete reaction block at point C and to the specimen at point B, was used to simulate a roller support at point B and to transfer the shear force to the reaction block. A 100-kip load cell was incorporated into this link.

2.4 TEST PARAMETERS

The principal parameters of the experimental program were (1) magnitude of applied axial load, (2) transverse reinforcement ratio, and (3) history of prescribed lateral displacements (Table 2.4).

The magnitude of applied axial load was chosen to simulate the actual condition in a lower, medium or upper story column of a multistory frame. This axial load was below the "balanced-point" axial load capacity of the cross-section, consistent with standard earthquake resistant design philosophy. Otani and Sozen [25] have carried out a nonlinear response analysis of a 3-story, 1-bay reinforced concrete structure subjected to a typical ground motion and report an axial force equal to 12% of the balanced point axial force in a first story column. Bouwkamp and Kustu [26] have designed a ten-story reinforced concrete building in accordance with the current code provisions and report design axial loads equal to 52%, 31% and 11% of the balanced point axial load at the first, fifth and tenth story columns respectively. In the present study, axial forces equal to approximately 25%, 50% and 75% of the balanced point axial force capacity for the cross-section were chosen for investigation.

Transverse reinforcement was designed to resist the maximum possible shear force that could be developed (see Table 3.2, column (6), for shear resistance provided by the transverse reinforcement). Design details to meet confined concrete requirements for the columns as would apply to ductile moment resistant frames were disregarded for purposes of investigating the effect of transverse reinforcement spacing on mode of failure of specimen, and on the strength, stiffness and energy dissipation degradation characteristics.

Prescribed lateral displacements, applied at specimen mid-length, were chosen to generate low or high strain rates of lateral loading. It has been shown, in the previous phases [7,8] of the overall program, that increasing rates of loading cause increases in yield strengths and yield stiffnesses of test specimens. It was again decided to study the effects of this parameter on member behavior.

The maximum ratio of high-to-low strain rate that could be generated by the available experimental equipment was 10. Strain rate at yield of tensile reinforcement, $\dot{\varepsilon}_y$, was defined as the ratio of yield strain in tensile reinforcement, ε_y, to the time to yield, t_y; and its values for all specimens are given in Table 2.4.

2.5 DATA ACQUISITION

2.5.1 Instrumentation

The instrumentation was designed to monitor the behavior of the specimen during the test by providing continuous time records of applied loads, displacement, and resulting rotations, curvatures, strains in longitudinal and transverse reinforcement, and shear deformations. Figs. 2.7 and 2.8 show some of the instrumentation. A brief description of the types and operation of the instrumentation is given below:

i - Load Cells - Three load cells were incorporated into the test system to measure the applied loads and resulting reactions. A 200 kip load cell, placed on the longitudinal axis of the specimen, between the 235 kip actuator and the specimen, measured the applied axial load. A 100 kip load cell built into the 70 kip actuator generating the prescribed lateral displacements measured the lateral load. A third load cell placed in the link $\overline{BC}$ (Fig. 2.6.b) measured the generated reaction taken by the link.

ii - Linear Variable Differential Transformers (LVDTs) - An LVDT was attached to the end of the actuator piston rod to sense the lateral displacement.

Fourteen other LVDTs were attached to four instrumentation frames to monitor average curvatures, shear deformations and relative displacements within the critical regions. Twelve of the LVDTs were Ametek Type 500-3K-9EL, the remaining two Daytronic type. All fourteen LVDTs had a displacement range $\pm$ 0.5 inches. A typical instrumentation frame, designed specially to take into account any vertical expansion of the specimen, was mounted at a cross-section perpendicular to the longitudinal axis of the specimen, by screwing the tips of four screws into four reference points which were epoxied to the side of the specimen (Fig. 2.9). The frames were attached 5 inches apart, a distance estimated to be the distance between major flexural cracks.

A pair of LVDTs measured the relative displacements at the top and the bottom of adjacent frames (or a frame and the side of the joint area). Assuming that plane sections remain plane, relative rotations and average curvatures within four zones, two at either side of the joint area, could be obtained (Fig. 2.10). These rotations and average curvatures included effects of deformations due to slip of longitudinal reinforcement.

A measure of shear deformations in the critical regions at either side of the joint area was obtained through the use of two sets of two LVDTs diagonally crossing each other. Each LVDT provided a measure of the relative displacement of two diagonally positioned points. Average shear deformation within the critical region could then be calculated (Fig. 2.11) from these measurements. Calculated deformations obtained in this manner should be used only as a qualitative index however, since the method is valid only for the uncracked range when there is some interference of flexural deformations [27].

Measurements of relative displacements in two zones, both at the same side of the joint area, were obtained using two Daytronic LVDTs. These units were clamped to an angle section which was attached to the top plate of the lateral loading yoke. One relative displacement was obtained for the zone between the face of the joint area and the first instrumentation frame while the other was obtained for the zone between the face of the joint area and the second instrumentation frame. These relative displacements included contributions from both flexural and shear deformations. Shear deformations could then be calculated by deducting the flexural deformations as measured by the average curvature LVDTs from these relative displacements (Fig. 2.12).

iii - Clip Gages - Average strains in the top and bottom reinforcement steel in the critical region were measured utilizing two clip gages. These gages which were attached to stubs silver-soldered to the reinforcement measured the relative displacements between the stubs over their known length (Fig. 2.13), hence providing values for average strains. Average curvatures could also be calculated from the measured relative displacements.

iv - Strain Gages - Micro-dot strain gages were spot welded on transverse reinforcement bars according to the schedule shown in Fig. 2.14.

2.5.2 Calibration

The instrumentation was calibrated using conventional methods. Through the use of a calibration jig which utilized a dial-gage, known relative displacements were imposed between the attachment points of the LVDTs and clip gages, and simultaneously, the output of the recorders were observed; thus, establishing the scale sensitivities. For the same purpose, known shunt resistances were introduced into the bridge circuits for the load cells and the strain gages on the transverse reinforcement, and again the output of the recorders were observed.

2.5.3 Data Acquisition Equipment

The signals from the instrumentation had to be conditioned and amplified before being fed into the recording equipment. The conditioners for actuator load cells and lateral displacement LVDT were built into the MTS Control Consoles. The twelve Ametek type LVDTs were conditioned by Honeywell Model 119 amplifiers, each a carrier amplifier supplying a 5000 Hz. excitation voltage and providing controls for balancing the resistance and capacitance of the bridge. Signals from the Daytronic LVDTs were conditioned by two Daytronic amplifiers. Signals from the strain gages on the transverse reinforcement, the reaction load cell, and the clip gages were input into Burr-Brown Model 3088/16 differential amplifiers. Bridge completion and balance for these signals were achieved by B&F Model IC-1613-1 signal conditioners.

The dynamic nature of the test program necessitated the use of special recording equipment. Most experimental data were recorded by two Honeywell Visicorders, Models 1508 and 906. Each visicorder employed light beam oscillographs to trace continuous records of the total of 23 signals on fast developing photographic paper. Both visicorders were supplied with timing pulses from a single time-mark-generator, so that signals from the two visicorders could later be matched in time.

A Varian Model F-80 X-Y Recorder was used to display and record the lateral force vs. lateral displacement relationship during the execution of the test. The writing speed of this X-Y recorder was limited however. Therefore, it was usefull only for the quasi-static tests.

The various conditioners, amplifiers, and recording units are illustrated in Fig. 2.15.

2.5.4 Data Reduction

The bulk of the data that was recorded on visicorder papers was digitized and processed after the tests for easier interpretation. A Calma Model 685 Graphic Data Digitizer converted the graphical data to digital forms on computer compatible magnetic tape. An operator manually traced the data with a moveable stylus-carriage assembly. Stylus movements were detected by optical encoders and the ordinates of the particular signal were converted to digital signals at chosen intervals of the abscissa which in this case happened to be the time axis. Thus, the resulting coordinates were stored on magnetic tape. The data were later recovered through a computer program which applied the proper calibration factor to each signal; thus, establishing the time-history variations of forces, moments, lateral displacement, average curvatures, shear deformations, average steel strains, and transverse reinforcement strains from the digitized raw data. The time histories of these various actions and deformations were then used as the input to another computer program. This latter program was developed using the University of California Computer Center's Graphical Display System (GDS), and automatically produced the various hysteresis curves presented later.

2.6 TESTING PROCEDURE AND LOADING PROGRAM

After curing, the specimens were prepared before being placed in the test frame. Basic preparation for each specimen was similar, and the purposes were to provide visual aid in detection of cracking through whitewashing the surfaces of the specimen and marking the positions of transverse reinforcement on the whitewashed surfaces. To provide for mounting the instrumentation frames, small (1/4 inch x 1/4 inch) aluminum plates were epoxied to the surfaces of the specimen at their exact prescribed locations, and the instrumentation frames were then installed in their proper positions. The specimen was then positioned in the test set-up, lining up the pins at points A, B and D (Fig. 2.6.a), to assure the application of the axial load through the longitudinal axis of the specimen. To achieve a uniform distribution of the axial load, hydrostone was applied at both ends of the specimen, between the 1 inch steel plate and the bracket that connected the specimen to the loading system. The loading yoke used with the lateral load actuator was also hydrostoned to the specimen at midlength, to assure proper distribution of lateral load. External instrumentation was installed and the lead wires were connected to the recording equipment. Bridges for each signal were nullified to position the instruments at the center of their displacement capacities. Visicorder paper speeds, time mark generator period, scales for X-Y recorder coordinates, and controls defining the velocity and the amplitude of the lateral displacement time history were set at their preselected values.

The constant magnitude axial load was applied, and then the specimen was subjected to a series of small amplitude (less than 0.2 inches), constant velocity lateral displacement cycles (hereafter referred to as Displacement Set 0), for purposes of system check and determination of elastic properties. Subsequently, lateral Displacement Sets 1 and 2 were applied to Specimens 1 through 8, and lateral Displacement Set 1 to Specimens 9 through 12. Lateral loading was discontinued as soon as a considerable drop in member strength was observed from the lateral force-lateral displacement curve being drawn by the X-Y recorder.

Each lateral displacement set nominally contained 20 cycles with successively proportional increase in amplitude and constant velocity (Fig. 2.16). Four cycles were applied to each displacement amplitude to establish the effects of cycling at an amplitude on the degrading mechanisms. This is in accordance with earlier findings [6] that inelastic hysteresis loops tend to stabilize, for specimens with low shear stresses, after a few repititious of loading to the same displacement amplitude. Cycles with displacement amplitudes 0.8 inches and 1.6 inches were incorporated into both Displacement Sets 1 and 2, to establish the effects of previous strain history on the resistance mechanisms.

The sequence, time variation, amplitude and velocity of lateral displacement time histories prescribed were selected to meet the test objectives rather than to simulate structural response to any hypothetical seismic excitation. It would have been desirable to subject the specimens to a deformation history that might be realized in a typical structure during an extreme earthquake. However, at present, neither the future extreme earthquake ground motion can be predicted with great accuracy nor can the seismic response of reinforced concrete buildings even with the simplest of mechanical models. Inelastic behavior of reinforced concrete members is highly path-dependent [28,29], and the selection of the loading program would have to be an iterative process where analytical results would suggest test programs and the resulting experimental data would be used to improve analytical modeling. This procedure, due to the complexities it presents, was considered to be beyond the scope of the study reported herein.

3. FLEXURAL AND SHEAR STRENGTHS, AND DEFORMATION CAPACITY OF SPECIMENS

3.1 FLEXURAL STRENGTH AND FLEXURAL DEFORMATION CAPACITY

Under monotonic loading, the action of bending moment will progressively cause flexural cracking, yielding of tensile reinforcement and inducing limiting (usable) and ultimate concrete strains in the extreme unconfined and confined compression fiber of the cross section of a reinforced concrete column. Such bending moments and corresponding deformations are functions of applied axial load and can be calculated through the procedures outlined below:

3.1.1 Bending Moment and Curvature at Flexural Cracking

Flexural cracking occurs when the stress in the extreme tensile fiber of the cross section reaches a value equal to the tensile strength of concrete, f_t. Bending moment, M_{cr}, and curvature, ϕ_{cr}, at this stage are given by:

$$M_{cr} = (f_t + \frac{N}{A_{tr}}) Z \tag{3.1}$$

$$\phi_{cr} = M_{cr}/E_c I_{tr} \tag{3.2}$$

where N is the applied axial load, A_{tr} and I_{tr} are the area and moment of inertia of the transformed section, and Z is the section modulus. Eqs. (3.1) and (3.2) are strictly true only if the specimen is free of initial stresses induced by shrinkage and creep of concrete or temperature changes. However, since in reality these stresses are present, proper estimation of M_{cr} and ϕ_{cr} is difficult.

Values of lateral load, F_{cr} inducing the cracking moment, M_{cr} and lateral displacement δ_{cr} generated at this stage can be calculated using conventional methods of structural analysis and are tabulated in Table 3.1.

3.1.2 Bending Moment and Curvature at Yield of Tensile Reinforcement

i - The Interaction Diagrams - Bending moments and curvatures corresponding to yielding of tensile reinforcement can be obtained from axial force - moment and axial force - curvature interaction diagrams.

The first step in developing the interaction diagrams is defining the plastic centroid, and the ultimate and balanced point axial load capacities of the cross section. The plastic centroid is the location of resultant of stresses such that concrete and reinforcement are under uniform compressions of $0.85\ f_c'$ and f_y, respectively, and coincides with the geometric centroid for cross sections with symmetric geometry. Axial forces and moments act at the plastic centroid. Ultimate axial force capacity, N_u, of the cross section is developed when concrete and reinforcement are under uniform compressive stresses equal to $0.85\ f_c'$ and f_y, respectively. Balanced point axial force and moment capacities, N_b and M_b, are developed when the strain in the tensile reinforcement, ε_s, equals the yield strain, ε_y, and simultaneously, the extreme compression fiber strain equals a specified limiting concrete strain, ε_c. Only for axial forces below the balanced point axial force does the tensile reinforcement yield before the extreme compression fiber attains the limiting value of concrete strain. In this case, the cross section exhibits so-called ductile behavior.

To calculate the bending moments causing yielding of the tensile reinforcement, for a range of axial forces below the balanced point axial force, a linear strain distribution across the cross section is used with the strain in the tensile reinforcement equal to the yield strain, ε_y, and the strain in the extreme compression fiber equal to an assumed value, ε_c. The strains are then converted to forces (Fig. 3.2.a) using the cross section geometry and idealized stress-strain relationships of the materials (Fig. 3.1), and the summation of forces gives values for the bending moment and axial force corresponding to the assumed strain in the extreme compression fiber. Corresponding value of curvature is given by $\phi_y = \varepsilon_c/c$. Changing the value for the strain in the extreme compression fiber provides additional points on the interaction diagrams, and the process is repeated until enough points are obtained to adequately define the entire relationship.

ii - <u>Relationships Suggested by Sugano and Koreishi [18]</u> - Bending moments and curvatures causing yielding of the tensile reinforcement in reinforced concrete columns can also be calculated through use of the relationships suggested by Sugano and Koreishi which are reproduced below. Assuming both tensile and compressive steel attain strains equal to the yield strain, ε_y, it can be shown that

$$M_y = \left[g_1 \, \rho \, \frac{f_y}{f'_c} + \frac{\eta_o \, (1 - \eta_o)}{2} \right] f'_c \, b \, D^2 \qquad (3.3)$$

where $g_1 = (d - d')/D$, is the distance between tension and compression reinforcement divided by depth of section, ρ is the tensile reinforcement ratio, and $\eta_o = N/(A_g \, f'_c)$, is the axial compression index. Curvature at yield of tensile reinforcement can be obtained from

$$\phi_y = M_y/\alpha_y E_c I_{tr} \tag{3.4}$$

where the stiffness reduction factor, α_y, is empirically defined as

$$\alpha_y = [0.043 + 0.043\ a/D + 1.64\ n\ \rho + \eta_o/3]\ (d/D)^2 \tag{3.5}$$

iii - Lateral Load and Lateral Displacement at Yield of Tensile Reinforcement - Lateral load, F_y to induce the yield moment M_y; and lateral displacement, δ_y corresponding to the curvature distribution shown in Fig. 3.3 can be calculated using conventional methods of structural analysis and are tabulated in Table 3.1. Displacement induced by the so-called "N-δ" effect is included in the calculations whereas shear deformations have been considered negligible.

3.1.3 Bending Moment and Curvature When Extreme Compression Fiber Strain $\varepsilon_c = \varepsilon_c^{us}$

Bending moments and curvatures inducing a limiting (usable) value of strain, ε_c^{us}, in the extreme compression fiber of a reinforced concrete column cross section can be calculated in a manner similar to that outlined in Section 3.1.2.i. The usable strain chosen here for analysis corresponds to that strain when unconfined concrete strength has dropped to 0.85 f'_c, and its value is 0.0040 (Section 2.2.2). As shown in Fig. 3.2.b, a linear strain distribution across the cross section is used with the extreme compression fiber strain, ε_c, set at 0.0040, and the tensile reinforcement strain, ε_s, assumed at a value larger than the yield strain, ε_y (for axial forces below the balanced point axial force). Assumed strain distribution is converted to stresses and forces through the use of idealized stress-strain relationships for the materials and the cross section geometry. Summation of forces gives values for bending moment and axial force corresponding to the assumed tensile reinforcement strain. Corresponding value of the curvature is $\phi^{us} = 0.0040/c$. Changing the value of the tensile reinforcement strain results in additional points on the interaction diagrams, and the process is repeated until enough points are obtained to define the interaction diagrams.

3.1.4 Bending Moment and Curvature when Extreme Compression Fiber Strain $\varepsilon_c = \varepsilon_c^{ult}$

Concrete core, under proper confinement, exhibits a stress-strain relationship as given in Fig. 3.1.c where strains higher than $\varepsilon_c^{us} = 0.0040$ can be reached without considerable drop in strength. Bending moments and curvatures inducing ultimate values of strain, ε_c^{ult}, in the extreme compression fiber of the core section can be calculated through a procedure similar to that outlined in Section 3.1.3, and shown in Fig. 3.2.c.

3.1.5 Summary of Results

Interaction diagrams developed for strain distributions described in Sections 3.1.2 through 3.1.4 are shown in Fig. 3.4. Moments and curvatures corresponding to the loading conditions described in Sections 3.1.1 through 3.1.4, and for the axial forces under study are summarized in Table 3.1, and illustrated graphically in Fig. 3.5.

3.2 SHEAR STRENGTH

Under monotonic loading the ultimate shear strength, V_u, of specimens is composed of contributions from concrete and transverse reinforcement, i.e.:

$$V_u = V_c + V_s \tag{3.6}$$

Shear resistance provided by concrete, V_c, is known to increase with increasing axial forces acting on the specimen, and is limited by Equation 11-4 of ACI Code '71 which can be rewritten as:

$$V_c = \phi\, b\, d \left[1.9 \sqrt{f'_c} + 2500\, \rho \frac{V_c\, d}{V_c\, a - N\left(\frac{4D-d}{8}\right)} \right] < 3.5\, b\, d \sqrt{f'_c} \tag{3.7}$$

where ϕ is a capacity reduction factor as defined by ACI Code 71. An alternate equation to calculate the shear resistance of concrete has been suggested by Olesen, et. al. [30], i.e.

$$V_c = \left[M_{cr}/(a-d/2) + 0.6\, b\, d \sqrt{f'_c} \right] \tag{3.8}$$

The first term of the above equation, derived from the statics of the specimen, represents the shear required to produce inclined cracks. The second term is added simply as a correction to make the results consistent with experimental data.

Shear resistance provided by the transverse reinforcement, V_s, can be calculated from

$$V_s = A_v\, f_{ys}\, d/s \tag{3.9}$$

assuming 45° inclined cracks. In Eq. 3.9; A_v, f_{ys} and s are the area, yield stress and spacing of transverse reinforcement, respectively.

Another means of predicting the ultimate shear strength, V_u, of specimens is through the use of the empirical relationship given below, as suggested by Ohno, et. al. [15], after an analysis of the data obtained from some 175 tests conducted on reinforced concrete columns.

$$V_u = \phi\ b\ d \left[k_u\ k_p\ \frac{0.23(f'_c + 180)}{a/d + 0.23} + 1.4\ \sqrt{\rho_w\ f_{ys}}\right]\left(0.9 + \frac{N}{250\ A_g}\right)^{\dagger} \quad (3.10)$$

where k_u and k_p are empirical constants depending on d and ρ respectively, and $\rho_w = A_v/bs$, is the transverse reinforcement ratio. Eq. (3.10) implies that the ultimate shear strength, V_u, is proportional to the square root of the ratio and yield stress of the transverse reinforcement, $\sqrt{\rho_w\ f_{ys}}$; an empirical finding contradictory to equilibrium requirements for the critical region as set forth in Eq.(3.9).

Results of calculations for the specimens under study based on Eqs. (3.6) through (3.10) are summarized in Table 3.2. Also included in Table 3.2, for purposes of comparison, are the shear forces required to produce the yield moments, M_y, calculated in Section 3.1. Effect of shear reversals on the shear resistance mechanism will be discussed later.

---

† The numerical coefficients in Eq. (3.10) are consistent with the metric system of units.

4. EXPERIMENTAL RESULTS

4.1 GENERAL

The objective of the experimental investigation is to identify and to characterize the effects of relevant parameters on the inelastic cyclic behavior of reinforced concrete members subjected to combined moment, shear, and axial force. Response quantities of importance from the point of view of inelastic cyclic behavior are identified as (1) forces and deformations on the monotonic loading curve ("skeleton" curve) where stiffness and strength properties of the member change, and (2) deformation capacity, strength and stiffness degradation characteristics and energy dissipation capacity of the member under cyclic loading.

Results pertaining to the skeleton curve are presented and discussed first; then the deformation capacity, strength and stiffness degradation characteristics, and energy dissipation capacity are each considered. Experimentally obtained response characteristics are compared with the respective values calculated in Chapter 3.

4.2 OVERALL BEHAVIOR

4.2.1 Elastic Behavior

Although it is not strictly true, a specimen will be called elastic until the main (longitudinal) reinforcement yields. Inferences on the elastic properties of the specimens are made from lateral force - displacement diagrams obtained during the execution of Displacement Set 0. Three such diagrams are reproduced in Fig. 4.1, one for each of the three axial loads used in this investigation. Amount of applied axial load is the only variable parameter controlling behavior in this small displacement amplitude range. Also shown in the figure are the values of cracking and yield lateral forces and displacements that were obtained in Section 3.1. Since Eqs. (3.1) and (3.2) are true only for monotonic loading and do not account for the stiffness degradation exhibited even under small amplitudes of cyclic excitation, the initial elastic stiffness, $K_E = F_{cr}/\delta_{cr}$, overestimates the actual initial elastic stiffness. Equivalent elastic stiffness, K_{eq}, which is defined as the slope of the straight line joining the two extreme points on the lateral force - displacement diagrams, can be seen to increase with increasing applied axial load.

Also notable in these diagrams is the energy dissipating characteristic of the specimens in the "elastic" range. As a measure of the energy dissipation capacity, the area inside the lateral force-displacement loop at a lateral displacement amplitude of 0.2 inches was calculated and found to be approximately 0.9 kip-in., which is relatively small in comparison to energy dissipated at higher lateral displacement amplitudes (see Section 4.6).

4.2.2 General Characteristics of Hysteretic Action - Deformation Diagrams

i - Lateral Force - Displacement Diagrams - Lateral force-displacement curves, corresponding to Displacement Set(s) 1 (and 2, if applicable) and measured by the load cell and the LVDT on the actuator generating the lateral load, are reproduced in Figs. 4.2.a through 4.2.ℓ. These diagrams provide the most important data for evaluation of specimen behavior in terms of strength and stiffness degradation characteristics and energy dissipation capacity.

The general shape of the typical lateral force-displacement curve reflects the relative contributions of flexural and shear deformations on the total specimen deflection, with the magnitude of each contribution changing with the test series variables. When high applied axial loads cause closing of inclined cracks and diminish the effect of shear deformations, the shape of the lateral force-displacement diagrams is similar to that of the moment - average curvature diagrams (Specimens 9 through 12); whereas, when the applied axial load is relatively low, considerable effect of "pinching" deformations becomes noticeable (Specimens 1 through 4).

The strength and stiffness degradation characteristics, and the variation of these with the test series variable parameters can also be observed from these diagrams.

ii - Moment-Longitudinal Reinforcement Strain Diagrams - Bending moment at specimen centerline (bending moment due to "N-δ" effect not included) is plotted against average strain measured over 5 inches of one of the top and bottom longitudinal bars.

Shapes of these experimental bending moment-strain curves (Fig. 4.3, typical[†]) closely resemble Ramberg-Osgood type stress-strain diagrams which are conventionally used to predict inelastic behavior of (reinforcing) steel: Upon reversal of applied bending moment, the moment-strain relationship is linear with a slope close to that of the elastic portion. However, as the sense (sign) of applied bending moment changes, pronounced Bauschinger effect causes the bending moment-strain relationship to become nonlinear.

[†]Because considerable amount of data in the form of hysteresis loops have been generated as a result of the experimental investigation and because of space limitations, only typical relationships are reproduced herein. For a complete catalogue of the hysteresis loops obtained see Appendix.

Magnitude and sense of net permanent strain[†] are functions of previous loading history and magnitude of applied axial load. Compressive net permanent strains are exhibited and accumulated, as concrete in the critical region loses its compressive resistance because of cycling well in the inelastic range or because of high magnitudes of applied axial load.

iii - Moment-Average Curvature Diagrams - Bending moment at specimen midspan as generated by the applied lateral load ("N-δ" effect not included) is plotted against average curvature measured by LVDTs in Zones 1 through 4, and by clip gages mounted on the longitudinal reinforcement (Fig. 4.4, typical). Average curvatures measured by the LVDTs include effect of rotations due to slip of longitudinal reinforcement, and therefore are generally greater in absolute value than the average curvatures obtained from measurements made on the longitudinal reinforcement (compare Fig. 4.4.b with Fig. 4.4.e). However, the hysteresis loops obtained through either measurement are similar in shape, with the implication that after several inelastic cycles causing the concrete in the critical region to be throughly cracked, flexural behavior is essentially controlled by the inelastic cyclic characteristics of longitudinal reinforcement.

iv - Shear Force-Relative Displacement Diagrams - Relative displacements measured by the two Daytronic LVDTs both in the same critical region in one half of the specimens, are plotted as functions of the measured shear force (Fig. 4.5, typical). These relative displacements

---

[†] Net permanent strain is defined as the irrecoverable strain induced in the compression reinforcement (see Fig. 4.3.b).

include contributions of flexural and shear deformations, and the hysteresis loops they generate are similar in shape to the lateral force-displacement diagrams.

v - Shear Force - Shear Deformation Diagrams - Average shear deformations measured in two critical regions, one in each half of the specimens, are plotted as functions of the measured shear force (Fig. 4.6, typical).

Inspection of these diagrams reveal increases in average shear deformation under cycling at a fixed lateral displacement amplitude, with the implication that shear stiffness degradation is a direct function of cyclic loading. Moreover, this degradation appears to be enhanced with increasing lateral displacement amplitudes, and with decreasing magnitudes of applied axial load.

Also noticeable in these diagrams is the so-called "pinching" effect, a range of considerably low shear stiffness near zero loads. In this range, flexure and shear cracks formed during the previous half cycle are open, especially if the applied axial load magnitude is relatively low; therefore, aggregate interlocking and friction along the cracks are ineffective in the shear resistance mechanism. After the open cracks are closed, the instantaneous shear stiffness starts increasing with the contribution of aggregate interlocking and friction. The "pinching" effect, therefore, becomes a more significant factor controlling inelastic cyclic behavior with increasing lateral displacement amplitude and with decreasing magnitudes of applied axial load.

vi - Shear Force - Transverse Reinforcement Strain Diagrams - Strains measured by gages attached to the transverse reinforcement ties are plotted against measured shear force (Fig. 4.7, typical).

Strains in the ties are small prior to occurrence of inclined shear cracks when almost all the applied shear is resisted by concrete. However, as the inclined cracks form, a corresponding increase occurs in the strain rate in the tie (Point 1 on Fig. 4.7). Upon reversal of the applied shear, closing of cracks causes decreases in the tensile strain existing in the tie, until formation of cracks in the opposite direction imposes an additional tensile strain (Point 2 on Fig. 4.7). Before spalling of concrete cover, transverse reinforcement strain is inversely related to magnitude of applied axial load, since under high magnitudes of applied axial load, crack widths are relatively small and aggregate interlocking and friction along the cracks are effective in the shear resistance mechanism. However, further increases in the transverse reinforcement strain occur as the concrete cover spalls off, and, thus, the resistance of the cross section against transverse expansion is reduced.

4.2.3 Inclined Shear Cracking

Inclined cracking shear force, V_{cr}, is considered to be a good measure of the shear resistance provided by concrete, and its value can be inferred from the experimentally obtained shear force - transverse reinforcement strain diagrams (Fig. 4.7, typical). Until the applied shear force reaches V_{cr}, concrete in the critical region provides almost all the shear resistance, and the transverse reinforcement strains are small. Upon further increase of the applied shear force, inclined shear cracks form causing abrupt increases in transverse reinforcement strains and thus the detection of the inclined cracking shear load. Values of V_{cr} thus obtained are summarized in Table 4.1, and averages of V_{cr} for the (-) and (+) directions of loading are compared graphically with the concrete shear capacity calculated in Section 3.2 (Fig. 4.8.a).

4.2.4 Yield of Longitudinal Reinforcement

Yield of tensile longitudinal reinforcement is probably the most important response characteristic. As yielding occurs stiffness characteristics of the reinforced concrete member change drastically, and deformation and energy dissipation characteristics and strength degradation mechanism are conventionally presented and discussed in terms of actions and deformations† at yield of longitudinal reinforcement.

Measured values of lateral force, lateral displacement, bending moment at specimen midspan and average curvature for both the negative (-) and positive (+) directions of lateral loading are tabulated in Table 4.1. Averages of (-) and (+) responses, and the values calculated in Section 3.1 are presented graphically in Fig. 4.8.b and 4.8.c. The test series parameter mainly controlling actions and deformations at yield of tensile reinforcement is the magnitude of applied axial load: Increasing applied axial load, N (within the range $0 < N < N_b$) results in increasing values for actions and deformations at yield. Actions and deformations at yield of tensile reinforcement as calculated in Section 3.1 are in fair agreement with measured actions and deformations.

4.2.5 Spalling of Concrete Cover

As lateral displacement amplitudes increase beyond the yield displacement, compressive strain in the concrete cover within the critical region reaches its usable limit, ε_c^{us}, and the cover concrete starts

---

†Lateral force, shear force, and bending moment are defined as actions. Lateral displacement, average shear deformation, and average curvature are defined as deformations.

spalling off. This point in lateral loading corresponds to the initiation of considerable strength degradation and therefore is a significant index of inelastic behavior. Values for lateral displacement amplitudes which cause the cover to spall off can be obtained through an inspection of the history of compressive strain in the longitudinal reinforcement. At the instant the cover starts spalling distinct increases in the compressive strain are observed, since compressive stresses induced by the applied bending moment are now resisted essentially by the compression reinforcement (Fig. 4.3 and Fig. 4.9, typical). Since the strains in the compressive and tensile reinforcement are measured known quantities at that instant of lateral loading, by assuming a linear strain distribution across the depth of the section, the limiting value of usable concrete strain in the extreme compression fiber, ε_c^{us}, can be calculated.

Values for lateral displacement amplitudes at the initiation of concrete cover spalling and for the usable concrete strain, ε_c^{us}, obtained in the manner just outlined are tabulated in Table 4.1. Lateral displacement amplitudes causing initiation of cover spalling and thus the initiation of strength degradation are inversely related to the magnitude of applied axial load. The average value of $\varepsilon_c^{us} = 0.0048$ (with a standard deviation = 0.0011) is in fair agreement with the value $\varepsilon_c^{us} = 0.0040$ which was obtained in Section 2.2.2 from the stress-strain tests on concrete cylinders.

4.2.6 Shear Resistance Mechanism

After the formation of inclined flexure-shear cracks, applied shear force is resisted by contributions from compressed concrete above the crack, ties crossed by the crack, aggregate interlocking and friction along the crack, and the dowel action of the longitudinal reinforcement (Fig. 4.10).

In the experimental investigation conducted, no measurements were made to obtain information on shear resistance provided by aggregate interlocking and friction forces or by the dowel action. The combined contribution of aggregate interlocking and friction forces along cracks should be expected to increase with increasing applied axial load (at low displacement amplitudes, as long as abrasion of core concrete is not instigated) because of the narrowness of inclined cracks. The contribution of dowel action of longitudinal reinforcement should be expected to increase with decreasing transverse reinforcement spacing because of increased lateral support of longitudinal reinforcement, but to decrease with increasing lateral displacement amplitudes because of spalling of cover concrete and loss of lateral support of longitudinal reinforcement.

Contribution of concrete can be estimated as proposed in Section 3.2, but equations suggested there are relevant only for monotonic loading and do not reflect the likely degradations cyclic loading would induce.

The contribution of ties crossed by the inclined crack can be closely estimated by calculations based on strain measurements made on the transverse reinforcement. The number of ties crossed by the inclined crack, n, is not a determined quantity, but can be estimated by assuming 45° inclined cracks. This assumption is less valid for increasing applied axial load, when the inclined cracks become steeper with respect to the longitudinal axis of the specimen. Assuming further, an elasto-plastic stress-strain relationship for the transverse reinforcement with the yield stress, f_{ys}, and yield strain, ε_y, (see Section 2.2.1), and a uniform strain distribution along the height of the tie (that is, assuming the measured strain to be equal to the strain where the inclined crack crosses the tie), then

$$V_s = A_v f_{ys} \sum_{i=1}^{n} \frac{\varepsilon_{si}}{\varepsilon_y} \tag{4.1}$$

where ε_{si} is the measured strain in the i^{th} tie and where the maximum value $\varepsilon_{si}/\varepsilon_y$ is permitted to take is 1. Variations of applied shear force and the shear resistance provided by the transverse reinforcement, V_s, with lateral displacement amplitude for the negative direction of loading of Specimens 5 (applied axial load = 120 kips) and 9 (applied axial load = 180 kips) are shown in Fig. 4.11. The shaded portion corresponds to shear resistance provided by concrete, aggregate interlocking and friction, and dowel action. Shear capacity of concrete, V_c, as calculated for monotonic loading (Section 3.2) accounts for most of the total shear resistance prior to occurrence of inclined cracking. Upon inclined cracking (see Section 4.2.3), resistance provided by the ties starts increasing. At low displacement amplitudes high axial loads keep cracks closed, transverse reinforcement strains and, therefore, the resistance provided by the ties are relatively low. However, as the displacement amplitude increases, high axial load enhances the degradation of shear resistance provided by the concrete, aggregate interlocking and friction; and therefore the shear resistance provided by the ties increases.

An analysis of experimental data obtained reveals that (see Table 4.2) while no ties attained yield strains in tests of Specimens 1 through 4 (applied axial load = 60 kips), high magnitudes of applied axial load caused yielding in some ties in tests of Specimens 5 through 12.

4.2.7 Cracking Pattern

The observed cracking pattern is closely related to the stresses generated at the critical region by the applied bending moment, shear and axial forces, with the direction of cracks formed perpendicular to the direction of principal stresses. Flexural cracks originate at the tension side of the cross section and are perpendicular to the longitudinal axis of the specimen. Upon further increase of lateral load, when shear stresses induce high enough principal tensile stresses, inclined cracks form,usually originating from the flexural cracks. Dowel action causes splitting cracks. Deterioration of bond between tensile reinforcement and concrete causes bond cracks. Axial force and compressive stresses combine to cause spalling cracks in the compression side (Fig. 4.12.a). Upon reversal of the direction of the applied lateral load, the cracking sequence repeats itself as a mirror image (Fig. 4.12.b). Cracks thus formed propagate under cyclic loading. Spalling and splitting cracks accumulate and cause eventual loss of concrete cover and inclined cracks fracture the concrete in the critical region into a mesh of concrete blocks.

High axial loads help keep inclined crack widths narrow at low lateral displacement amplitudes, but enhance the spalling of concrete cover (Fig. 4.15). Increasing transverse reinforcement spacing causes increases in length of region of inelastic behavior. The length of region where concrete cover spalled off was approximately 10.5 inches for Specimen 9 (transverse reinforcement spacing = 3 inches), whereas the same length was more than 20 inches for Specimen 10 (transverse reinforcement spacing = 5 inches) (Fig. 4.15.a and b). Decreasing transverse reinforcement spacing causes the inclined cracks to be more closely clustered in a shorter critical region with the slopes of inclined cracks steeper with respect to the longitudinal axis of the specimen (Fig. 4.13.c).

4.2.8 Modes of Failure

Test specimens were nominally subjected to Lateral Displacement Set(s) 1 (and 2 for Specimens 1 through 8). However, loading, lateral and axial, was discontinued when a specimen was considered to have failed. Failure was assumed to have taken place if either there was a considerable degradation of lateral load resistance capacity as observed from the X-Y recorder during the execution of the test, or the observed damage to the specimen was severe enough to indicate that further lateral loading would cause lateral instability of the specimen (under moderate-to-high applied axial loads). The number of lateral displacement cycles and the maximum lateral displacement that each specimen could endure are listed in Table 4.3.

Specimens 1 through 3 (applied axial load = 60 kips) withstood the prescribed lateral displacement time histories without failing. Additional lateral loading until failure was not stipulated because it was felt that sufficient experimental data had been obtained. However, there was considerable damage in the forms of crushed and spalled concrete cover (with the length of spalled region directly related to transverse reinforcement spacing), and wide flexure and inclined flexure-shear cracks (Fig. 4.13.a, b, and c). Specimen 4 (applied axial load = 60 kips, transverse reinforcement spacing = 5 inches) failed due to buckling of longitudinal compression reinforcement (Fig. 4.13.d), as the lateral support provided by the ties proved insufficient. Concrete in the core, not confined adequately, was subjected to severe abrasion and a plastic hinge had formed by the propagation(due to cycling at large displacement amplitudes)of the intersecting inclined cracks.

Specimens 5 through 8 (applied axial load = 120 kips) exhibited similar plastic hinges. For Specimen 5, closer spacing of transverse reinforcement (at 3 inches) prevented buckling of longitudinal reinforcement. Damage observed in the critical regions at either side of the joint area was of similar magnitudes (Fig. 4.14.b). Specimen 7 (transverse reinforcement spacing also at 3 inches) failed due to lateral instability one of its halves (under a moderately high applied axial load). Concentration of accumulated damage only on one critical region was the result of probable slight unsymmetry in the lateral load application mechanism or of non-uniformity in the properties of the specimen along its length. Buckling of longitudinal reinforcement was observed upon inspection of damage to Specimens 6 and 8 (transverse reinforcement spacing = 5 inches) at a lateral displacement amplitude of 3.2 inches.

The high magnitude of the axial load applied to Specimens 9 through 12 enhanced the abrasion of core concrete and thus the transformation of the critical region into practically a plastic hinge (Fig. 4.15). (Note that maximum lateral displacement applied to Specimen 11 is 2.4 inches, compared to 2.0 inches for Specimens 9, 10, and 12). Under high compressive stresses, even at relatively low displacement amplitudes, severe spalling cracks formed inducing an accumulation of compressive strains in the longitudinal reinforcement and in the concrete core. Closer spacing of transverse reinforcement (at 3 inches) for Specimens 9 and 11 provided lateral support sufficient to prevent buckling of longitudinal reinforcement. The effect of the applied axial load on the amount of damage to the critical region can be observed by comparing Figs. 4.14.a and 4.15.a, from Specimens 5 and 9, respectively, at a lateral displacement amplitude of 2.0 inches.

In summary, the failure mechanism exhibited by each specimen was similar with the mechanism enhanced by increasing magnitudes of applied axial load, lateral displacement amplitude, and transverse reinforcement spacing.

4.3 DEFORMATION CAPACITY

4.3.1 Ductility

Deformation capacity of specimens are discussed in terms of various ductility factors. While the term ductility may often be used loosely in literature and practice, distinctions should be made with reference to the deformation component used as the basis of the definition, and also with reference to the nature of loading, i.e. cyclic or monotonic. Because generalized earthquake-like excitations (and the excitations used in this investigation) contain reversals of deformation; the displacement, strain, and average curvature ductility factors that are discussed herein are defined as the ratios of maximum cyclic usable displacement, strain, and average curvature to the displacement, strain, and the average curvature at the first yield of longitudinal reinforcement, respectively. Further, maximum usable deformation is defined as that deformation beyond which there is considerable loss of strength or stiffness.

The lateral displacement ductility factor (Table 4.3), calculated as the ratio of maximum lateral displacement at failure, δ_{max}, to the lateral displacement at yield, δ_y, decreases with increasing applied axial load.

The cyclic strain ductility factor, μ_ε^c, is defined as the ratio of maximum usable total (summation of tensile and compressive) strain in the longitudinal reinforcement to the summation of tensile and compressive strains at yield (Fig. 4.16.a). Calculated values of μ_{ε}^{c} (Table 4.4) indicate a decrease in the cyclic strain ductility factor with increasing applied axial load. Average values of cyclic strain ductility factors are 7.8, 4.8, and 3.8 corresponding to applied axial loads of 60, 120, and 180 kips, respectively.

Variation of tensile strain ductility, $\mu_{\varepsilon} = \varepsilon_s/\varepsilon_y$, with lateral displacement ductility, $\mu_{\delta} = \delta/\delta_y$ (see Fig. 4.17, typical) is linear up to $\mu_{\delta} = \mu_{\varepsilon} = 1$. At this point there is a sudden jump in recorded strains (corresponding to strains in the yield plateau), and beyond it the strains increase almost linearly with increasing lateral displacement ductility factor, but with a slope greater than unity; that is, strain ductility factors are generally larger than lateral displacement ductility factors (with the ratio of the two factors close to 2.5).

The cyclic average curvature ductility factor, μ_{ϕ}, is defined (Fig. 4.16.b) in a manner similar to the cyclic strain ductility factor. The average curvatures used in the calculations will be the average curvatures obtained from strain measurements made on the longitudinal reinforcement. Experimentally obtained values for the average curvature at yield, $\phi_y = (\phi_y^+ + |\phi_y^-|)/2$, the ultimate average curvature, $\phi_{ult} = (\max. \{\phi^+ + |\phi^-|\})/2$, and the average curvature ductility factor, $\mu_{\phi} = \phi_{ult}/\phi_y$, indicate (Table 4.4) that, with increasing applied axial load, the average curvature at yield increases, the ultimate average curvature and the cyclic average curvature ductility factor decrease. Average values of ϕ_{ult} are 0.00395, 0.00263, and 0.00189; and average values of μ_{ϕ} are 14.0, 6.7, and 4.0 corresponding to applied axial loads of 60, 120, and 180 kips, respectively . Furthermore, a comparison of experimentally obtained values for ϕ_y, ϕ_{ult}, and μ_{ϕ} with the respective values of ϕ_y, ϕ_{ult}, and μ_ϕ calculated in Section 3.1 indicates fair agreement (Fig. 4.8.c). The calculated values were based on the assumption that $\varepsilon_c^{ult} = 0.0100$, a value suggested by Blume, et. al. [31] for maximum available concrete strain; and the agreement of calculated values with the experimental results is a verification of this assumption. Use of ultimate strains that can be developed by confined concrete as suggested by Park, et. al. [21] (also see Fig. 3.1.c) would, on the other hand, have led to an overestimation of ultimate average curvatures and average curvature ductility factors available. (Application of equations suggested by Park, et. al. yields values for $\varepsilon_c^{ult} = 0.0368$ and 0.0194 for transverse reinforcement spacing $s = 3$ and 5 inches, respectively).

4.3.2 Components of Lateral Displacement

i - Lateral Displacement due to Flexural Deformations - Measured average curvatures in Zones 1 and 2 of the specimens are used to arrive at an estimate of the lateral displacement component due to flexural deformations (Fig. 4.18.a). Deformations outside the critical regions covered by Zones 1 through 4 are assumed to be in the elastic range, and to be negligible in the calculation of lateral displacement components in the inelastic range. Values of average curvature in Zone 2 are of a higher magnitude than those in Zone 1, and therefore contribute to and affect more strongly the displacement component due to flexural deformations. The variation of the average curvature in Zone 2, ϕ_2, with lateral displacement amplitude, δ, indicates (Fig. 4.19, typical) that flexural deformations increase with increasing magnitudes of applied axial load. However, the effect of transverse reinforcement spacing on the amount of flexural deformations is not pronounced[†].

Displacement component due to flexural deformations, δ_{flex}, calculated as proposed above is plotted against the measured lateral force (Fig. 4.20.a, typical), and the ratio δ_{flex}/δ is tabulated in Table 4.5.

The method proposed above to calculate the contribution of flexural deformations is valid only prior to formation of a plastic hinge. However, when a plastic hinge forms at either one of the two critical regions, because of probable non-uniformity in the properties of the specimen along its length, flexural deformations at the two halves no longer have similar magnitudes (see Fig. 4.21), and a curvature distribution such as one shown in Fig. 4.18.a can no longer be used to estimate the displacement components. Plastic hinge rotations can be calculated from a typical diagram like Fig. 4.21 by multiplying the ordinate of the shaded portion of the diagram by the length over which the average curvature measurement is made. One half of the specimen undergoes practically no bending, while the plastic hinge rotation at the other half accounts for almost all the lateral displacement (Fig. 4.18.b). Plastic hinge rotations thus calculated and their contribution to the lateral displacement are tabulated in Table 4.6.

ii - <u>Lateral Displacement due to Shear Deformations</u> - Calculation of contribution of shear deformations on the lateral displacement were based on relative displacements measured in Zones 1 and 2 of the

---

[†]Most of the analytical methods proposed to generate cyclic moment - average curvature relationships require the curvature values to have assigned values corresponding to which a bending moment is calculated. However, studies as above can be used to relate the expected value of average curvature to the displacement amplitude.

specimens. The contribution of flexural deformations to the relative displacements are accounted for as shown in Figs. 2.12 and 4.18.c. The calculated displacement component due to shear deformations are plotted as a function of the measured lateral force (Fig. 4.20.b, typical). A study of the variation of this displacement component with lateral displacement amplitude indicates (Fig. 4.22) increasing contributions of shear deformations with increasing transverse reinforcement spacing and decreasing magnitudes of applied axial load (see also Table 4.5).

iii - Estimation of Lateral Displacement from Flexural and Shear Deformations - The displacement components due to flexural and shear deformations, as calculated above, were combined and plotted as a function of measured lateral force (Fig. 4.20.c, typical). Comparison of this diagram with the diagram showing the measured lateral displacement as a function of measured lateral force (Fig. 4.2.c) indicates fair agreement, with the implication that internal deformation components, once defined in terms of test parameters and mathematically generated, can be combined to yield a method of predicting the member force - displacement relationship.

4.4 STIFFNESS DEGRADATION

4.4.1 Stiffness Characteristics of the Overall Specimen

By adopting a dimensionless coordinate system, i.e. expressing the lateral force, F^*, in the dimensionless form F^*/F^*_y (where the superscript* denotes forces adjusted by the "N-δ" effect) and the lateral displacement, δ, in the form δ/δ_y, equivalent yield stiffness of the member, K_y, can be defined to be equal to unity (Fig. 4.23). Omitting the effect of strength degradation - which will later be treated separately - equivalent stiffness for a half cycle in the inelastic range starting from a point ($\pm$ 1, $\delta^{\pm}/\delta_y$) can be seen to have deteriorated by a factor α where

$$\alpha = \frac{2\ \delta_y}{\max\{\delta^+\} + \max\{|\delta^-|\}} \tag{4.2}$$

and where $\max\{\delta^+\}$ and $\max\{|\delta^-|\}$ are maximum absolute values of lateral displacements already applied to the specimen in the (+) and (-) directions of lateral loading, respectively. Returning stiffness, K_r, can be approximated by

$$K_r = \alpha\ K_{cr} \tag{4.3}$$

where K_{cr} is the cracking stiffness expressed (in the dimensionless form) as $(F^*_{cr}/F^*_y)/(\delta_{cr}/\delta_y)$. The agreement between the return stiffnesses approximated by the above approach and obtained experimentally is satisfactory (Fig. 4.24, typical). The conventionally used method [32] to predict the stiffness upon return from a displacement level δ in the form $K_r = K_y\ (\delta/\delta_y)^{\beta}$, where β is an empirical constant varying between 0.3 and 0.6, has the disadvantage of neglecting the effect of previous loading history.

4.4.2 Stiffness Characteristics of the Critical Region

The initial cracked sectional stiffness, K_I, can be defined as the ratio of bending moment to average curvature at yield of longitudinal reinforcement. Its calculated and measured values can be obtained from calculated and measured values of bending moments and average curvatures already reported in Sections 3.1.2 and 4.2.4, respectively. Upon yield of tensile reinforcement, when strain in the tensile reinforcement is in the yield plateau, instantaneous bending stiffness (slope of the bending moment vs. average curvature diagram) is virtually reduced to zero. However, as unloading starts, instantaneous stiffness is restored to a value close to the initial cracked sectional stiffness. As the applied bending moment is reduced to zero, instantaneous bending stiffness starts degrading considerably due to the Bauschinger effect; and the amount of the degradation is directly proportional to the lateral displacement amplitude and inversely proportional to the magnitude of applied axial load (Fig. 4.25.a). The variation of instantaneous bending stiffness from this point of zero lateral load (where the instantaneous bending stiffness has the value shown in Fig. 4.25.a) to the point of maximum lateral displacement in the reversed direction (where the instantaneous bending stiffness equals approximately zero) is almost linear.

Of particular interest from the point of view of instantaneous shear stiffness is the range of low stiffness exhibited in the shear force - average shear deformation diagrams. Lateral force - displacement diagrams reflect the effect of this range of low stiffness by exhibiting a "pinched" portion, beginning at about zero lateral load when cracks are open. Degradation of instantaneous shear stiffness (slope of the shear force - average shear deformation diagram) at such a point in lateral loading seems to be enhanced with increasing lateral displacement amplitudes (Fig. 4.25.b). However, such a pronounced range of low instantaneous shear stiffness cannot be detected in tests of specimens under high magnitudes of applied axial load, since the axial load tends to keep the inclined cracks narrow and increase the shear stiffness.

4.5 STRENGTH DEGRADATION

Lateral force - displacement diagrams obtained experimentally are studied to extract information on the mechanism of strength (lateral load resistance capacity) degradation. A preliminary analysis of experimental data indicates strength degradations with increasing lateral displacement amplitudes and with cycling at a displacement amplitude in the inelastic range.

The study on strength degradation with increasing lateral displacement amplitudes indicated (Fig. 4.26) the following. (1) Strength degradation starts at lower displacement amplitudes for increasing magnitudes of applied axial load, and the displacement amplitude at the initiation of strength degradation approximately corresponds to the displacement amplitude when the concrete cover starts spalling off (as has already been reported in Section 4.2.5). (2) The degradation (decrease of F^*/F^*_y ratio) is almost linearly related to the lateral displacement amplitude, i.e. the F^*/F^*_y vs. μ_δ relationship can be approximated by a straight line with a slope S_μ. (3) The negative slope, S_μ, increases in absolute value with increasing magnitudes of applied axial load and increasing transverse reinforcement spacing.

The study on strength degradation with cycling at a lateral displacement amplitude in the inelastic range indicated (Fig. 4.27) that, prior to failure, i.e. for values of F^*/F^*_y greater than $F^*_{failure}/F^*_y$, the degradation is almost linearly related to the number of inelastic cycles applied after the initiation of the degradation. Further, the negative slope of the approximating straight line, S_J, exhibits increasing absolute values with increasing magnitudes of applied axial load and increasing transverse reinforcement spacing. After the strength drops below the failure load, the absolute value of this slope increases noticeably.

4.6 ENERGY DISSIPATION CAPACITY

A measure of energy dissipated by a test specimen during a cycle of lateral loading is the area enclosed within the lateral force - displacement hysteresis loop. This area can be expressed as the algebraic sum of areas underneath lateral force - displacement curves corresponding to consecutive half cycles of lateral loading. The area is calculated by a numerical method employing a three-point Gauss-Legendre quadrature and Lagrangian interpolation at the three integration points, implemented in a computer program.

The study of the variation of areas enclosed within the lateral force - displacement diagrams (i.e. of energy dissipated, ΔW, per cycle by the specimen) with the test parameters indicated the following results (Fig. 4.28). (1) Energy dissipated increases almost linearly with increasing lateral displacement amplitudes. (2) Increasing magnitudes of applied axial load cause increases in energy dissipated at a lateral displacement amplitude; and this increase is mainly attributable to the increase in lateral yield force due to increasing axial load. (3) Energy dissipation capacity deteriorates because of cycling at a lateral displacement amplitude (two values shown in the figures at a displacement amplitude correspond to first and last cycles of loading at that amplitude); except that at lateral loading stages of imminent failure there is an apparent increase in energy dissipation capacity due to cycling. This increase is the reflection of shaded portion (Fig. 4.29.a) of lateral force displacement diagrams resulting from considerable strength degradation. (4) Transverse reinforcement spacing has no pronounced effect on energy dissipation capacity. (5) Measured energy dissipation capacity, ΔW, of the test specimens at a displacement level can be closely approximated by

$$\Delta W^c = 2 F_y^* (\delta - \delta_y) \qquad (4.4)$$

where ΔW^c is the area enclosed within a cycle of a hysteresis loop generated by the stiffness degrading model suggested by Clough and Johnston [33] (Fig. 4.29.b). Experimentally obtained values for F_y^* and δ_y (as reported in Table 4.1) were used in establishing ΔW^c as the approximating dashed line in Fig. 4.28.

It was pointed out earlier that the increase in energy dissipation capacity with increasing magnitudes of applied axial load was mainly attributable to increases in lateral yield force due to increasing axial load. To isolate this effect and to render the study on energy dissipation capacity dimensionless, a definition of equivalent damping factor, ξ, as suggested by Jennings [34] is adopted herein. Accordingly,

$$\xi_i = \frac{\Delta W}{4 \pi W_i} \qquad (4.5)$$

where W_i is an energy measure for the monotonic force - displacement relationship, with its various definitions shown in Fig. 4.29.c. The damping factor ξ_2 (corresponding to the energy measure W_2) increases and approaches an asymptotic upper limit for increasing lateral displacement amplitude (Fig. 4.30). The effect of increasing magnitudes of applied axial load (with the effect of increasing lateral yield load now removed from consideration) is to increase the energy dissipation capacity at a given lateral displacement amplitude.

Energy dissipated within a unit length of the critical region can be inferred from the areas enclosed within the bending moment - average curvature diagrams obtained experimentally. Areas within these diagrams are calculated by the method used to calculate the areas inside the lateral force - displacement diagrams. Most of the energy dissipated within the critical region is attributable to the work done by the forces in the longitudinal reinforcement undergoing strains. At a given lateral displacement amplitude, energy dissipated per unit length of the critical region increases with increasing magnitudes of applied axial load and with increasing transverse reinforcement spacing (Fig. 4.31), since the response of the longitudinal reinforcement is intensified under such conditions.

5. MATHEMATICAL MODEL

5.1 INELASTIC HYSTERETIC BEHAVIOR

To formulate an appropriate mathematical model for reinforced concrete members subjected to cyclic inelastic deformations under combined moment, shear, and axial force, the lateral force-displacement behavior must be modelled realistically; i.e. one must be able to obtain the lateral force time history corresponding to a controlled lateral displacement time history.

Suppose for example, the lateral displacement time history of a member is that function shown in Fig. 5.1a. The corresponding lateral force-displacement relation will be very similar to that shown by the solid line in Fig. 5.2. Knowing these two relations, the lateral force time history can be obtained as shown in Fig. 5.1.b.

In modelling the force-displacement relation of a member under constant axial load, one should first establish the so called "skeleton" curve. This curve is defined as the lateral force-displacement relation under separate but independent positive and negative monotonically increasing lateral displacements. Referring to Fig. 5.2, if the member under constant axial load is initially subjected to a positive monotonically increasing lateral displacement, the lateral load will increase "elastically" to point M, remain at essentially a constant value F_y[†] under yielding conditions to point Q, and then will drop off along line QS showing a decrease in strength with increasing displacement beyond δ_N. This decrease is due primarily to crushing and spalling of the

[†]Usually there will be an increase in the lateral force beyond F_y due to strain hardening of the longitudinal reinforcement. On the other hand, if the axial load is very large, a descendent curve will be exhibited due to "N-δ effect.

concrete on the compression sides of the member in the critical region. If instead the member under the same axial load had initially been subjected to a negative monotonically increasing lateral displacement, the lateral load would change along curve OM'Q' and then drop off with further increases in lateral displacement along line Q'S'. The force-displacement relations under these two monotonic conditions combine to form the basic skeleton curve S'Q'M'OMQS.

Let us now examine in more detail the force-displacement relation shown in Fig. 5.2 for cyclic loading. If initially, cyclic loading should take place at amplitudes in the range $-\delta_y < \delta < \delta_y$, the member will remain "elastic" and the corresponding force-displacement time history will be along line MM'. However as soon as the lateral displacement exceeds the yield level, hysteretic inelastic response follows with each subsequent cycle of deformation. In Fig. 5.2, the yield level is first exceeded at point M' with the displacement continuing to a value δ_1 as shown at point P'. The displacement then reverses and continues to δ_2 along curve P'MP (J = 1) which constitutes the first full half-cycle of deformation following initial yielding of the member. Again reversing the lateral displacement and continuing to δ_3 along curve PP'Q'R' (J = 2), the second full half-cycle of deformation is completed. Had this particular half-cycle terminated at point P' rather than R', continuing repeated cycles of deformation from δ_1 to δ_2 and back to δ_1 would produce stable hysteretic loops connecting points P and P'. Such stable behavior is experienced provided the absolute values of δ_1, δ_2, and all previous displacements have not exceeded δ_N and provided the shear stresses are relatively low. The third full half-cycle of deformation in Fig. 5.2 starts at point R', proceeds along curve J = 3 to point T, and then follows the skeleton curve to point R where the deflection equals δ_4. Note that at deflection δ_2 along this curve, the lateral force is somewhat reduced from the value F_y experienced on the previous half-cycle as represented by point P. Such a reduction at a fixed amplitude is experienced when the previous deformation time history has exceeded $\delta = \pm \delta_N$. This represents unstable hysteretic behavior which follows with each subsequent half-cycle as shown by curves J = 4,5,6,7 and 8. Note that quantities J, δ_J, t_J, and F_J shown in Figs. 5.1, 5.2, and 5.3 refer to the number of inelastic half-cycles following initial yielding, the displacement at the initial point of the Jth inelastic half-cycle, time at the initial point of the Jth inelastic half-cycle, and the lateral force at the initial point of the Jth inelastic half-cycle,respectively.

Three important characteristics of inelastic cyclic behavior become apparent (1) the reduction in overall (or average) stiffness with increasing amplitudes of inelastic deformation beyond $\delta = \pm \delta_Y$, (2) the reduction in lateral resistance at a fixed displacement with each repeated full half-cycle of inelastic deformation beyond $\delta = \pm \delta_N$, and (3) the shape of the hysteretic loops as influenced by certain member parameters and loading conditions. It is important when formulating an appropriate mathematical model that these characteristics be represented in a realistic manner. To be practical however this model must be easily adapted to numerical procedures. Therefore, a proper balance must be maintained between simplicity and accuracy.

5.2 FORM OF MATHEMATICAL MODEL

To formulate an appropriate force-deflection mathematical model, an analytical expression must be developed which will characterize the Jth inelastic half-cycle ($J = 1,2,\ldots$) starting at time t_J. Since in applications, the extent of the Jth half is not known prior to its occurrence, this expression must be formulated knowing only the initial point (δ_J, F_J) representing $t = t_J$ and the previous force-deflection time history.

To accomplish this, a function $F_J(\delta)$ will be written which passes through the known initial point (δ_J, F_J), designated here as point A, and an index point B whose location reflects the influence of the member's force-deflection time history prior to $t = t_J$. The deflection at point B, designated as δ_J^M, is the maximum deflection which occurred prior to $t = t_J$ for half-cycles of increasing deflection and is the minimum deflection which occurred prior to $t = t_J$ for half-cycles of decreasing deflection, i.e.

$$\delta_J^M = \begin{cases} \text{Max. } \delta(t) \quad 0 < t < t_J; \begin{cases} J = 3,5,7,\ldots; & F_1 = -F_y \\ J = 2,4,6,\ldots; & F_1 = +F_y \end{cases} \\ \\ \text{Min. } \delta(t) \quad 0 < t < t_J; \begin{cases} J = 2,4,6,\ldots; & F_1 = -F_y \\ J = 3,5,7,\ldots; & F_1 = +F_y \end{cases} \end{cases} \tag{5.1}$$

The first inelastic half-cycle is one exception however in which case

$$\delta_1^M = \begin{cases} +\delta_y \quad ; & F_1 = -F_y \\ -\delta_y \quad ; & F_1 = +F_y \end{cases} \tag{5.2}$$

The lateral force at point B, designated as F_J^M, is given by

$$F_J^M = \begin{cases} F_J^P - \Delta F_{J-1} - \Delta F_J \;; & \begin{cases} J = 3,5,7,\ldots;\; F_1 = -F_y \\ J = 2,4,6,\ldots;\; F_1 = +F_y \end{cases} \\ \\ F_J^P + \Delta F_{J-1} + \Delta F_J \;; & \begin{cases} J = 2,4,6,\ldots;\; F_1 = -F_y \\ J = 3,5,7,\ldots;\; F_1 = +F_y \end{cases} \end{cases} \tag{5.3}$$

where F_J^P is equal to instantaneous lateral force which was present when $\delta(t)$ last reached the value δ_J^M as defined by Eq. (5.1) and where ΔF_{J-1} and ΔF_J are positive quantities representing resistance losses due to possible unstable hysteretic behavior during half-cycles $J-1$ and J, respectively. Each of these losses exist only if the deflection time-history during or prior to the half-cycle represented has exceeded $+\delta_N$ or $-\delta_N$. The value of F_J^M for the first inelastic half-cycle is given by

$$F_1^M = \begin{cases} +F_y \;; & F_1 = -F_y \\ -F_y \;; & F_1 = +F_y \end{cases} \tag{5.4}$$

The inelastic half-cycles for $J = 1$ through $J = 8$ in Fig. 5.2 are separated and shown again in Fig. 5.3. The initial point A, the index point B, and the terminal point C is shown for each half-cycle.

In formulating function $F_J(\delta)$, it is convenient to use the slope of the straight line passing through points A and B, i.e.

$$K_J \equiv \frac{F_J^M - F_J}{\delta_J^M - \delta_J} \quad J = 1,2,3\ldots \tag{5.5}$$

This function, with certain restrictions on its use, can be expressed by the following approximate empirical relations:

$$F_J(\delta) = F_J + K_J(\delta-\delta_J) + A_J \cos \frac{\pi}{2}\left[\frac{2\delta - \delta_J^M - \delta_J}{\delta_J^M - \delta_J}\right] - B_J\left(\frac{1}{2} + \frac{1}{2}\cos\frac{\pi\delta}{\delta_{PJ}}\right) \quad (5.6)$$

$\delta_{PJ} < 0$; $\delta_{PJ} \le \delta \le - \delta_{PJ}$; $J = 1,3,5,\ldots$; $F_1 = - F_y$ (a)

$\delta_{PJ} < 0$; $\delta_{PJ} \le \delta \le - \delta_{PJ}$; $J = 2,4,6,\ldots$; $F_1 = + F_y$ (b)

$$F_J(\delta) = F_J + K_J\,(\delta-\delta_J) + A_J \cos \frac{\pi}{2}\left[\frac{2\delta - \delta_J^M - \delta_J}{\delta_J^M - \delta_J}\right] \quad (5.7)$$

$\delta_{PJ} < 0$; $\delta \le \delta_{PJ}$; $\delta \ge \delta_{PJ}$; $J = 1,3,5,\ldots$; $F_1 = - F_y$ (a)

$\delta_{PJ} < 0$; $\delta \le \delta_{PJ}$; $\delta \ge \delta_{PJ}$; $J = 2,4,6,\ldots$; $F_1 = + F_y$ (b)

$\delta_{PJ} > 0$; $- \infty < \delta < \infty$; $J = 1,3,5,\ldots$; $F_1 = - F_y$ (c)

$\delta_{PJ} > 0$; $- \infty < \delta < \infty$; $J = 2,4,6,\ldots$; $F_1 = + F_y$ (d)

$$F_J(\delta) = F_J + K_J\,(\delta-\delta_J) - A_J \cos \frac{\pi}{2}\left[\frac{2\delta - \delta_J^M - \delta_J}{\delta_J^M - \delta_J}\right] + B_J\left(\frac{1}{2} + \frac{1}{2}\cos\frac{\pi\delta}{\delta_{PJ}}\right) \quad (5.8)$$

$\delta_{PJ} > 0$; $- \delta_{PJ} \le \delta \le \delta_{PJ}$; $J = 2,4,6,\ldots$; $F_1 = - F_y$ (a)

$\delta_{PJ} > 0$; $- \delta_{PJ} \le \delta \le \delta_{PJ}$; $J = 1,3,5,\ldots$; $F_1 = + F_y$ (b)

$$F_J(\delta) = F_J + K_J\,(\delta-\delta_J) - A_J \cos \frac{\pi}{2}\left[\frac{2\delta - \delta_J^M - \delta_J}{\delta_J^M - \delta_J}\right] \quad (5.9)$$

$\delta_{PJ} > 0$; $\delta \le - \delta_{PJ}$; $\delta \ge \delta_{PJ}$; $J = 2,4,6,\ldots$; $F_1 = - F_y$ (a)

$\delta_{PJ} > 0$; $\delta < - \delta_{PJ}$; $\delta \ge \delta_{PJ}$; $J = 1,3,5,\ldots$; $F_1 = + F_y$ (b)

$\delta_{PJ} < 0$; $- \infty < \delta < \infty$; $J = 2,4,6,\ldots$; $F_1 = - F_y$ (c)

$\delta_{PJ} < 0$; $- \infty < \delta < \infty$; $J = 1,3,5,\ldots$; $F_1 = + F_y$ (d)

Quantities A_J and B_J appearing in Eqs. (5.6) - (5.9) are positive coefficients. Quantity δ_{PJ} appearing in Eq. (5.6) and the conditional relations for both Eqs. (5.6) and (5.7) is that value of δ which yields a zero value for $F_J(\delta)$ using Eq. (5.7). Likewise, the quantity δ_{PJ} appearing in Eq. (5.8) and the conditional relations for both Eqs. (5.8) and (5.9) is that value of δ which yields a zero value for $F_J(\delta)$ using Eq. (5.9).

The first two terms on the right hand side of Eqs. (5.6)-(5.9) express the equation of the straight line passing through points A and B while the remaining two terms in Eqs. (5.6) and (5.8) and the remaining single term in Eqs. (5.7) and (5.9) represent the deviation of the function $F_J(\delta)$ from this straight line. The last term in Eqs. (5.6) and (5.8) containing the coefficient B_J represents the pinched form of the hysteretic loop. Implicit in the form of this last term is the simplifying assumption that the pinched form is symmetric with respect to $\delta = 0$. This assumption is, of course, not strictly true.

Function $F_J(\delta)$ as defined by Eqs. (5.6)-(5.9) can represent the entire Jth half-cycle only when it stays within certain bounds of the skeleton curve $F_S(\delta)$; i.e. the function $F_J(\delta)$ must never be extended across the skeleton curve for $|\delta| > \delta_Y$. For example in Fig. 5.2, while half-cycles J=4 through J=8 can be represented entirely by Eqs. (5.6)-(5.9), half-cycles J=1 through J=3 can only be partly represented by these equations. Function $F_J(\delta)$ as defined by Eqs. (5.6)-(5.9) represents half-cycles J=1, J=2, and J=3 from their initial points to points M, P', and T, respectively. The remaining portions of these half-cycles, namely portions MP, P'Q'R', and TQR, must follow the skeleton curve. Mathematically this means that when $F_J(\delta)$ as defined by Eqs. (5.6)-(5.9) satisfies the condition

$$|F_J(\delta)| < |F_S(\delta)| \qquad \delta < -\delta_y \ ; \ \delta > \delta_y \ ; \ J = 1,2,\ldots \tag{5.10}$$

it is applicable. However, when Eqs. (5.6)-(5.9) do not satisfy Eq. (5.10), it is not applicable in which case $F_S(\delta)$ should be used for $F_J(\delta)$. Obviously therefore, the skeleton curve must be represented in mathematical terms. Referring to Fig. (5.2), this relation can be expressed in the form

$$F_S(\delta) = \begin{cases} \dfrac{F_y}{\delta_y}\,\delta & -\delta_y \le \delta \le \delta_y \\ F_y & \delta_y \le \delta \le \delta_N \\ -F_y & -\delta_N \le \delta \le -\delta_y \\ F_y\left[1 - \beta_S\left(\dfrac{\delta_y}{\delta_N} - \dfrac{\delta_y}{\delta}\right)\right] & \delta \ge \delta_N \\ -F_y\left[1 - \beta_S\left(\dfrac{\delta_y}{\delta_N} + \dfrac{\delta_y}{\delta}\right)\right] & \delta \le -\delta_N \end{cases} \tag{5.11}$$

where β_S is a positive scalar factor.

Parameters δ_N, β_S, ΔF_J, A_J, and B_J appearing in the above relations which formulate the overall mathematical model must be obtained from experimental evidence. Having their numerical values along with the numerical values for F_y and δ_y, the Jth inelastic half-cycle is completely defined. Once the Jth half-cycle is complete, its terminal point becomes the initial point for the J+1 half-cycle. One defines this half-cycle in exactly the same manner used for the Jth half-cycle. By this method, one can obtain the entire force-displacement time history.

5.3 EVALUATION OF PARAMETERS IN MATHEMATICAL MODEL

The parameters of the mathematical model presented in the previous section can be identified as F_y, δ_y, δ_N, β_S, ΔF_J, A_J, and B_J. Based on experimental data, empirical relations have been formulated for their numerical evaluation.

5.3.1 Factors F_y and δ_y

Numerical values for lateral force and displacement at initial yield, F_y and δ_y, would normally be obtained through the analytical method presented in Section 3.1. Because this method is for monotonic loading, and does not take into consideration stiffness degradations induced by cycling in the "elastic" range, the calculated lateral displacement at yield, δ_y, slightly underestimates the true value.

The numerical values for F_y and δ_y used in the subsequent calculations were obtained by averaging the experimentally measured values (Table 4.1) for specimens under the same axial load. These values are reproduced in Table 5.1.

5.3.2 Factor δ_N

The lateral displacement at initiation of loss of lateral resistance, δ_N, is an inverse function of the magnitude of applied axial load, N. Although the numerical values of δ_N used in the calculations herein were obtained by averaging the experimental values (Section 4.5; Table 5.1), they could be evaluated using the empirical relation

$$\frac{\delta_y}{\delta_N} = 0.05 + 2.58\ \eta_o \tag{5.12}$$

where $\eta_o = N/bD\ f'_c$ is an axial compression index. This relation agrees quite well with the experimental data.

5.3.3 Factor β_S

Factor β_S is a measure of the loss of lateral resistance due to increasing lateral displacement and, as shown by experimental results, is a function of applied axial load, N, and transverse reinforcement spacing, s. Experimental values of β_S as used in the subsequent calculations are shown in Table 5.1. These values can be estimated using the empirical relation

$$\beta_S = 0.27 - 0.045\ \frac{d}{s} + \left(2.92 - 0.49\ \frac{d}{s}\right)\eta_o \qquad (5.13)$$

5.3.4 Factor ΔF_J

For displacement amplitudes less than $\pm\ \delta_N$, there is no loss in resistance over a full half-cycle of deformation; therefore,

$$\Delta F_J = 0 \qquad \max.\ \{|\delta(t)|\} \leq \delta_N \qquad 0 < t < t_J \qquad (5.14)$$

For displacement amplitudes greater than $\pm\ \delta_N$ a loss in resistance does occur which can be approximated by the relation

$$\Delta F_J = \beta\ F_y \qquad \delta_M > \max.\ \{|\delta(t)|\} > \delta_N \qquad 0 < t < t_J \qquad (5.15)$$

where β is a constant for a given test specimen but does depend upon magnitude of axial load and, spacing of transverse reinforcement. Displacement δ_M is that value of δ beyond which the loss in resistance per full half-cycle ΔF_J becomes significantly larger than that given by Eq. (5.15).

The numerical values of β obtained from experimental data are shown in Table 5.1. These values can be estimated using the empirical relation

$$\beta = 0.15\,\eta_o^2 + 0.002\left(3.33 - \frac{d}{s}\right) \tag{5.16}$$

5.3.5 Factors A_J and B_J

Numerical values for A_J and B_J were obtained by a least square fit of the experimentally obtained lateral force displacement relationships (Figs. 4.2a through 4.2ℓ) using the polynomials appearing on the right hand side of Eqs. (5.6) through (5.9). This least-squares fit shows that simple empirical relationships can be used in the estimation of factors A_J and B_J, namely:

$$\frac{A_J}{F_y} = -\,0.17 + (0.27 + 0.30\,\eta_o)\mu_J - (0.02 + 0.04\,\eta_o)\mu_J^2 \qquad \mu_J \geq 1 \tag{5.17}$$

and

$$\frac{B_J}{F_y} = \left(0.245 - 0.284\,\eta_o - 0.008\,\frac{d}{s}\right)\left(\mu_J - 1\right)^{1/2} \qquad \mu_J \geq 1 \tag{5.18}$$

The quantity μ_J appearing in Eqs. (5.17) and (5.18) is the cyclic lateral displacement ductility factor defined as:

$$\mu_J = \frac{\left|\delta_J^M - \delta_{J-1}^M\right|}{2\delta_y} \tag{5.19}$$

The experimental relationships (A_J/F_y) vs. μ_J and (B_J/F_y) vs. μ_J for the test series parameters η_o and d/s are shown in Figs. 5.4 and 5.5, respectively.

Factor B_J reflects the amount of "pinching", or the reduction of instantaneous shear stiffness near zero lateral load. It is well established (see, for example [8]) that this reduction in stiffness is an inverse function of a/D, the moment arm-to-depth ratio. Since in the present experimental investigation only one a/D ratio (fairly high to prevent shear type failures) was used, the effect of this ratio is not apparent in Eq. (5.18); therefore it is suggested that the quantity B_J/F_y be increased properly for decreasing and critical values of a/D.

5.4 CALCULATED LATERAL FORCE-DISPLACEMENT RELATIONSHIPS

The mathematical model presented in the preceeding sections can be checked against the experimental test data using a specially developed computer program. The input to the program is summarized in Table 5.1. Magnitudes of applied axial load, and transverse reinforcement spacing, and the number of cycles at each lateral displacement amplitude must also be input. Lateral force-displacement relationships calculated through the use of the mathematical model are presented graphically in Figs. 5.6a through 5.6d, each corresponding to a different set of test series variables. Only the relationships corresponding to the first and last half cycles of lateral loading at a lateral displacement amplitude in the inelastic range are duplicated (except in Fig. 5.6d). A direct comparison of the calculated lateral force-displacement relationships (Fig. 5.6, "N-δ" effect included) with the measured lateral force-displacement relationships (Fig. 4.2, "N-δ" effect not included) is generally not possible, except when the measured lateral force-displacement diagrams are adjusted by the "N-δ" effect (as in Figs. 4.2ℓ for Specimen 12, and in Fig. 5.6b for Specimen 5). The mathematical model reproduces satisfactorily the important response characteristics pertinent to inelastic cyclic behavior. As evidence of its simplicity it is worth noting that the calculations required to generate the lateral force-displacement diagrams for 6 specimens, each with a different combination of applied axial load and transverse reinforcement spacing and each containing about 40 half cycles of loading, requires about 3 seconds of central processor time in the CDC-6400 computer.

6. SUMMARY AND CONCLUSIONS

6.1 SUMMARY

On the basis of the experimental results and analyses carried out, inelastic cyclic behavior of the test specimens can be summarized according to the following observations:

(1) Monotonic loading force-deformation relationships can be predicted by defining the forces and deformations corresponding to flexural cracking, yield of tensile reinforcement, spalling of concrete cover and yield of transverse reinforcement. Each of these factors brings about a change in the strength and/or stiffness characteristics of the overall specimen. Forces and deformations at flexural cracking and yield are directly proportional to the magnitude of axial load. Lateral displacements corresponding to initiation of spalling of concrete cover (and the degradation of strength) and yield of transverse reinforcement are inversely proportional to the magnitude of axial load. A monotonic loading force-deformation relationship showing the above characteristics can be used as a basis in the prediction of inelastic cyclic behavior.

(2) Degradation of strength and member stiffness with cyclic loading are enhanced with increasing magnitudes of axial load, transverse reinforcement spacing and lateral displacement amplitude. Degradation of instantaneous stiffness in the critical region is due to Baushinger and "pinching" effects.

(3) Ultimate deformation capacity of a specimen decreases with increasing magnitudes of axial load and increasing transverse

reinforcement spacing. Lateral displacement is composed of flexural (the rotations due to slip of longitudinal reinforcement included) and shear deformations taking place in the critical regions. The length over which inelastic deformations take place increases with increasing magnitude of axial load and increasing transverse reinforcement spacing.

(4) Energy dissipation capacity increases with increasing magnitude of axial load due to more contact friction along cracks, but decreases with repeated cycling at a fixed displacement amplitude. Transverse reinforcement spacing has no significant effect on the energy dissipation capacity.

(5) Strain measurements made on the transverse reinforcement provide reliable indications of inclined cracking and of the changes in the shear resistance mechanism. Shear resistance capacity of concrete deteriorates considerably and eventually diminishes to zero under cyclic loading in the inelastic range.

(6) Failure of a specimen is the culmination of all degrading mechanisms. First, accumulation of damage in the form of spalled cover concrete, intersecting inclined cracks, and abrased concrete core transforms the critical regions into "plastic hinges", and then lack of lateral stability of the longitudinal reinforcement brings about ultimate failure. This lateral instability, naturally, is directly related to increasing magnitudes of axial load and transverse reinforcement spacing.

6.2 CONCLUSIONS

(1) Axial force can significantly affect and alter the behavior of critical regions and members subjected to inelastic cyclic loading. Stiffness and strength characteristics and deformation capacity of critical regions deteriorate with increasing axial force. Therefore, extreme care should be taken in the design of critical regions which may be subjected to substantial axial force (> 0.4 N_b) and inelastic deformations.

(2) The effect of transverse reinforcement spacing on member behavior was found to be minimal. This lack of significant influence is undoubtedly due to relatively large shear span to depth (a/D) ratio used for these tests. Realizing the detrimental effects of combined high shear and axial forces, care must be exercised in using the results reported herein for applications where the shear force is a potentially controlling factor of the behavior. It is quite apparent that further experimental research is needed to characterize inelastic cyclic behavior of critical regions under moment, high shear and axial forces.

(3) Rate of loading as observed in the overall investigation has no significant effect on inelastic cyclic behavior [7,8].

(4) The proposed mathematical model adequately reflects the important characteristics of the inelastic cyclic behavior of members under combined flexure, shear and axial force. Its application to structural modelling under more general loading conditions needs further investigation.

REFERENCES

1. Seismology Committee, "Recommended Lateral Force Requirements and Commentary," Structural Engineers Association of California, 1969.

2. International Conference of Building Officials, "Uniform Building Code," Vol. 1, Pasadena, California, 1970.

3. Anderson, J. C. and Bertero, V. V., "Seismic Behavior of Multistory Frames Designed by Different Philosophies," Earthquake Engineering Research Center Report No. EERC 69-11, University of California, Berkeley, October 1969.

4. Clough, R. W., Benuska, K. L., and Wilson, E. L., "Inelastic Earthquake Response of Tall Buildings," Proceedings of the Third World Conference on Earthquake Engineering, Wellington, New Zealand, 1965.

5. Porter, F. L. and Powell, G. H., "Static and Dynamic Analysis of Inelastic Frame Structures," Earthquake Engineering Research Center Report No. EERC 71-3, University of California, Berkeley, June 1971.

6. Bertero, V. V., Bresler, B., and Liao, H., "Stiffness Degradation of Reinforced Concrete Members Subjected to Cyclic Flexural Moments," Earthquake Engineering Research Center Report No. EERC 69-12, University of California, Berkeley, December 1969.

7. Mahin, S. A., Bertero, V. V., Atalay, M. B., and Rea, D., "Rate of Loading Effects on Uncracked and Repaired Reinforced Concrete Members," Earthquake Engineering Research Center Report No. EERC 72-9, University of California, Berkeley, December 1972.

8. Celebi, M. and Penzien, J., "Experimental Investigation into the Seismic Behavior of Critical Regions of Reinforced Concrete Components as Influenced by Moment and Shear," Earthquake Engineering Research Center Report No. EERC 73-4, University of California, Berkeley, January 1973.

9. Walpole, W. R. and Shepherd, R., "Elasto-Plastic Seismic Response of Reinforced Concrete Frames", Journal of the Structural Division, ASCE, Vol. 95, No. ST-10, October 1969.

10. Anderson, J. C. and Gupta, R. P., "Earthquake Resistant Design of Unbraced Frames," Journal of the Structural Division, ASCE, Vol. 98, No. ST-11, November 1972.

11. Bertero, V. V. and Collins, R. G., "Investigations of the Failures of the Olive View Stairtowers During the San Fernando Earthquake and Their Implications on Seismic Design," Earthquake Engineering Research Center Report No. EERC 73-26, University of California, Berkeley, December 1973.

12. Architectural Institute of Japan, "Report on the Investigations of Damage Due to 1968 Tokachi-Oki Earthquake," December 1968.

13. Yamada, M., "Ultimate Deformation of Reinforced Concrete," Proceedings of the International Conference on Planning and Design of Tall Buildings, IABSE-ASCE, Vol. III, pp. 467-472, Leheigh University, Bethlehem, Pennsylvania, August 1972.

14. Okamoto, S. and Hirosawa, M., "Full Size Tests of Reinforced Concrete Short Columns with regard to Shear Strength," Research Report of Architectural Institute of Japan, 1970.

15. Ohno, K., Shibata, T., and Hattori, T., "Strength and Deformability of Reinforced Concrete Columns at Shear Failure," Symposium on Resistance and Ultimate Deformability of Structures Acted on by Well Defined Repeated Loads, IABSE, pp. 213-220, Lisbon, June 1973.

16 Ikeda, A., "Load-Deflection Characteristics of Reinforced Concrete Columns Subjected to Alternate Loading," Report of the Training Institute for Engineering Teachers, Yokohama National University, March 1968.

17. Umemura, H., Aoyama, H., and Ito, M., "Experimental Studies of Reinforced Concrete Members and Composite Steel and Reinforced Concrete Members," Umemura Laboratory Report, University of Tokyo, December 1970.

18. Hisada, T., Ohmori, N., and Bessho, S., "Earthquake Design Considerations in Reinforced Concrete Columns," Kajima Institute of Construction Technology Report No. 1, Tokyo, January 1972.

19. Sugano, S. and Koreishi, I., "Empirical Evaluation of Inelastic Behavior of Structural Elements in Reinforced Concrete Frames Subjected to Lateral Forces," Proceedings of the Fifth World Conference on Earthquake Engineering, Session 2D, Rome, 1973.

20. Higashi, Y. and Takeda, T., "Stiffness and its Influence on Dynamic Behavior," Proceedings of the International Conference on Planning and Design of Tall Buildings, IABSE-ASCE, Vol. III, pp. 655-670, Leheigh University, Bethlehem, Pennsylvania, August 1972.

21. Park, R., Kent, D. C. and Sampson, R. A., "Reinforced Concrete Members with Cyclic Loading," Journal of the Structural Division, ASCE, Vol. 98, No. ST-7, July 1972.

22. Mugurama, H., Tominaga, M. and Watanabe, F., "Analytical and Experimental Studies on the Deformation Evaluation of Reinforced Concrete Columns Under Seismic Forces," Symposium on Resistance and Ultimate Deformability of Structures Acted on by Well Defined Repeated Loads, IABSE, pp. 67-72, Lisbon, June 1973.

23. Wight, J. K. and Sozen, M. A., "Shear Strength Decay in Reinforced Concrete Columns Subjected to Large Deflection Reversals," Civil Engineering Studies, Structural Research Series No. 403, University of Illinois, Urbana, August 1973.

24. American Concrete Institute, "Building Code Requirements for Reinforced Concrete, (ACI-318-71)," 1971.

25. Otani, S. and Sozen, M. A., "Behavior of Reinforced Concrete Multistory Frames During Earthquakes," Civil Engineering Studies, Structural Research Series No. 392, University of Illinois, Urbana, November 1972.

26. Bouwkamp, J. G. and Kustu, O., "Experimental Study of Spandrel Wall Assemblies," Proceedings of the Fifth World Conference on Earthquake Engineering, Session 2D, Rome, 1973.

27. Ma, S. M., "Experimental and Analytical Studies of Hysteretic Behavior of Reinforced Concrete Rectangular and T-Beams," Dissertation for the Degree of Doctor of Philosophy, University of California, Berkeley, 1975.

28. Bertero, V. V., "Effects of Variable Repeated Loading on Structures," University of California, Berkeley, July 1966.

29. Bertero, V. V., "Effects of Generalized Excitations on the Nonlinear Behavior of Reinforced Concrete Structures," Proceedings of the International Conference on Planning and Design of Tall Buildings, IABSE-ASCE, Vol. III, pp. 431-453, Leheigh University, Bethlehem, Pennsylvania, August 1972.

30. Olesen, S. O., Sozen, M. A., and Siess, C. P., "Investigation of Prestressed Reinforced Concrete for Highway Bridges; Part IV: Strength in Shear of Beams with Web Reinforcement," Engineering Experimental Station, Bulletin 493, University of Illinois, July 1967.

31. Blume, J. A., et. al., "Design of Multistory Reinforced Concrete Buildings for Earthquake Motions," Portland Cement Association, 1961.

32. Timoshenko, S., and Goodier, J. N., "Theory of Elasticity," McGraw-Hill Book Co., Inc., New York, 1951.

33. Clough, R. W. and Johnston, S. B., "Effect of Stiffness Degradation on Earthquake Ductility Requirements," Proceedings of Japan Earthquake Engineering Symposium, October 1966.

34. Jennings, P. C., "Equivalent Viscous Damping for Yielding Structures," Journal of the Engineering Mechanics Division, ASCE, Vol. 94, No. EM-1, February 1968.

TABLE 2.1 SUMMARY OF TESTS FOR DETERMINING STRESS-STRAIN RELATIONSHIP OF REINFORCING STEEL

SPECIMEN	#3 BARS						#7 BARS					
	YIELD STRESS, f_{ys}	YIELD STRAIN, ε_y	E	ε_{SH}	E_{SH}	ULTIMATE STRESS, f_{max}	YIELD STRESS, f_y	YIELD STRAIN, ε_y	E	ε_{SH}	E_{SH}	ULTIMATE STRESS, f_{max}
	KSI	—	KSI	—	KSI	KSI	KSI	—	KSI	—	KSI	KSI
1	52.6	0.00182	28960	0.0229	707	77.6	53.3	0.00195	27350	0.0116	937	83.8
2	"	"	"	"	"	"	"	"	"	"	"	"
3	"	"	"	"	"	"	"	"	"	"	"	"
4	"	"	"	"	"	"	62.2	0.00205	30250	0.0144	1015	95.3
5	56.8	0.00195	29850	0.0293	562	76.9	"	"	"	"	"	"
6	"	"	"	"	"	"	"	"	"	"	"	"
7	"	"	"	"	"	"	52.7	0.00194	28200	0.0147	849	81.7
8	"	"	"	"	"	"	"	"	"	"	"	"
9	"	"	"	"	"	"	"	"	"	"	"	"
10	"	"	"	"	"	"	"	"	"	"	"	"
11	54.1	0.00186	29850	0.0305	399	71.3	"	"	"	"	"	"
12	"	"	"	"	"	"	"	"	"	"	"	"
MEAN	55.0	0.00189	29550	0.0274	583	76.2	55.2	0.00197	28500	0.0139	913	85.6

NOTE: ALL VALUES ABOVE BASED ON AVERAGE OF RESULTS FOR THREE SAMPLE COUPONS

TABLE 2.2 SUMMARY OF COMPRESSIVE TESTS ON 6 x 12 INCH CONCRETE CYLINDERS

SPECIMEN	SLUMP	AGE SPECIMEN TESTED	AVER.† 7-DAY STRENGTH	AVER.† 14-DAY STRENGTH	AVER.† 28-DAY STRENGTH	AVER.† STRENGTH AT SPECIMEN TEST DAY
	IN.	DAYS	PSI	PSI	PSI	PSI
1	3 1/2	98	2795	3560	—	4220
2		113				4450
3	3 1/2	54	2565	3255	3855	4235
4		63				4005
5	3 3/8	90	2800	—	4410	4260
6		97				4610
7	3 1/8	72	2925	3990	4505	4615
8		100				4440
9	4 1/8	69	2880	3820	4335	4825
10		74				4700
11	5	71	2670	3670	4300	4500
12		77				4605
MEAN††			2770	3650	4260	4470
STANDARD DEVIATION††			145	265	240	220

†BASED ON AVERAGE OF TESTS OF THREE CYLINDERS.

††BASED ON THE TOTAL NUMBER OF CYLINDERS TESTED.

TABLE 2.3 SUMMARY OF TESTS FOR DETERMINING STRESS-STRAIN RELATIONSHIP OF CONCRETE

CONCRETE CYLINDER NO.	CYLINDER FROM BATCH FOR SPECIMENS	AGE WHEN CYLINDER TESTED	ULTIMATE COMPRESSIVE STRENGTH	TANGENT MODULUS, E_c	STRAIN @ ULTIMATE STRENGTH, ε_o	POISSON'S RATIO, ν	USABLE STRAIN, ε_c^{us}
		DAYS	PSI	KSI			
1	3,4	166	4565	3260	0.00265	0.11	0.00450
2	3,4	166	4530	3390	0.00232	0.18	0.00335
3	5,6	97	4475	3190	0.00272	0.14	—
4	5,6	97	4580	3150	0.00276	0.16	0.00410
5	5,6	97	4740	2890	0.00307	0.15	—
6	5,6	97	4635	3200	0.00322	0.14	—
7	9,10	41	4705	3170	0.00290	0.19	—
8	9,10	41	5095	3280	0.00295	0.18	—
9	11,12	28	4265	2970	0.00277	0.16	0.00430
10	11,12	28	4335	3360	0.00266	0.14	0.00375
MEAN			4595	3190	0.00280	0.16	0.00400
STANDARD DEVIATION			220	150	0.00024	0.02	

TABLE 2.4 TEST SERIES VARIABLE PARAMETERS

SPECIMEN	AXIAL LOAD, N	TRANSVERSE REINFORCEMENT SPACING, s	TRANSVERSE REINFORCEMENT RATIO, ρ"	LATERAL DISPLACEMENT VELOCITY AT DISPLACEMENT SET 1, $\dot{\delta}_1$	LATERAL DISPLACEMENT VELOCITY AT DISPLACEMENT SET 2, $\dot{\delta}_2$	CORRESPONDING APPROXIMATE STRAIN RATE $\dot{\varepsilon}_y$ † AT YIELD OF TENSILE REINFORCEMENT
	KIPS	IN.	—	IN/SEC	IN/SEC	μ IN/IN/SEC
1	60	3	0.0154	0.2	0.4	560
2	60	5	0.0093	0.2	0.4	560
3	60	3	0.0154	2.0	4.0	5600
4	60	5	0.0093	2.0	4.0	5600
5	120	3	0.0154	0.2	0.4	425
6	120	5	0.0093	0.2	0.4	425
7	120	3	0.0154	2.0	1.0	4250
8	120	5	0.0093	2.0	1.0	4250
9	180	3	0.0154	0.2	—	410
10	180	5	0.0093	0.2	—	410
11	180	3	0.0154	1.0	—	2060
12	180	5	0.0093	1.0	—	2060

† $\dot{\varepsilon}_y = 10^6\ \varepsilon_y/t_y$; $t_y \equiv$ time to yield $= \delta_y/\dot{\delta}_1$

TABLE 3.1 BENDING MOMENTS, LATERAL FORCES, CURVATURES AND LATERAL DISPLACEMENTS AT CRITICAL LOADING STAGES

AXIAL LOAD	M_{cr}	ϕ_{cr}	F_{cr}	δ_{cr}	M_y	ϕ_y	$M_y^{\dagger}$	$\phi_y^{\dagger}$	F_y	δ_y	M^{us}	ϕ^{us}	M^{ult}	ϕ^{ult}
KIPS	K-IN	RAD/IN	KIPS	IN	K-IN	RAD/IN	K-IN	RAD/IN	KIPS	IN	K-IN	RAD/IN	K-IN	RAD/IN
60	281	0.000043	8.4	0.062	798	0.000347	952	0.00046	27.8	0.607	892	0.00153	894	0.00435
120	406	0.000062	12.0	0.090	1013	0.000399	1210	0.00055	34.0	0.738	1086	0.00116	923	0.00285
180	531	0.000081	15.4	0.117	1206	0.000457	1404	0.00060	38.1	0.812	1245	0.00086	929	0.00198

†CALCULATED FROM EQUATIONS SUGGESTED BY SUGANO AND KOREISHI [19].

TABLE 3.2 CALCULATED SHEAR STRENGTH OF SPECIMENS

SPECIMENS	AXIAL LOAD, N	TRANSVERSE REINFORCEMENT SPACING, s	TRANSVERSE REINFORCEMENT RATIO, ρ_w	V_c[†] EQ.(3.7)	V_s EQ.(3.9)	V_c EQ.(3.8)	V_u (5)+(6)	V_u EQ.(3.10)	$V_y \equiv M_y/a$[††]
	KIPS	IN	—	KIPS	KIPS	KIPS	KIPS	KIPS	KIPS
(1)	(2)	(3)	(4)	(5)	(6)	(7)	(8)	(9)	(10)
1,3	60	3	0.0061	13.4	40.3	9.9	53.7	32.8	12.1
2,4		5	0.0037		24.2		37.6	30.0	
5,7	120	3	0.0061	13.9	40.3	12.3	54.2	36.4	15.3
6,8		5	0.0037		24.2		38.1	33.4	
9,11	180	3	0.0061	15.3	40.3	14.8	55.6	40.4	18.3
10,12		5	0.0037		24.2		39.5	36.9	

[†] ϕ = CAPACITY REDUCTION FACTOR = 0.85

[††] a = SHEAR SPAN = 66 IN.

TABLE 4.1 SUMMARY OF EXPERIMENTAL RESULTS DEFINING THE MONOTONIC LOADING ACTION - DEFORMATION RELATIONSHIPS

SPECIMEN	DIRECTION OF LOADING	V_{cr}^{*}	F_y	δ_y	M_y^{*}	ϕ_y	ε_c^{us}	DISPLACEMENT AMPLITUDE AT INITIATION OF COVER SPALLING
		KIPS	KIPS	IN.	K-IN.	RAD/IN.	—	IN.
1	-	—	-26.6	-0.68	-919.	-0.00034	—	—
	+	—	26.4	0.72	914.	0.00030	—	—
2	-	-8.8	-26.7	-0.69	-923.	-0.00029	0.0059	1.6
	+	7.7	26.1	0.67	902.	0.00023	0.0059	3.2
3	-	-12.2	-25.9	-0.68	-896.	-0.00028	0.0041	3.2
	+	10.6	26.6	0.63	916.	0.00029	—	—
4	-	—	-27.1	-0.73	-938.	-0.00027	0.0050	1.6
	+	10.9	27.1	0.73	938.	0.00026	0.0052	2.4
5	-	-12.1	-33.1	-0.91	-1202.	-0.00030	—	—
	+	14.6	33.3	0.84	1200.	0.00049	0.0045	2.0
6	-	-15.1	-30.2	-0.87	-1101.	-0.00043	0.0062	2.4
	+	16.9	35.6	0.93	1286.	—	0.0061	2.4
7	-	-14.5	-32.6	-0.93	-1187.	-0.00037	—	—
	+	15.6	33.3	0.96	1214.	—	—	—
8	-	-15.5	-31.7	-0.88	-1152.	-0.00036	0.0061	2.4
	+	—	30.4	0.90	1111.	0.00035	0.0033	2.0
9	-	-17.3	-33.1	-0.91	-1256.	-0.00041	0.0032	0.8
	+	17.1	34.5	0.92	1304.	0.00050	0.0048	1.2
10	-	—	-36.7	-0.89	-1371.	-0.00031	—	—
	+	17.1	36.3	0.92	1364.	—	0.0028	1.6
11	-	-19.7	-36.7	-0.84	-1380.	-0.00046	0.0050	1.8
	+	14.7	34.5	0.82	1299.	0.00043	0.0040	1.2
12	-	-13.3	-35.2	-0.95	-1333.	-0.00050	0.0032	1.2
	+	15.8	34.4	0.92	1301.	0.00053	0.0064	1.6

*ADJUSTED FOR BY "N-δ" EFFECT; $M_y^{*} = F_y a/2 + N \delta_y$

TABLE 4.2 YIELD OF TRANSVERSE REINFORCEMENT

SPECIMEN	DIRECTION OF LOADING	CYCLE NO.	LATERAL DISPLACEMENT, IN.	TRANSVERSE REINFORCEMENT NO.†
1 2 3 4	NO TRANSVERSE REINFORCEMENT YIELD OBSERVED			
5	-	38	4.00	3
6	- -	32 35	2.07 3.30	2 1
7	NO TRANSVERSE REINFORCEMENT YIELD OBSERVED, DAMAGE TO SOUTH HALF OF SPECIMEN ; STRAIN GAGES ON TRANSVERSE REINFORCEMENT IN NORTH HALF.			
8	-	33	3.10	2
9	+ - -	18 19 17	1.92 1.88 1.89	1 2 3
10	-	17	1.56	2
11 12	STRAIN GAGES ON TRANSVERSE REINFORCEMENT NOT OPERATIVE			

†SEE FIG. 2.14

TABLE 4.3 LATERAL DISPLACEMENT CAPACITY OF SPECIMENS

SPECIMEN	$\delta_y \equiv$ AVE. $\{\delta_y^+, \lvert\delta_y^-\rvert\}$	δ_{MAX}	TOTAL NO. OF CYCLES	$\mu_\delta = \delta_{MAX}/\delta_y$
	IN.	IN.		
1	0.700	4.0	38	5.71
2	0.680	3.2	36	4.71
3	0.655	3.5†	36	5.34
4	0.730	4.0	37 ½	5.48
5	0.875	4.0	40	4.57
6	0.900	3.2	34 ½	3.56
7	0.945	3.2	35 ½	3.39
8	0.890	3.2	32 ¼	3.60
9	0.915	2.0	20	2.19
10	0.905	2.0	19	2.21
11	0.830	2.4	16	2.89
12	0.935	2.0	20	2.14

†AFTER ADDITIONAL LATERAL LOADING NOT REPORTED HEREIN

TABLE 4.4 CYCLIC STRAIN AND AVERAGE CURVATURE DUCTILITY FACTORS

SPECIMEN	TOP LONGITUDINAL BAR		BOTTOM LONGITUDINAL BAR		MAX. USABLE $\{\phi^{+}+\lvert\phi^{-}\rvert\}$	LATERAL DISPLACEMENT AMPLITUDE	$(\phi_y^{+}+\lvert\phi_y^{-}\rvert)$ †††	μ_ϕ
	MAX. USABLE $\{\varepsilon^{+}+\lvert\varepsilon^{-}\rvert\}$	μ_ε^c ††	MAX. USABLE $\{\varepsilon^{+}+\lvert\varepsilon^{-}\rvert\}$	μ_ε^c ††				
	—	—	—	—	RAD/IN.	IN.	RAD/IN.	—
1	0.0323	8.08	0.0355	8.88	0.00880	4.0	0.00064	13.75
2	0.0322	8.05	0.0238	5.95	0.00700	3.2	0.00052	13.46
3†	0.0181†				0.00430†		0.00057	
4	0.0311	7.78	0.0325	8.13	0.00790	3.2	0.00053	14.91
5†	0.0124†						0.00079	
6	0.0269	6.73	0.0159	3.98	0.00580	2.4	0.00086	6.74
7†							0.00074	
8	0.0204	5.10	0.0140	3.50	0.00470	2.4	0.00071	6.62
9	0.0157	3.93	0.0102	2.55	0.00340	1.6	0.00091	3.74
10	0.0094	2.35	0.0189	4.73	0.00390	2.0		
11	0.0211	5.28	0.0170	4.25	0.00420	1.8	0.00089	4.72
12	0.0134	3.38	0.0147	3.68	0.00360	1.6	0.00103	3.50

† DAMAGE ACCUMULATED AT CRITICAL REGION AT SOUTH HALF OF SPECIMEN; STRAIN READINGS MADE AT CRITICAL REGION AT NORTH HALF OF SPECIMEN.

†† μ_ε^c = (MAX. USABLE $\{\varepsilon^{+}+\lvert\varepsilon^{-}\rvert\})/(\varepsilon_y^{+} + \lvert\varepsilon_y^{-}\rvert)$ WHERE $\varepsilon_y^{+} = -\varepsilon_y^{-} \cong \varepsilon_y \cong 0.00200$

††† SEE TABLE 4.1

TABLE 4.5 CONTRIBUTION OF FLEXURAL AND SHEAR DEFORMATIONS TO LATERAL DISPLACEMENT

	NOMINAL LATERAL DISPLACEMENT AMPLITUDE, IN.	SPECIMEN 3			SPECIMEN 4
		δ_{flex}/δ	δ_{shear}/δ	$(\delta_{flex} + \delta_{shear})/\delta$	δ_{shear}/δ
DISPLACEMENT SET 1	0.4	0.780	0.029	0.809	0.037
	0.8	0.901	0.044	0.945	0.053
	1.2	0.905	0.048	0.953	0.060
	1.6	0.989	0.054	1.043	0.080
	2.0	0.970	0.053	1.023	0.080
DISPLACEMENT SET 2	0.8	0.926	0.052	0.978	
	1.6	0.956	0.055	1.011	
	2.4	0.934	0.054	0.988	
	3.2	0.845	0.053	0.898	

TABLE 4.6 LATERAL DISPLACEMENT COMPONENT DUE TO PLASTIC HINGE ROTATION

SPECIMEN	LATERAL DISPLACEMENT AMPLITUDE	δ_{PH} †
	IN.	IN.
10	0.4	0.023
	0.8	0.053
	0.91 (= δ_y)	0.068
	1.2	0.225
	1.6	0.630
	2.0	0.885
11	0.6	0.030
	0.83 (= δ_y)	0.045
	1.2	0.105
	1.8	0.705
	2.4	1.463

† $\delta_{PH} = \theta_{PH} \frac{x}{2}$ (see Fig. 4.18.b)

$x \cong 60$ inches

$\theta_{PH} = (\phi_2 - \phi_3)\ \ell$ (see Fig. 4.21)

TABLE 5.1 EXPERIMENTALLY MEASURED VALUES OF THE PARAMETERS IN MATHEMATICAL MODEL

AXIAL LOAD, N	TRANSVERSE REINFORCEMENT SPACING, s	F_Y	δ_Y	δ_N	β_S	β
KIPS	IN.	KIPS	IN.	IN.	—	—
60.	3.	27.7	0.69	2.39	0.24	0.0013
	5.				0.36	0.0038
120.	3.	35.5	0.90	1.70	0.36	0.0063
	5.				0.54	0.0088
180.	3.	39.8	0.91	1.18	0.48	0.0115
	5.				0.72	0.0140

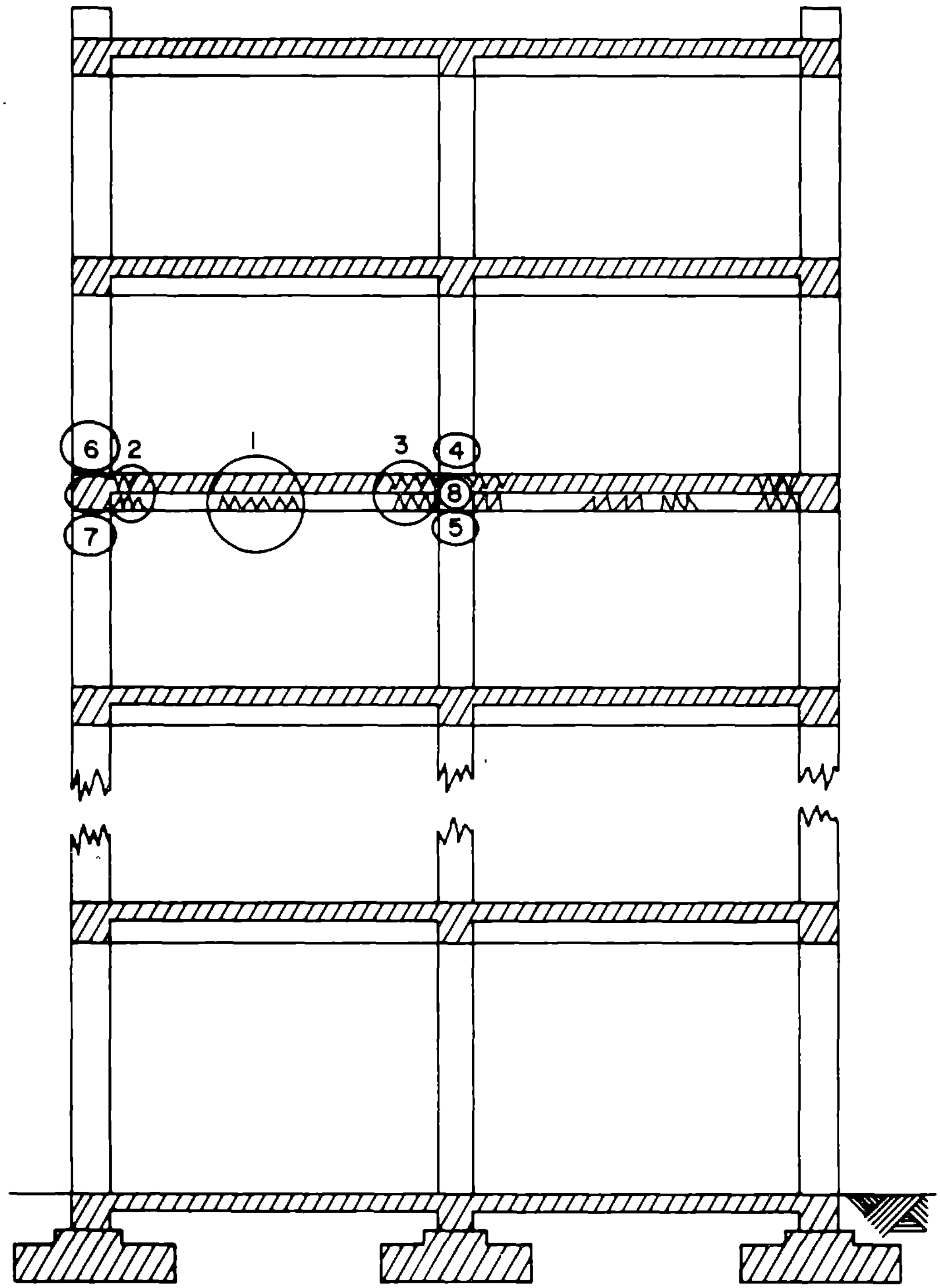

FIG. 1.1 CRITICAL REGIONS THAT MAY BE DEVELOPED IN A REINFORCED CONCRETE FRAME [6]

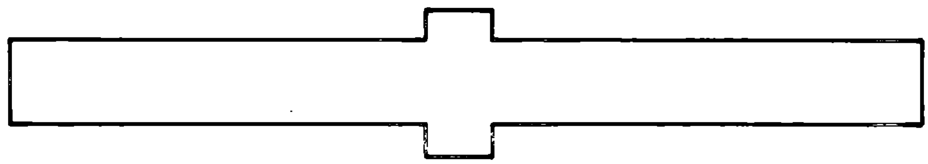

(a) UNLOADED SPECIMEN

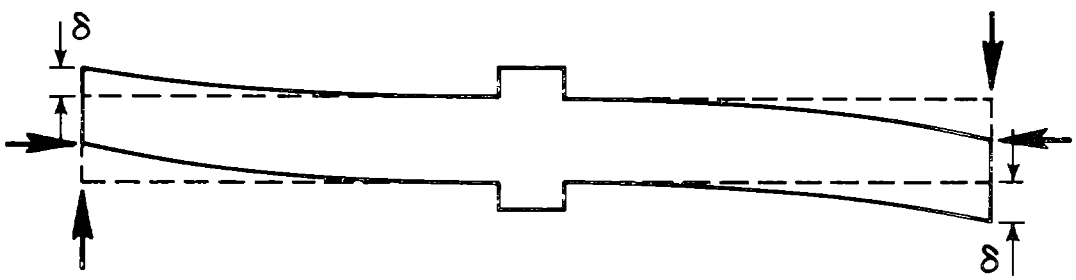

(b) POSSIBLE TEST SET-UP FOR THE SPECIMEN

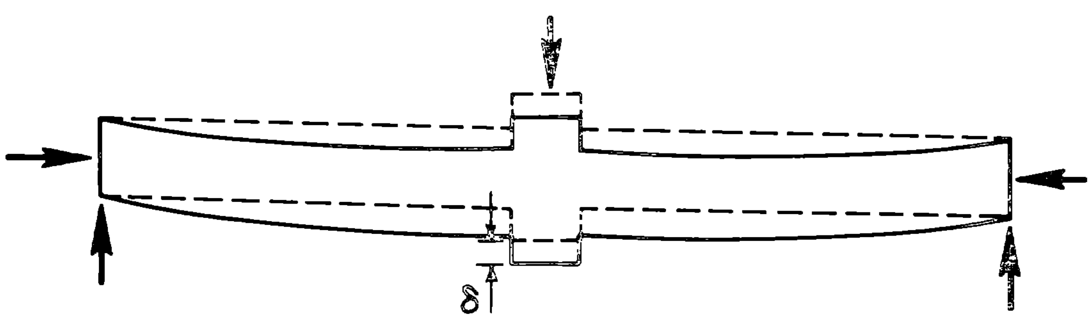

(c) IDEALIZED TEST SET-UP

FIG. 2.1 POSSIBLE AND IDEALIZED TEST SET-UPS

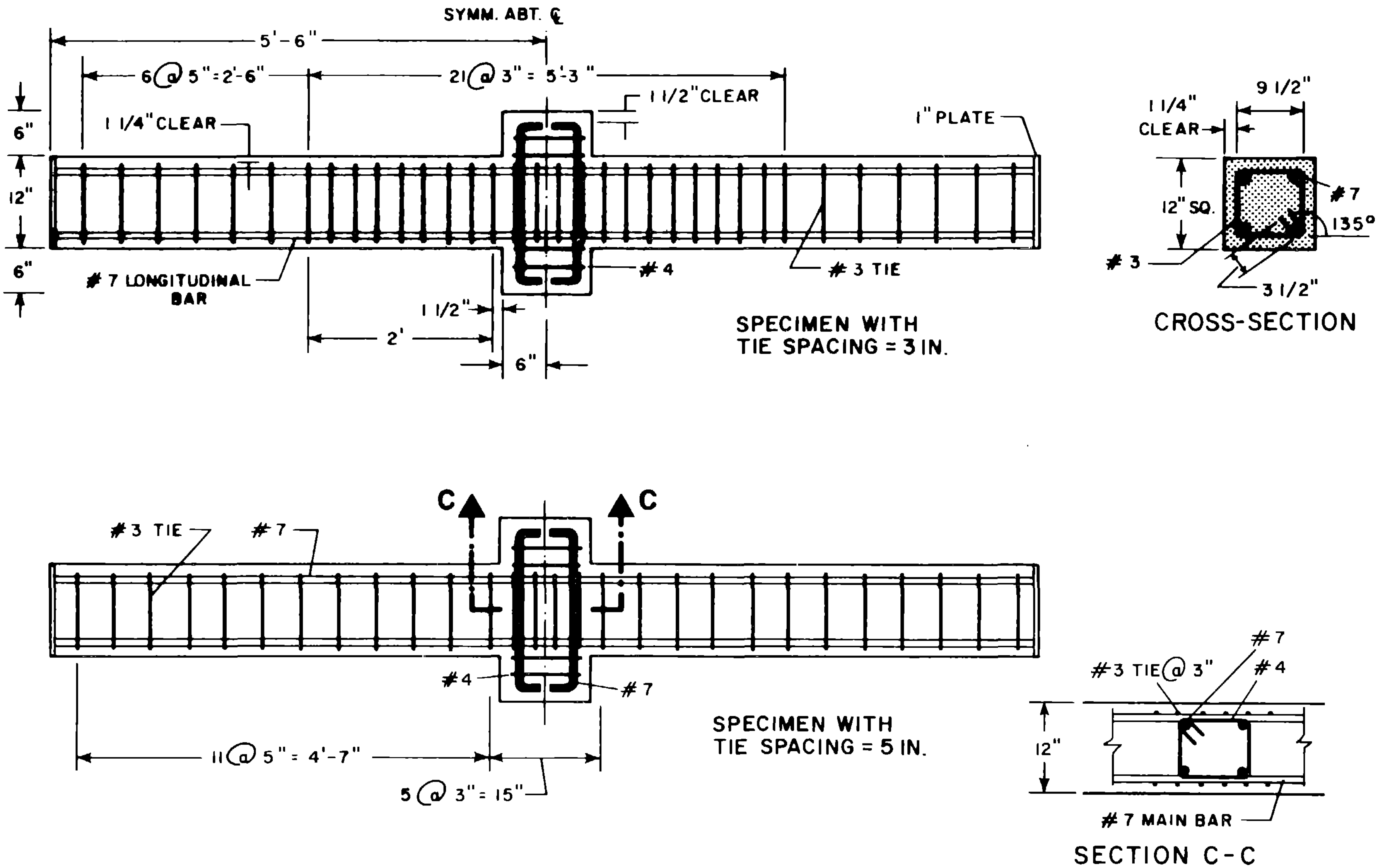

FIG. 2.2 SPECIMEN GEOMETRY & REINFORCEMENT DETAILS

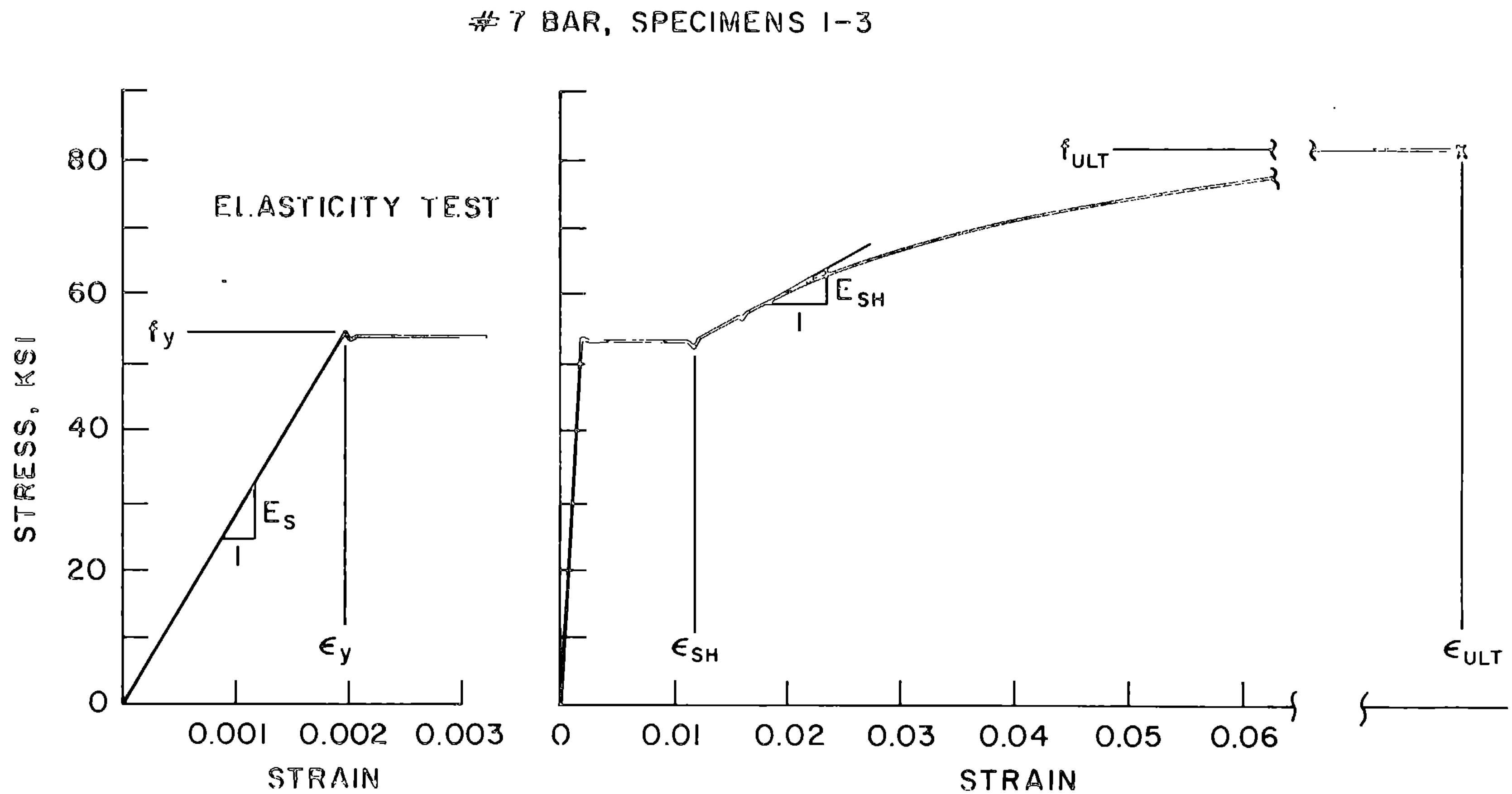

FIG. 2.3 REINFORCEMENT BAR STRESS-STRAIN DIAGRAM, TYPICAL

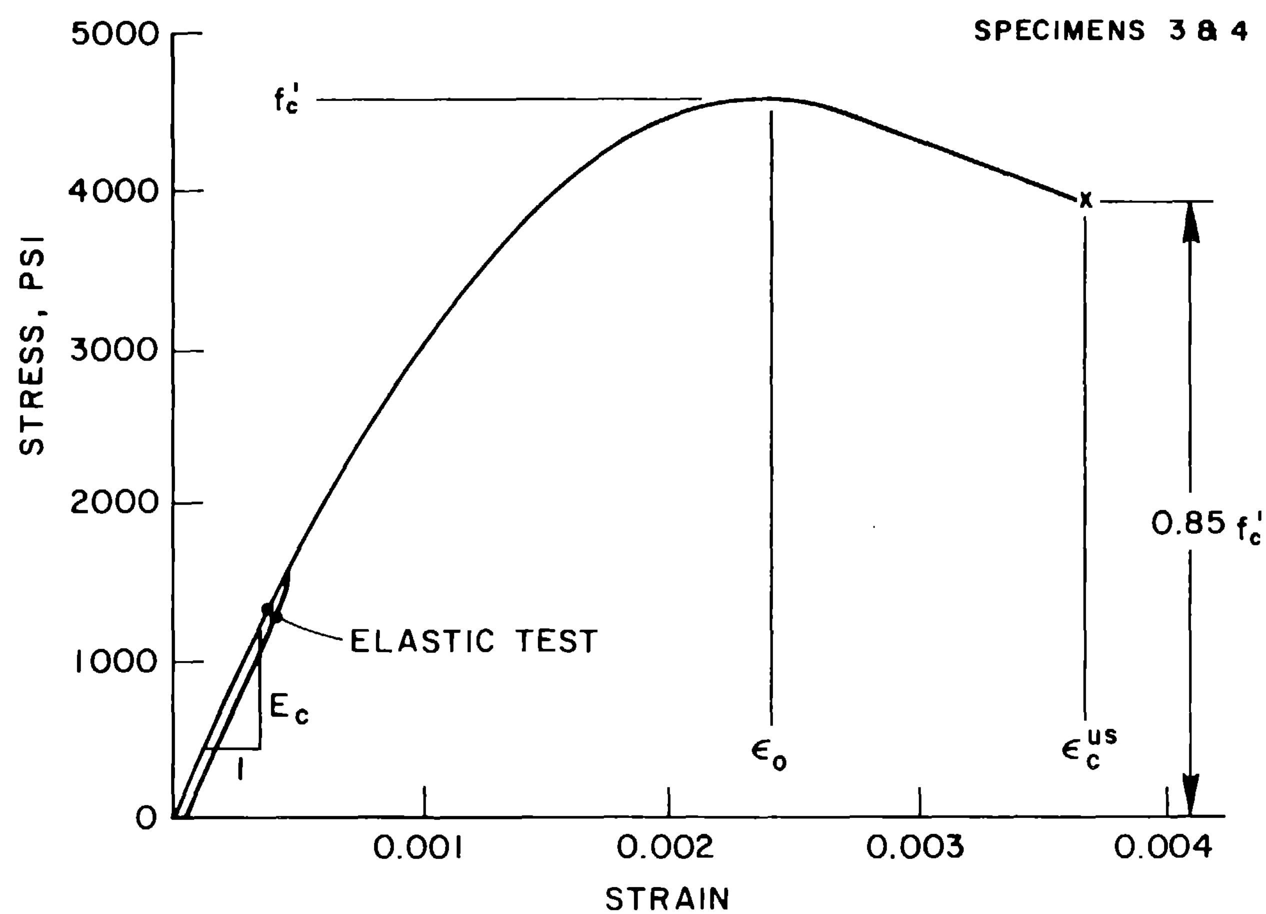

FIG. 2.4 CONCRETE TEST CYLINDER STRESS–STRAIN DIAGRAM, TYPICAL

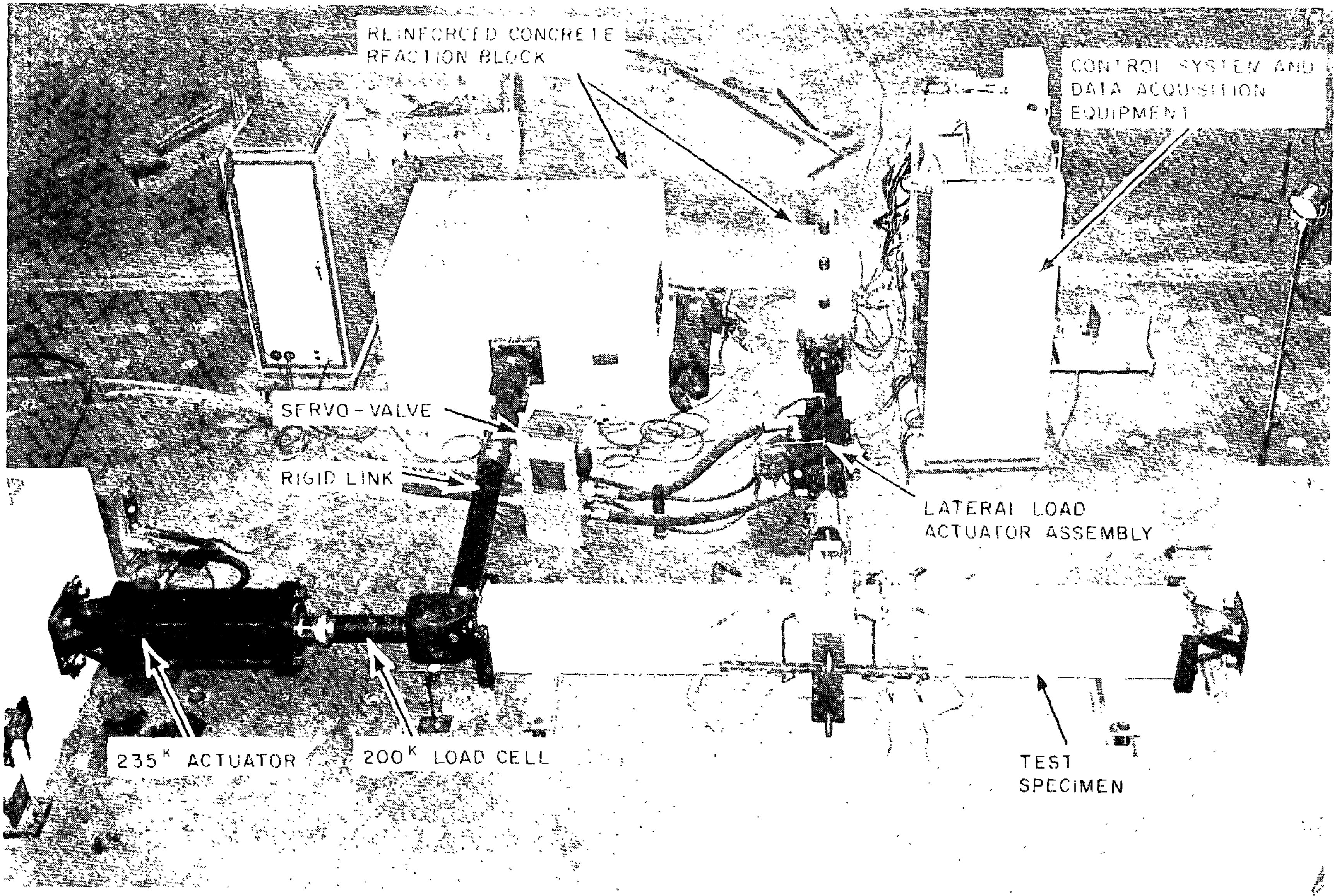

FIG. 2.5 OVERALL VIEW OF TEST SET-UP

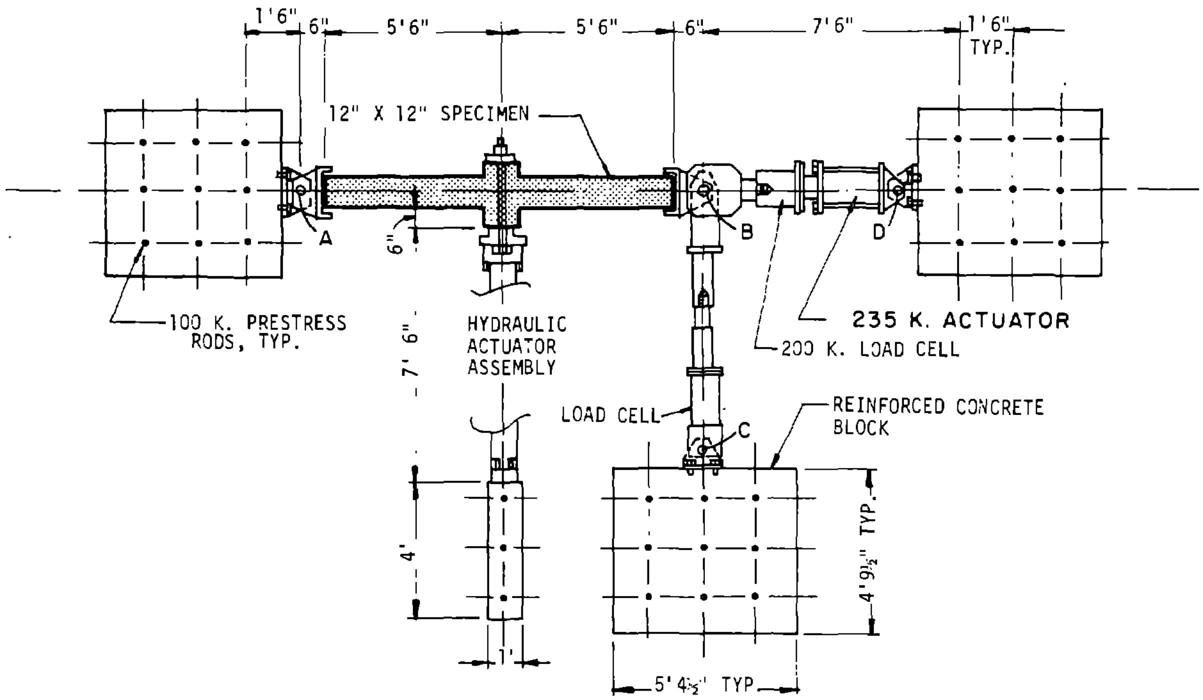

(a) THE TEST SET-UP

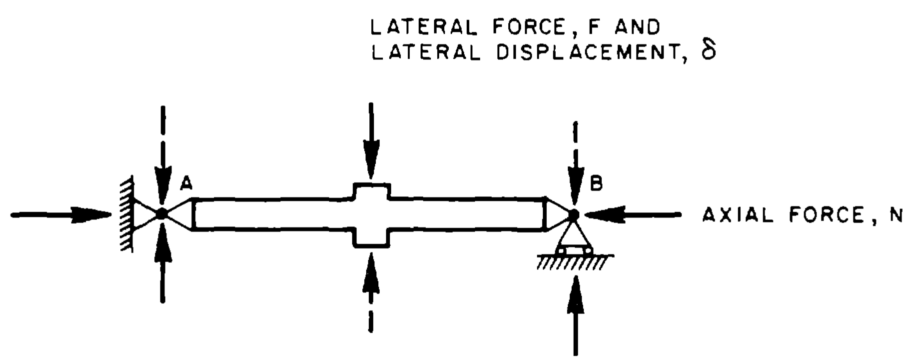

(b) SCHEMATIC REPRESENTATION OF SPECIMEN LOADING

FIG. 2.6 TEST SET-UP AND SCHEMATIC REPRESENTATION OF SPECIMEN LOADING

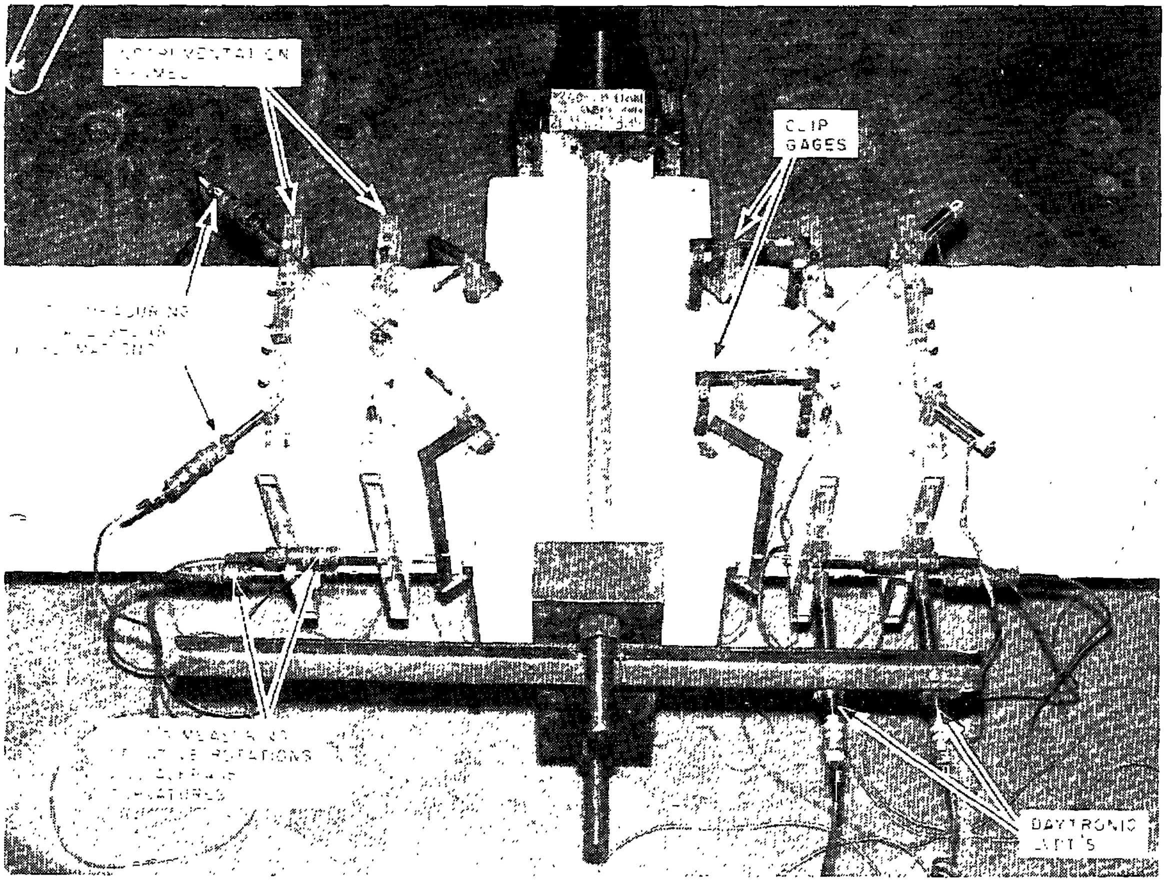

FIG. 2.7 INSTRUMENTATION

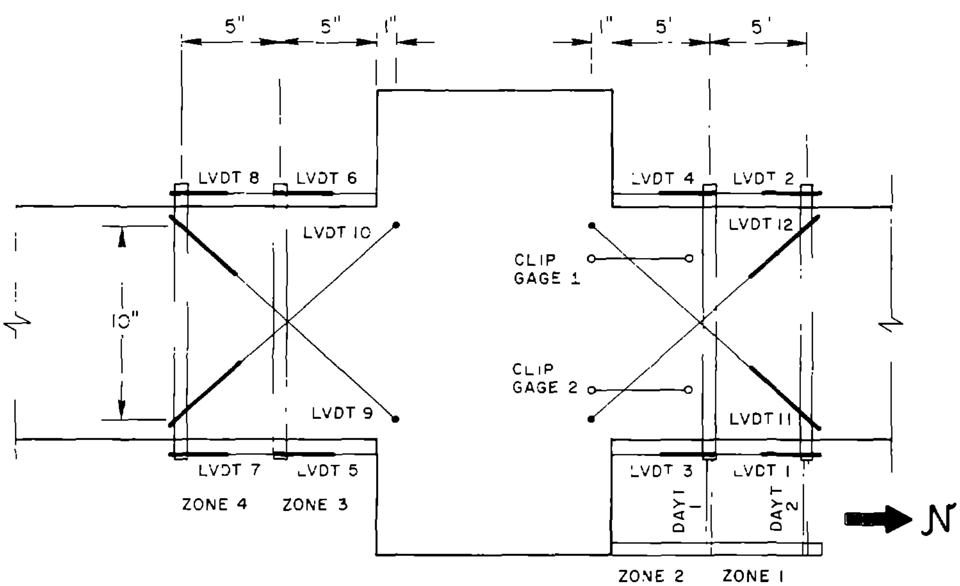

FIG. 2.8 NOMINAL LOCATIONS OF INSTRUMENTATION

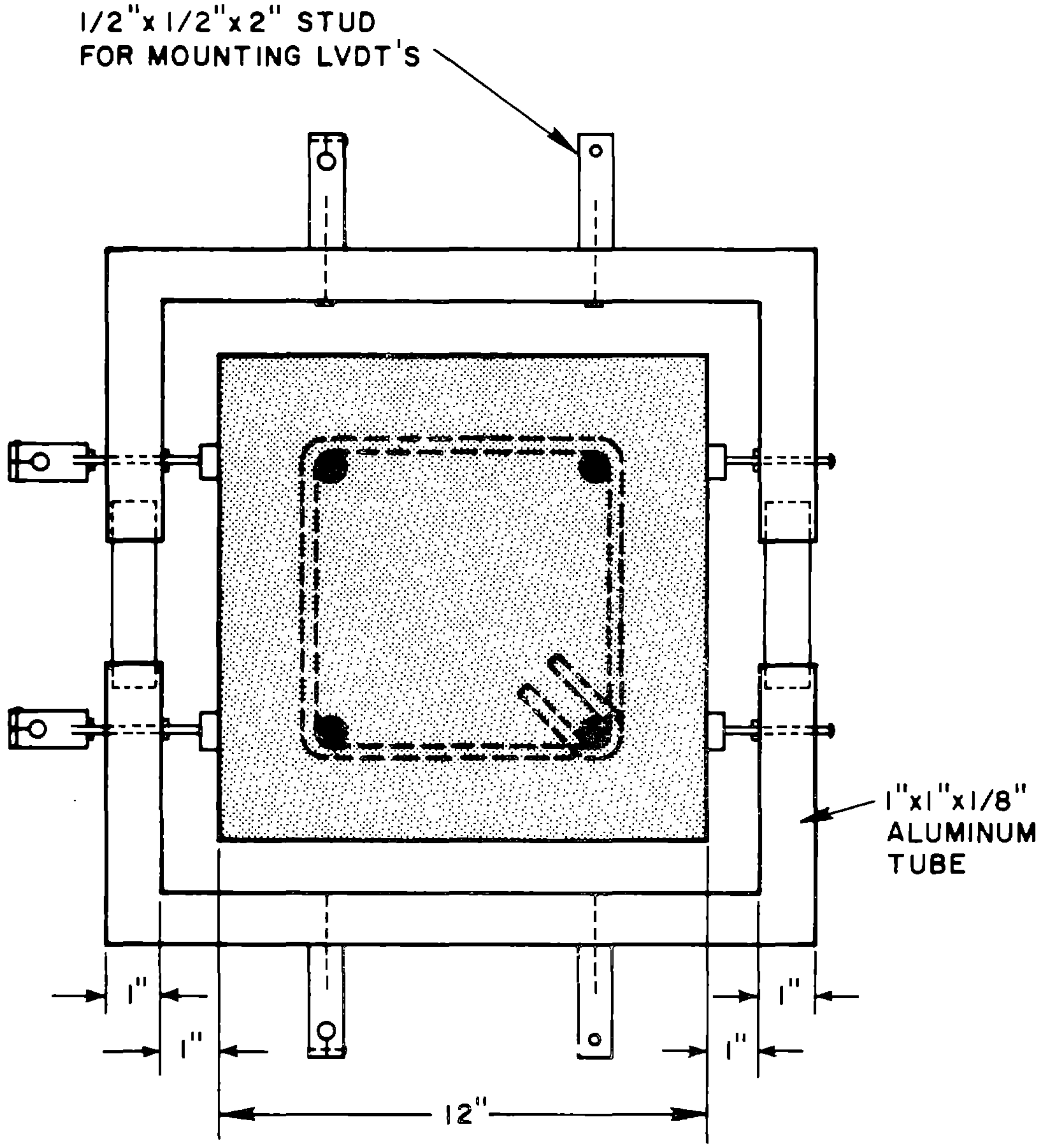

FIG. 2.9 INSTRUMENTATION FRAME

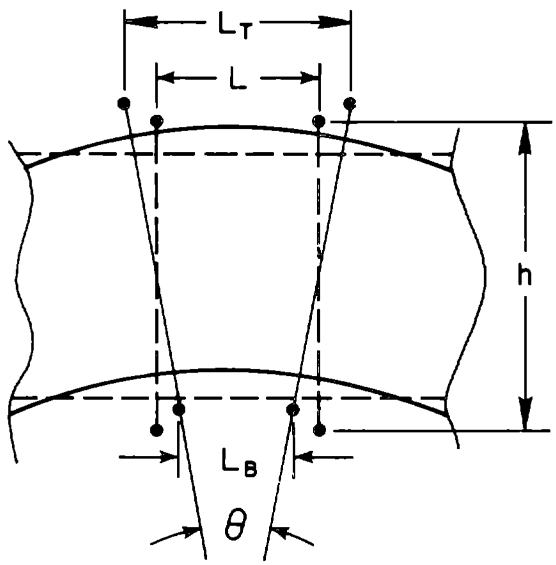

$$\theta = \frac{(L-L_T)-(L-L_B)}{h}$$

$$\phi_{AVE.} = \frac{\theta}{L}$$

FIG. 2.10 MEASUREMENT OF RELATIVE ROTATION AND AVERAGE CURVATURE

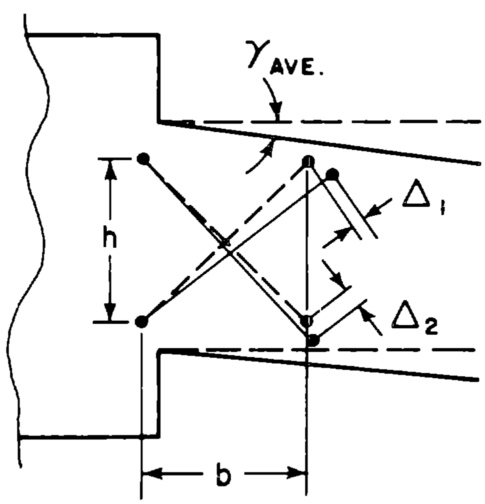

$$\gamma_{AVE.} = \frac{(\Delta_1+\Delta_2)\sqrt{b^2+h^2}}{2bh}$$

FIG. 2.11 MEASUREMENT OF AVERAGE SHEAR DEFORMATION

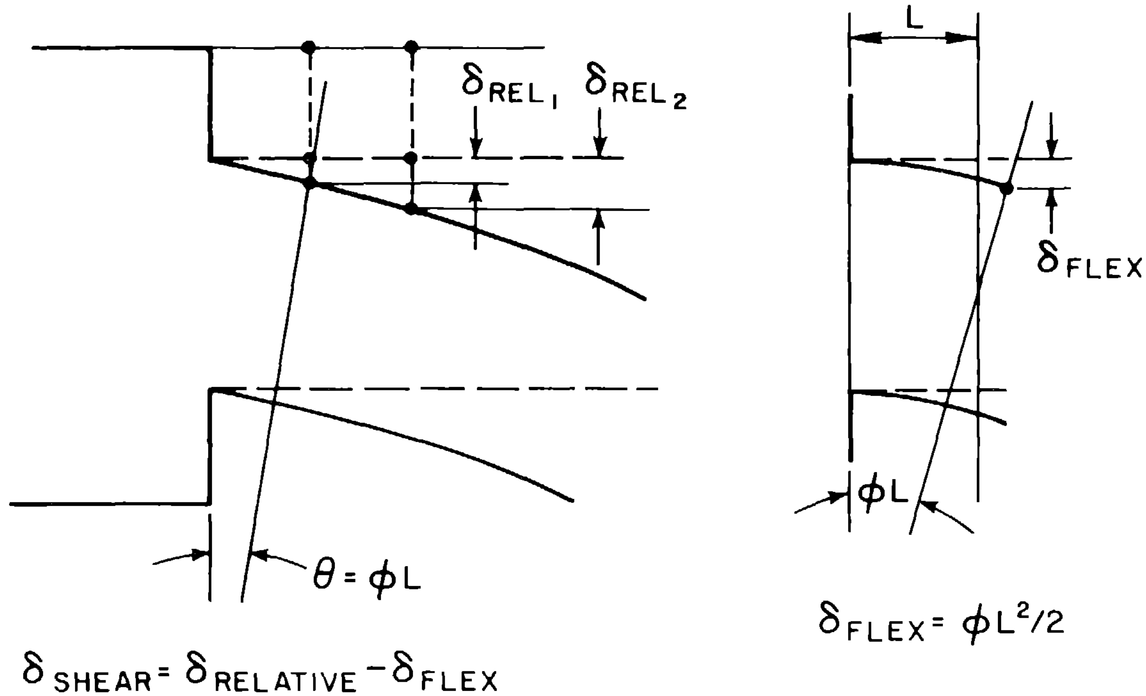

FIG. 2.12 MEASUREMENT OF RELATIVE DISPLACEMENTS

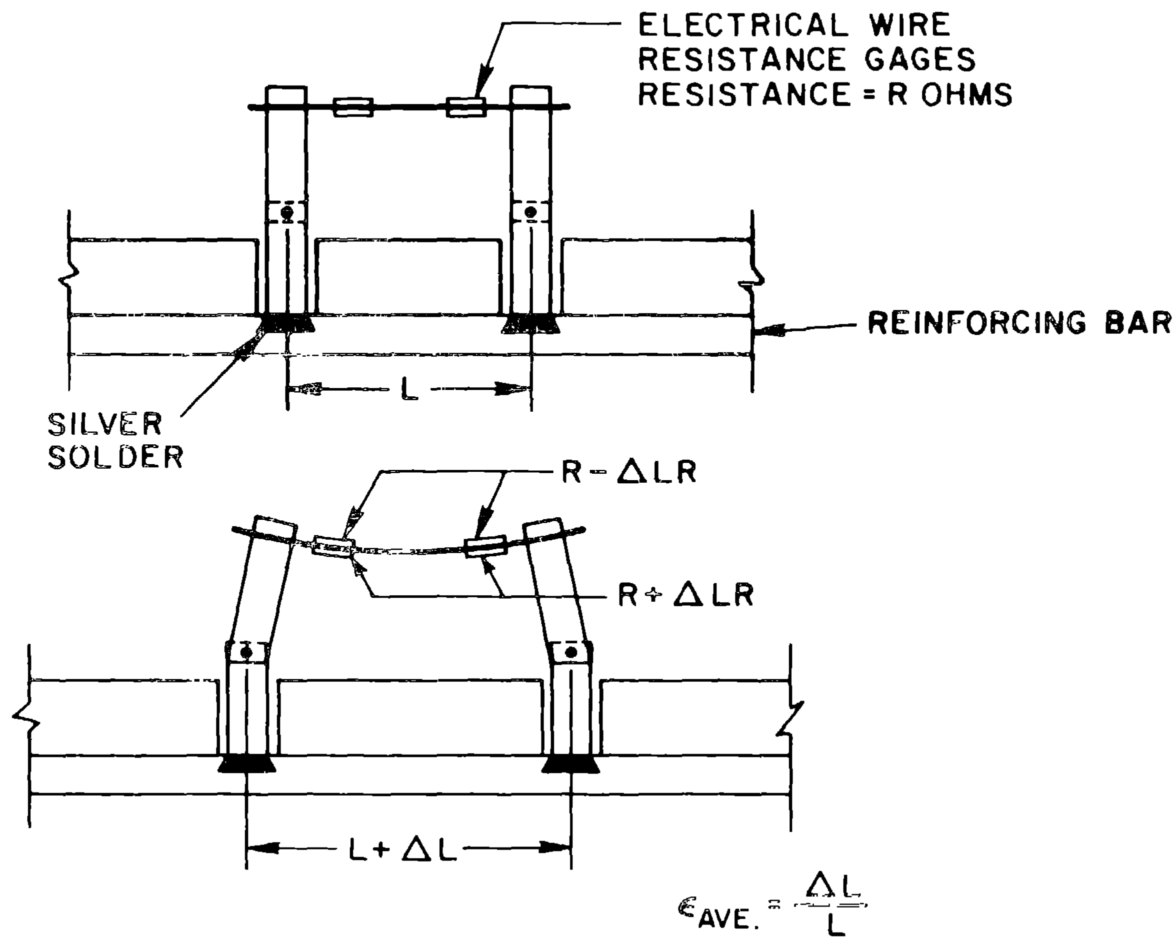

FIG. 2.13 MEASUREMENT OF AVERAGE LONGIDUTINAL REINFORCEMENT STRAIN

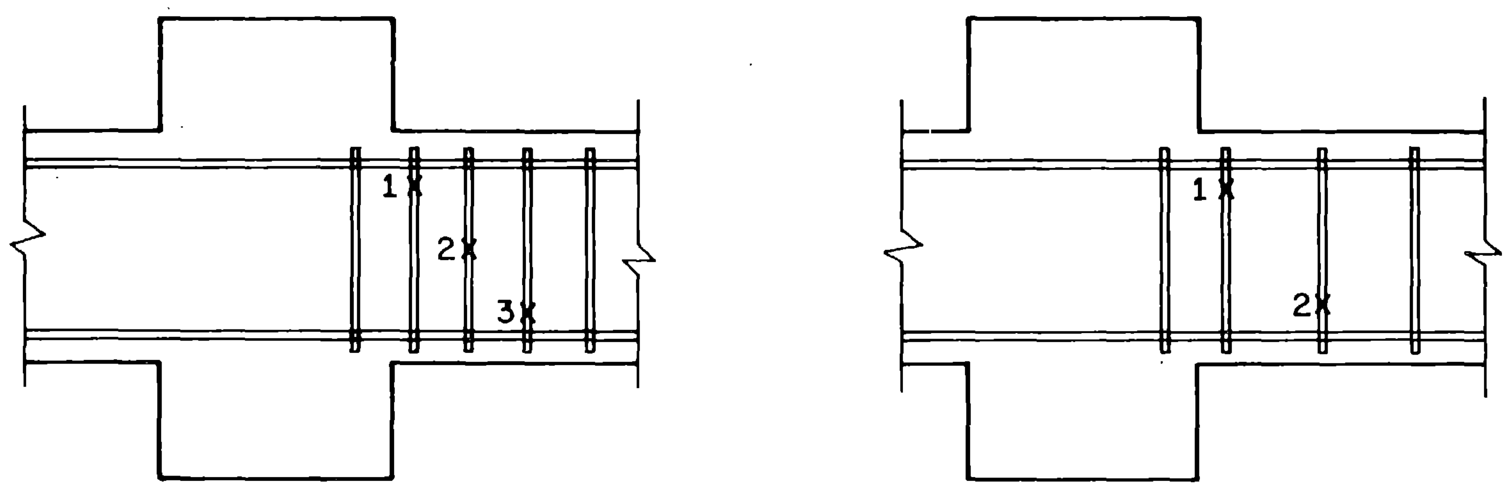

SPECIMENS WITH TRANSVERSE REINFORCEMENT SPACING S = 3"

SPECIMENS WITH TRANSVERSE REINFORCEMENT SPACING S = 5"

FIG. 2.14 LOCATIONS OF STRAIN GAGES ON TRANSVERSE REINFORCEMENT

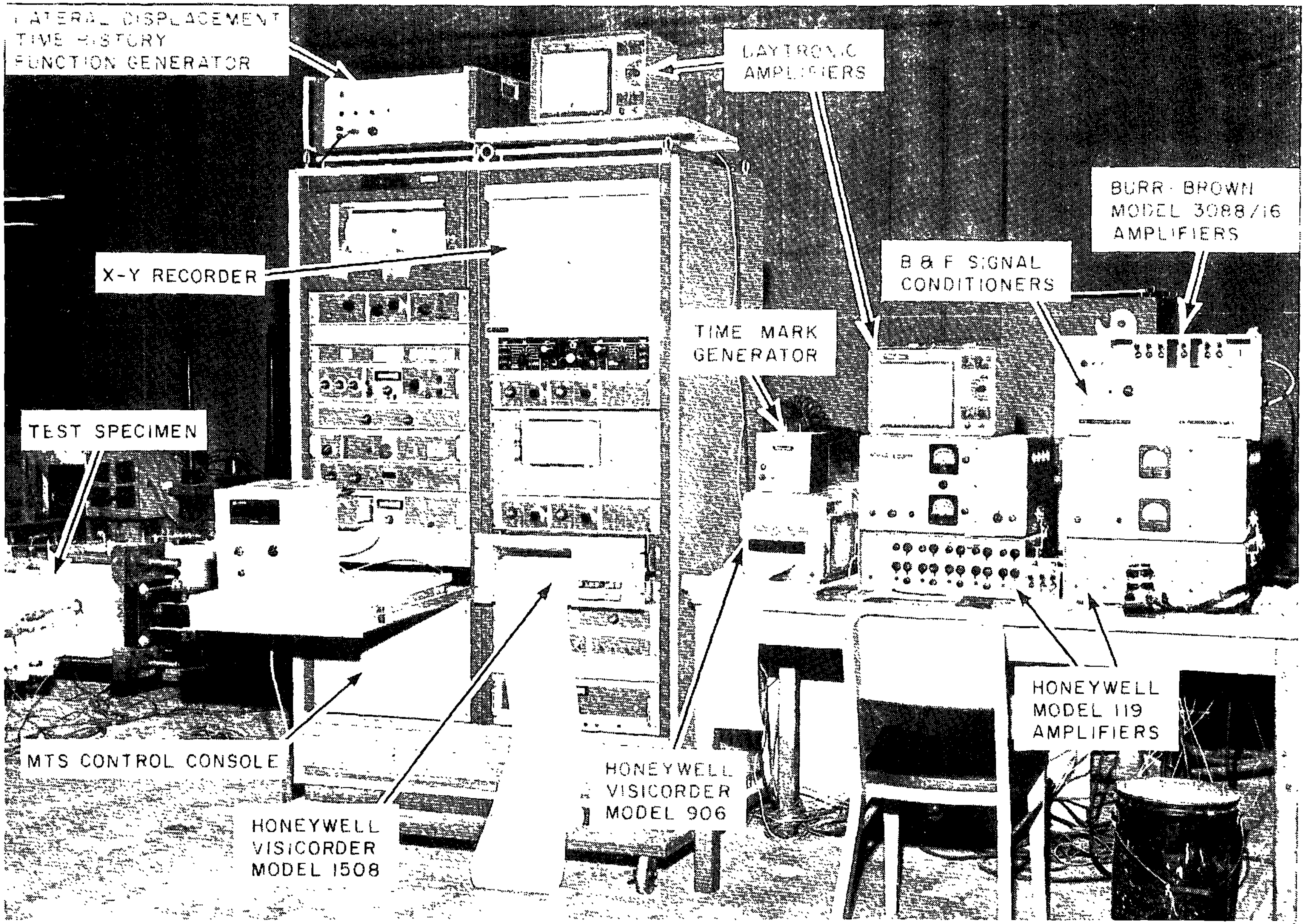

FIG. 2.15 DATA ACQUISITION EQUIPMENT

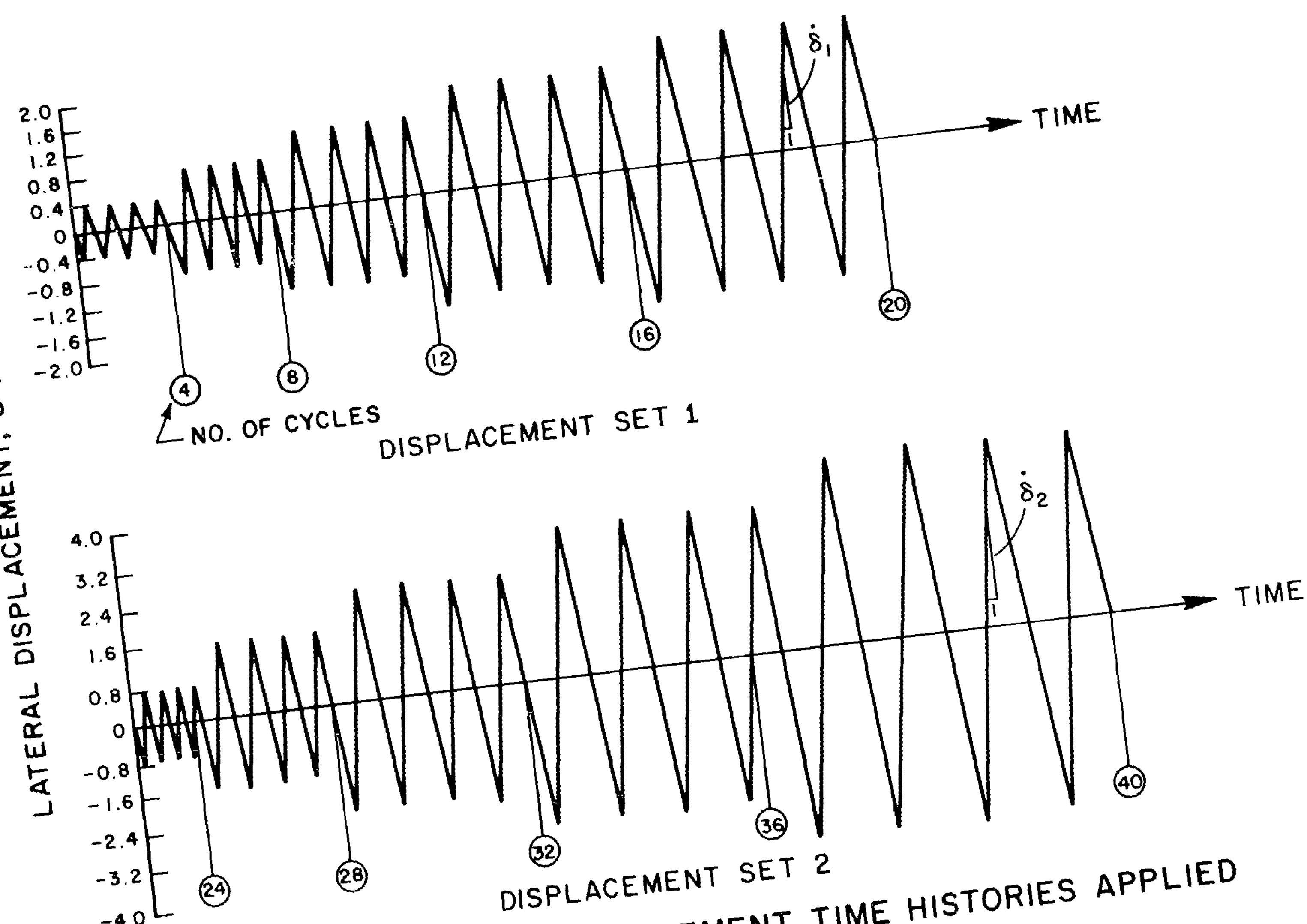

FIG. 2.16 LATERAL DISPLACEMENT TIME HISTORIES APPLIED

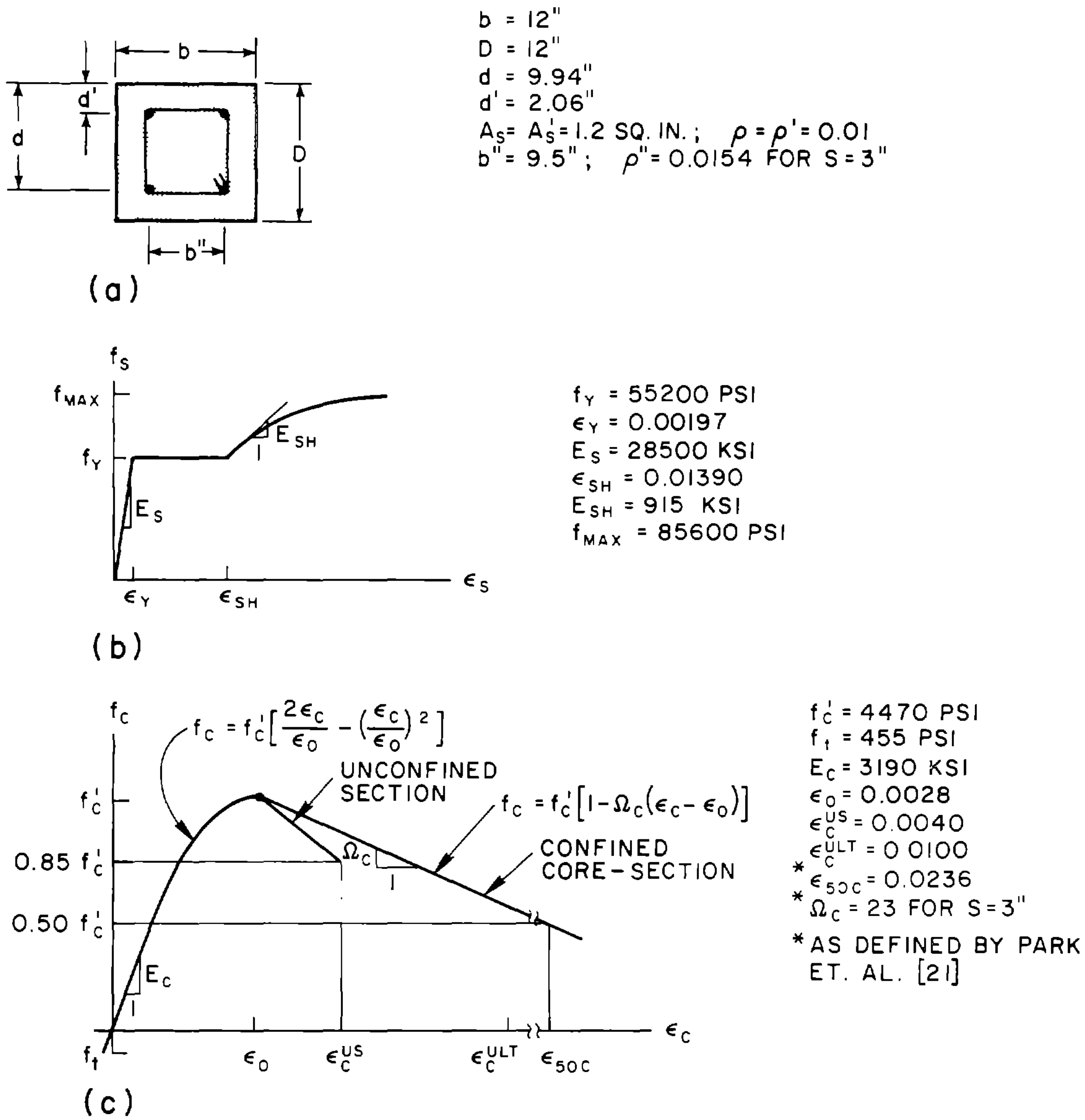

FIG. 3.1 CROSS-SECTION GEOMETRY & IDEALIZED MATERIAL PROPERTIES USED IN DEVELOPING THE INTERACTION DIAGRAMS

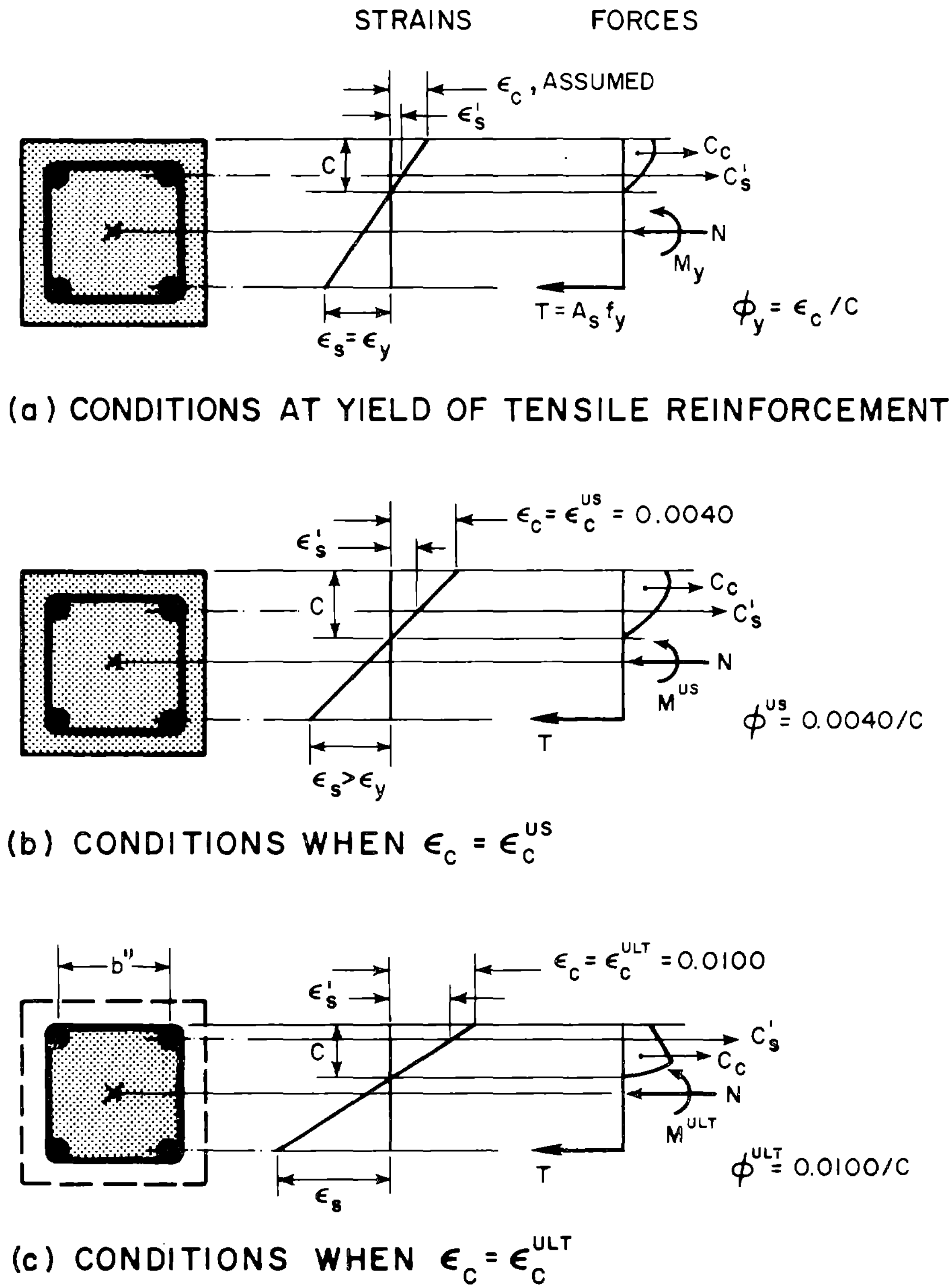

FIG. 3.2 DEVELOPMENT OF THE INTERACTIONS DIAGRAMS

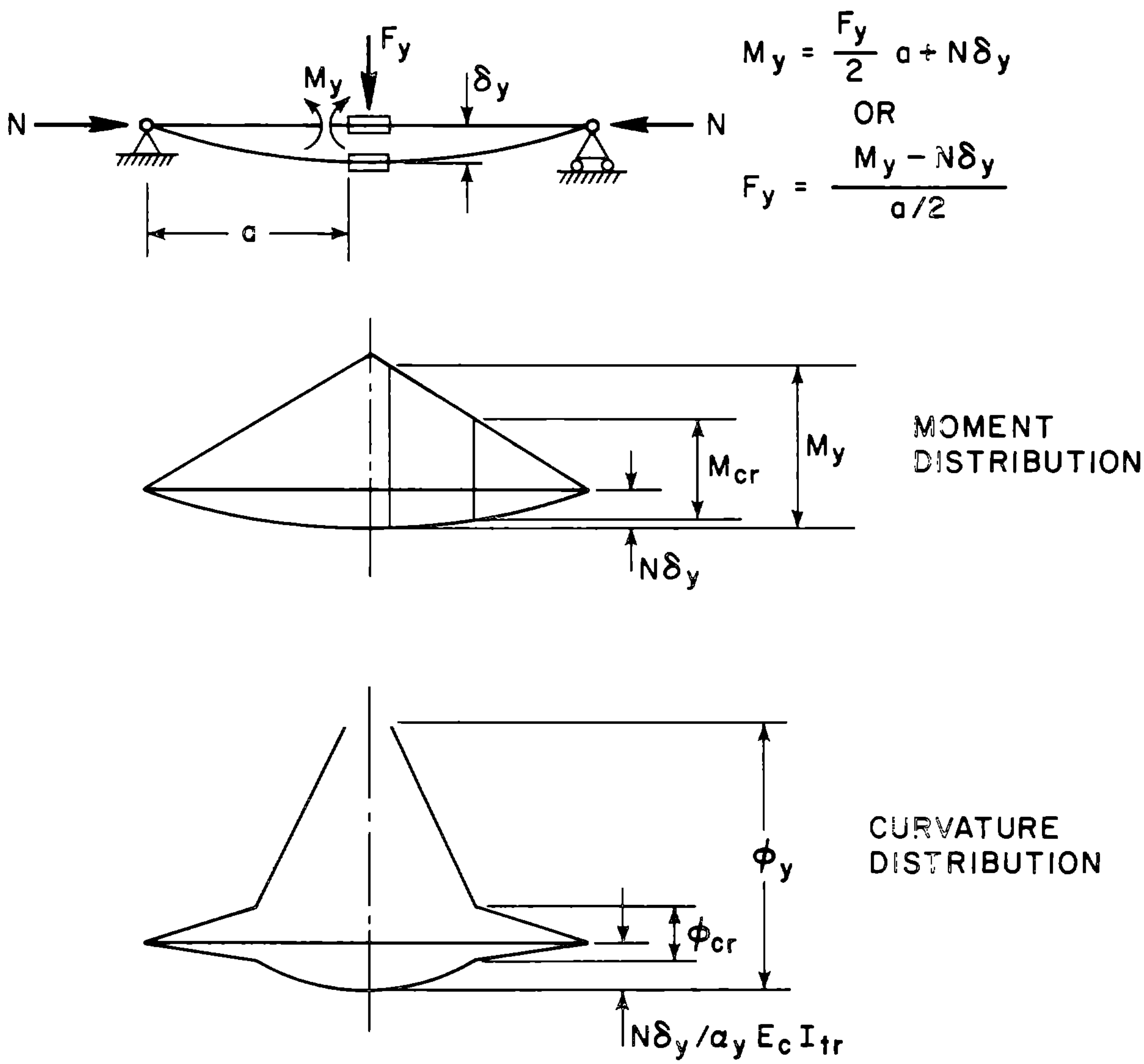

FIG. 3.3 CALCULATION OF LATERAL LOAD AND DISPLACEMENT AT YIELD

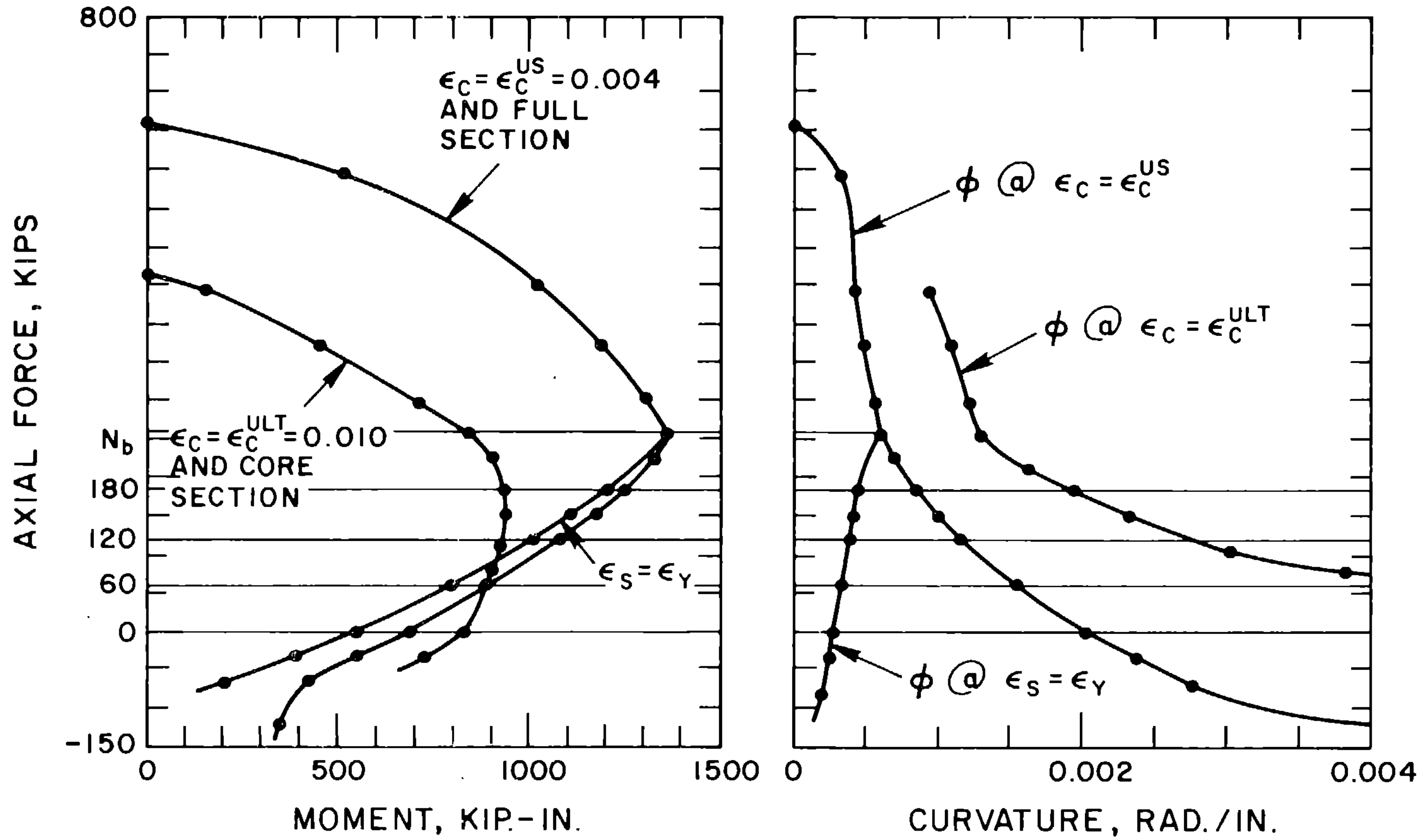

FIG. 3.4 AXIAL FORCE-MOMENT AND AXIAL FORCE-CURVATURE INTERACTION DIAGRAMS

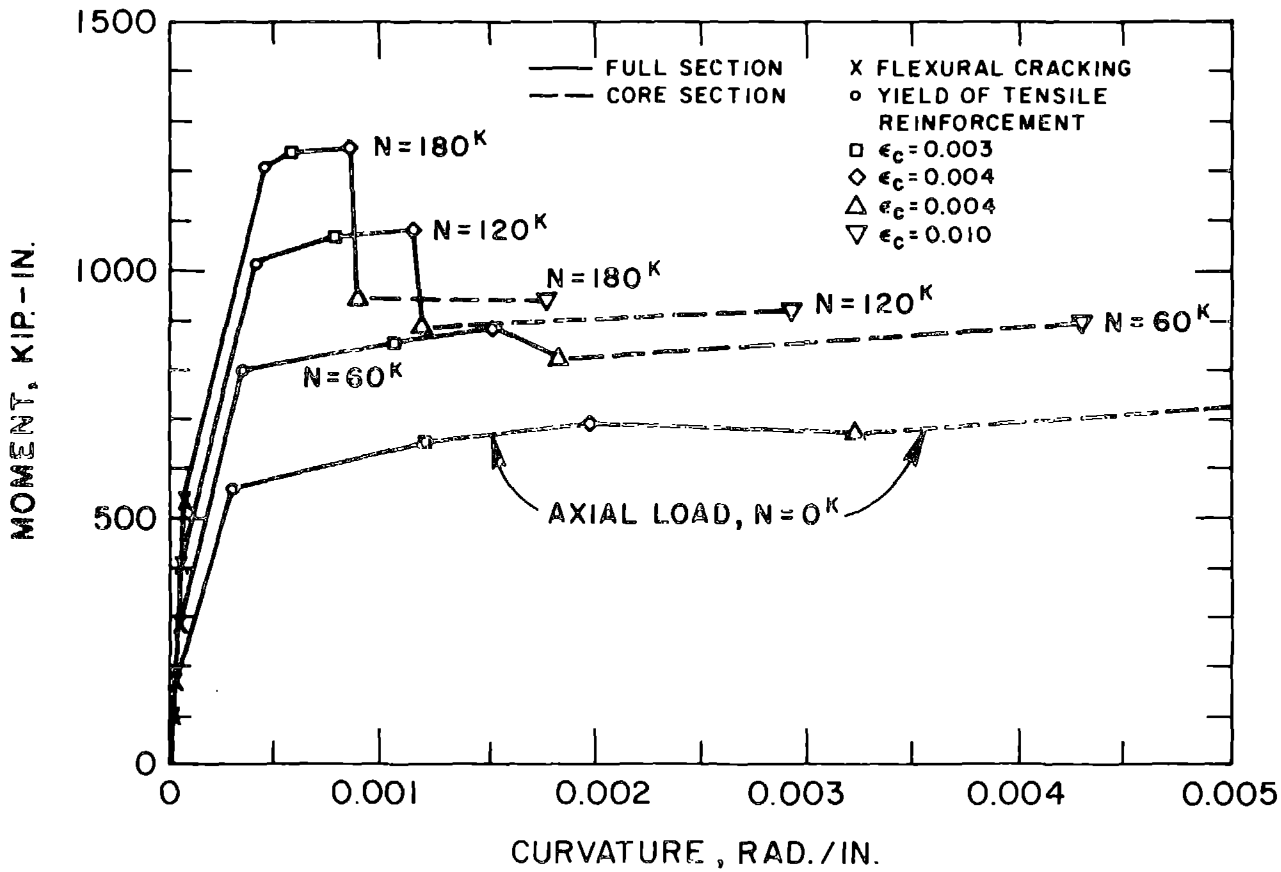

FIG. 3.5 MOMENT-CURVATURE DIAGRAMS

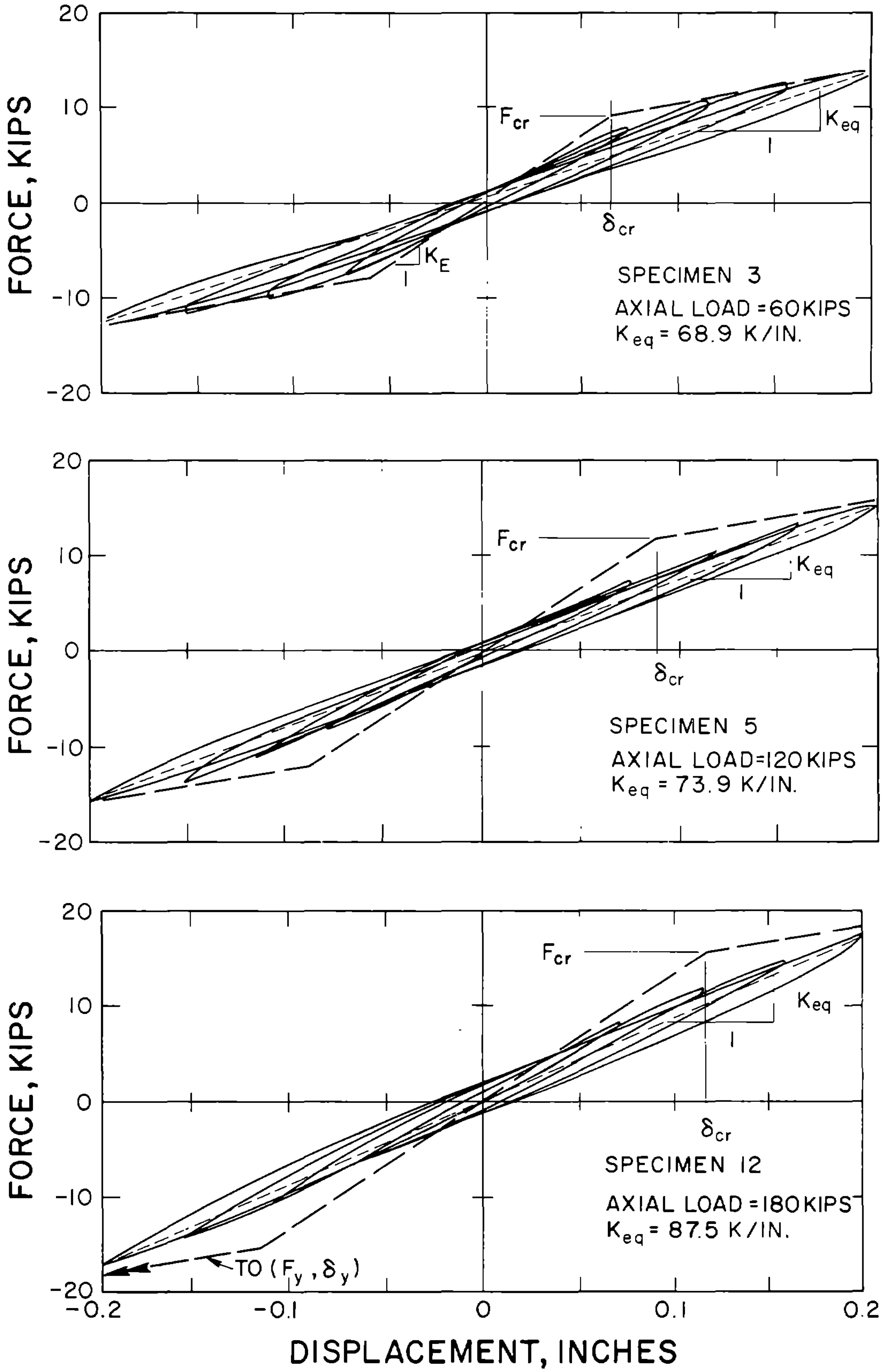

FIG. 4.1 LATERAL FORCE-DISPLACEMENT RELATIONSHIPS IN THE "ELASTIC" RANGE

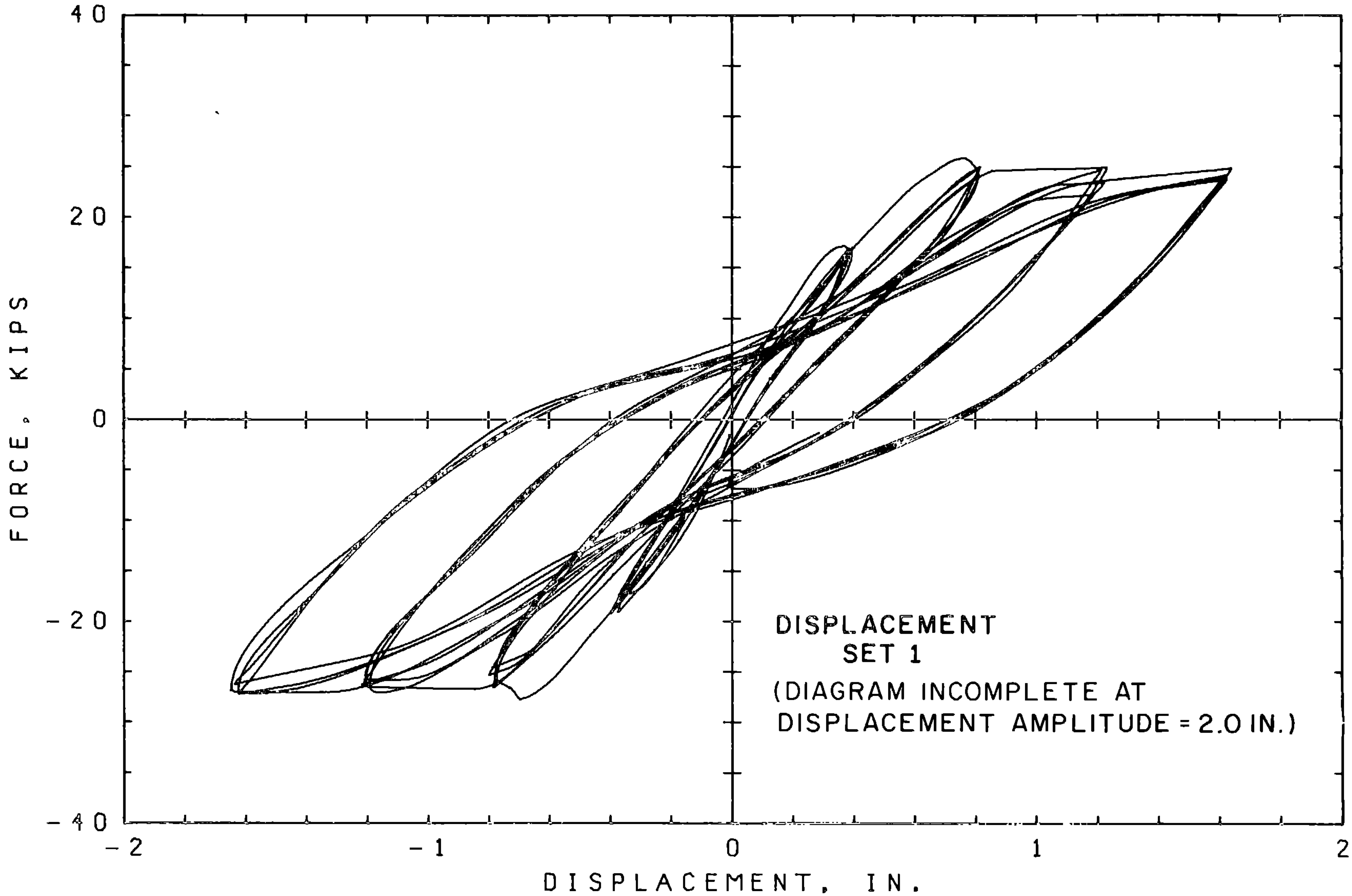

FIG. 4.2.a LATERAL FORCE-DISPLACEMENT DIAGRAMS, SPECIMEN 1

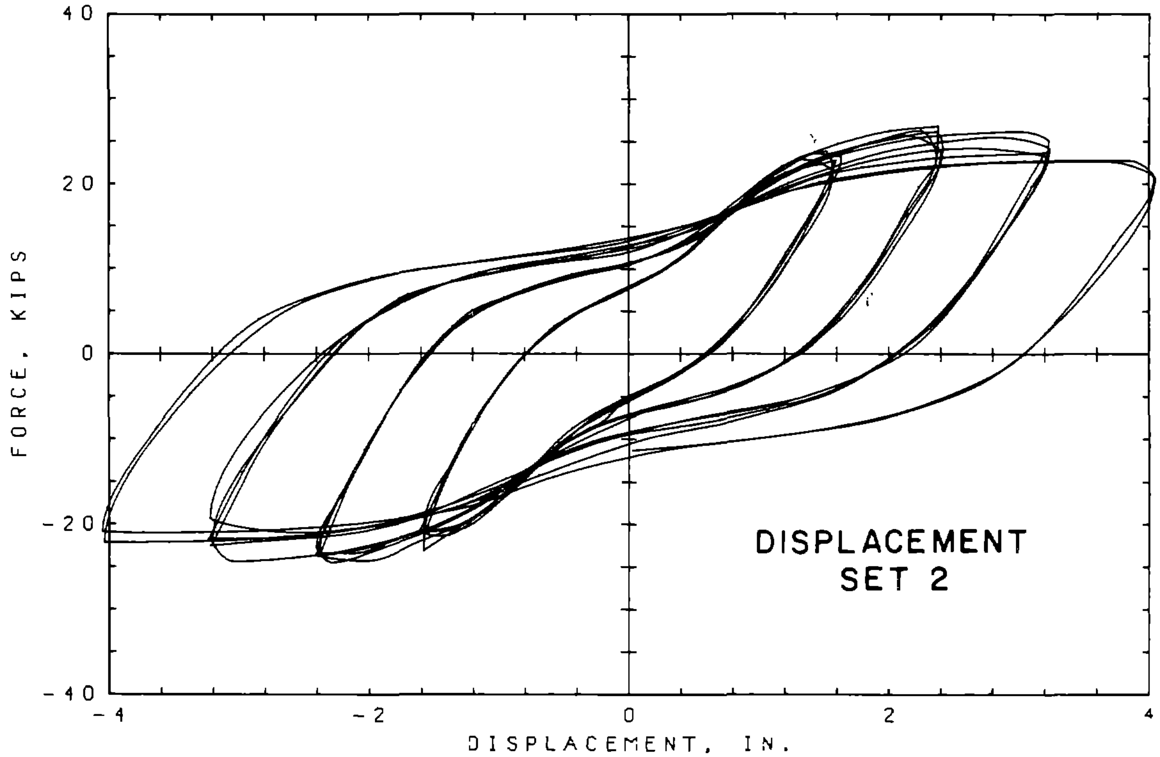

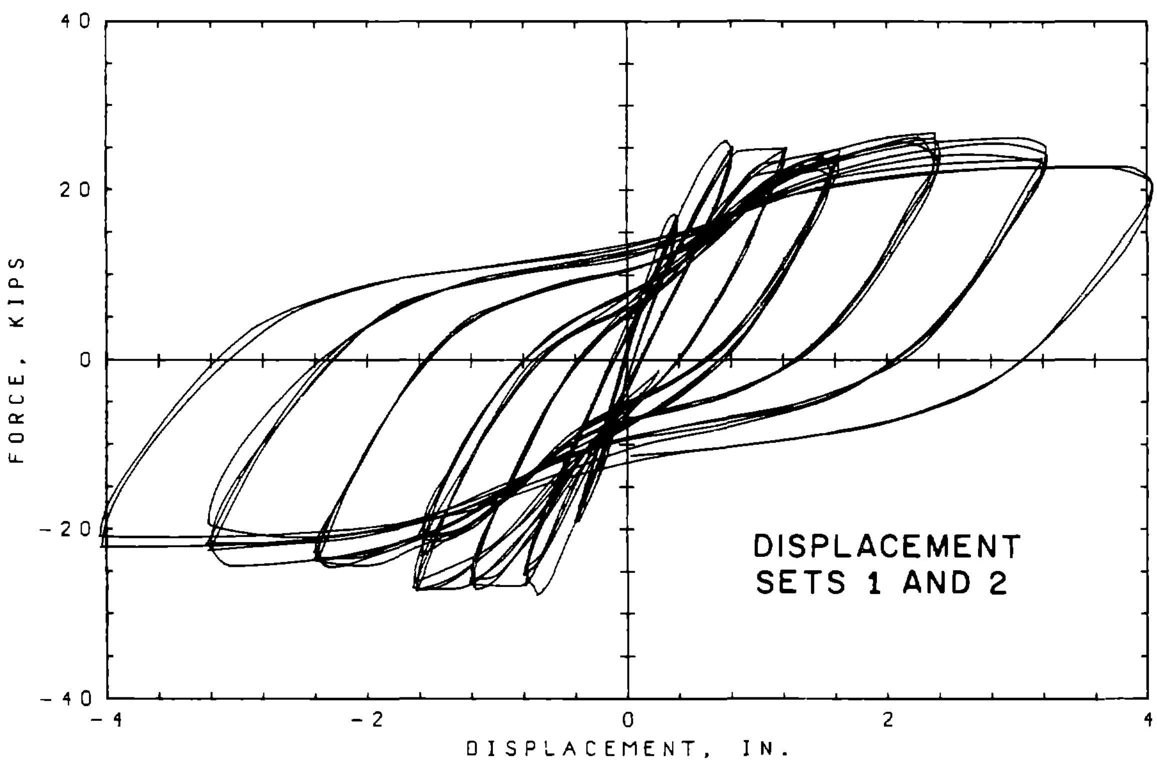

FIG. 4.2.a (CONTINUED) LATERAL FORCE-DISPLACEMENT DIAGRAMS, SPECIMEN 1

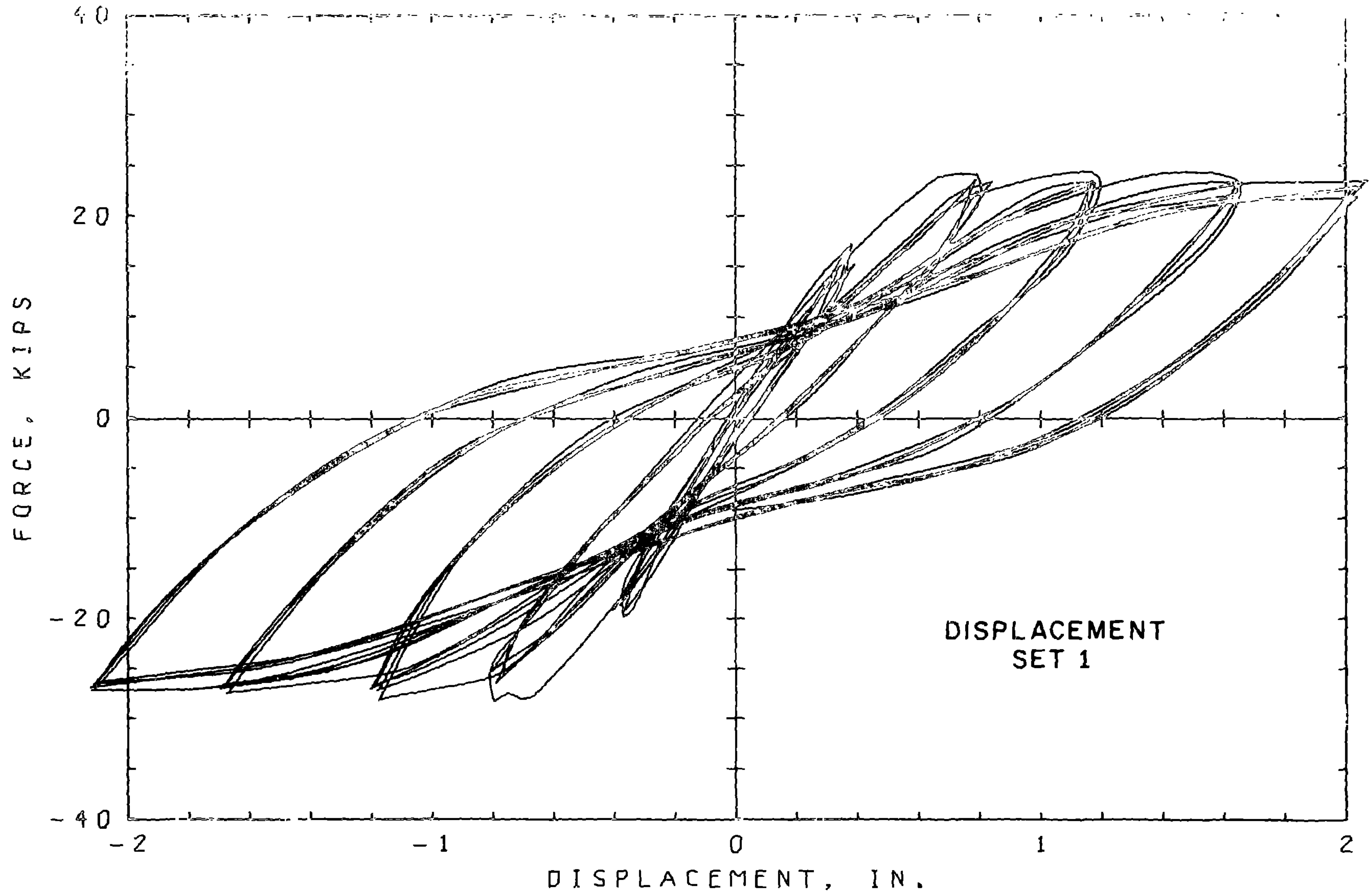

FIG. 4.2.b LATERAL FORCE-DISPLACEMENT DIAGRAMS, SPECIMEN 2

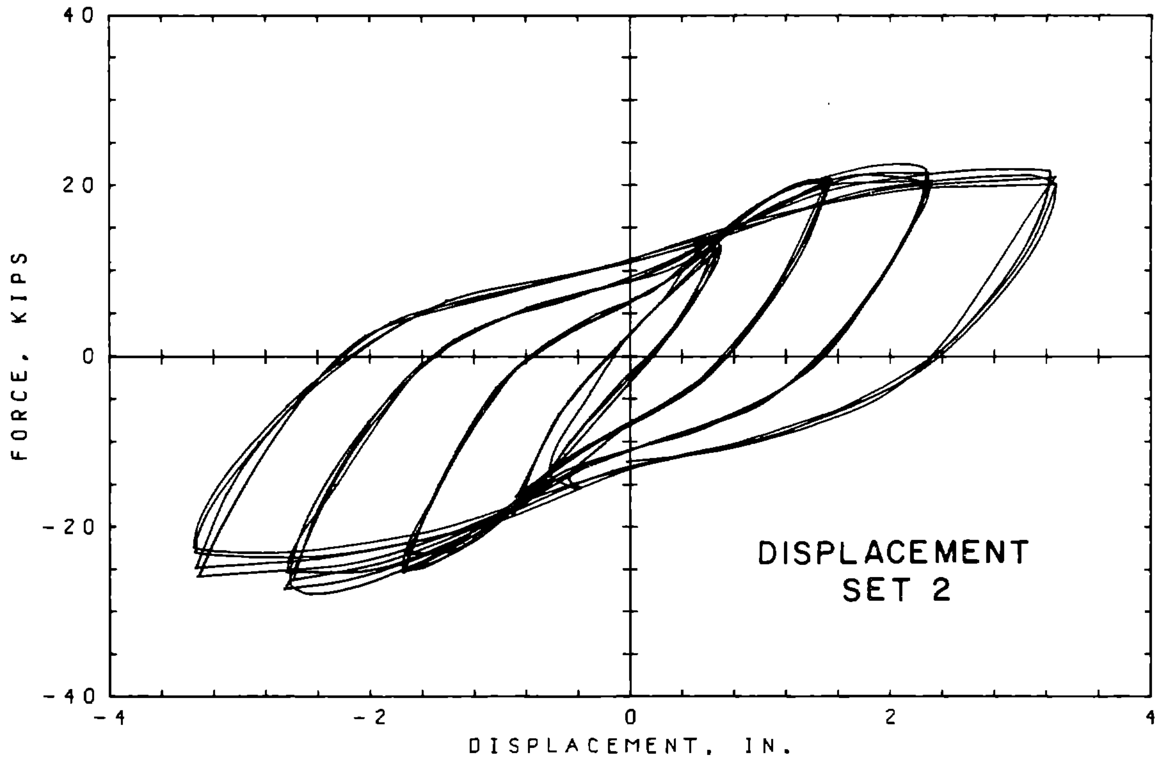

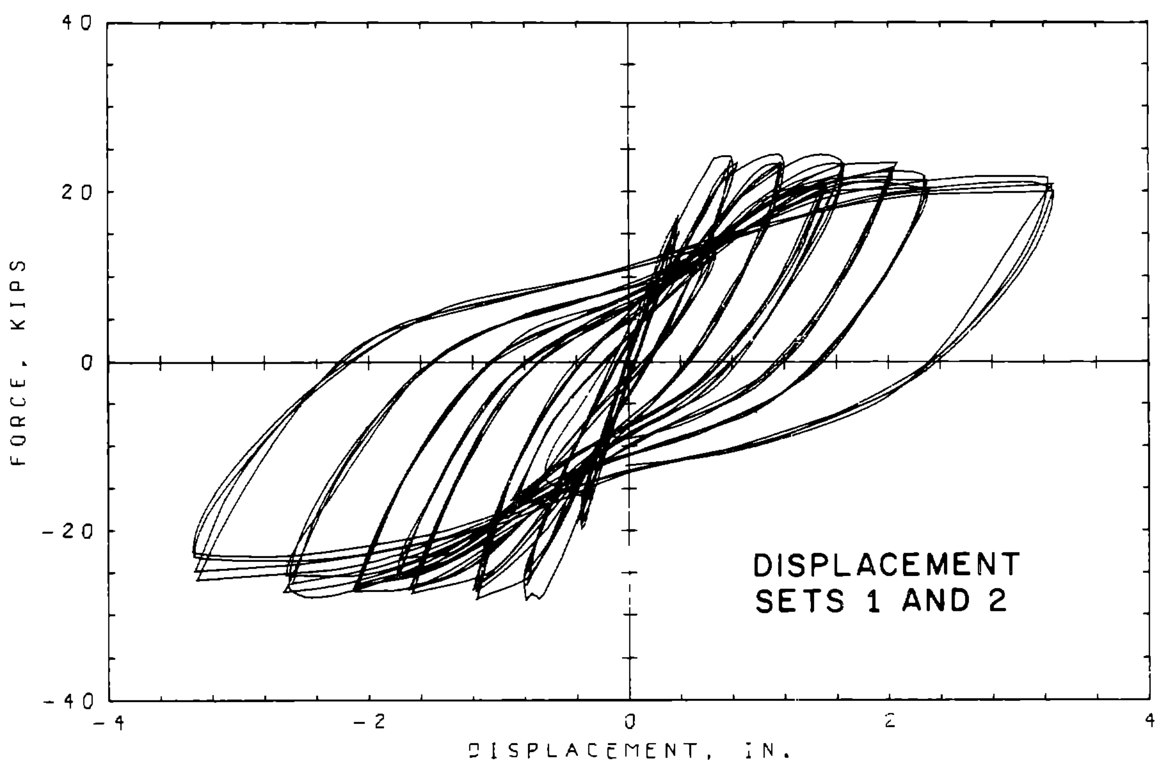

FIG. 4.2.b (CONTINUED) LATERAL FORCE-DISPLACEMENT DIAGRAMS, SPECIMEN 2

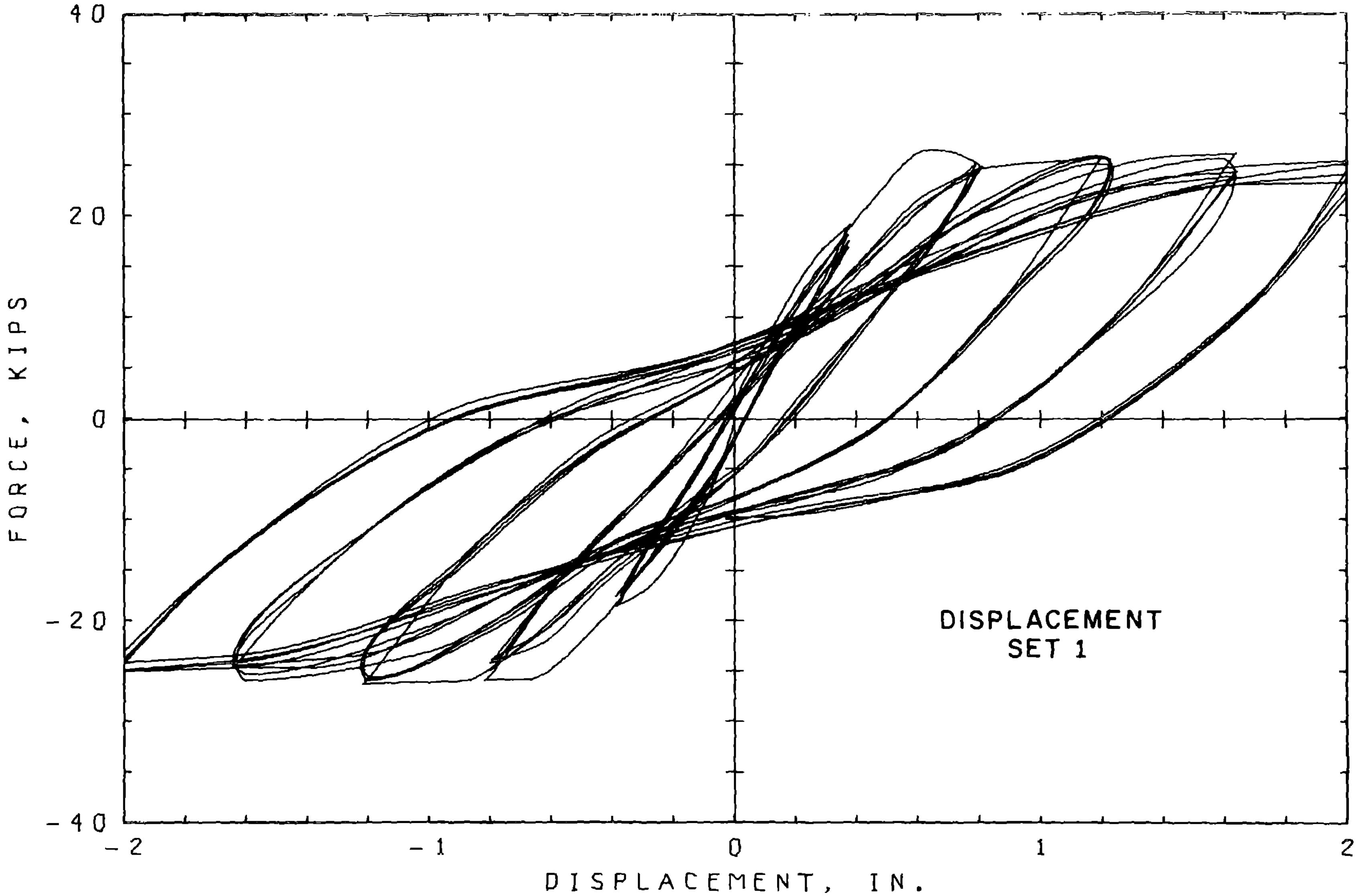

FIG. 4.2.c LATERAL FORCE-DISPLACEMENT DIAGRAMS, SPECIMEN 3

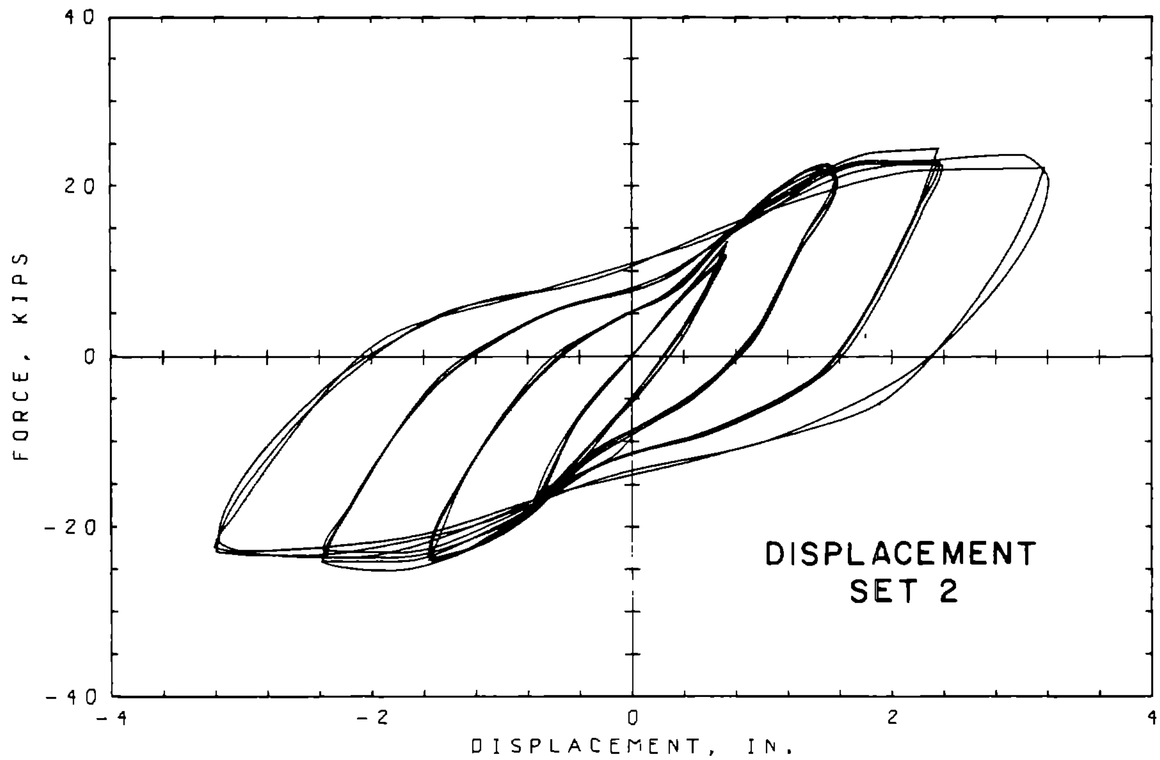

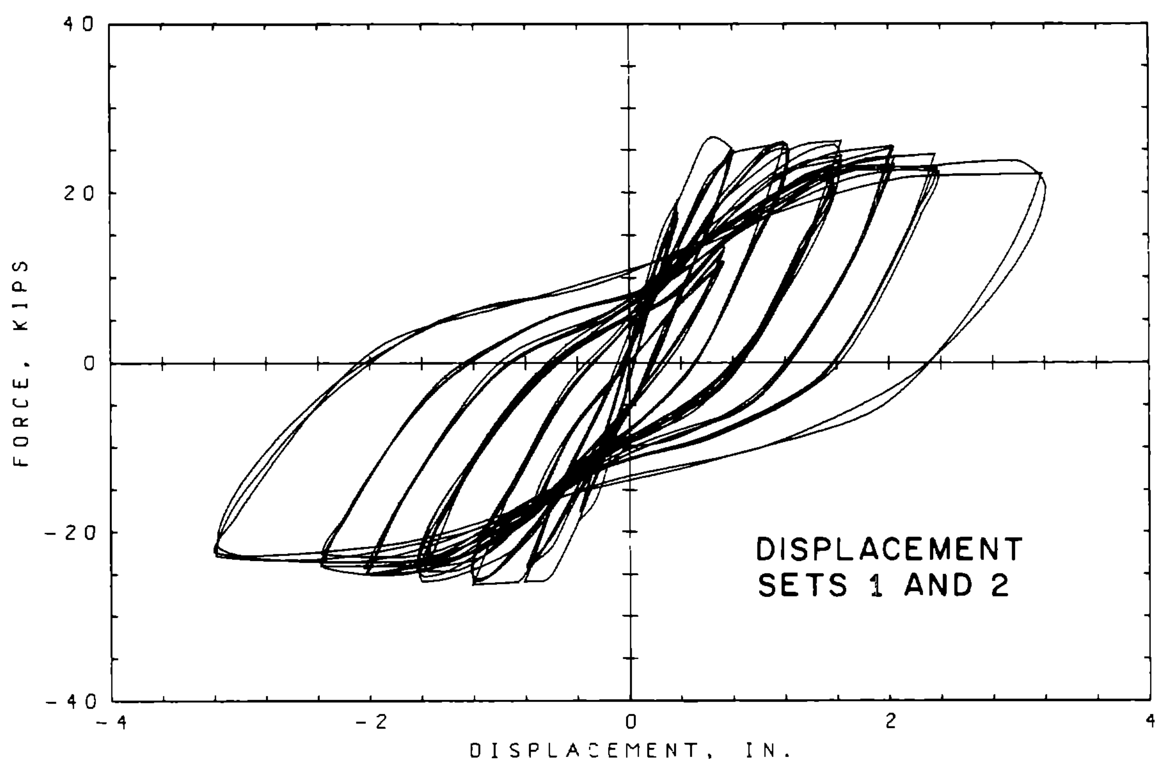

FIG. 4.2.c (CONTINUED) LATERAL FORCE-DISPLACEMENT DIAGRAMS, SPECIMEN 3

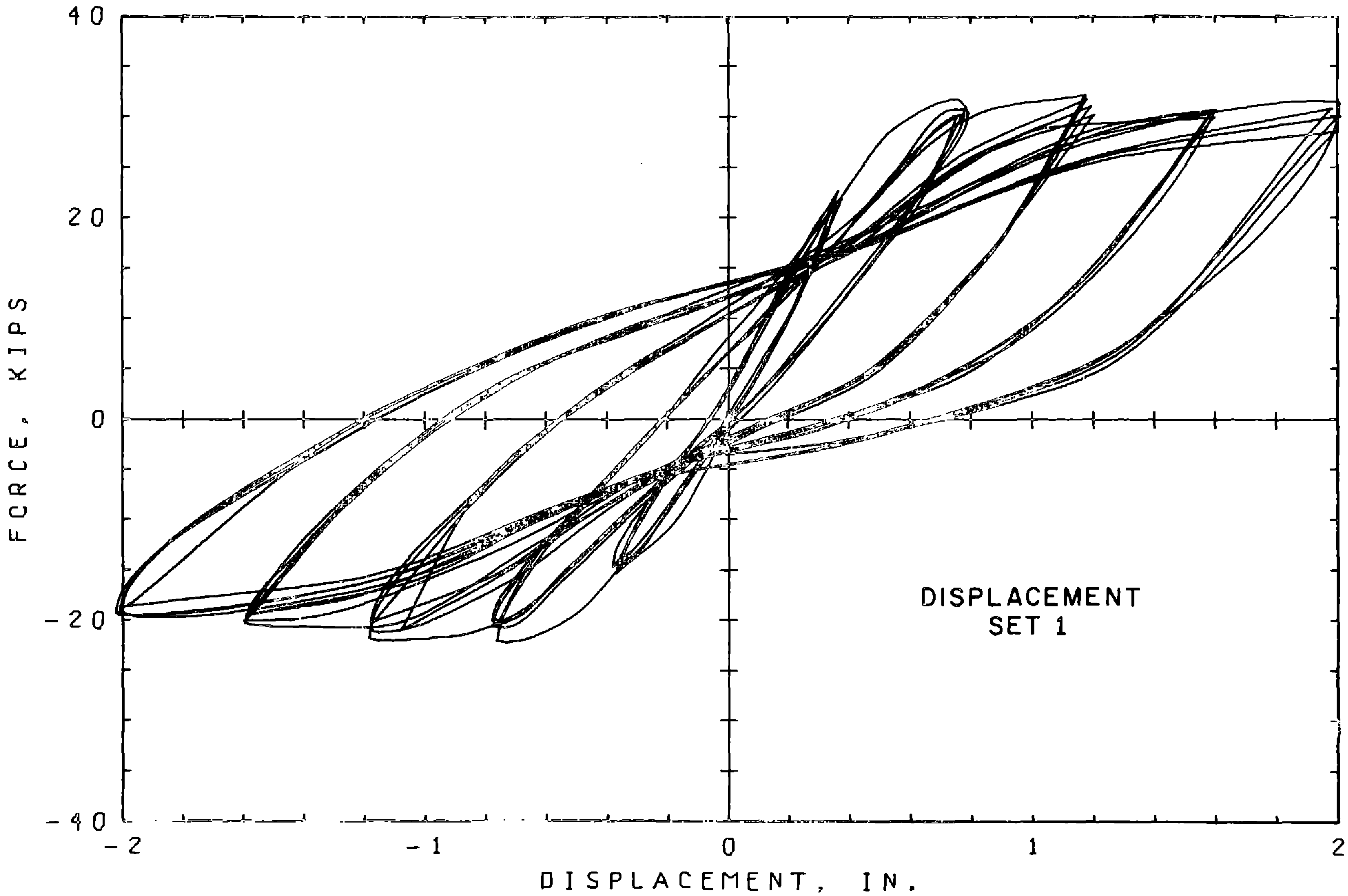

FIG. 4.2.d LATERAL FORCE-DISPLACEMENT DIAGRAMS, SPECIMEN 4

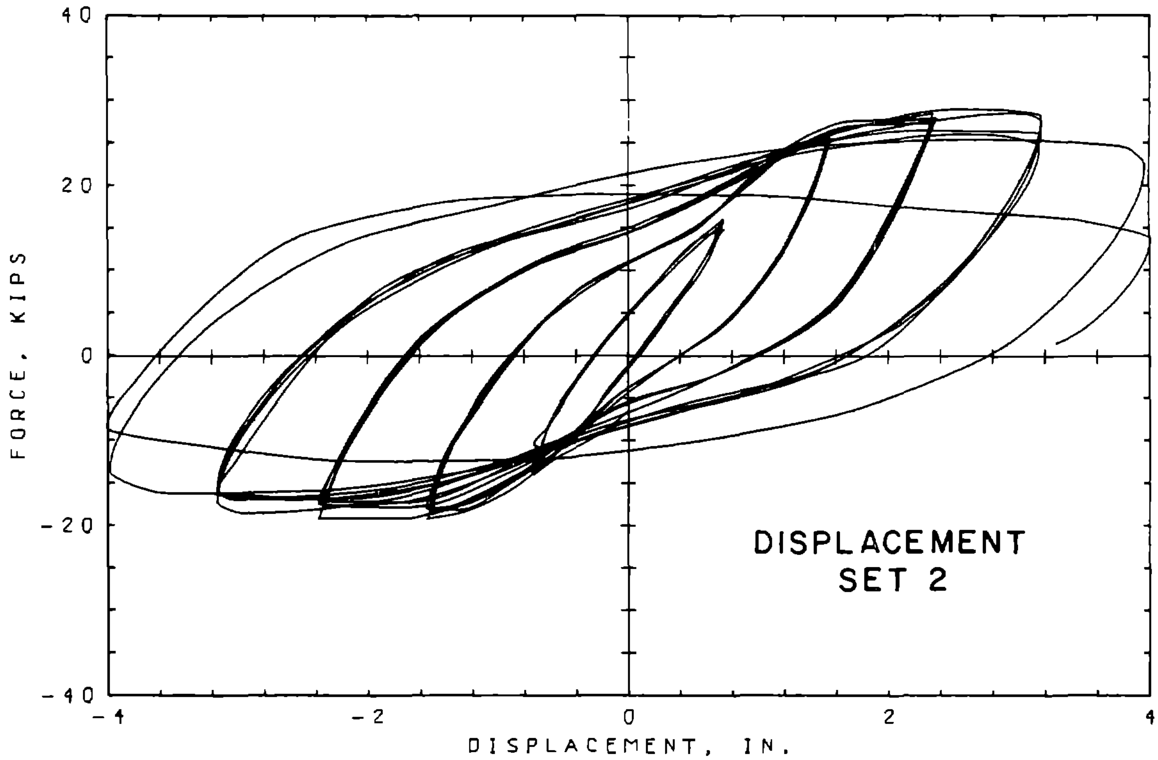

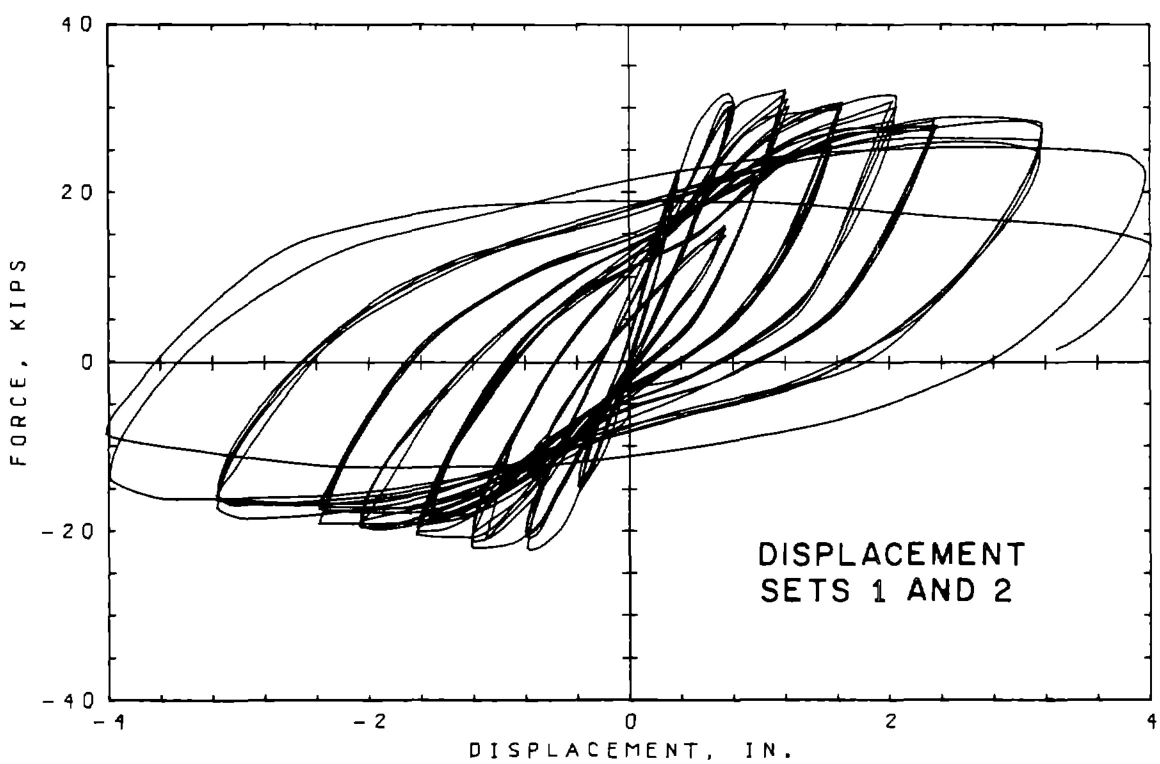

FIG. 4.2.d (CONTINUED) LATERAL FORCE-DISPLACEMENT DIAGRAMS, SPECIMEN 4

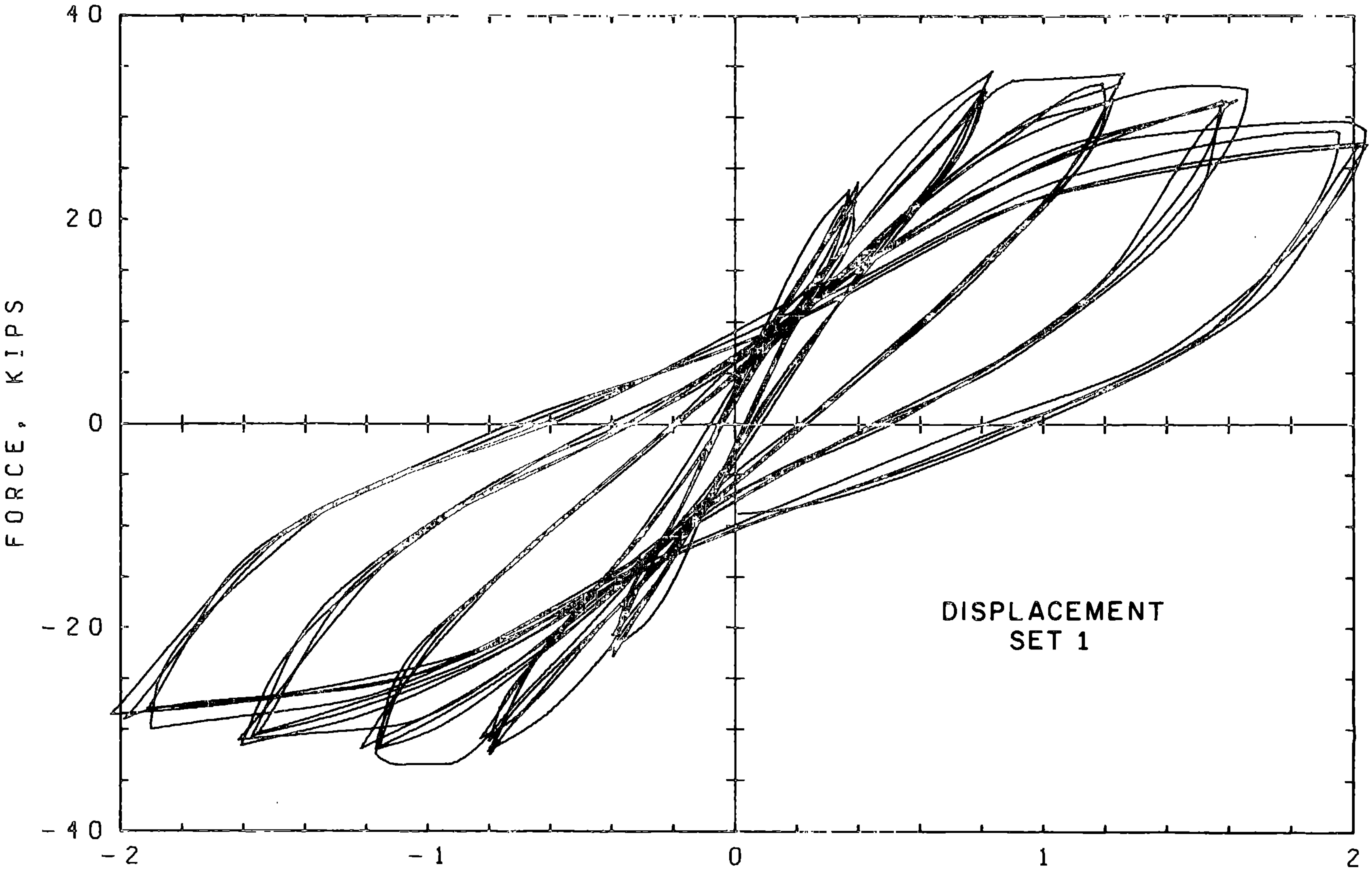

FIG. 4.2.e LATERAL FORCE-DISPLACEMENT DIAGRAMS, SPECIMEN 5

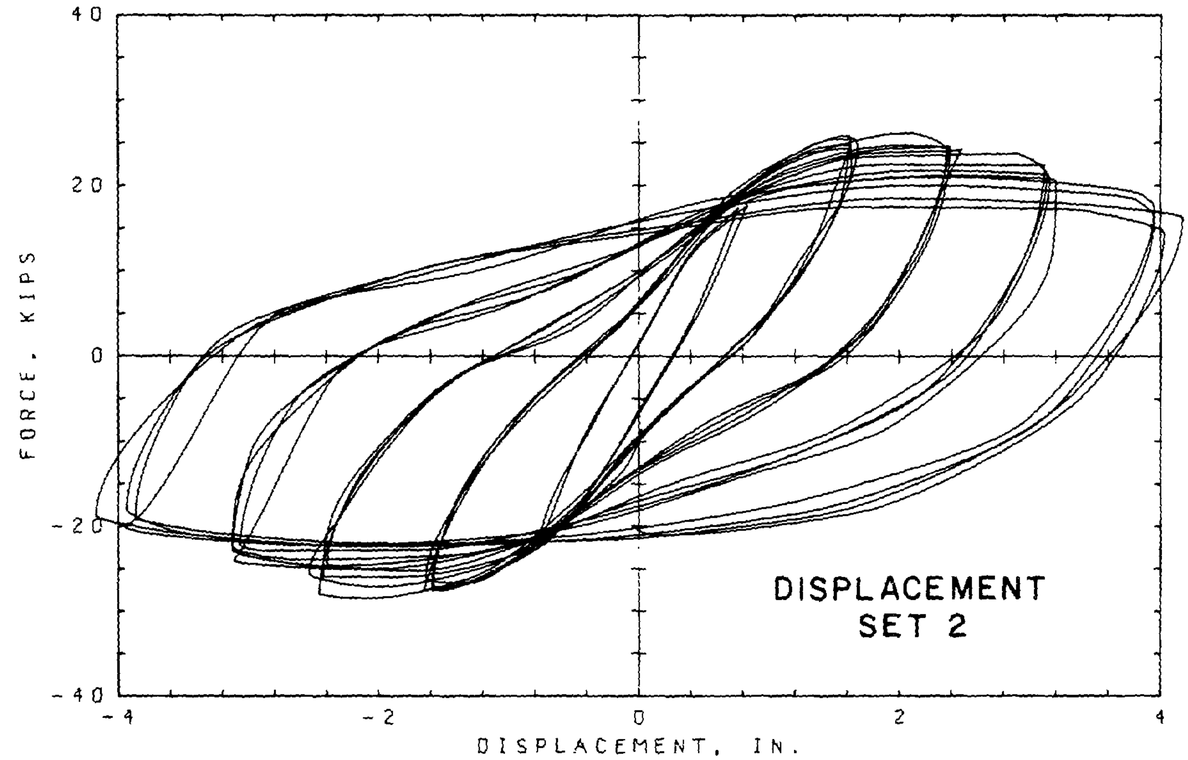

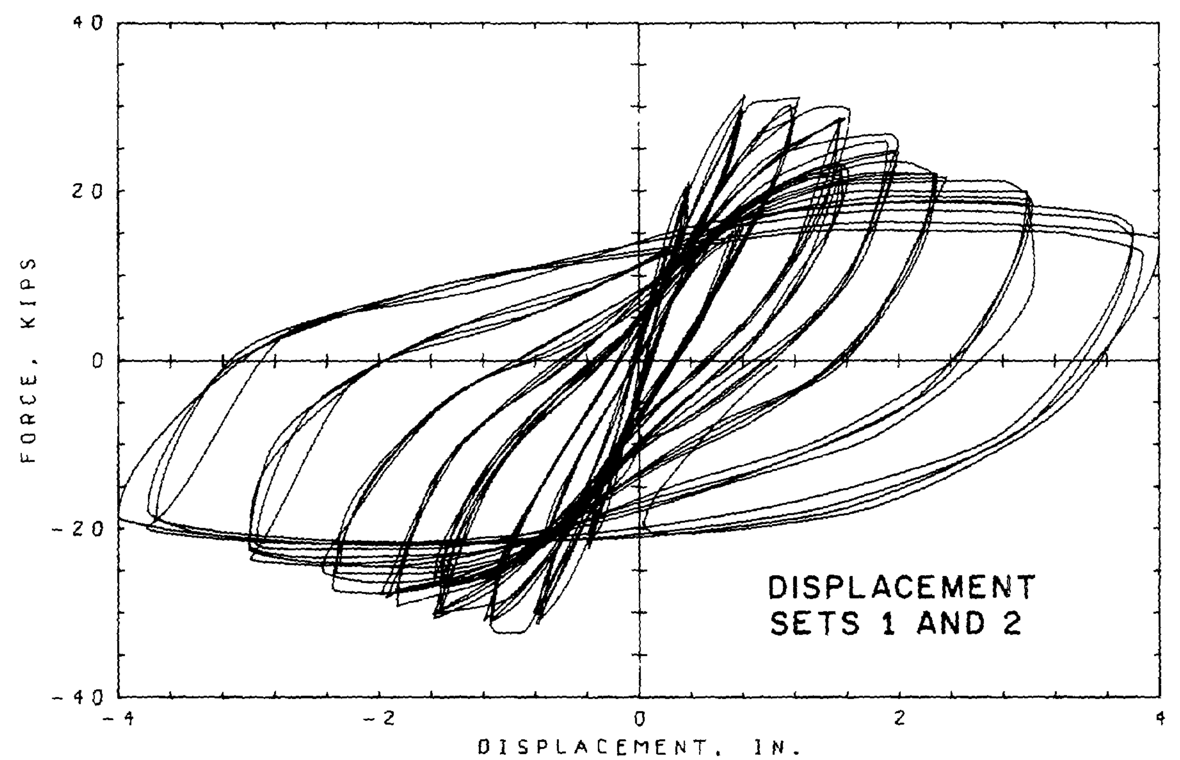

FIG. 4.2.e (CONTINUED) LATERAL FORCE-DISPLACEMENT DIAGRAMS, SPECIMEN 5

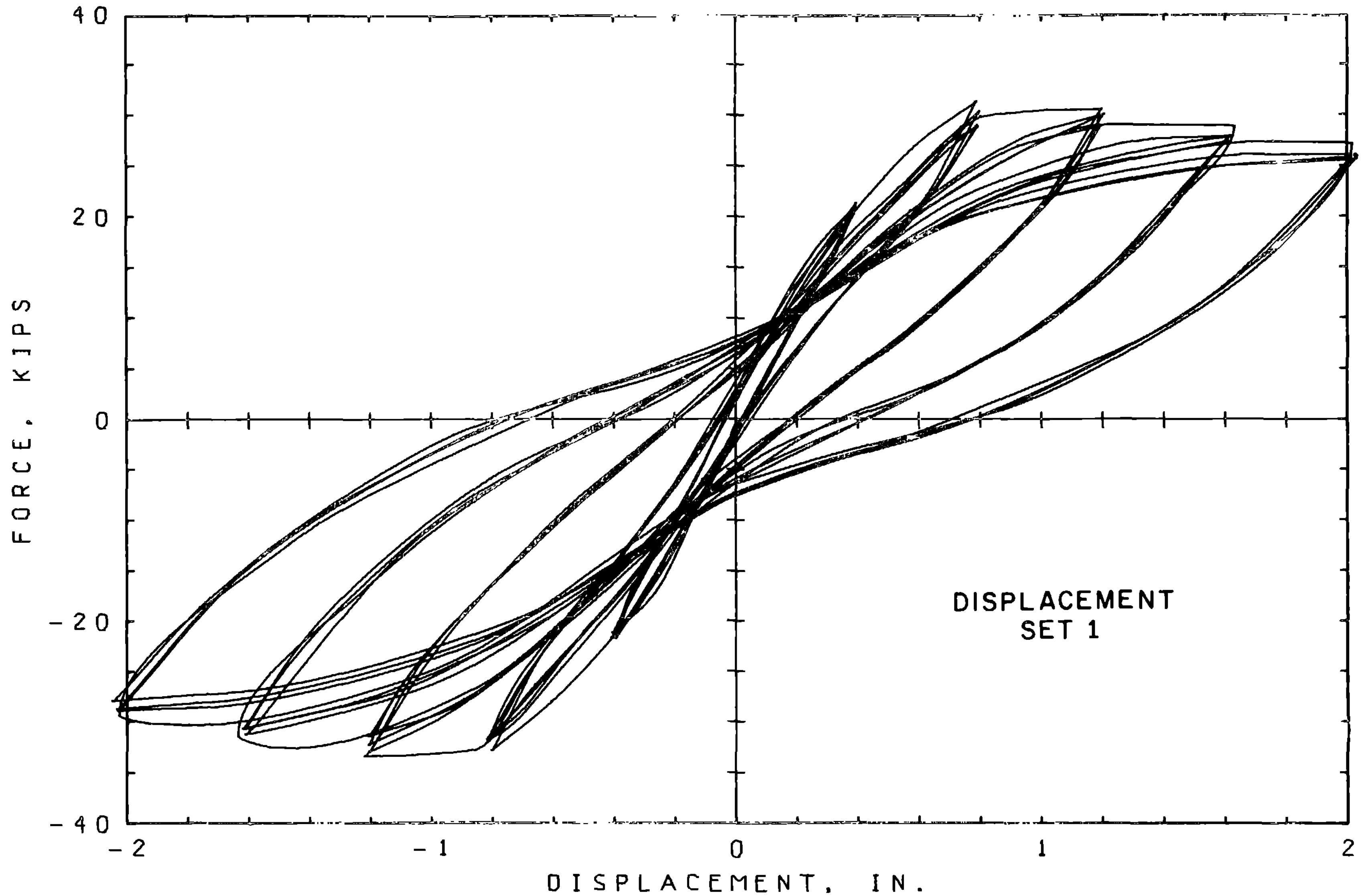

FIG. 4.2.f LATERAL FORCE-DISPLACEMENT DIAGRAMS, SPECIMEN 6

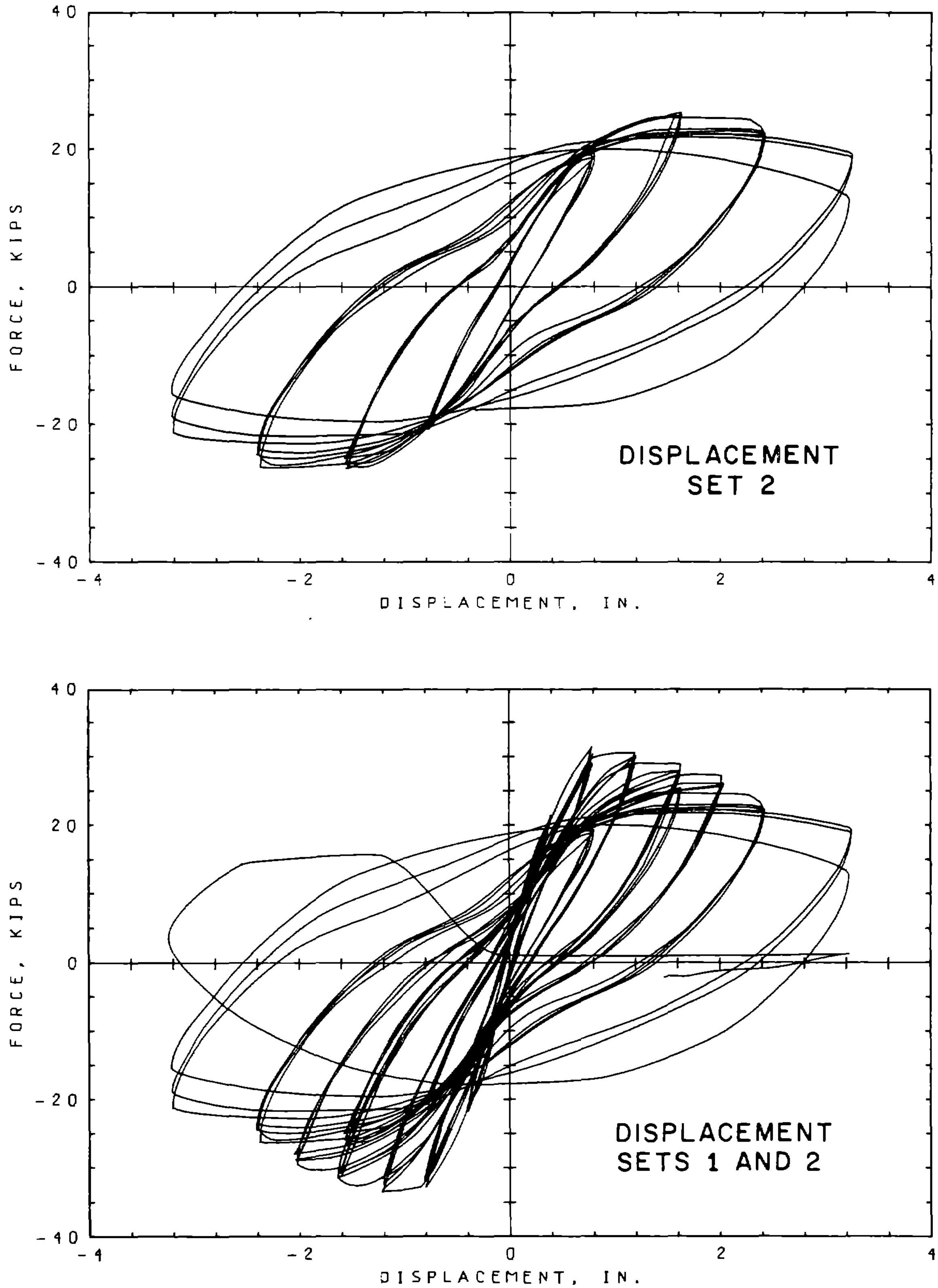

FIG. 4.2.f (CONTINUED) LATERAL FORCE-DISPLACEMENT DIAGRAMS, SPECIMEN 6

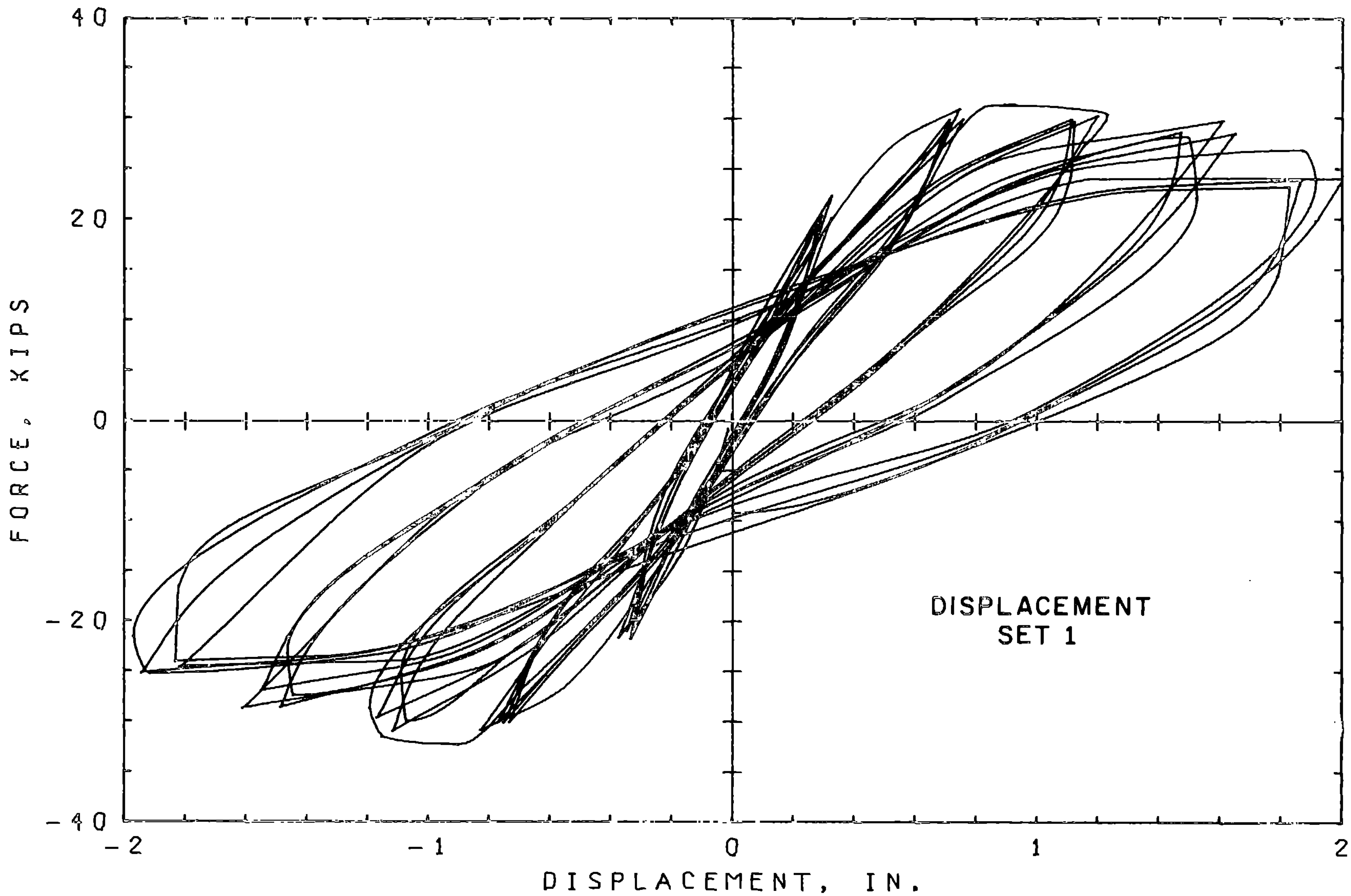

FIG. 4.2.g LATERAL FORCE-DISPLACEMENT DIAGRAMS, SPECIMEN 7

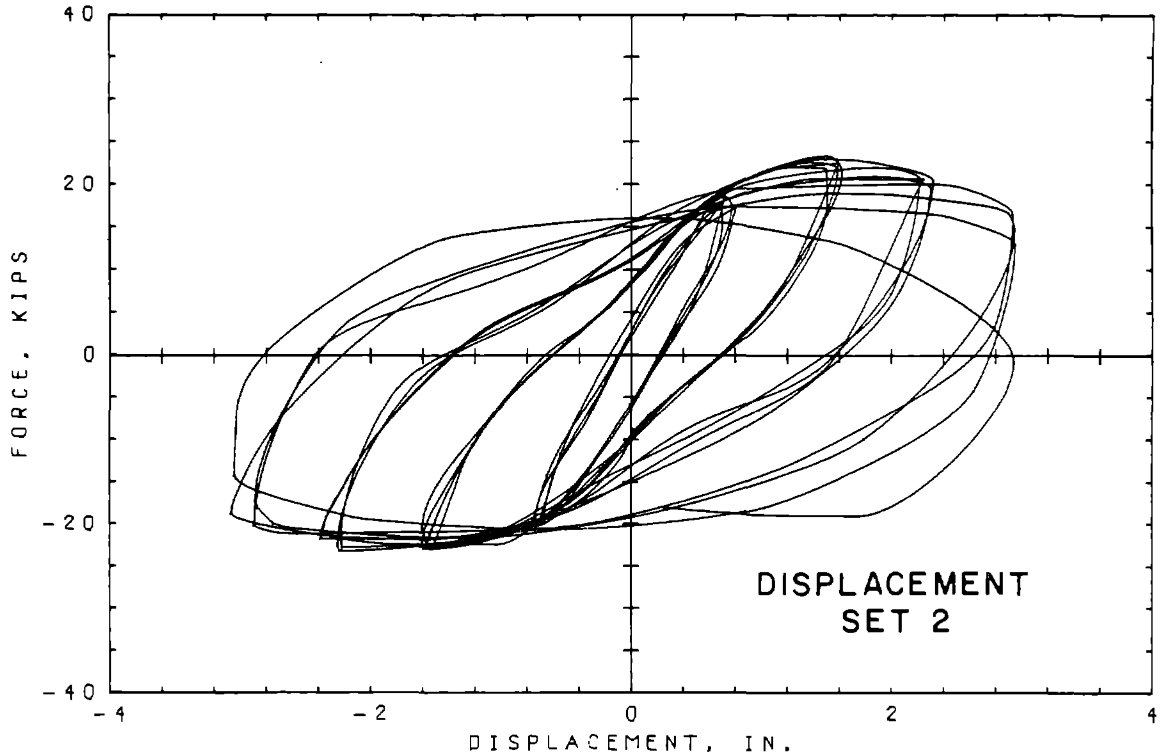

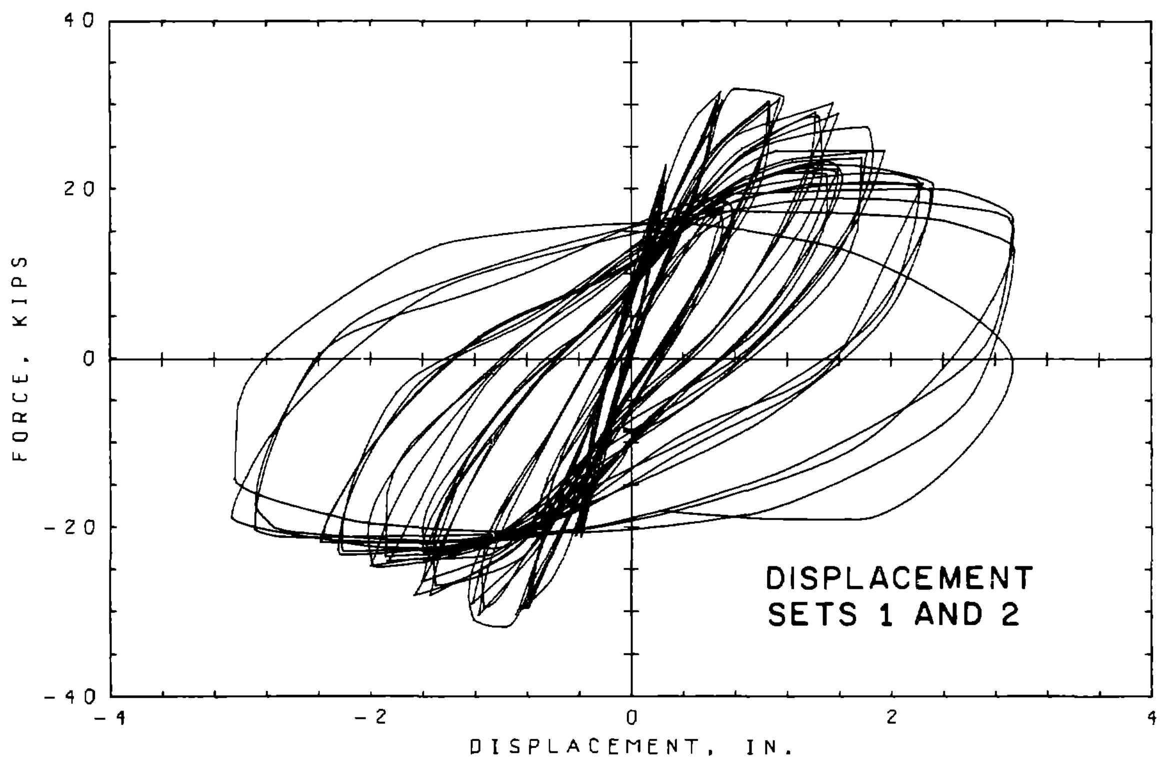

FIG. 4.2.g (CONTINUED) LATERAL FORCE-DISPLACEMENT DIAGRAMS, SPECIMEN 7

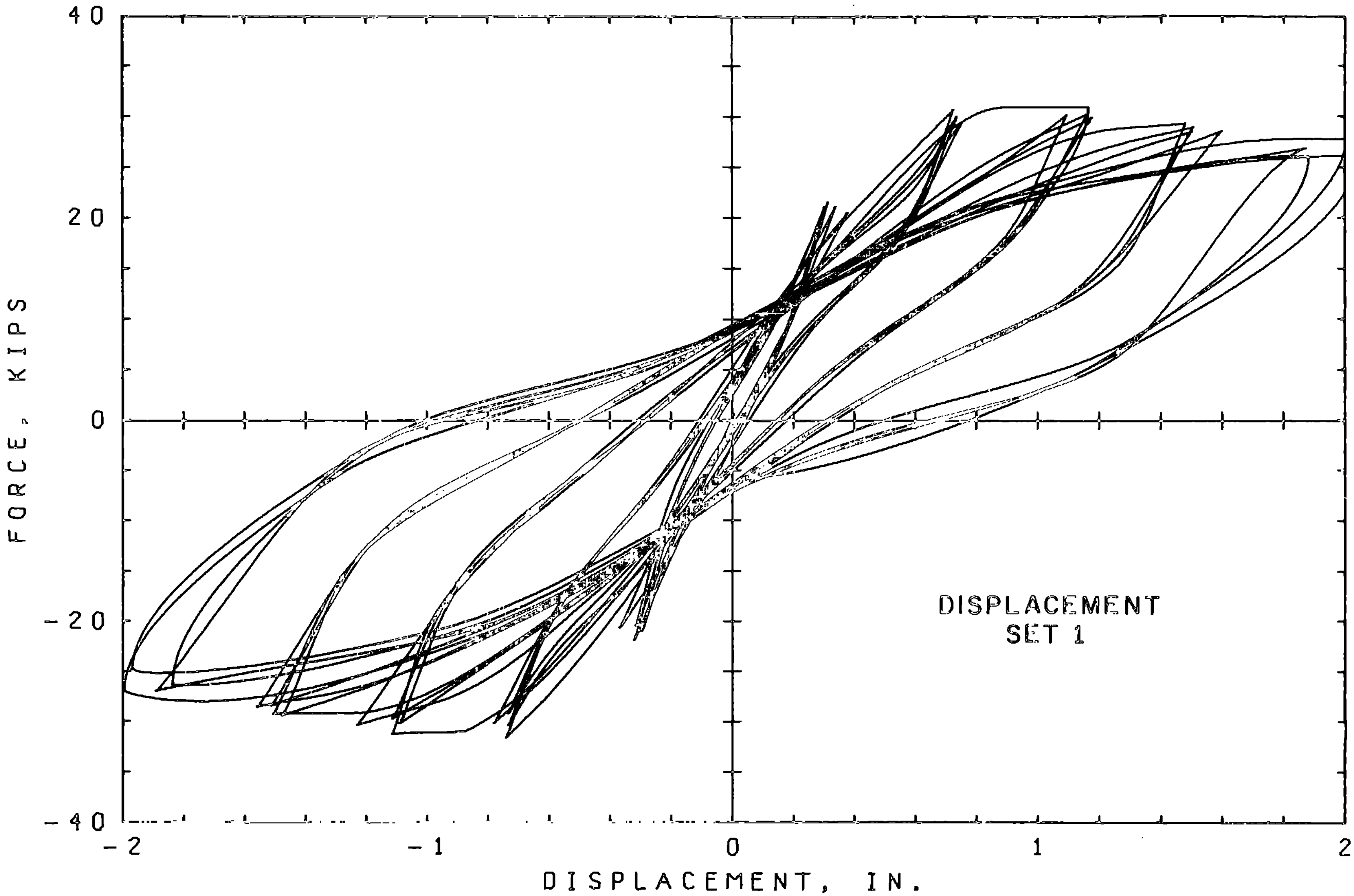

FIG. 4.2.h LATERAL FORCE-DISPLACEMENT DIAGRAMS, SPECIMEN 8

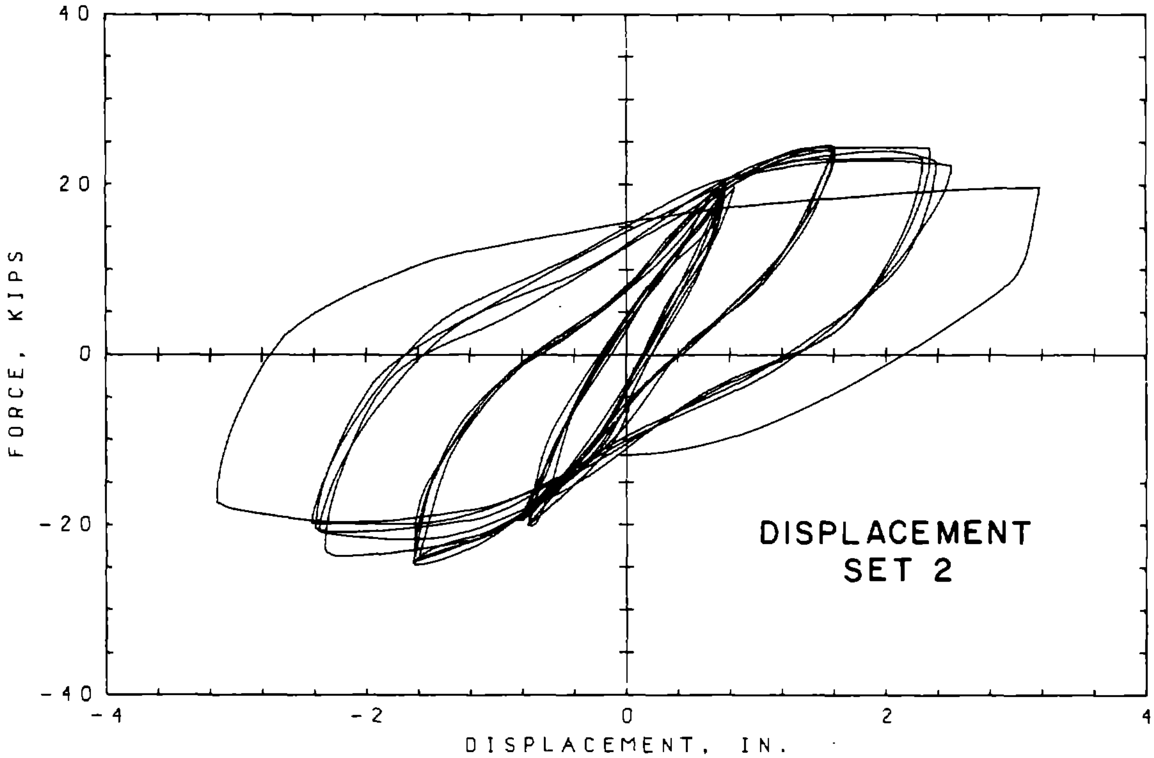

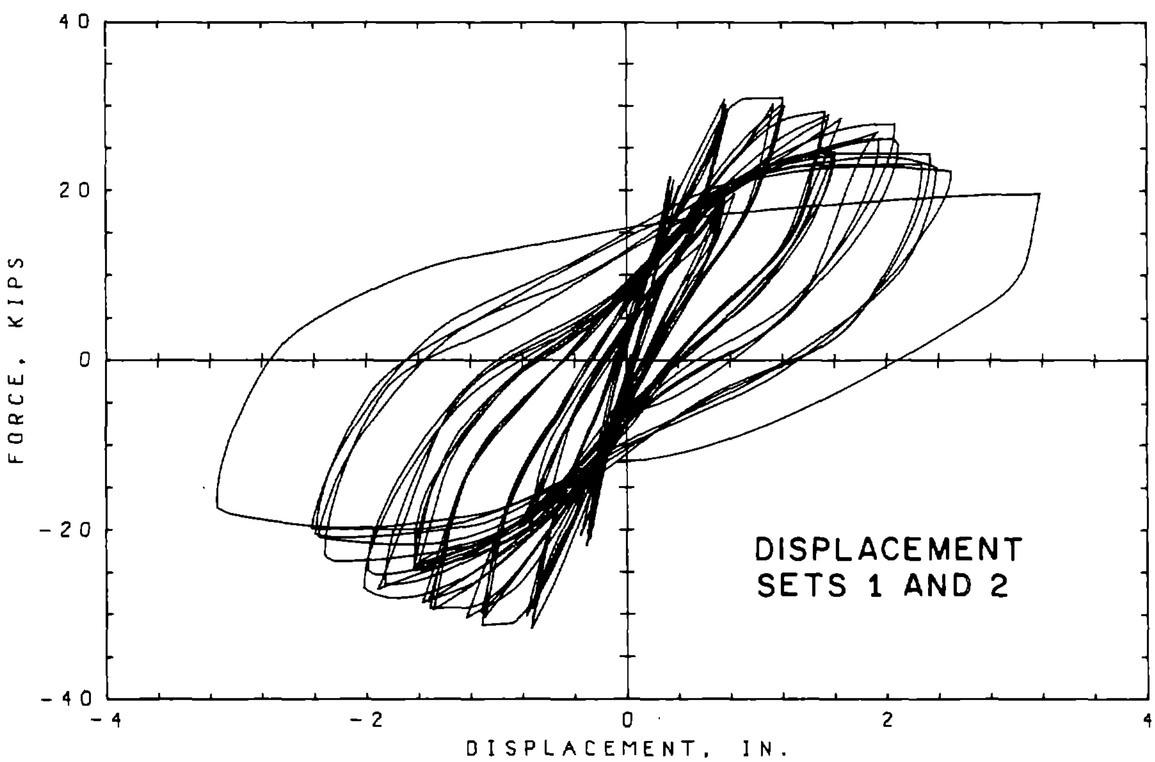

FIG. 4.2.h (CONTINUED) LATERAL FORCE-DISPLACEMENT DIAGRAMS, SPECIMEN 8

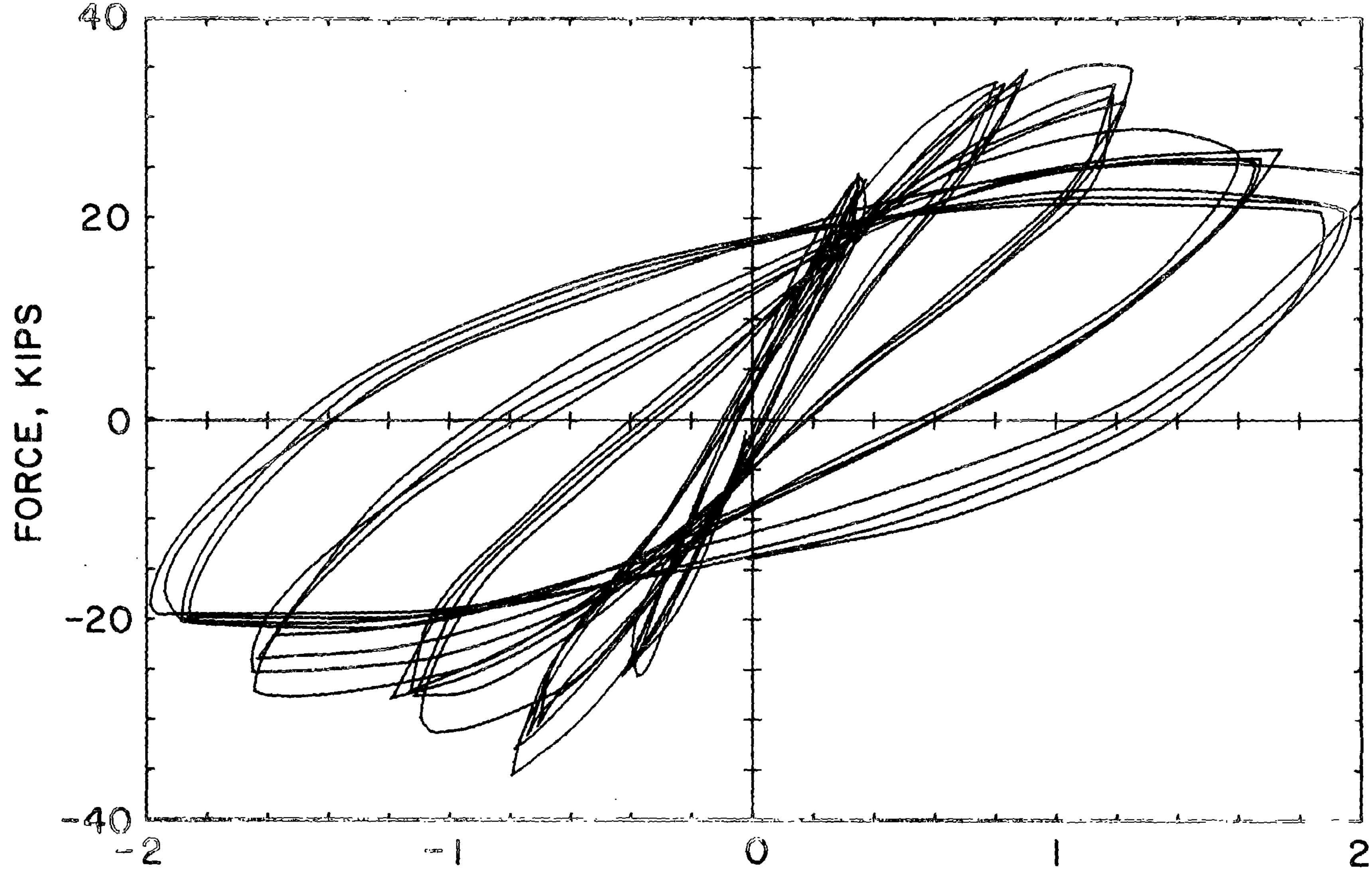

FIG. 4.2.i LATERAL FORCE-DISPLACEMENT DIAGRAM , SPECIMEN 9

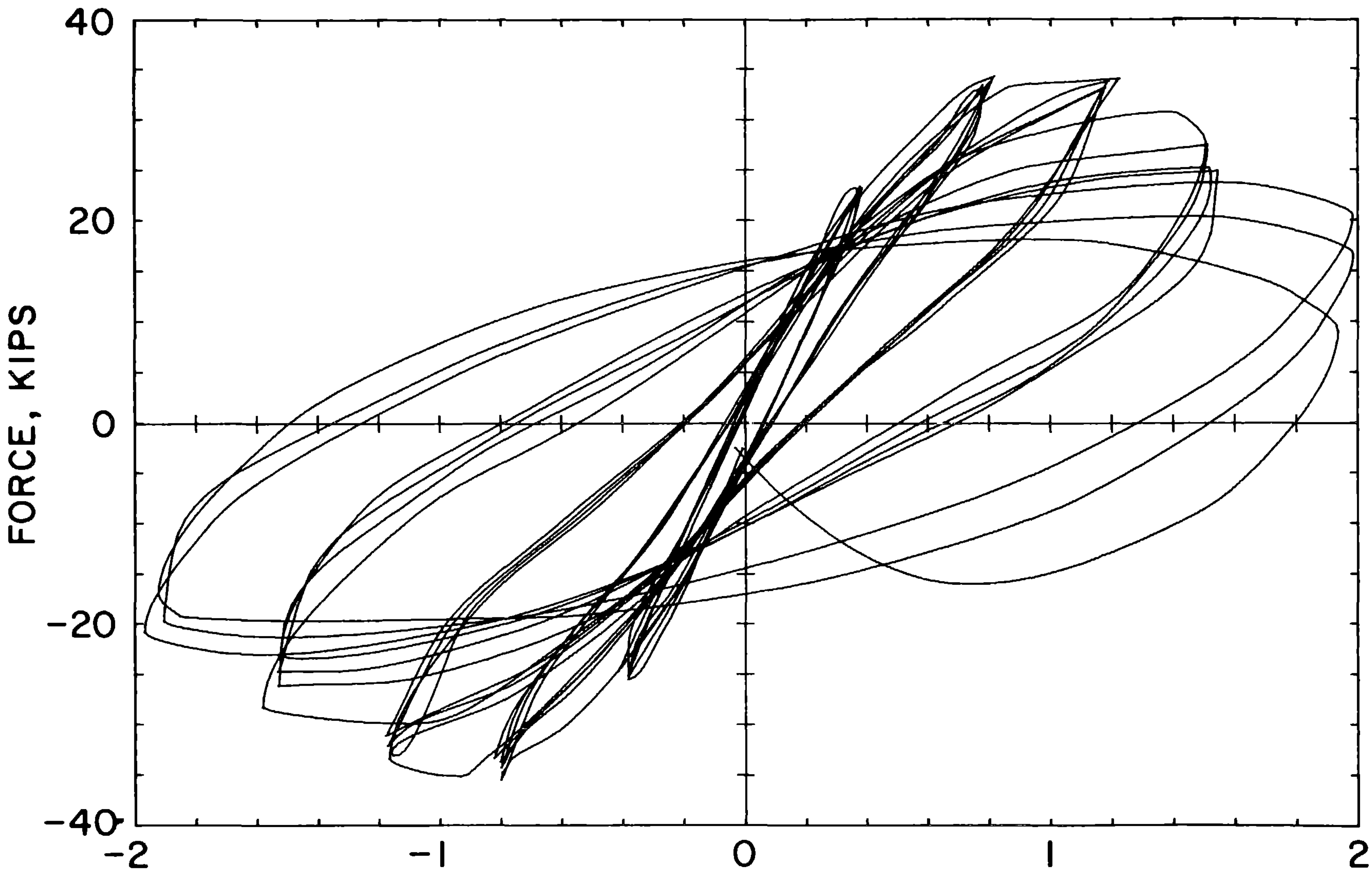

FIG. 4.2.j LATERAL FORCE-DISPLACEMENT DIAGRAM , SPECIMEN 10

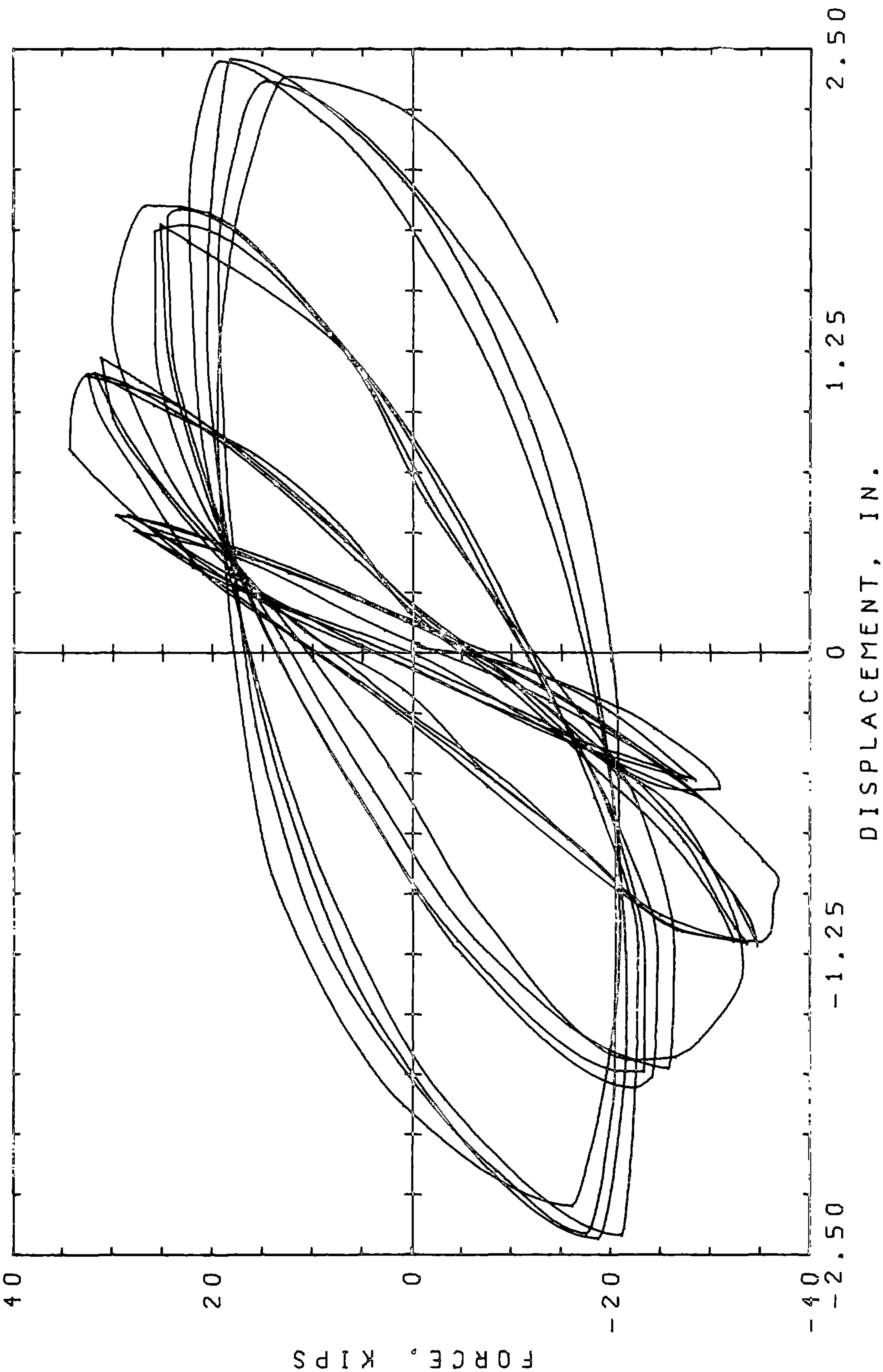

FIG. 4.2.k LATERAL FORCE-DISPLACEMENT DIAGRAM , SPECIMEN II

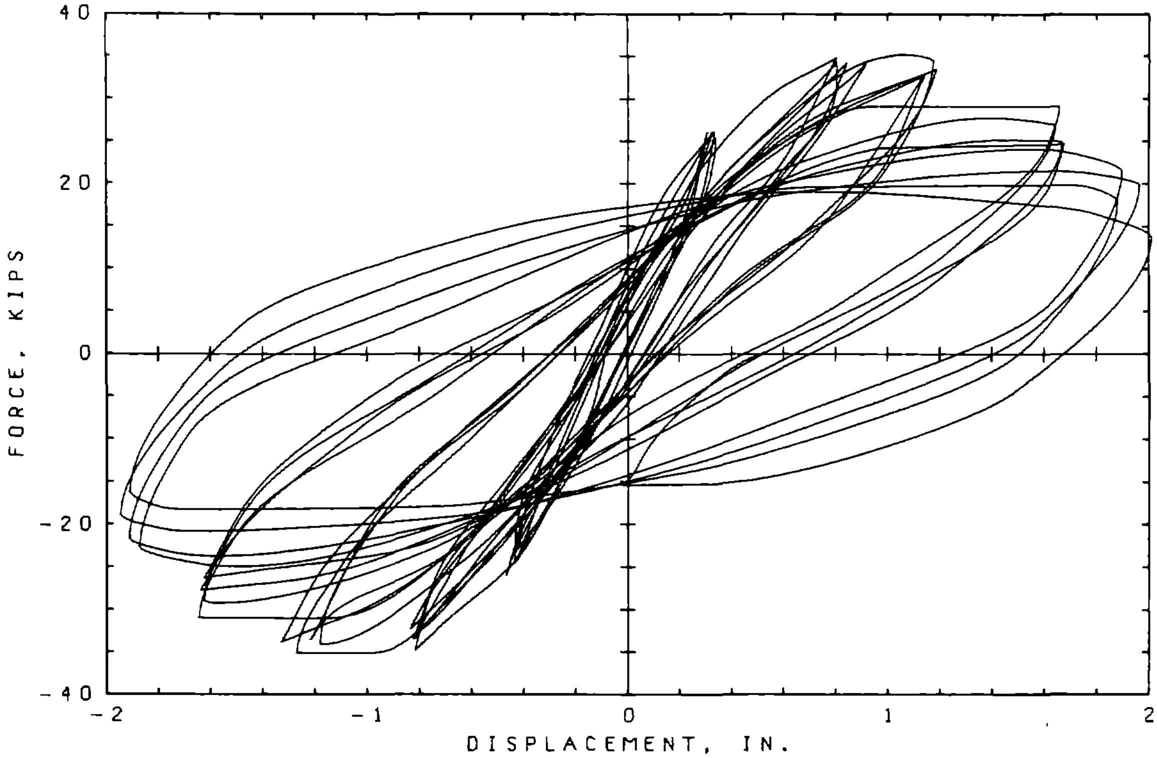

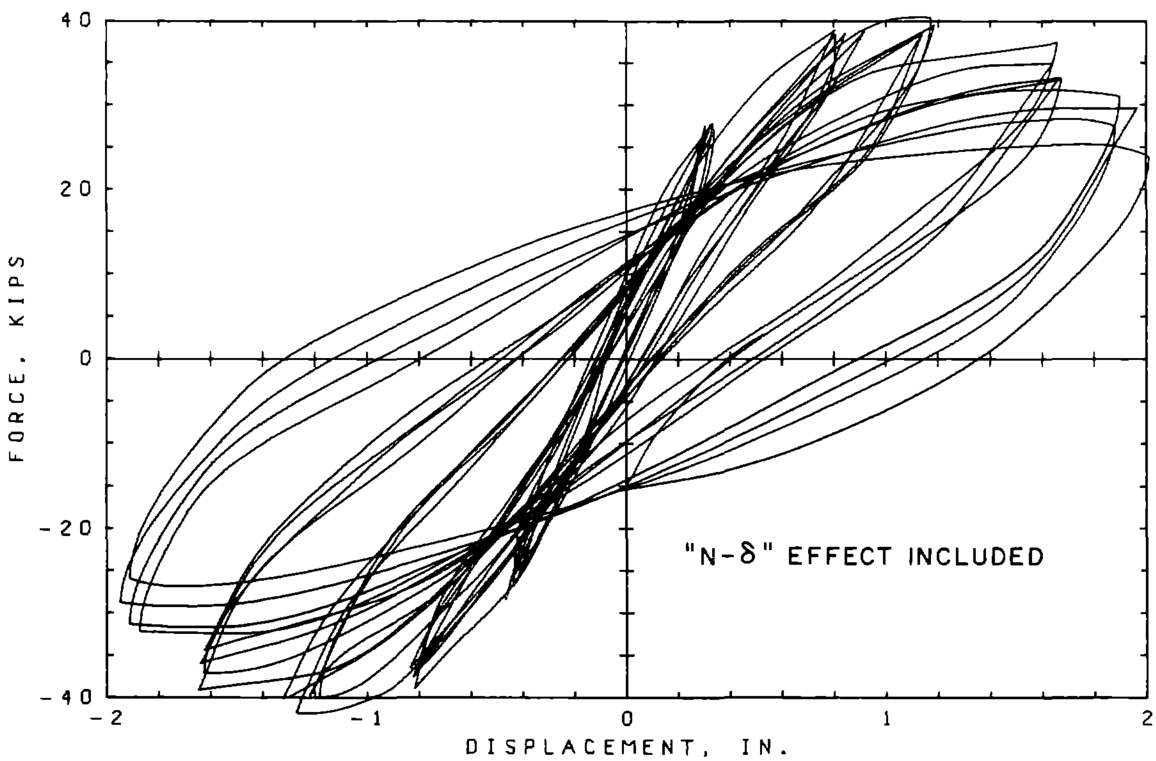

FIG. 4.2.ℓ LATERAL FORCE-DISPLACEMENT DIAGRAMS, SPECIMEN 12

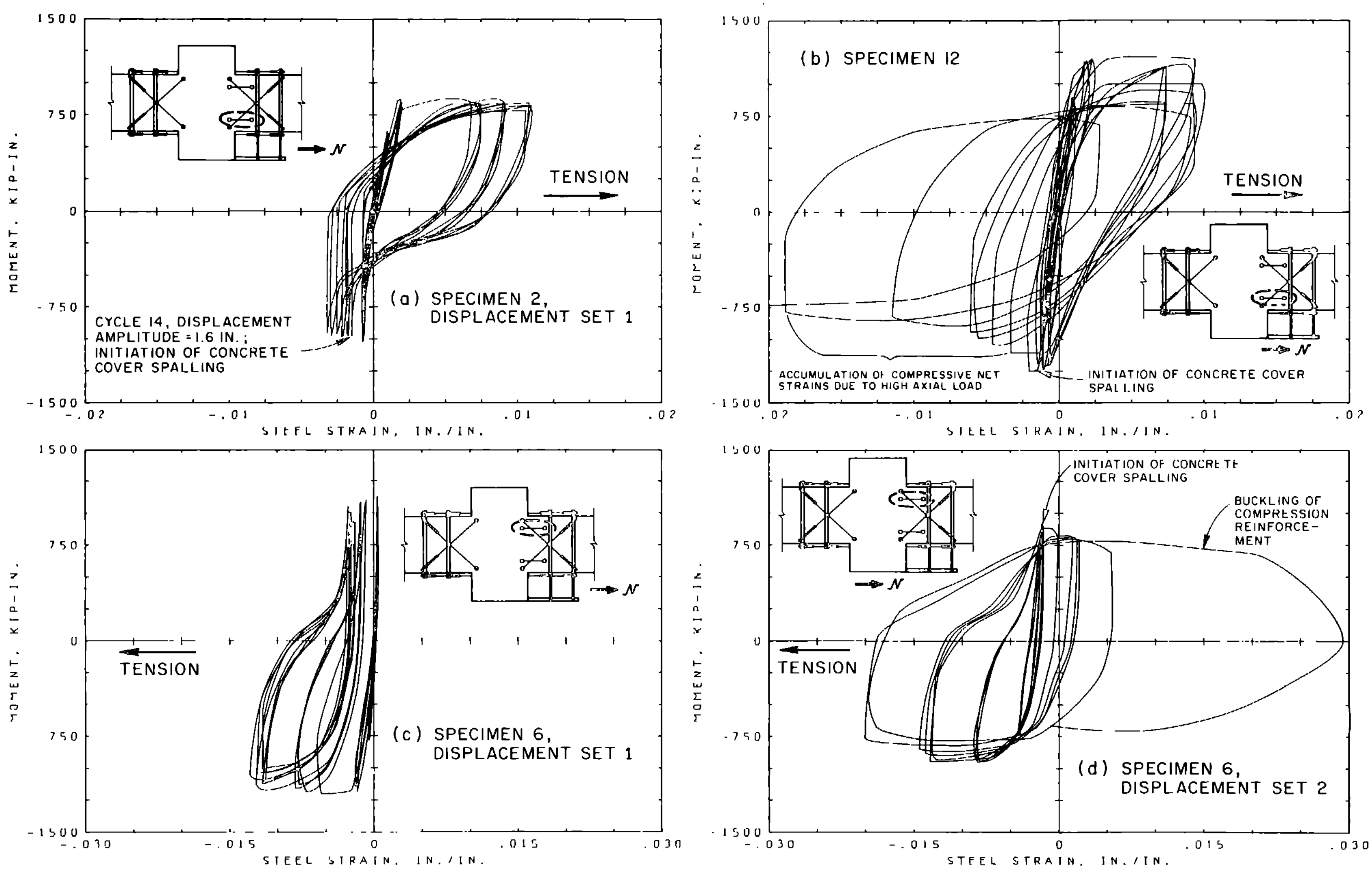

FIG. 4.3 MOMENT--LONGITUDINAL REINFORCEMENT STRAIN DIAGRAMS, TYPICAL

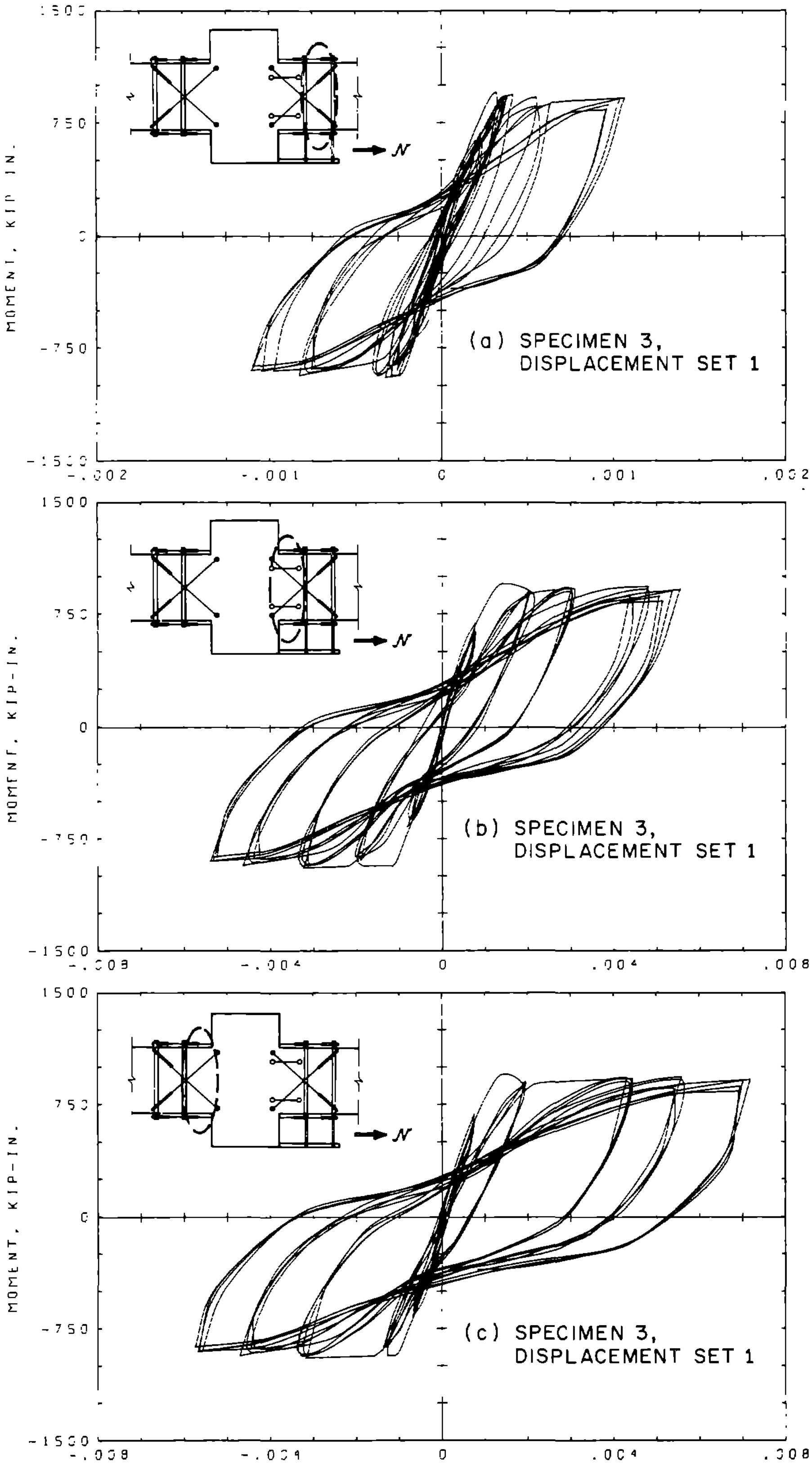

FIG. 4.4 MOMENT-AVERAGE CURVATURE DIAGRAMS, TYPICAL

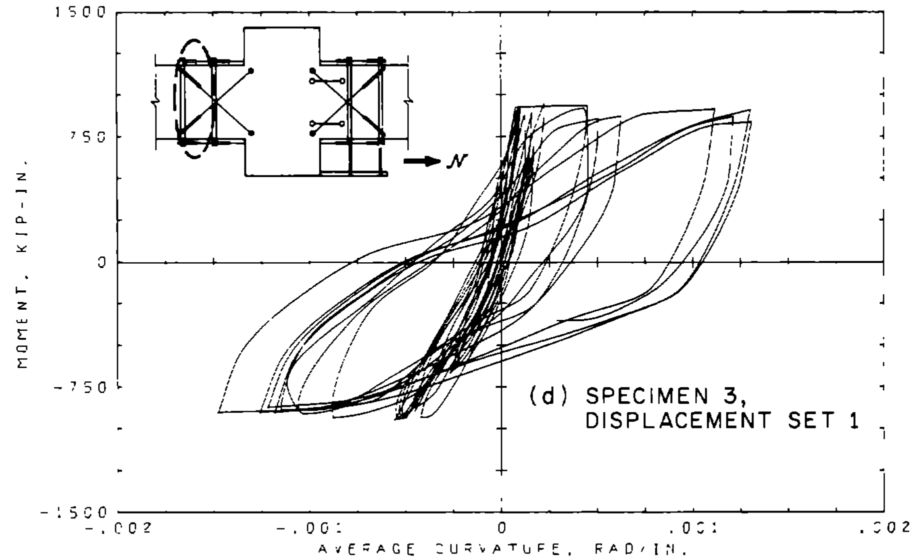

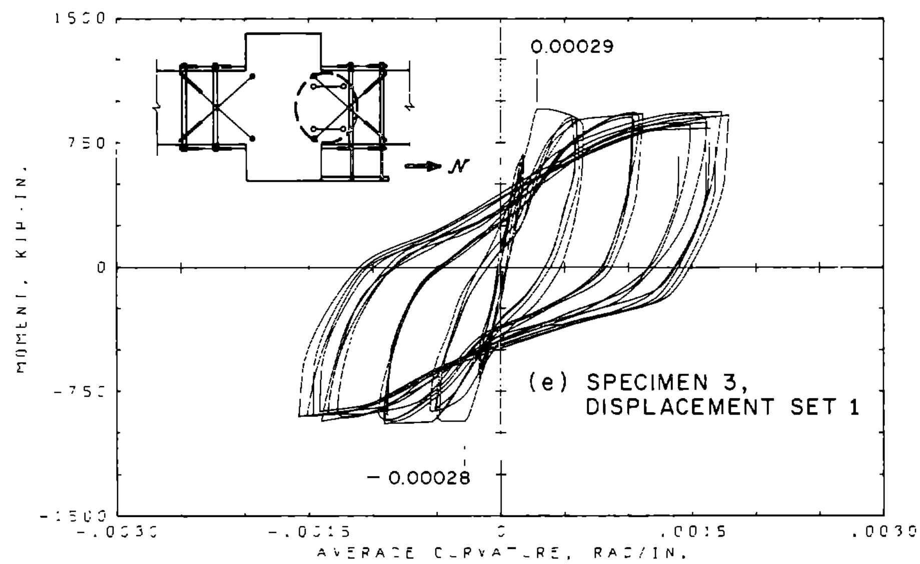

FIG. 4.4 (CONTINUED) MOMENT-AVERAGE CURVATURE DIAGRAMS, TYPICAL

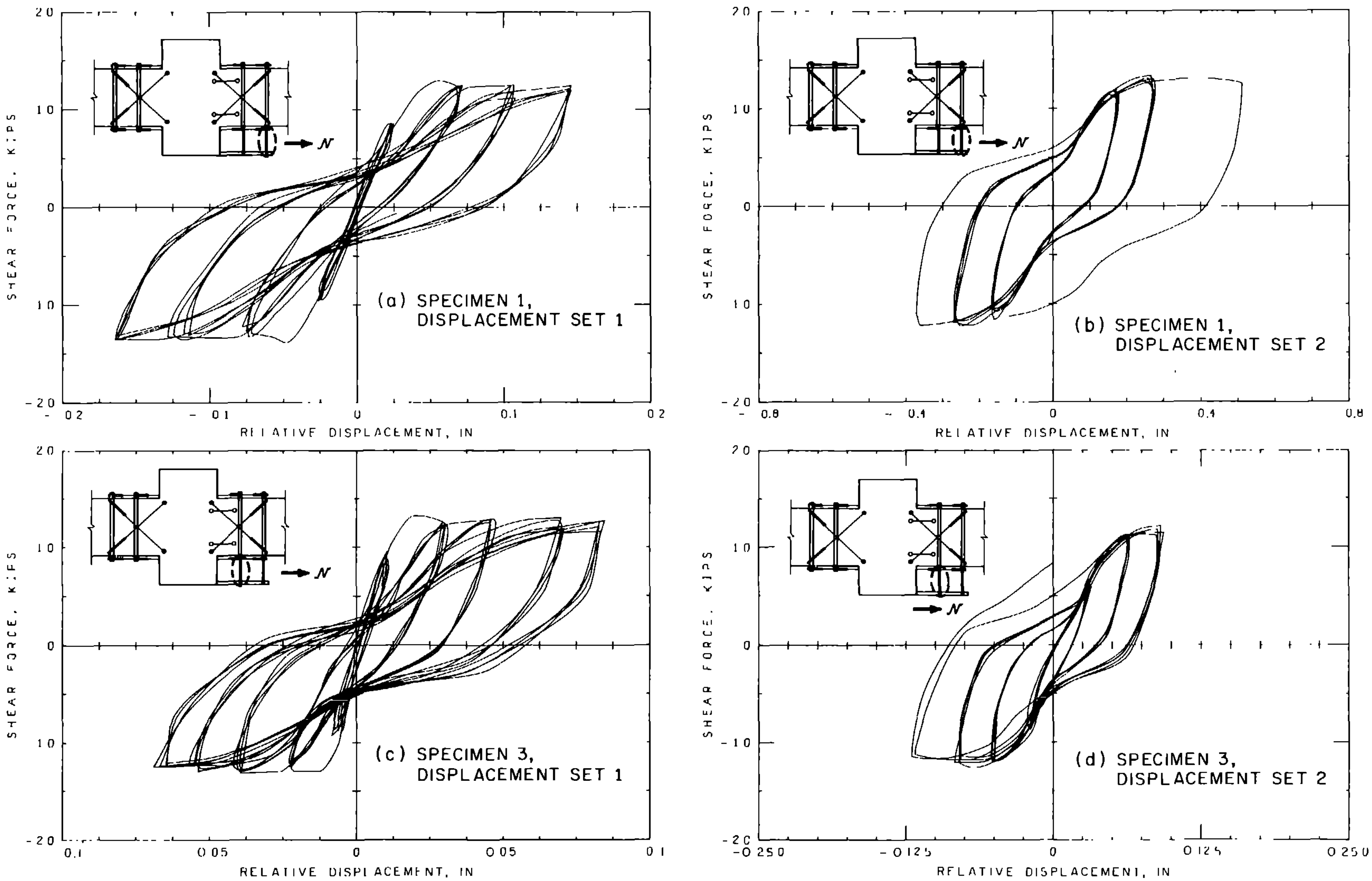

FIG. 4.5 SHEAR FORCE-RELATIVE DISPLACEMENT DIAGRAMS, TYPICAL

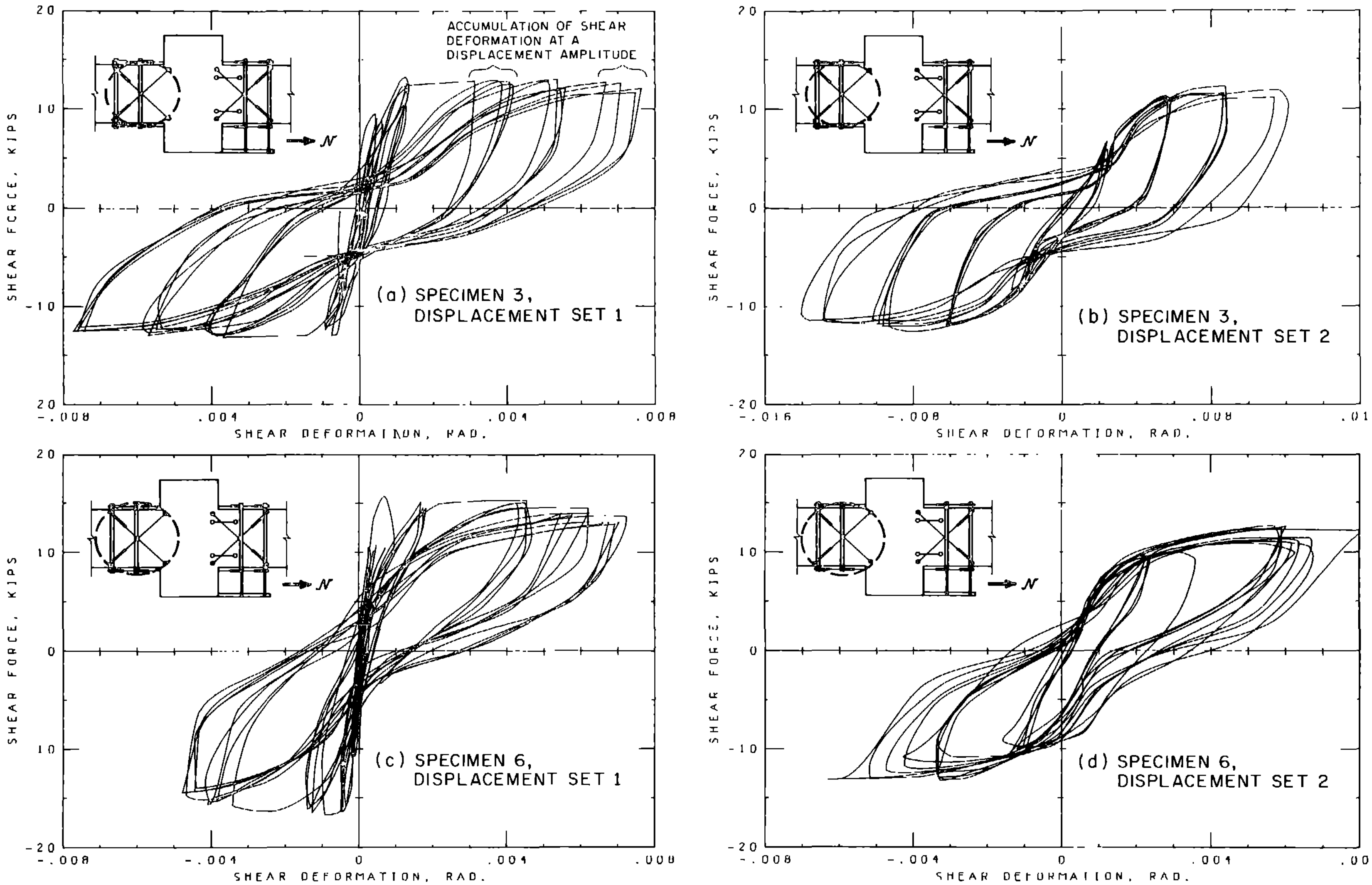

FIG. 4.6 SHEAR FORCE-SHEAR DEFORMATION DIAGRAMS, TYPICAL

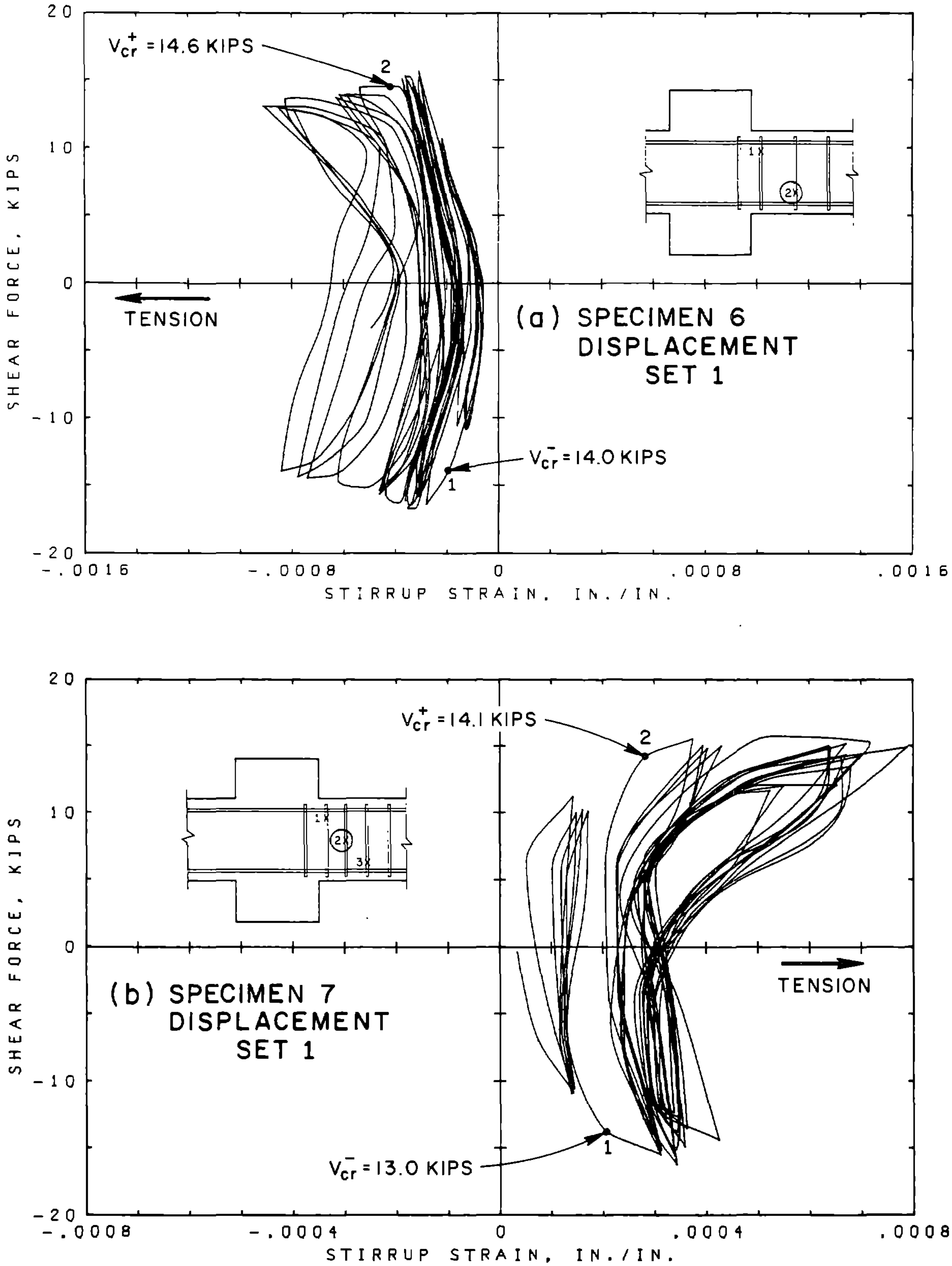

FIG. 4.7 SHEAR FORCE-TRANSVERSE REINFORCEMENT STRAIN DIAGRAMS, TYPICAL

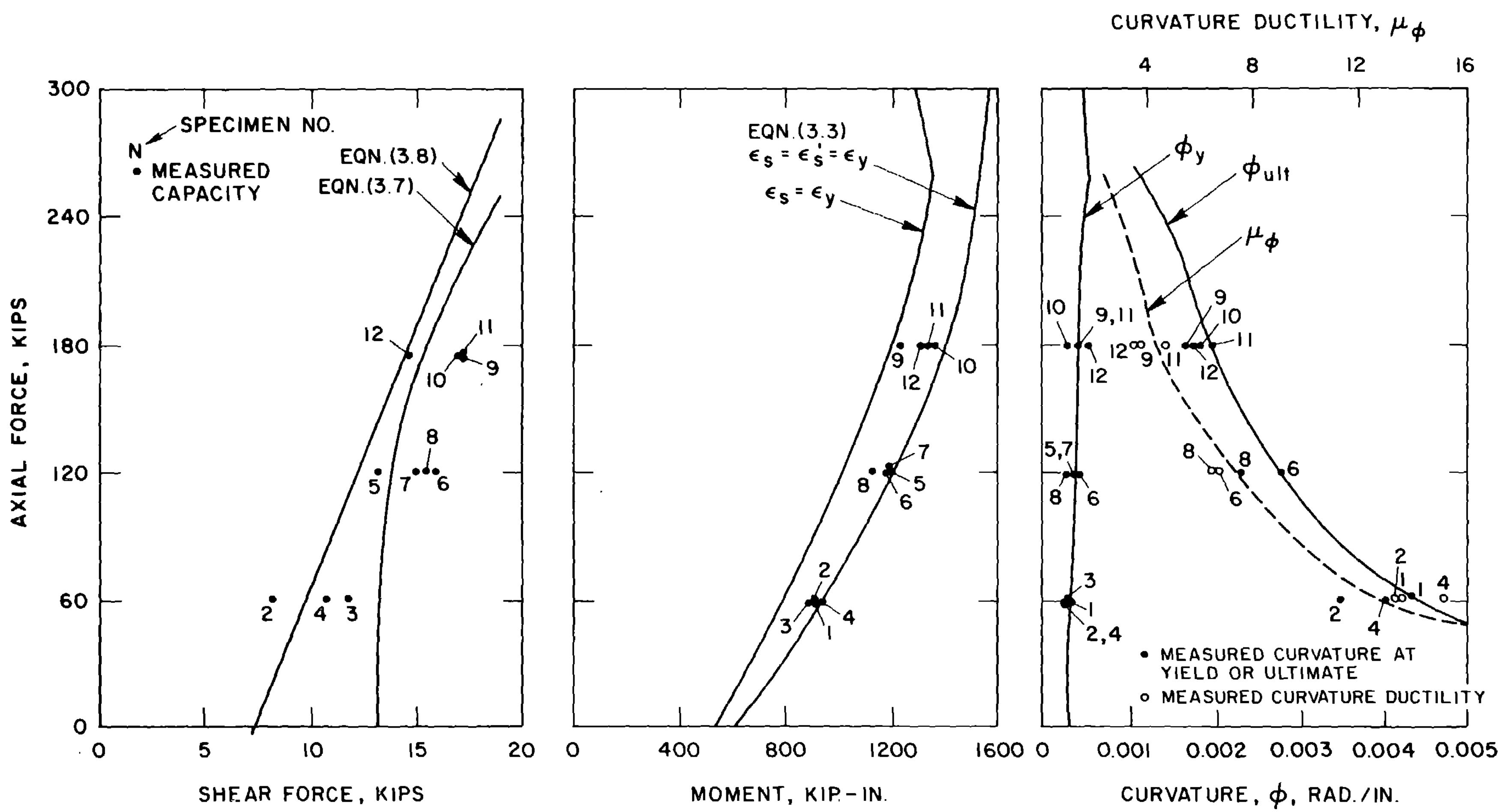

FIG. 4.8 AXIAL FORCE–SHEAR, MOMENT AND AVERAGE CURVATURE INTERACTION DIAGRAMS

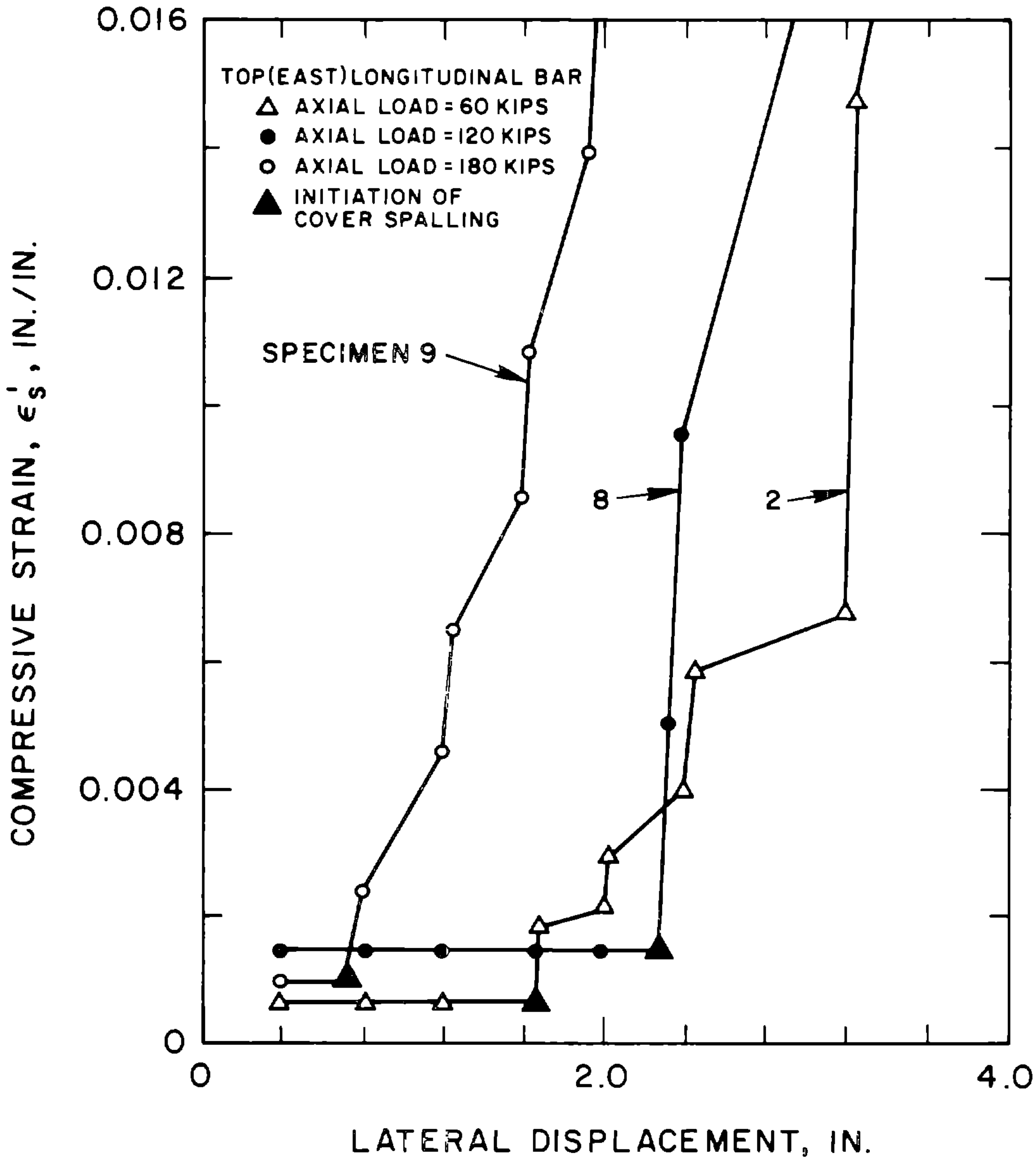

FIG. 4.9 COMPRESSIVE STRAIN - LATERAL DISPLACEMENT RELATIONSHIP AND INITIATION OF COVER SPALLING

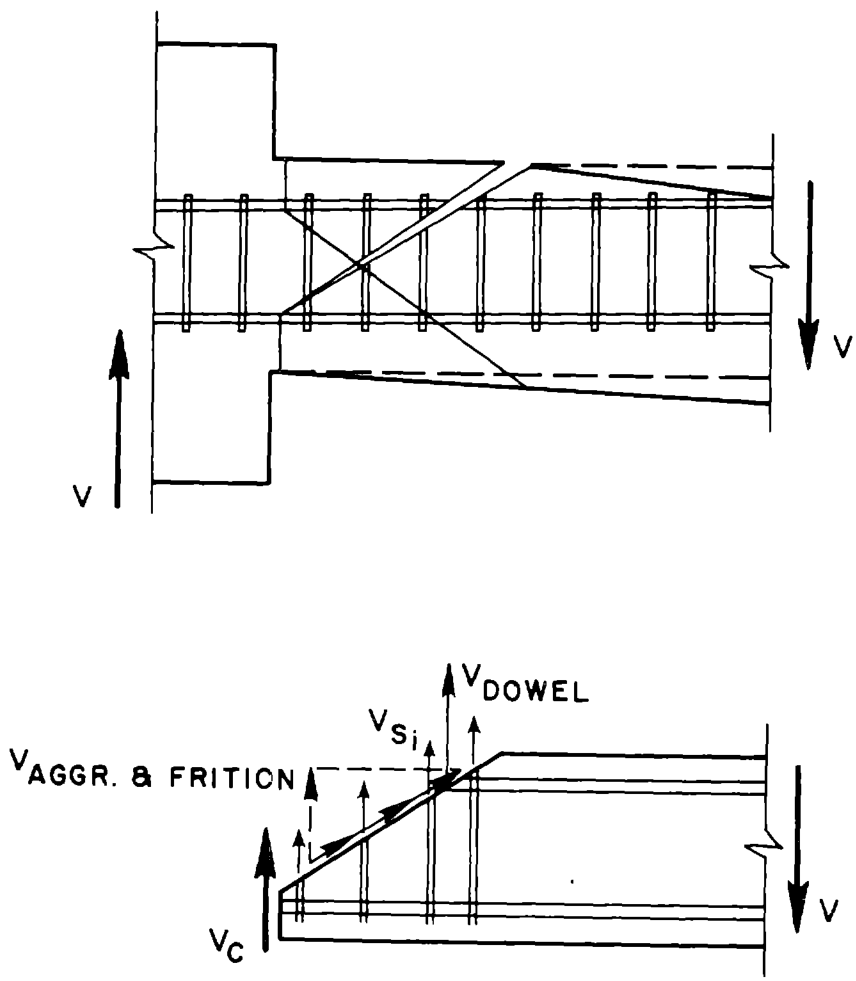

$$V = V_C + \Sigma V_{S_i} + V_{DOWEL} + V_{AGGR.\ \&\ FRICTION}$$

FIG. 4.10 SHEAR RESISTANCE MECHANISM

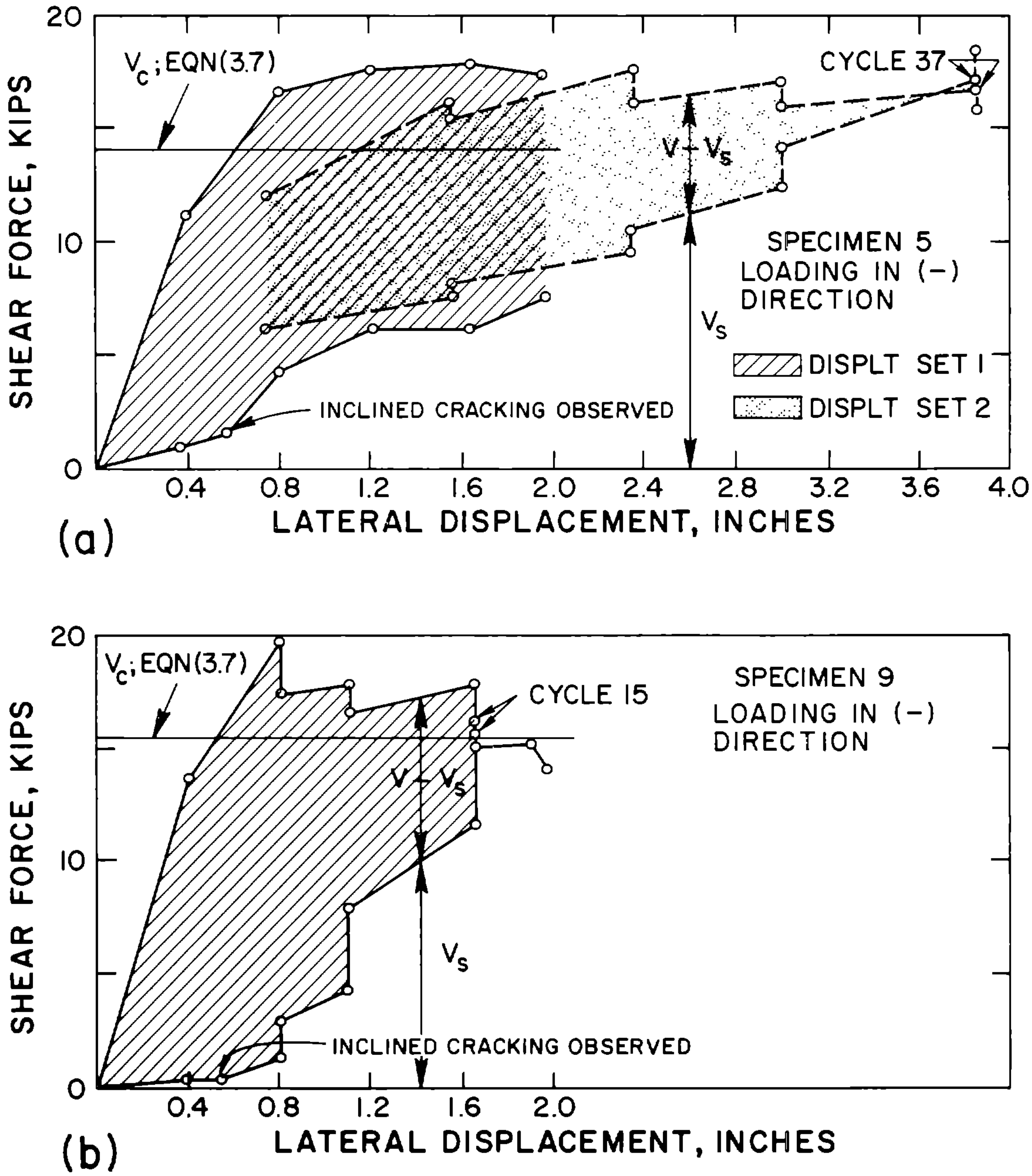

FIG. 4.11 SHEAR RESISTANCE MECHANISM

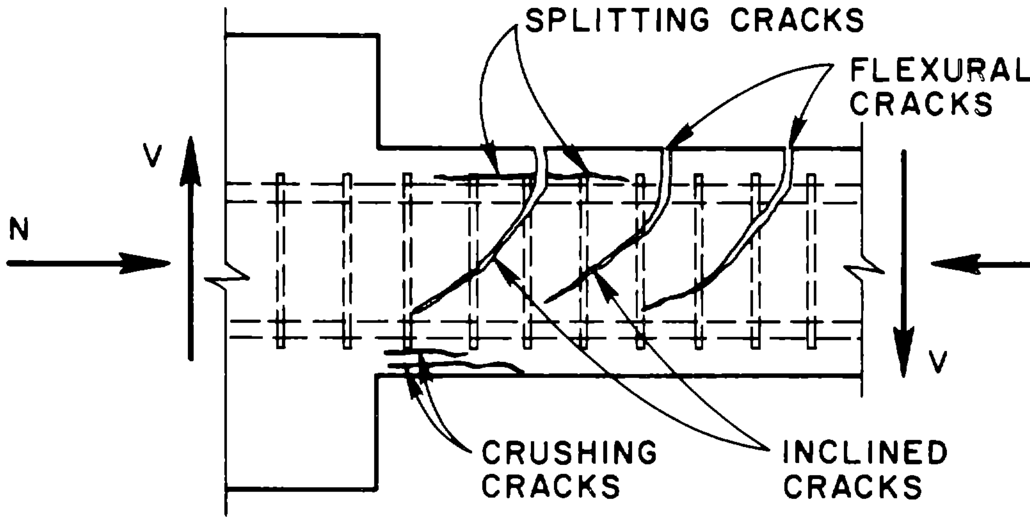

(a) CRACKING PATTERN AFTER LATERAL LOADING IN ONE DIRECTION

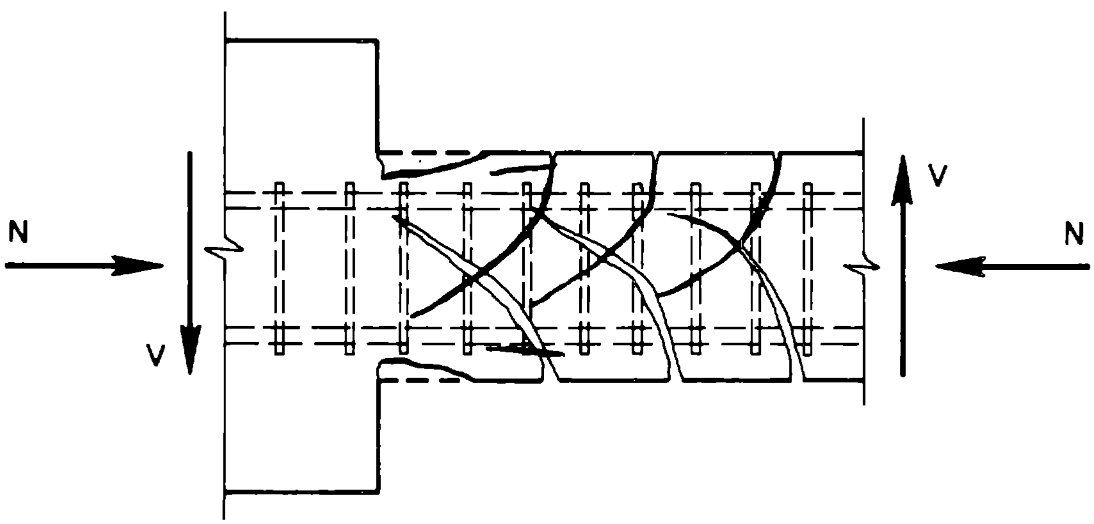

(b) CRACKING PATTERN AFTER REVERSAL OF LATERAL LOADING

FIG. 4.12 CRACKING PATTERN

(a) SPECIMEN 1

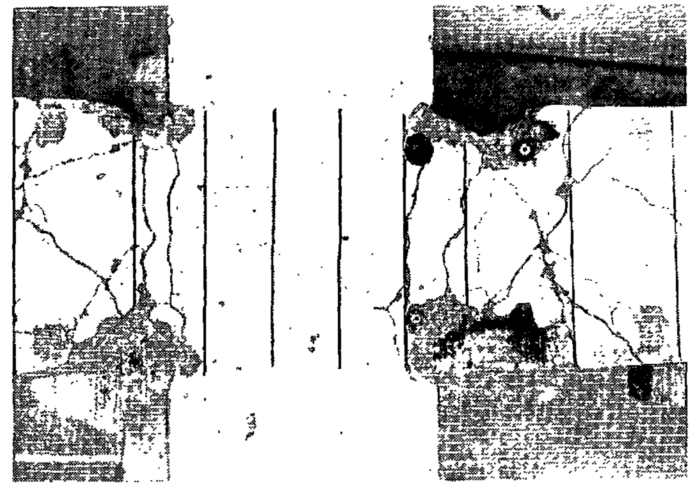

(b) SPECIMEN 2

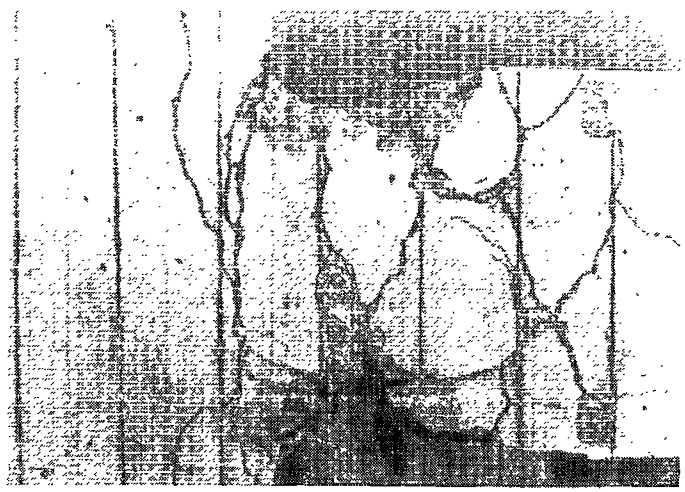

(c) SPECIMEN 3

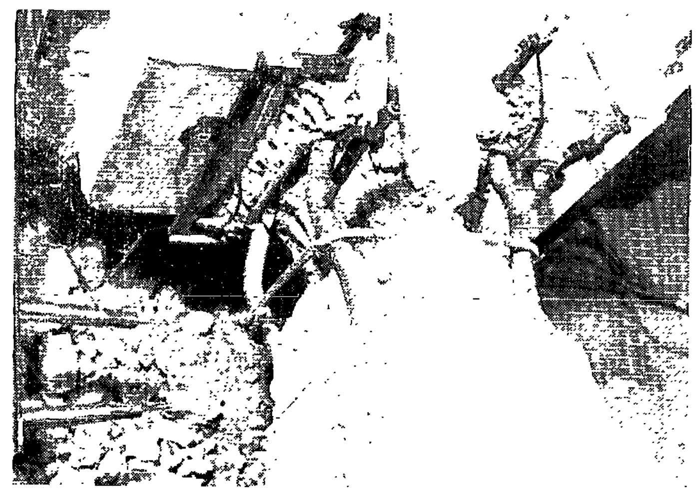

(d) SPECIMEN 4

FIG. 4.13 CONDITIONS AT FAILURE, SPECIMENS 1 THROUGH 4, APPLIED AXIAL LOAD = 60 KIPS

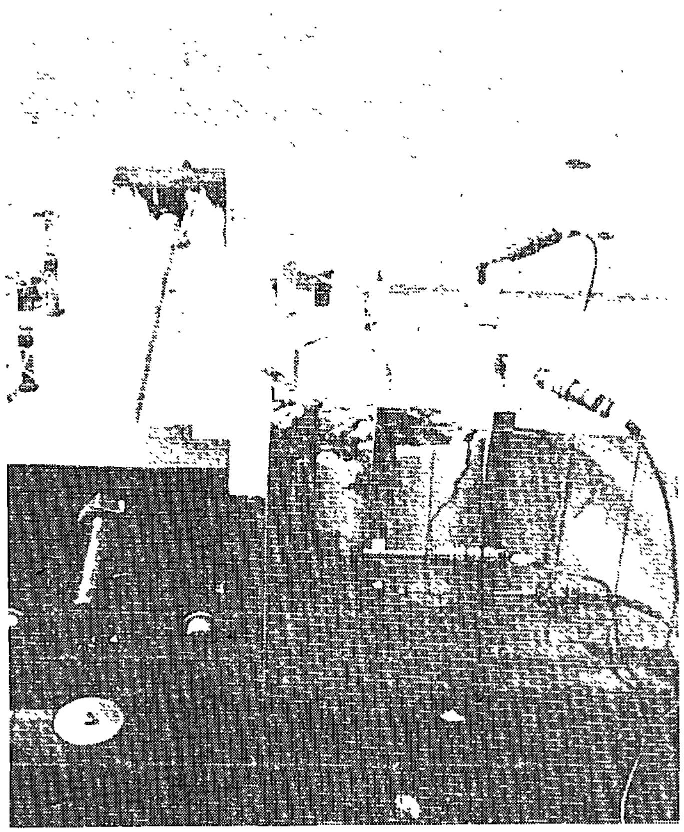

(a) DAMAGE AT END OF DISPLACEMENT SET 1. MAX. LATERAL DISPLACEMENT AMPLITUDE 2.0 IN.

(b) DAMAGE AT END OF DISPLACEMENT SET 2. MAX. LATERAL DISPLACEMENT AMPLITUDE 4.0 IN.

FIG. 4.14 DAMAGE TO SPECIMEN 5, APPLIED AXIAL LOAD = 120 KIPS

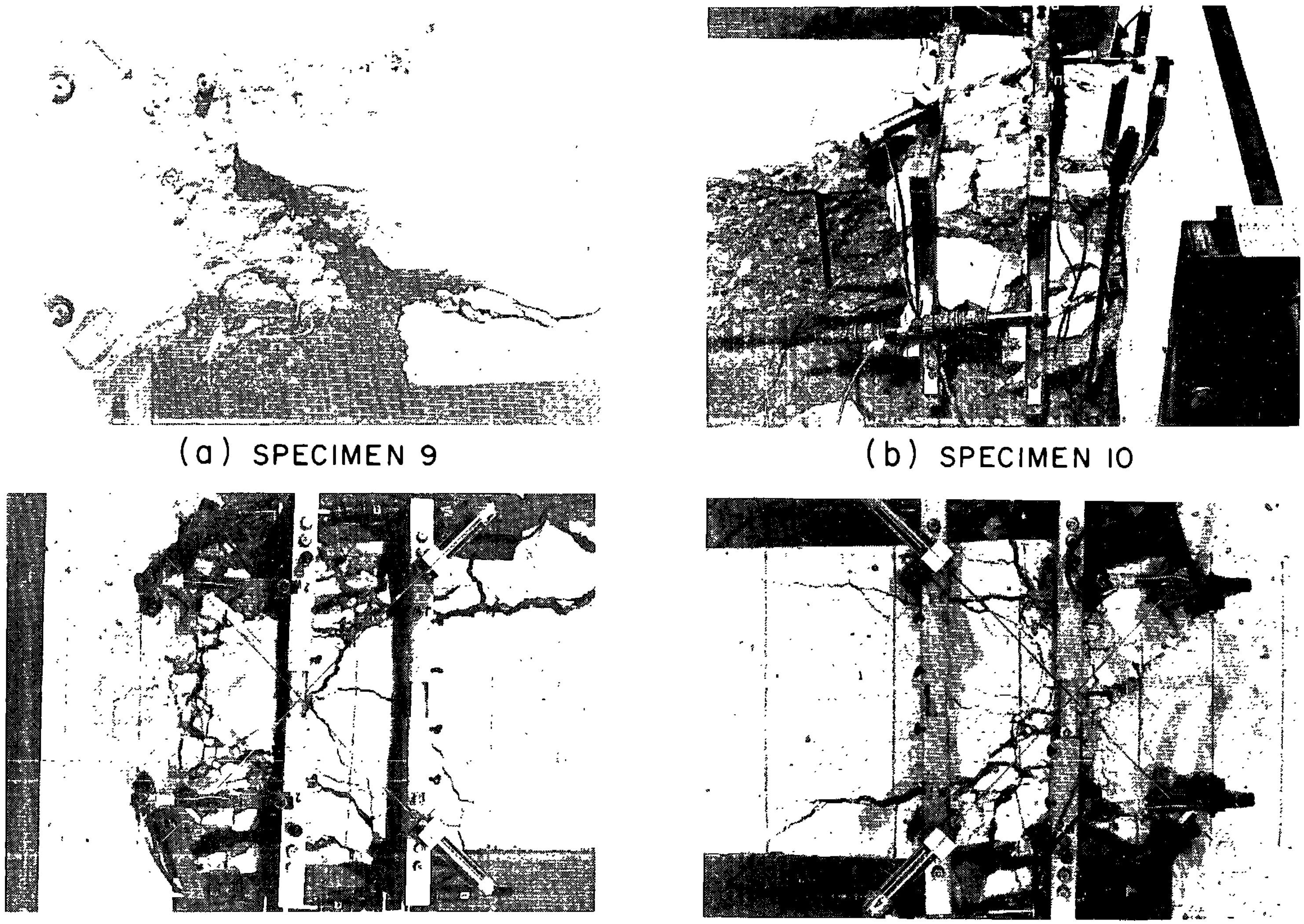

(a) SPECIMEN 9

(b) SPECIMEN 10

(c) SPECIMEN 11

(d) SPECIMEN 12

FIG. 4.15 CONDITIONS AT FAILURE, SPECIMENS 9 THROUGH 12, APPLIED AXIAL LOAD = 180 KIPS

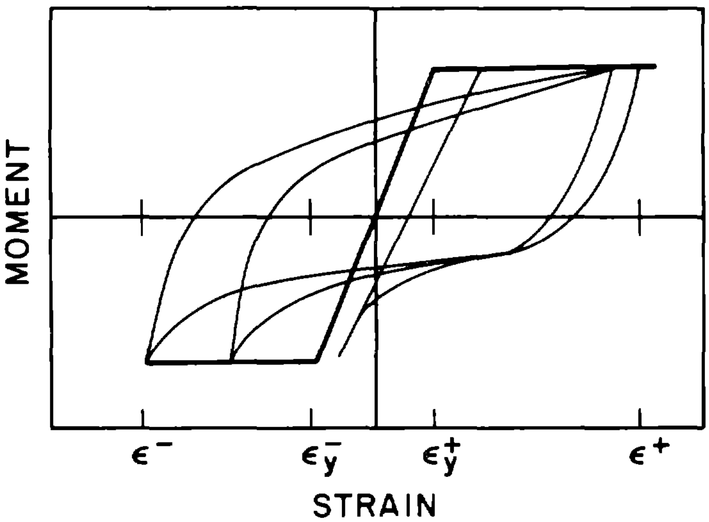

$$\mu_\epsilon^c = \text{MAX. USABLE } \{\epsilon^+ + |\epsilon^-|\}/(\epsilon_y^+ + |\epsilon_y^-|)$$

(a) CYCLIC STRAIN DUCTILITY FACTOR

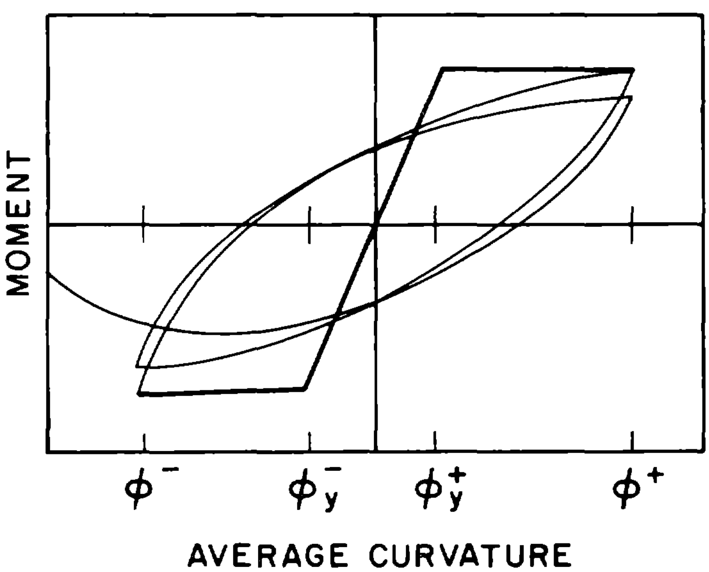

$$\phi_y \equiv \frac{\phi_y^+ + |\phi_y^-|}{2}$$

$$\phi_{ult} \equiv \frac{\text{MAX. USABLE } \{\phi^+ + |\phi^-|\}}{2}$$

$$\mu_\phi = (\text{MAX. USABLE } \{\phi^+ + |\phi^-|\})/(\phi_y^+ + |\phi_y^-|) = \phi_{ult}/\phi_y$$

(b) CYCLIC AVERAGE CURVATURE DUCTILITY FACTOR

FIG. 4.16 DEFINITIONS ON CYCLIC DUCTILITY FACTORS

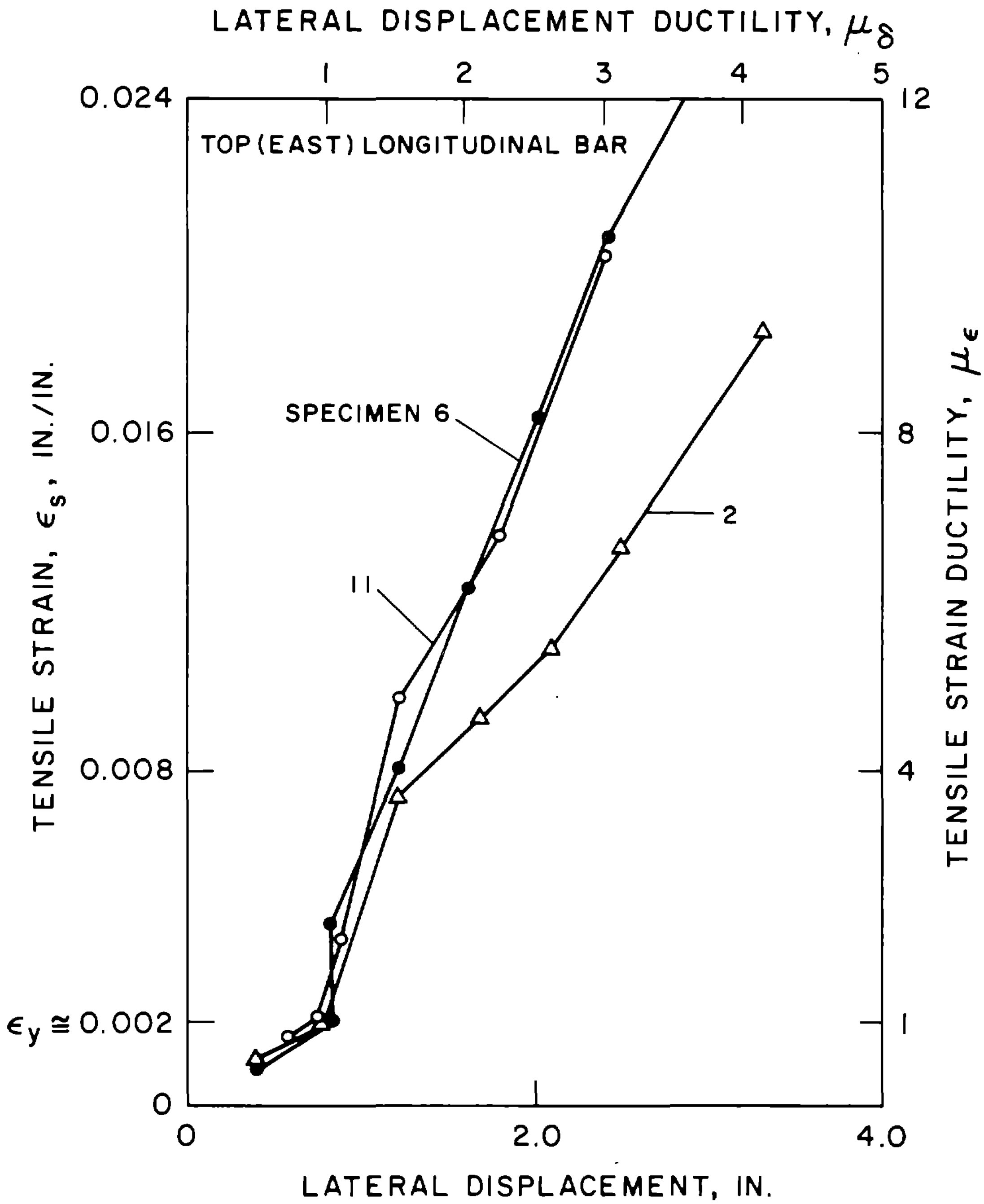

FIG. 4.17 TENSILE STRAIN DUCTILIY-LATERAL DISPLACEMENT DUCTILIY RELATIONSHIP

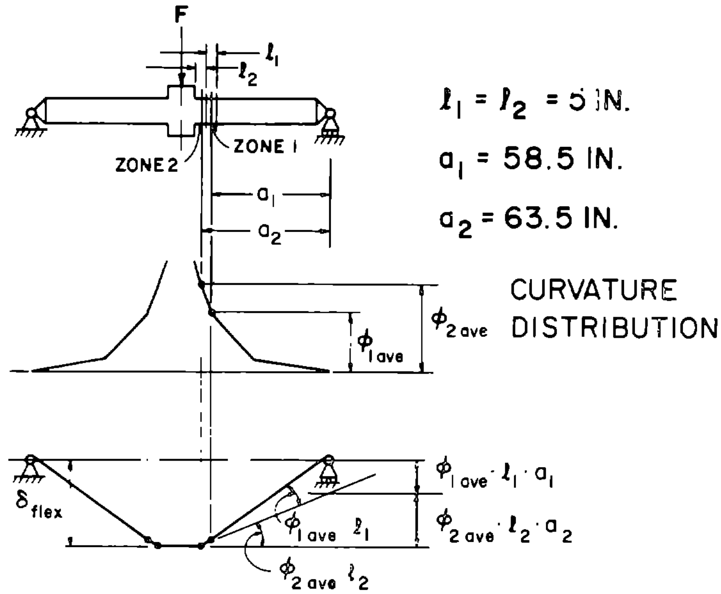

$$\delta_{flex} = \phi_{1\,ave}\, l_1 a_1 + \phi_{2\,ave}\, l_2 a_2$$

(a) LATERAL DISPLACEMENT COMPONENT
DUE TO FLEXURAL DEFORMATIONS

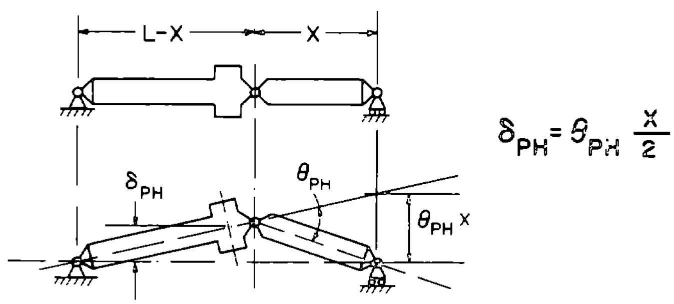

(b) LATERAL DISPLACEMENT COMPONENT
DUE TO PLASTIC HINGE ROTATIONS

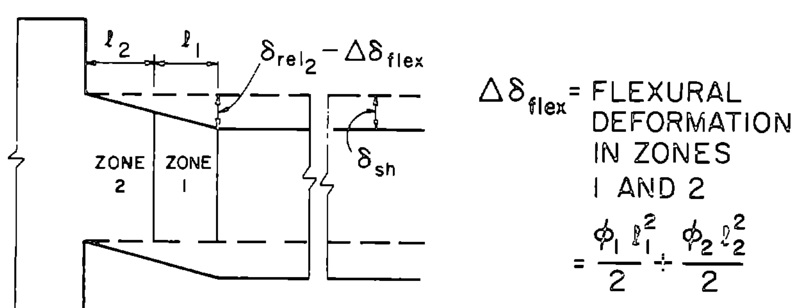

$$\delta_{sh} = \delta_{rel_2} - \left(\frac{\phi_1 l_1^2}{2} + \frac{\phi_2 l_2^2}{2}\right)$$

(C) LATERAL DISPLACEMENT COMPONENT
DUE TO SHEAR DEFORMATIONS

FIG. 4.18 COMPONENTS OF LATERAL DISPLACEMENT

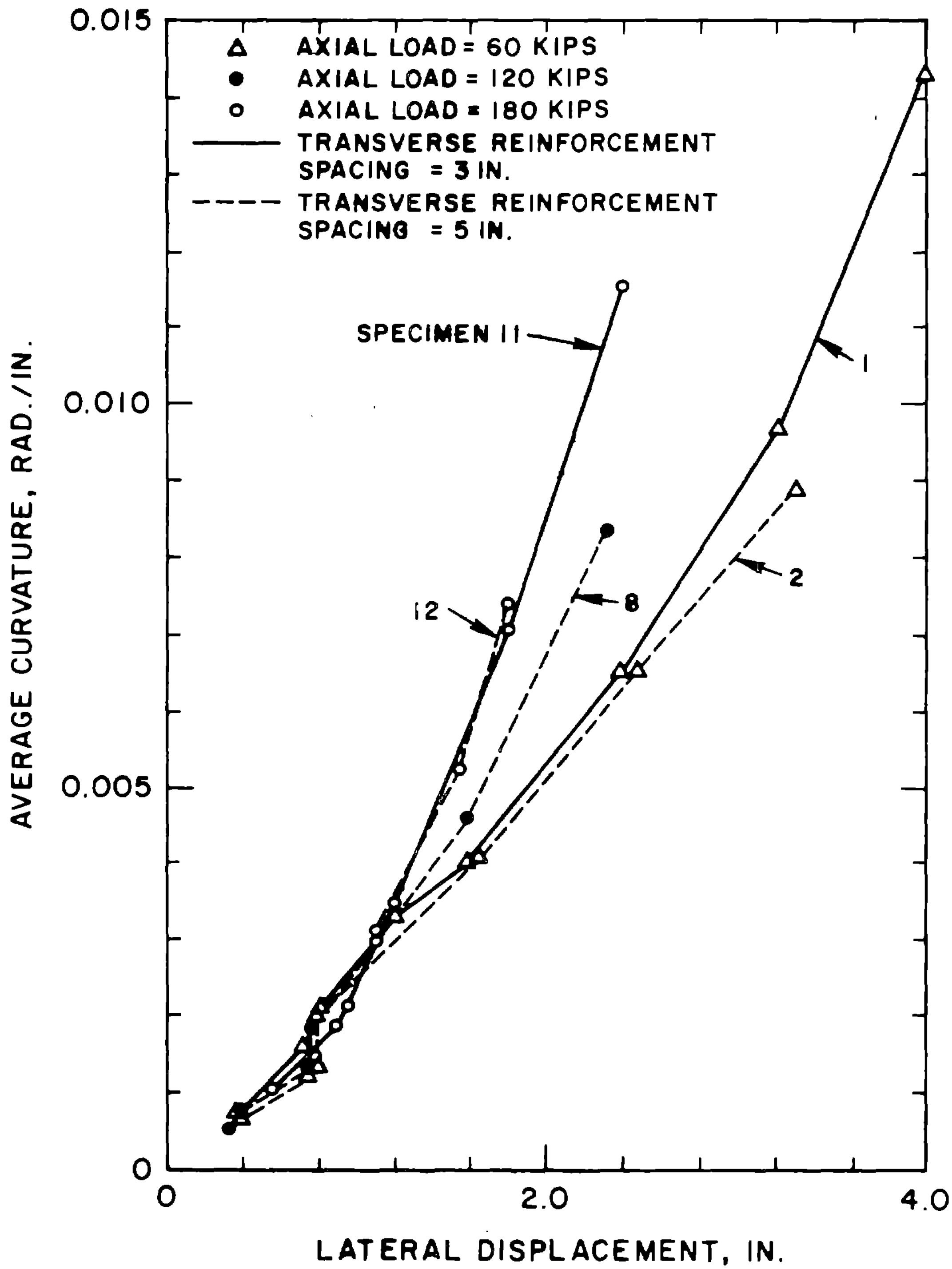

FIG. 4.19 AVERAGE CURVATURE-LATERAL DISPLACEMENT RELATIONSHIP

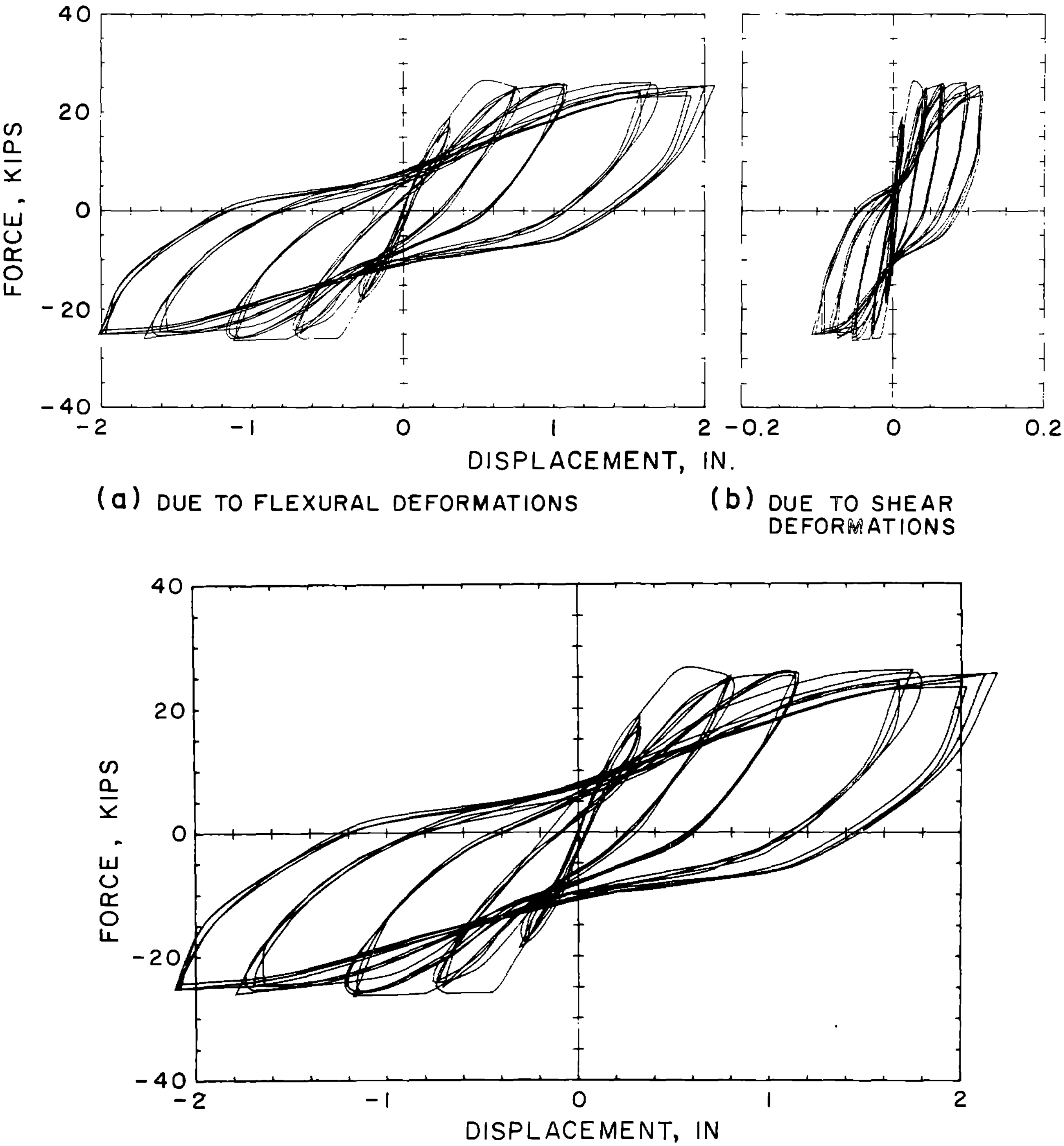

(a) DUE TO FLEXURAL DEFORMATIONS

(b) DUE TO SHEAR DEFORMATIONS

(c) DUE TO FLEXURAL AND SHEAR DEFORMATIONS

FIG. 4.20 ESTIMATION OF LATERAL DISPLACEMENT COMPONENTS, SPECIMEN 3, DISPLACEMENT SET 1

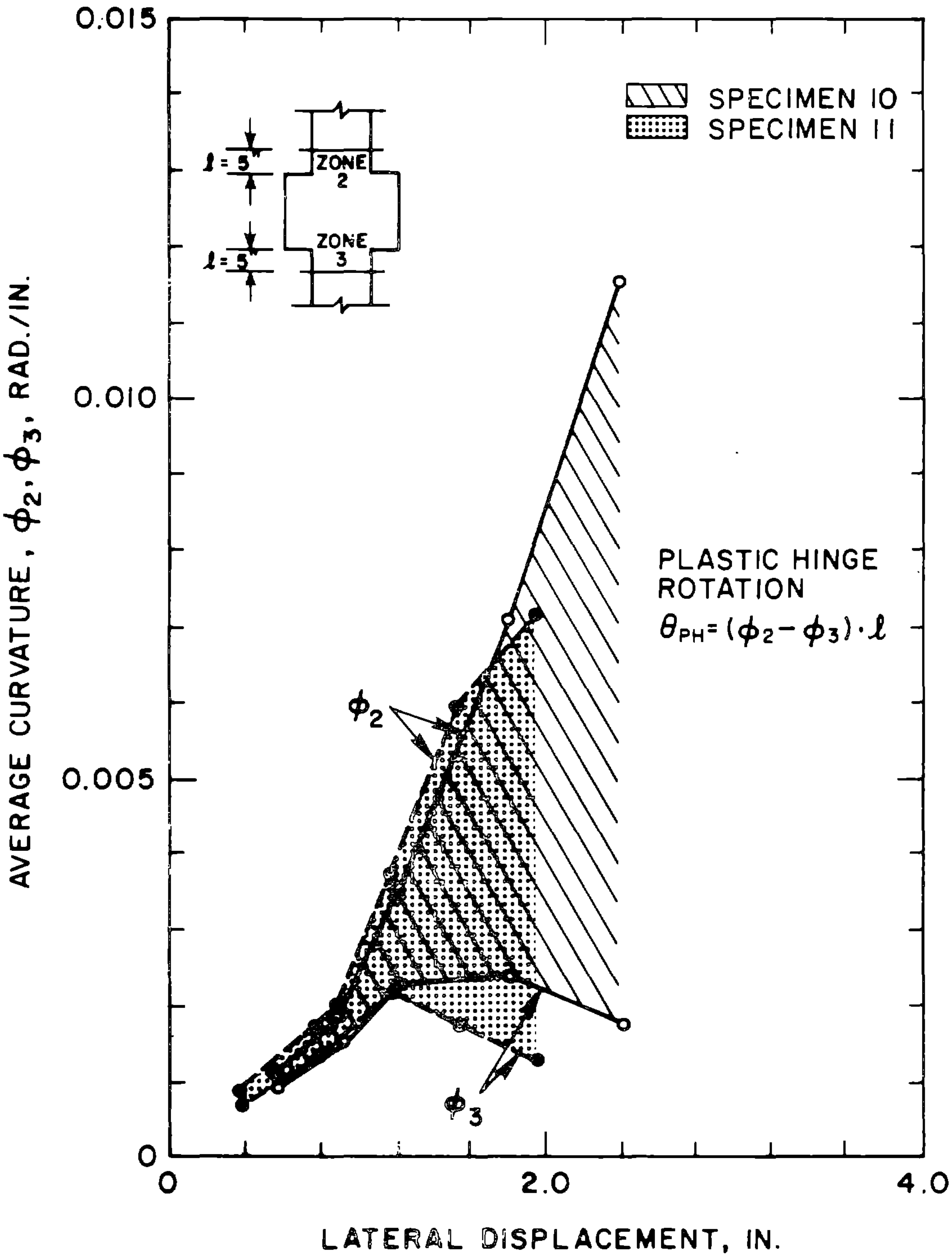

FIG. 4.21 "PLASTIC HINGE" ROTATION

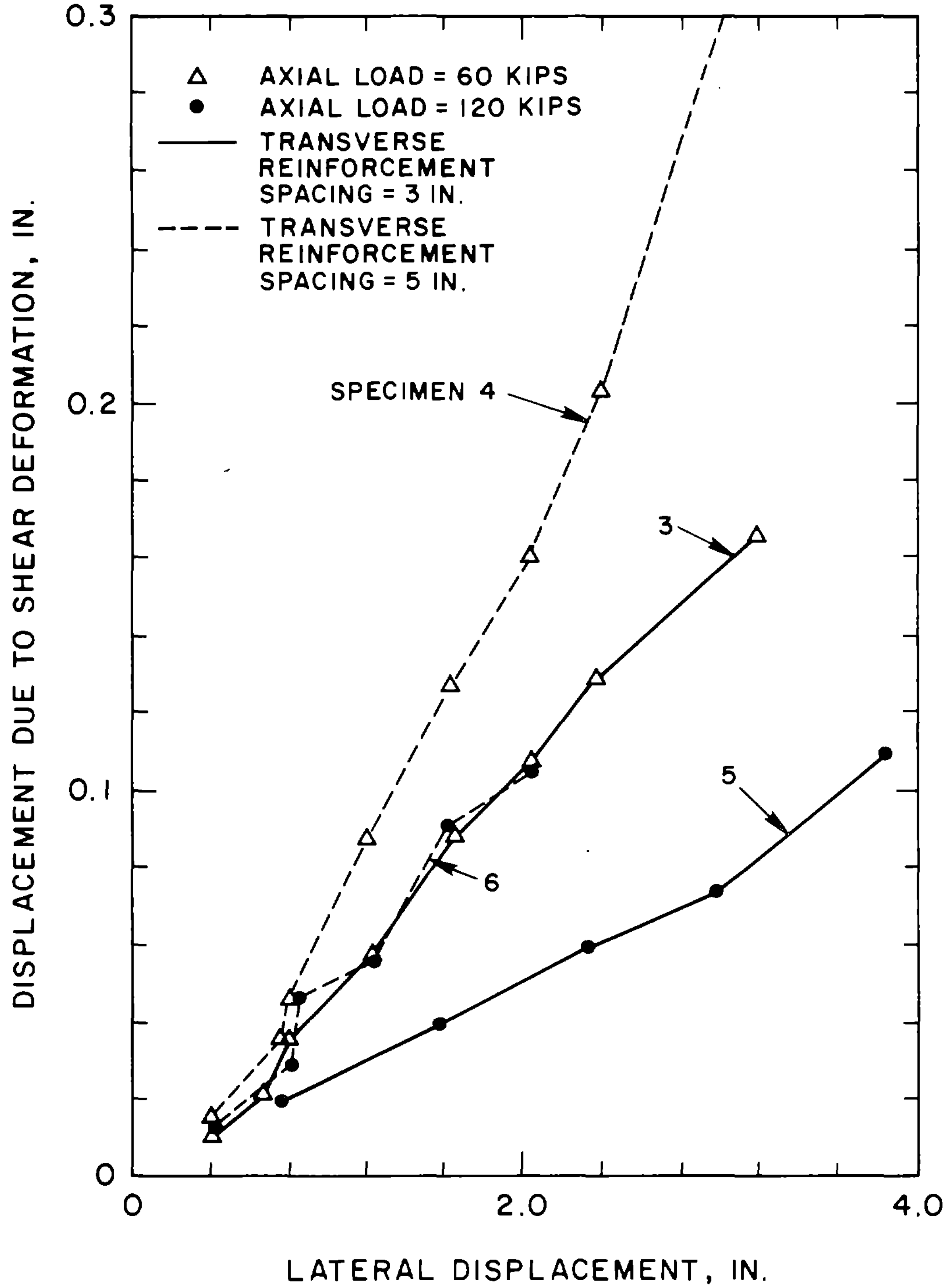

FIG. 4.22 LATERAL DISPLACEMENT DUE TO SHEAR DEFORMATION – LATERAL DISPLACEMENT RELATIONSHIP

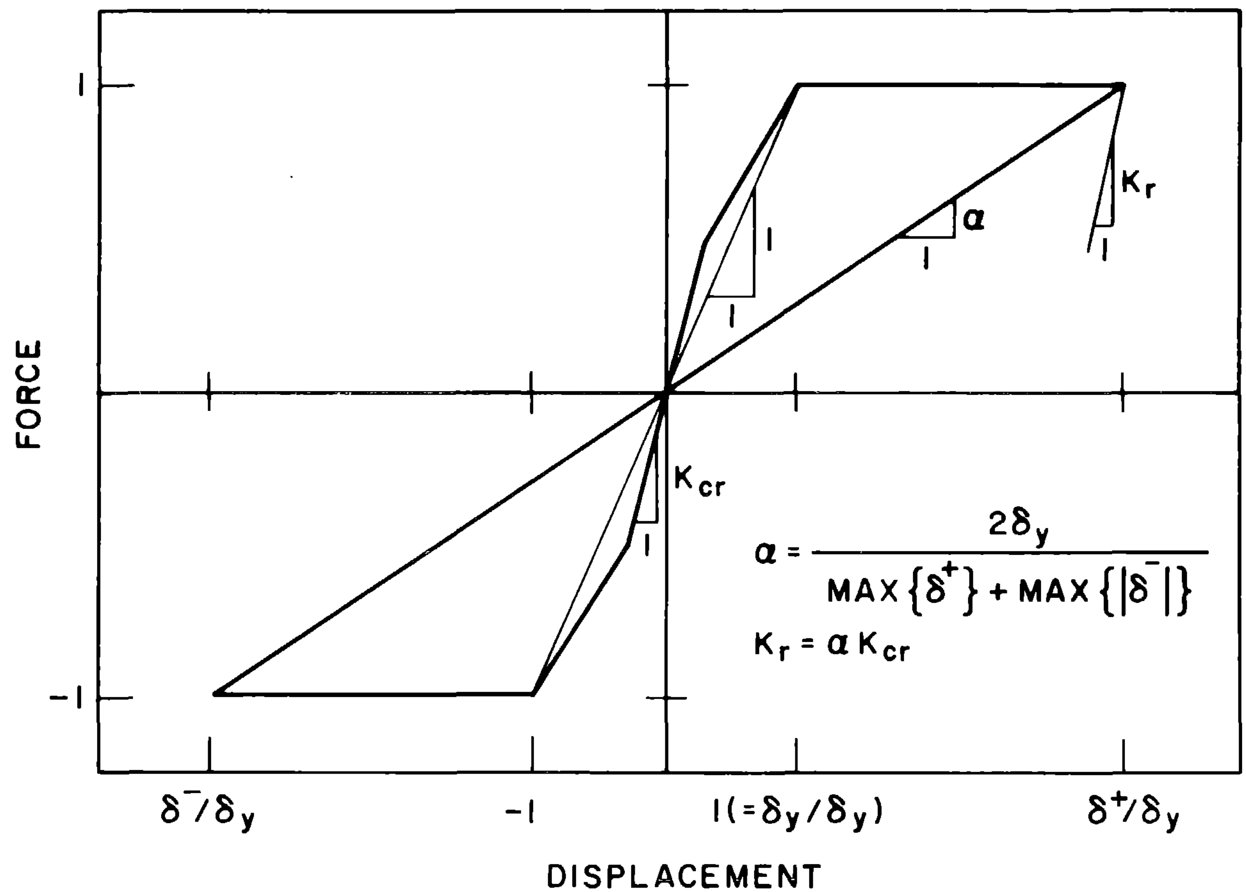

FIG. 4.23 DEFINITIONS ON THE STUDY OF STIFFNESS DEGRADATION

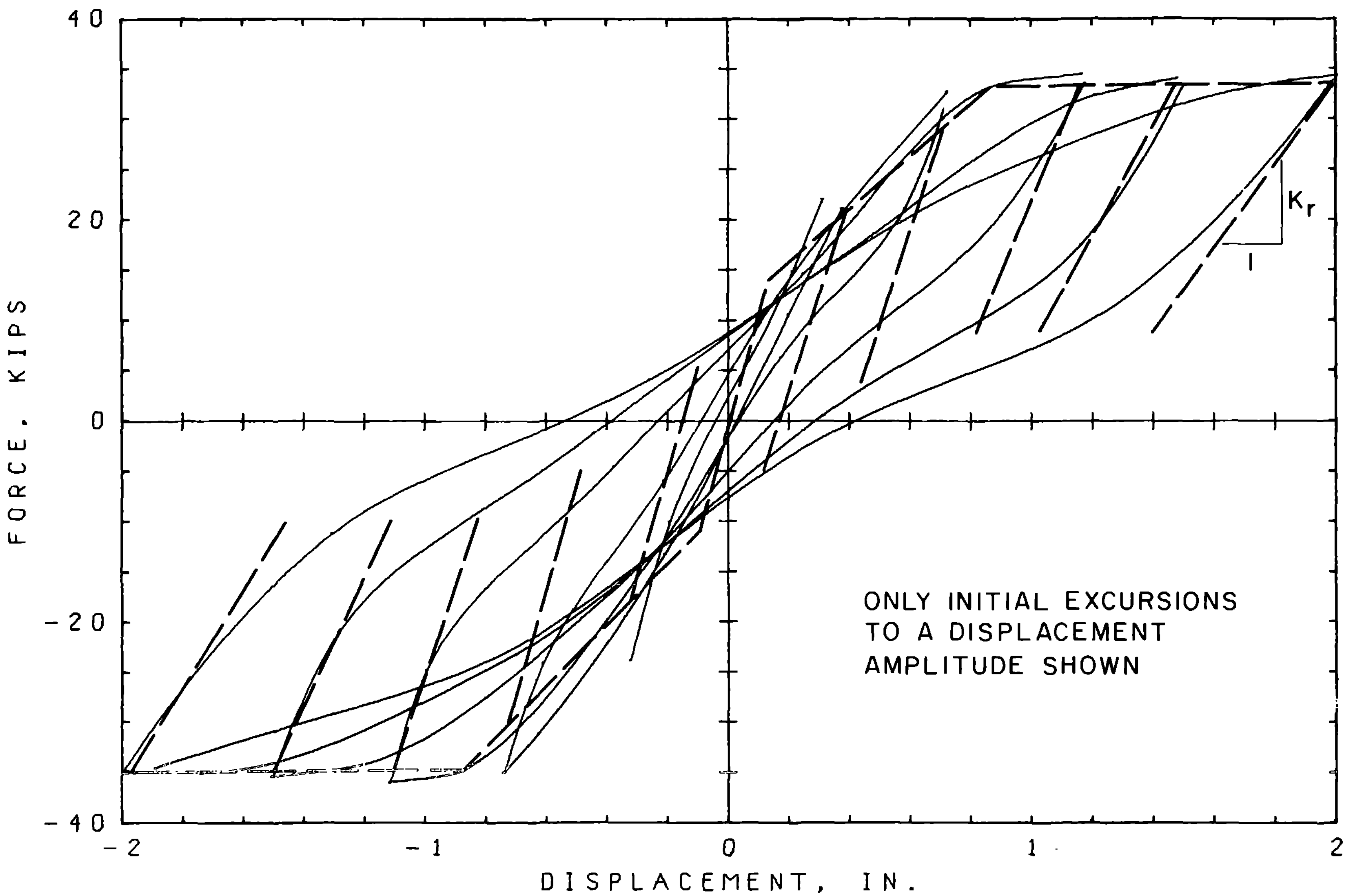

FIG. 4.24 ESTIMATION OF RETURN STIFFNESS; SPECIMEN 8; TYPICAL

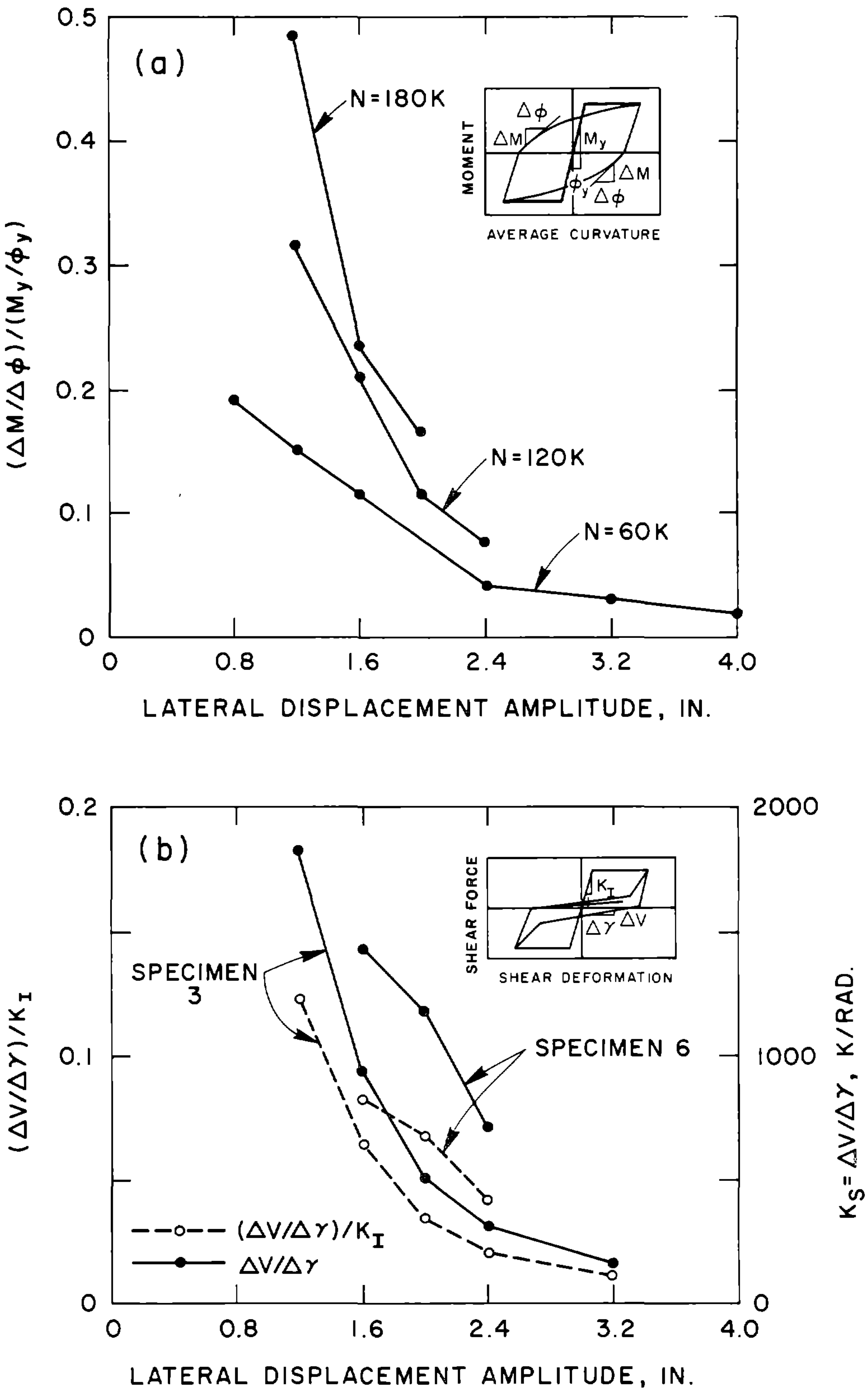

FIG. 4.25 DEGRADATION OF INSTANTANEOUS STIFFNESS IN THE CRITICAL REGION

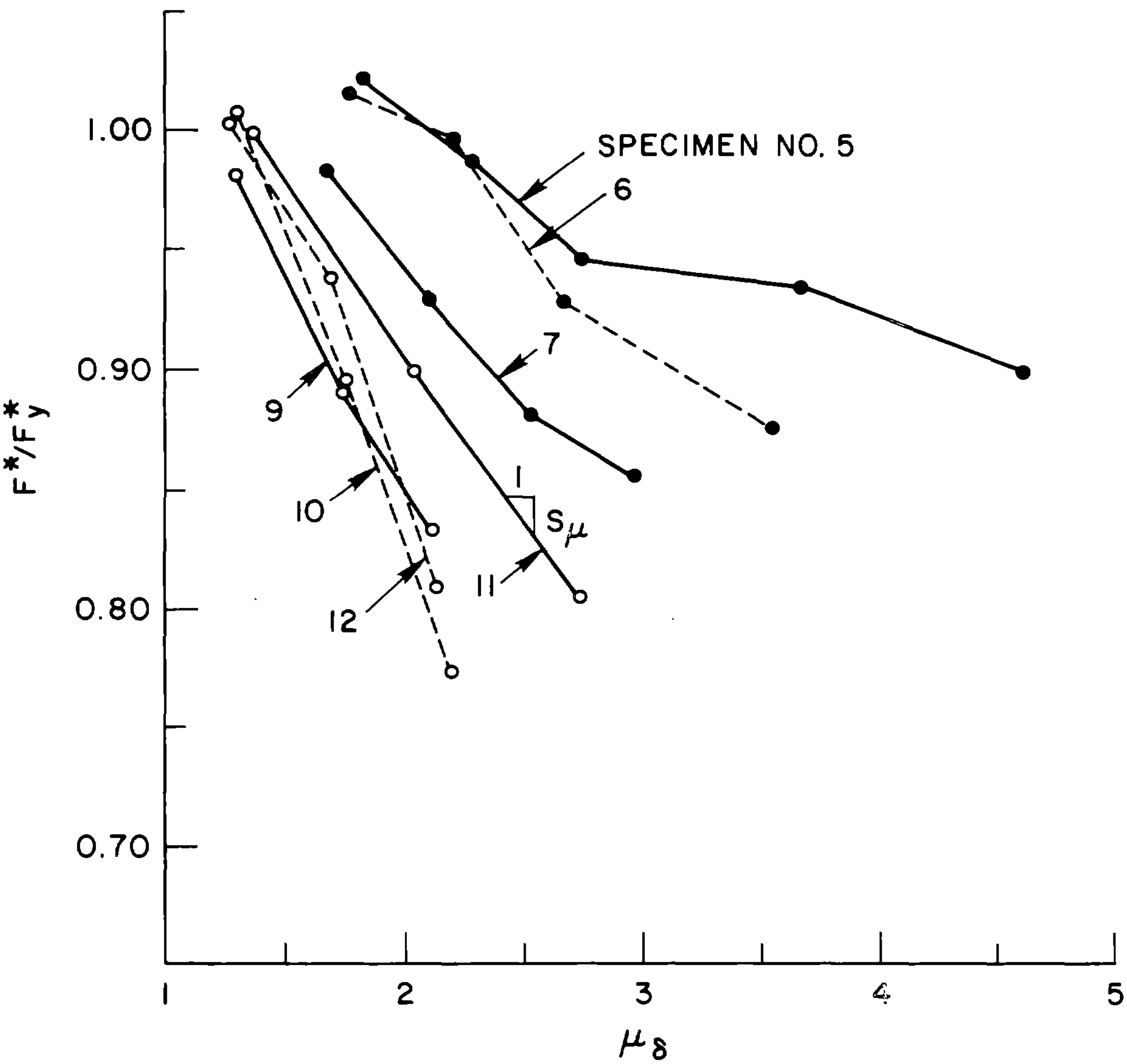

FIG. 4.26 STRENGTH DEGRADATION DUE TO INCREASING LATERAL DISPLACEMEMENT AMPLITUDES

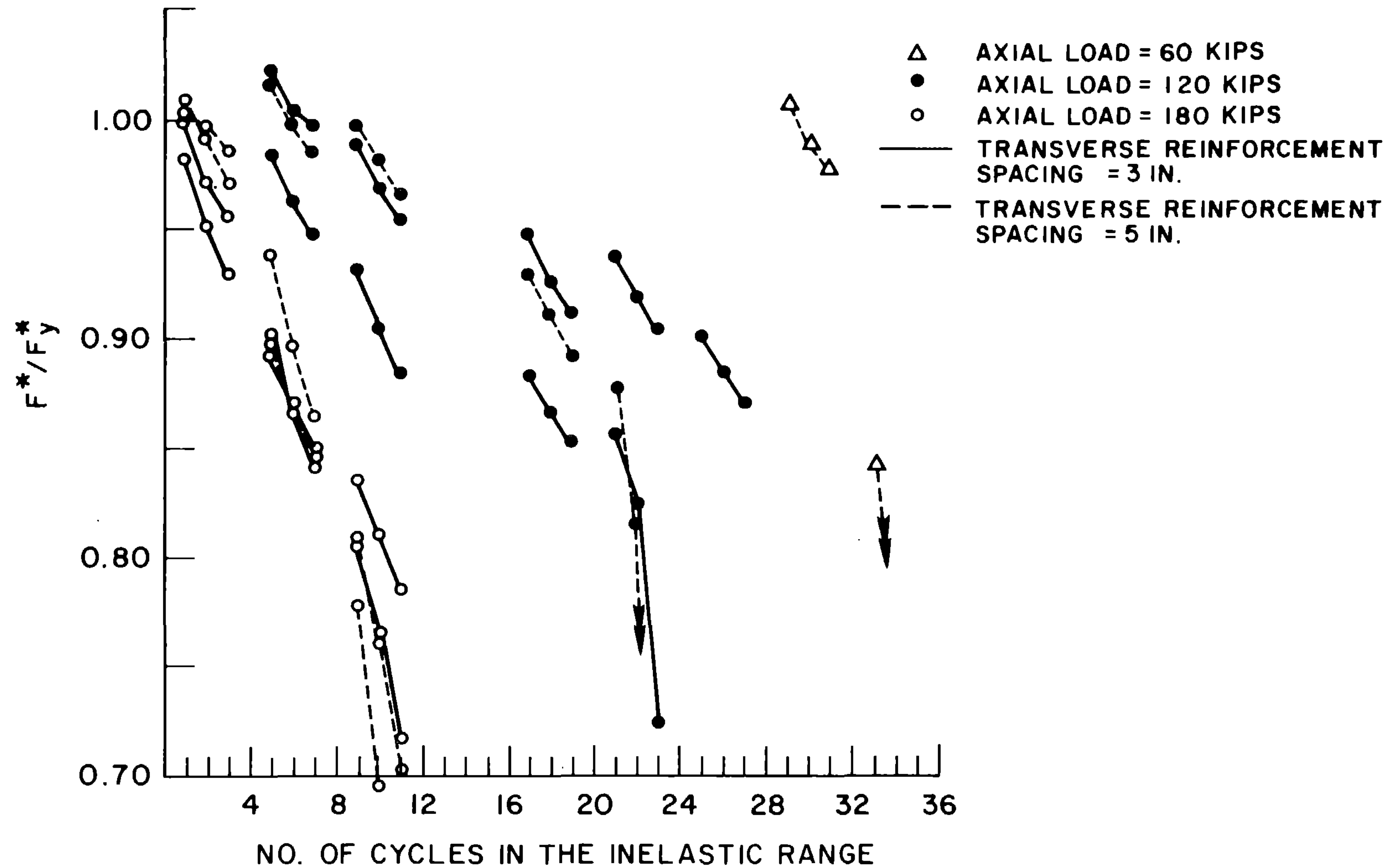

FIG. 4.27 STRENGTH DEGRADATION DUE TO CYCLING

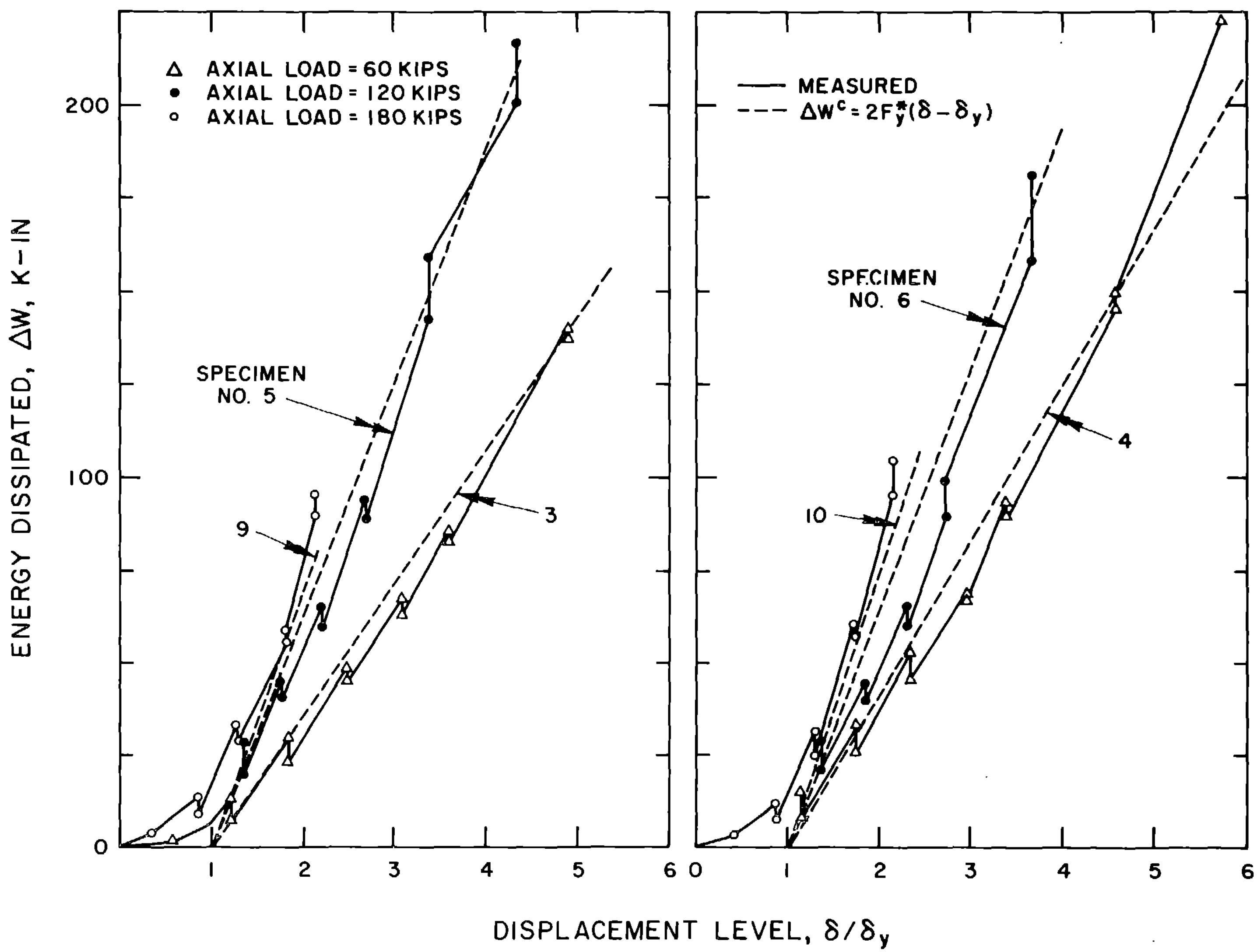

FIG. 4.28 ENERGY DISSIPATION CAPACITY

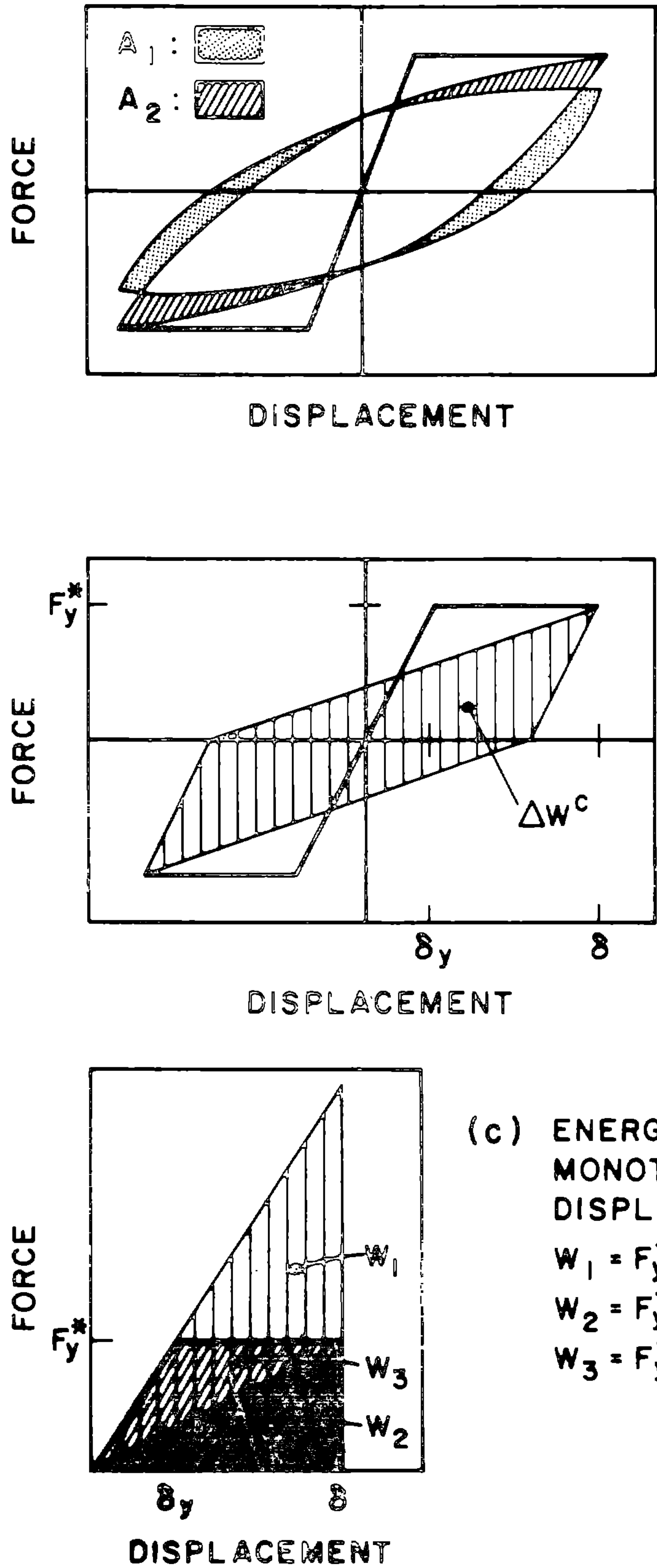

(a) INCREASE IN ΔW DUE TO STRENGTH DEGRADATION ($A_1 > A_2$)

(b) ENERGY DISSIPATED BY STIFFNESS DEGRADING MODEL [33]

$\Delta W^c = 2 F_y^* (\delta - \delta_y)$

(c) ENERGY MEASURE OF THE MONOTONIC LOADING FORCE-DISPLACEMENT RELATIONSHIP [34]

$W_1 = F_y^* \delta^2 / 2\delta_y$

$W_2 = F_y^* \delta / 2$

$W_3 = F_y^* (\delta - \delta_y / 2)$

FIG. 4.29 VARIOUS DEFINITIONS ON THE STUDY OF ENERGY DISSIPATION CAPACITY

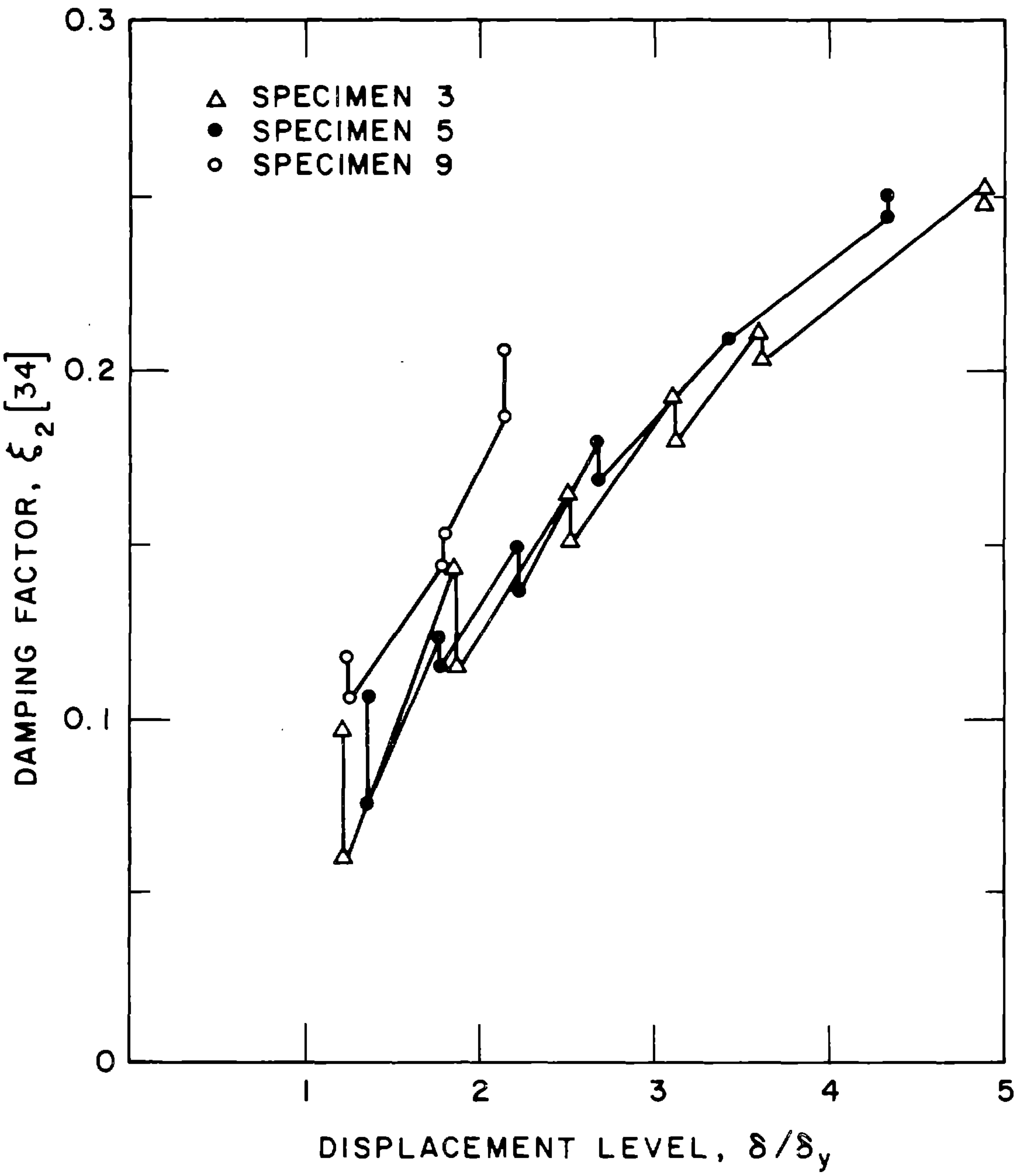

FIG. 4.30 EQUIVALENT DAMPING FACTORS

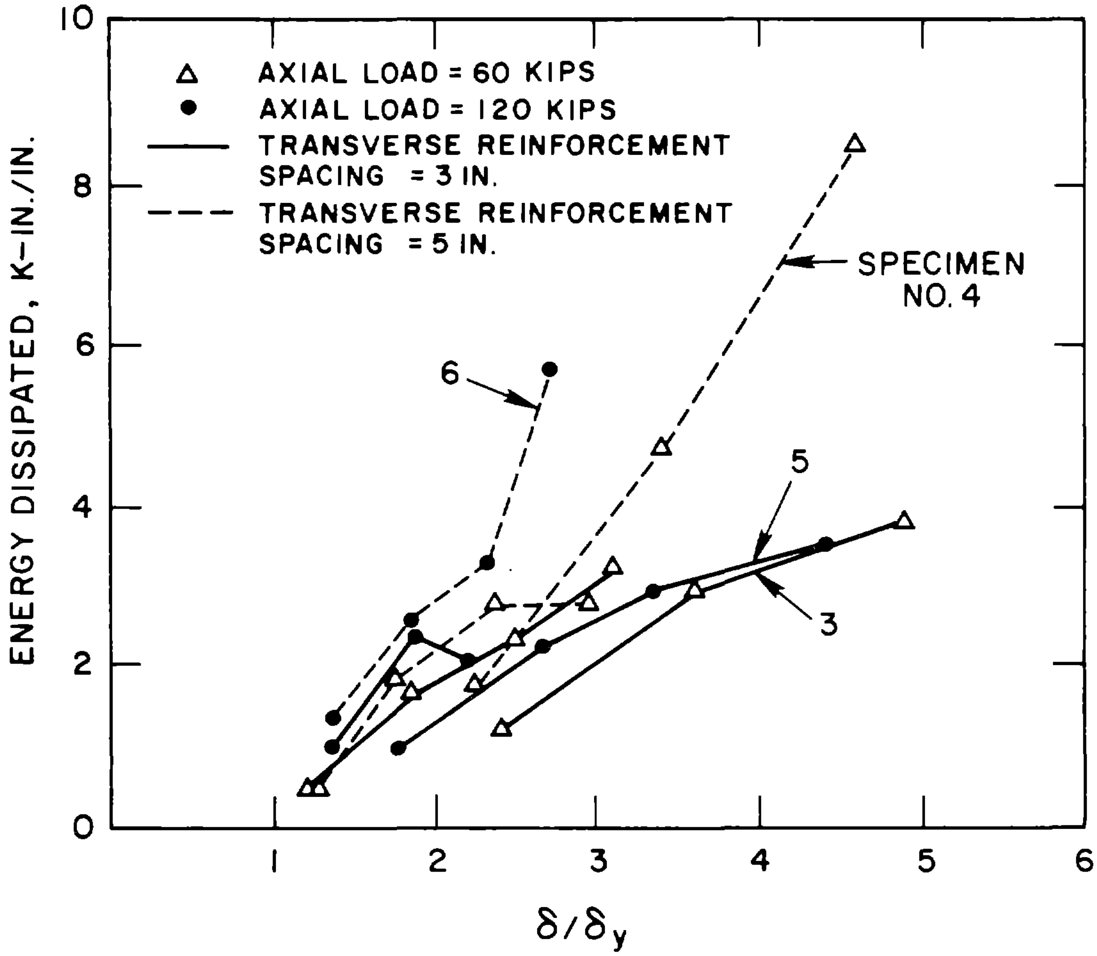

FIG. 4.31 ENERGY DISSIPATED PER UNIT LENGTH OF THE CRITICAL REGION

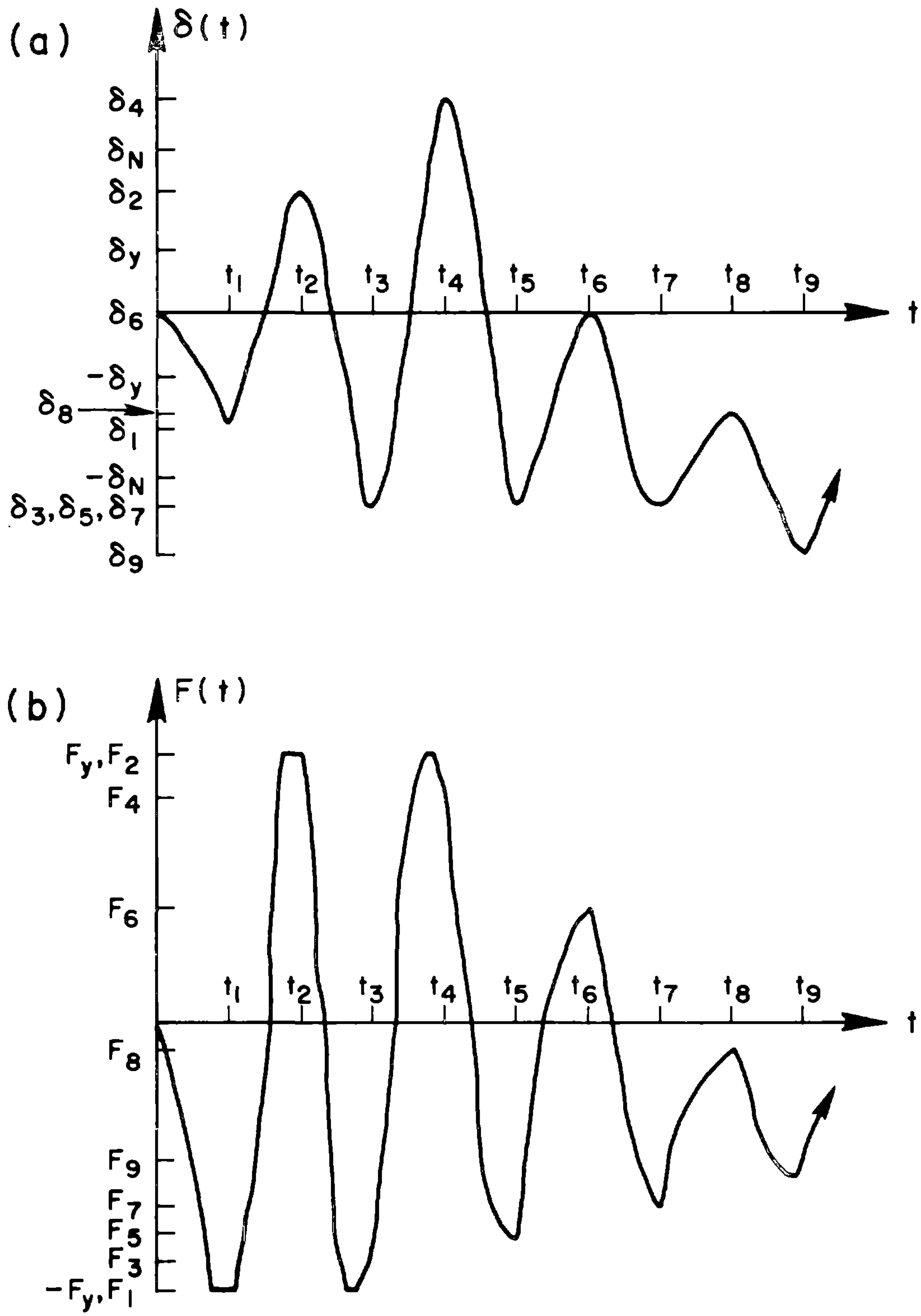

FIG. 5.1 EXAMPLE LATERAL DISPLACEMENT-TIME AND CORRESPONDING LATERAL FORCE-TIME HISTORIES

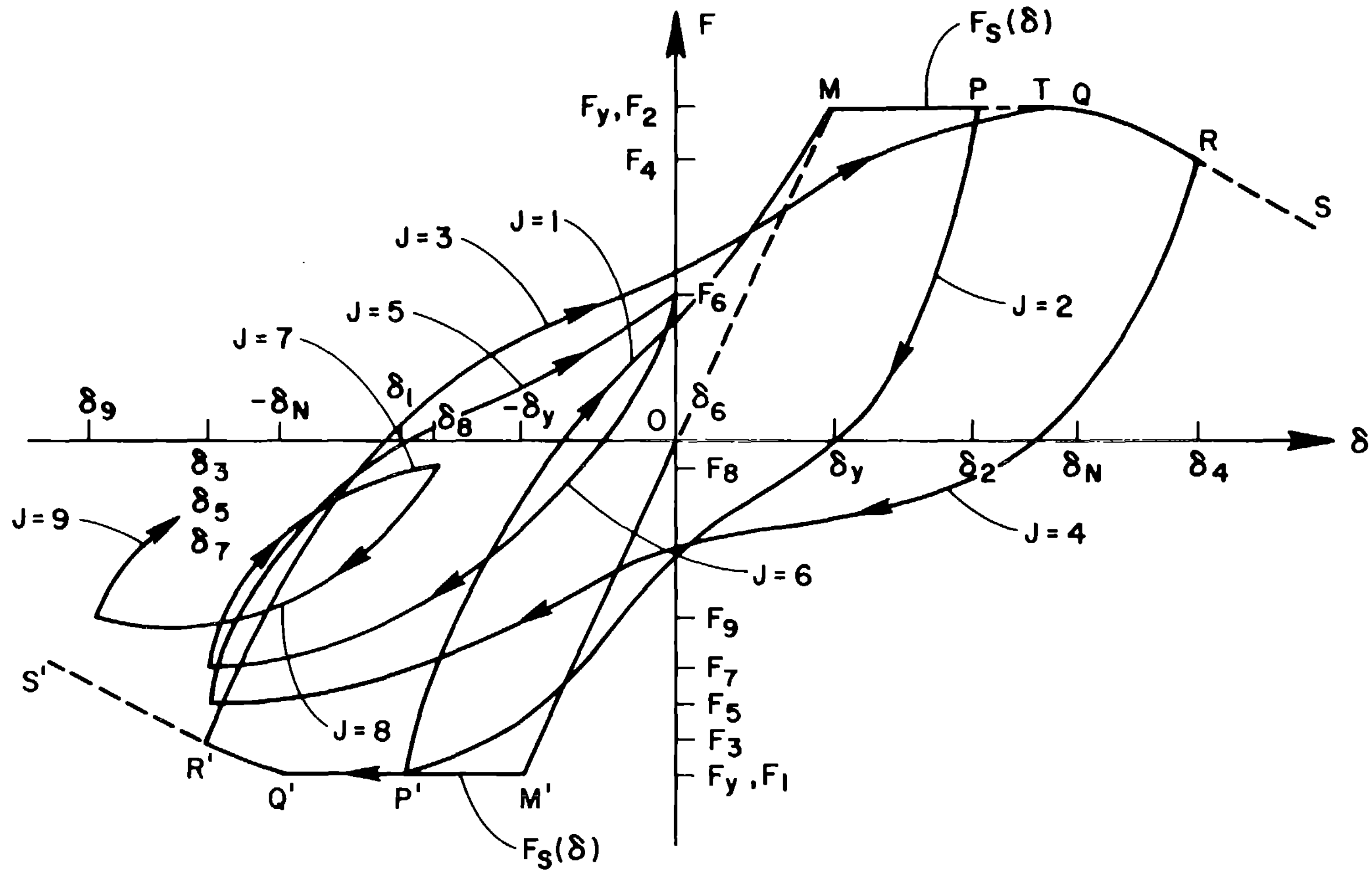

FIG. 5.2 EXAMPLE LATERAL FORCE-DISPLACEMENT RELATION

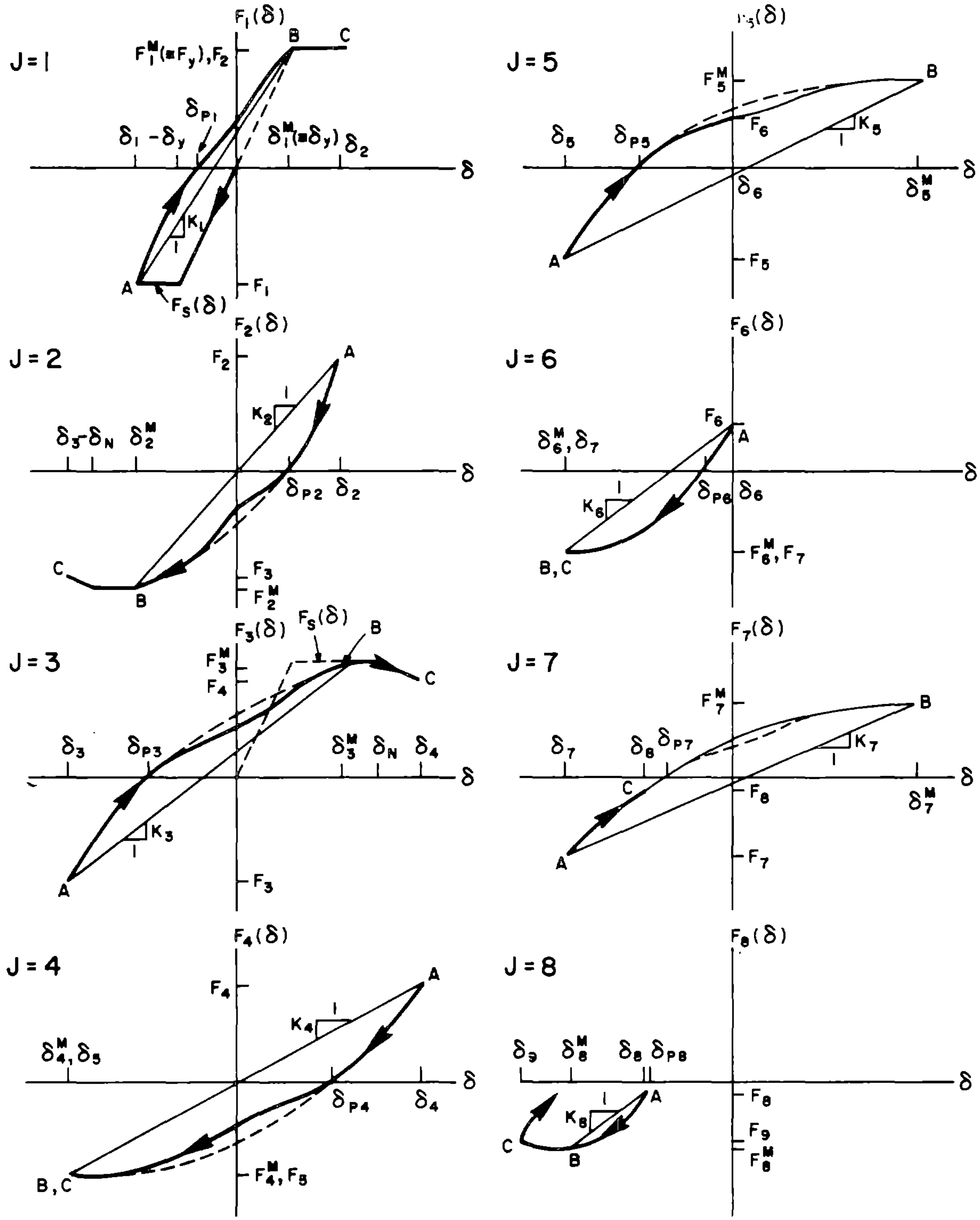

FIG. 5.3 LATERAL FORCE-DISPLACEMENT RELATIONS FOR INELASTIC HALF CYCLES OF LOADING

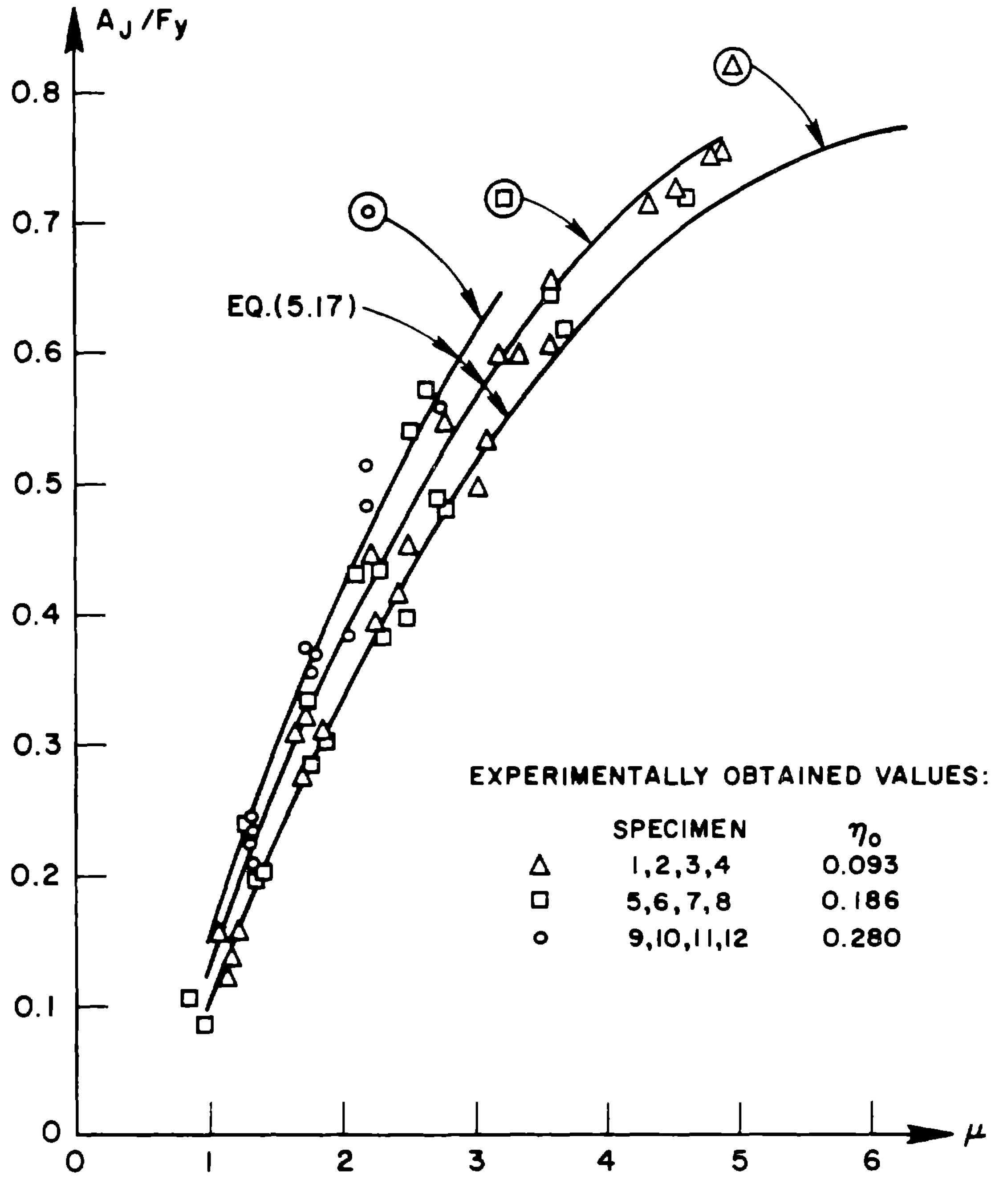

FIG. 5.4 EMPIRICAL RELATIONSHIP A_J/F_y vs. μ_J

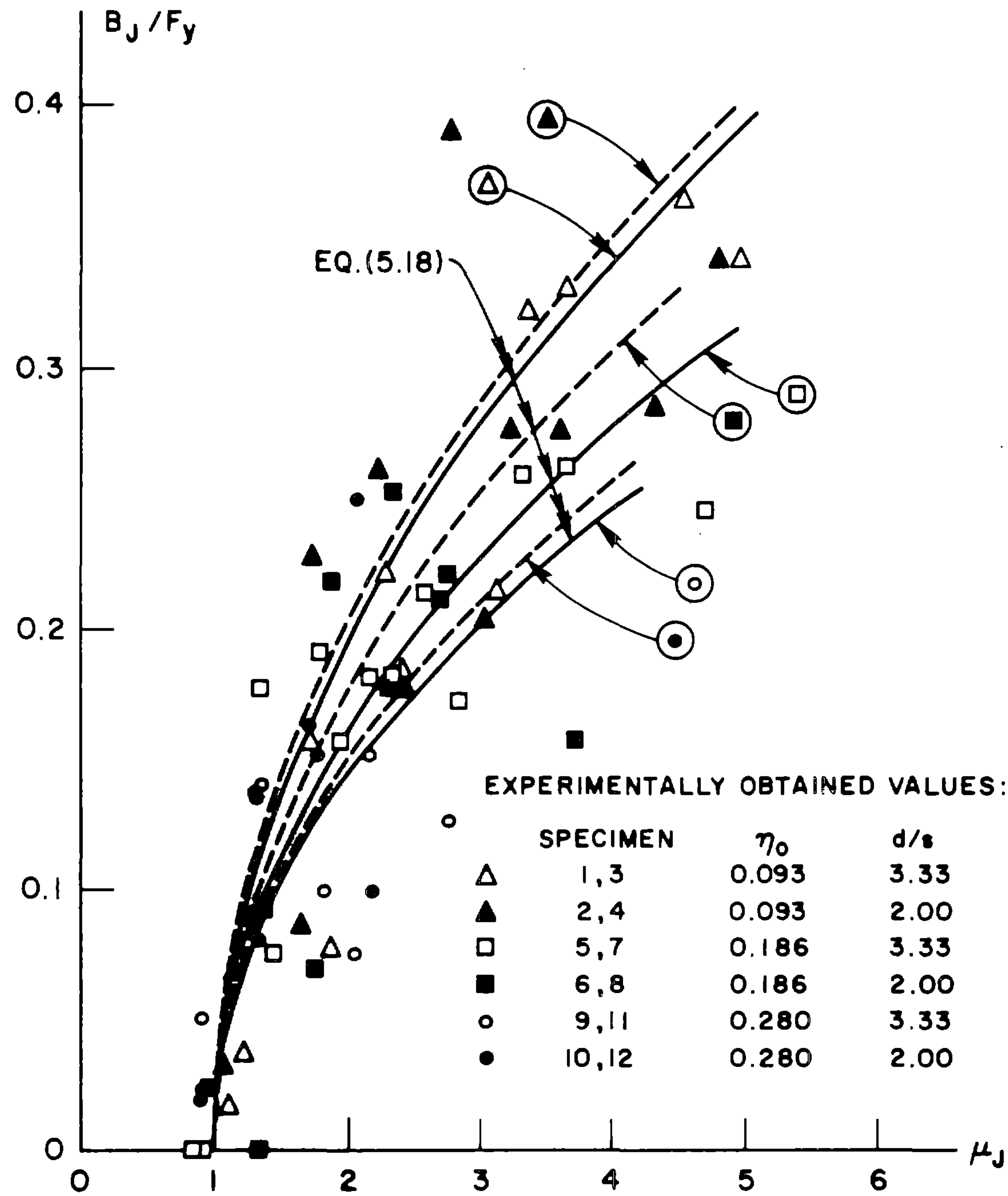

FIG. 5.5 EMPIRICAL RELATIONSHIP B_J/F_y vs. μ_J

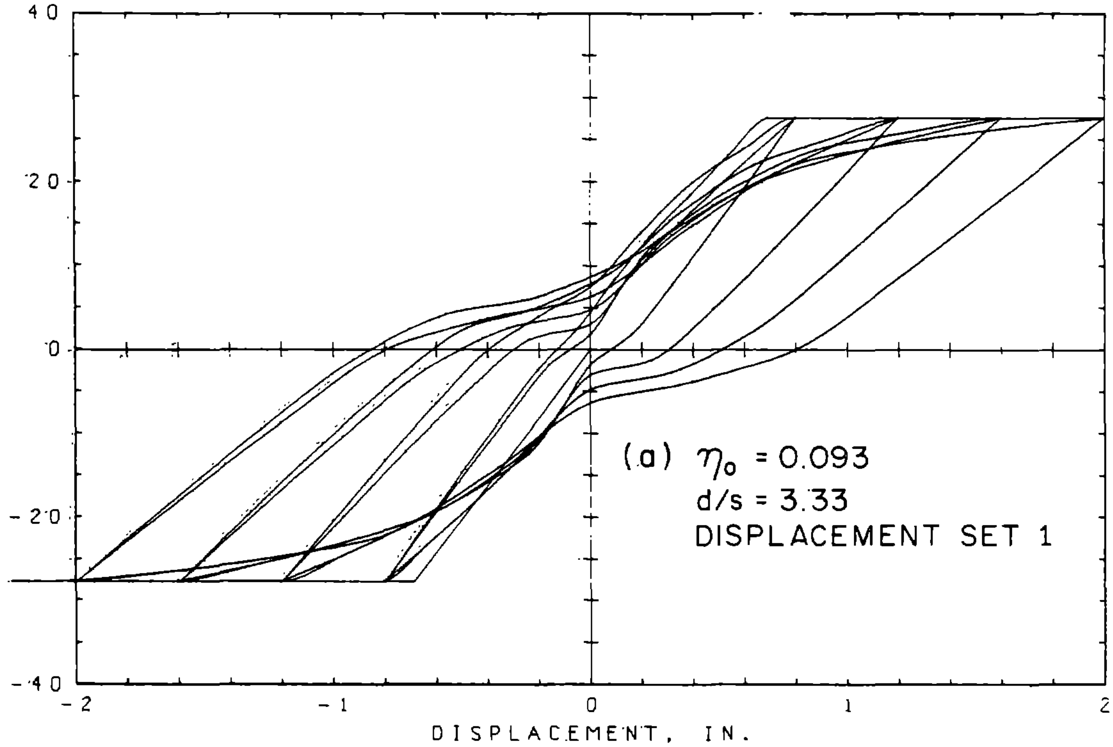

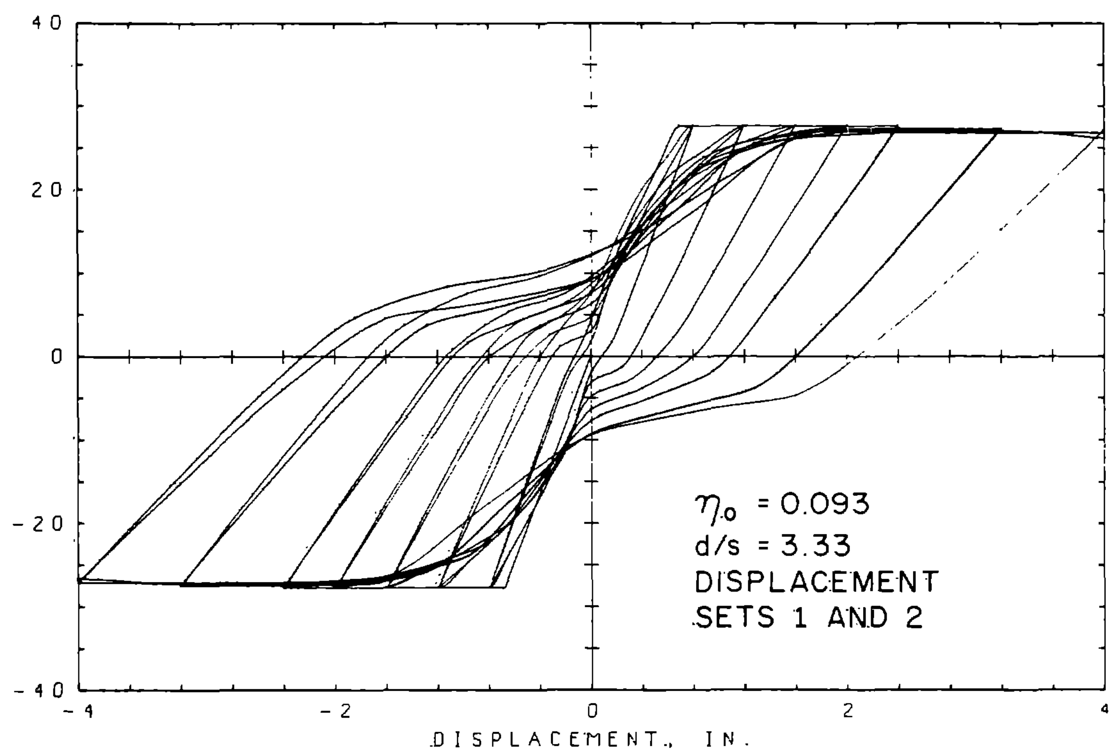

FIG. 5.6 CALCULATED LATERAL FORCE-DISPLACEMENT RELATIONSHIPS

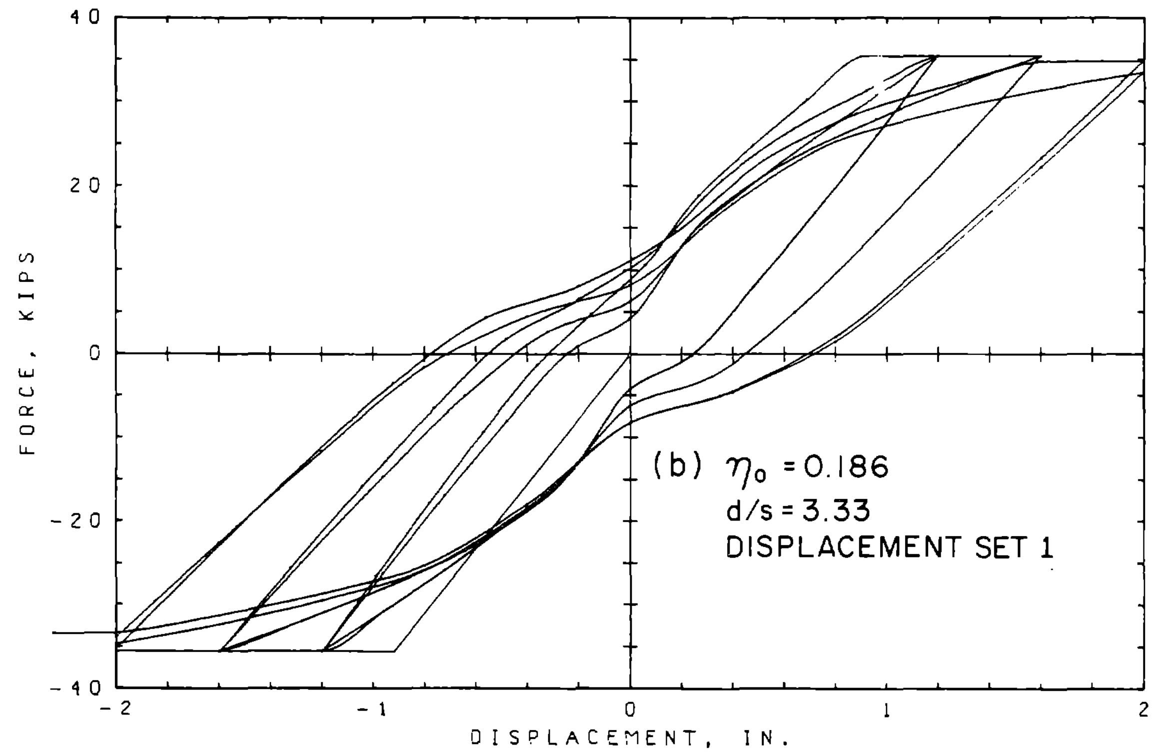

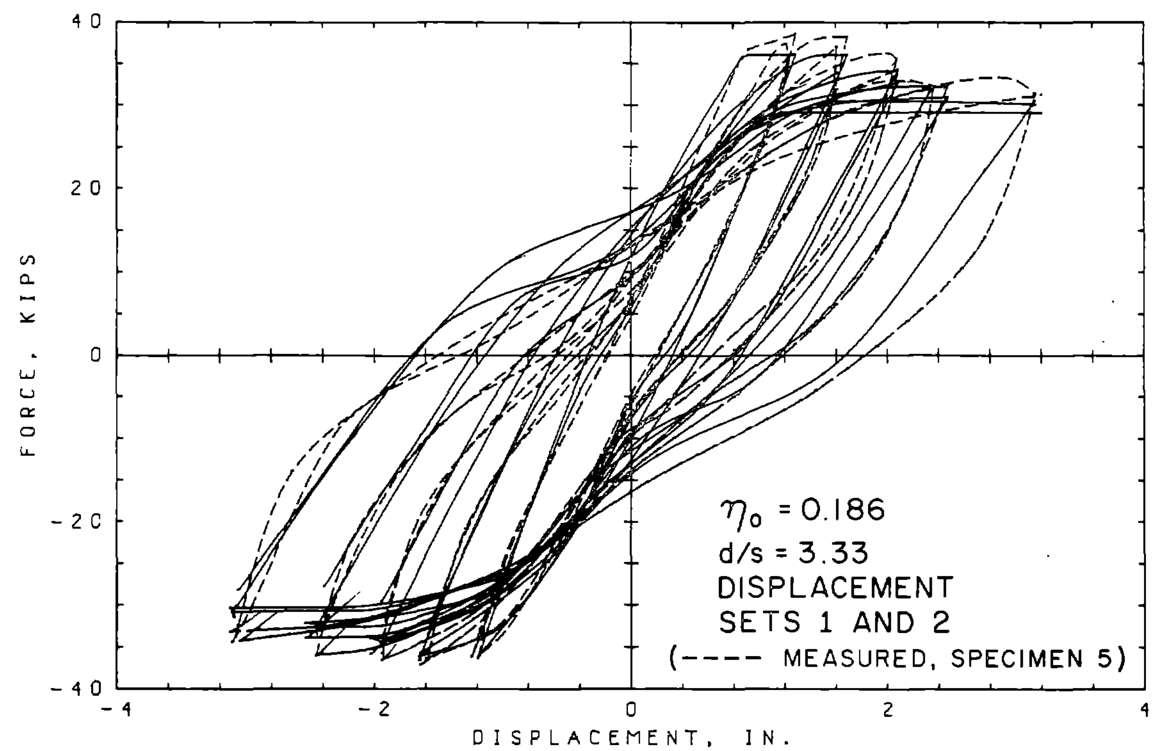

FIG. 5.6 (CONTINUED) CALCULATED LATERAL FORCE-DISPLACEMENT RELATIONSHIPS

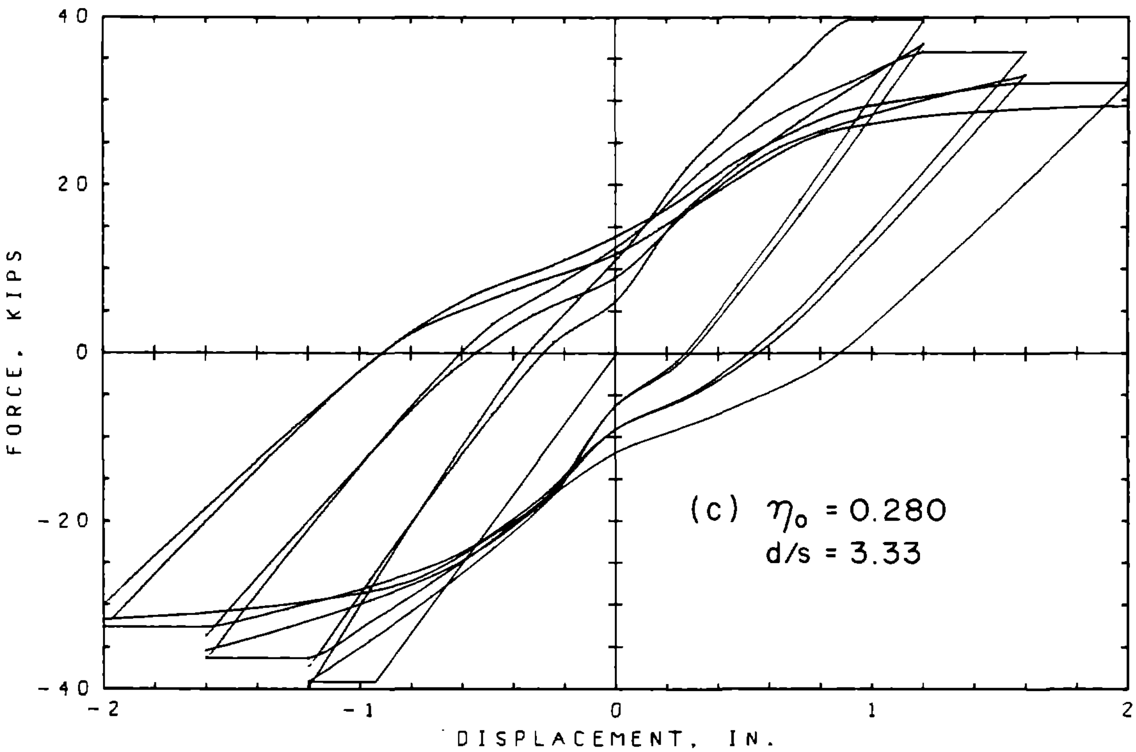

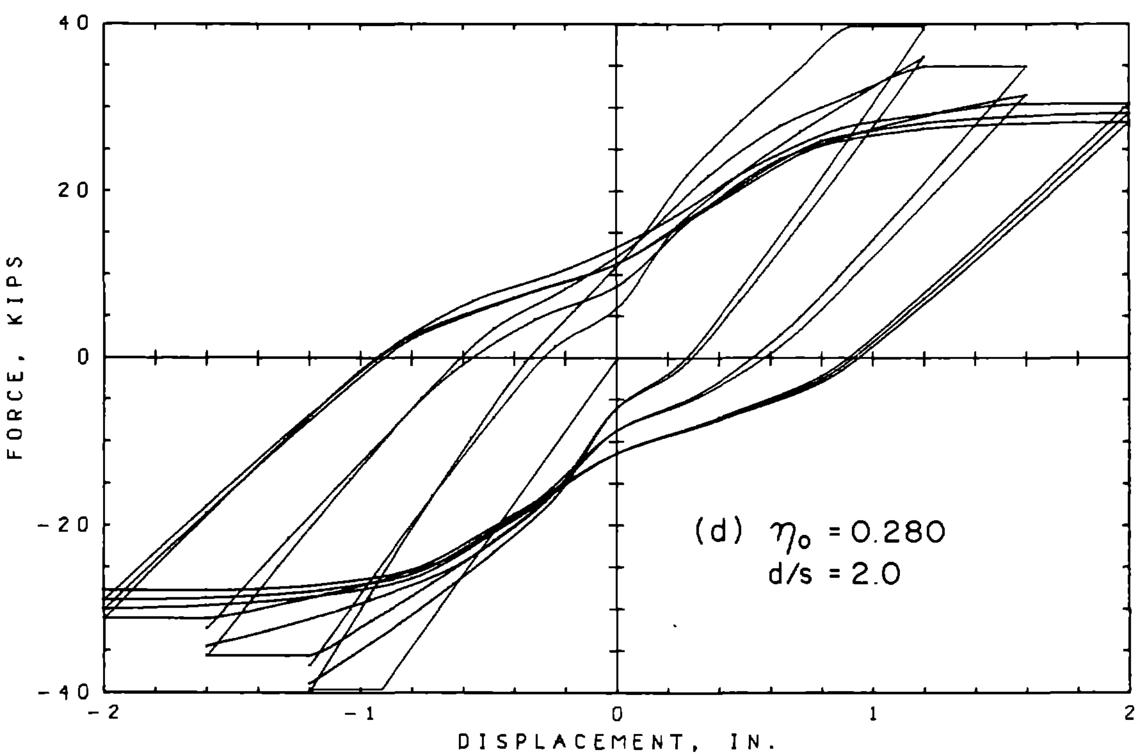

FIG. 5.6 (CONTINUED) CALCULATED LATERAL FORCE-DISPLACEMENT RELATIONSHIPS

APPENDIX

A complete catalogue of the hysteresis loops obtained as the result of the experimental investigation is presented in Figs. A.1 through A.5. These figures should be viewed within the context of the remarks in Sections 4.2.2.ii through 4.2.2.vi.

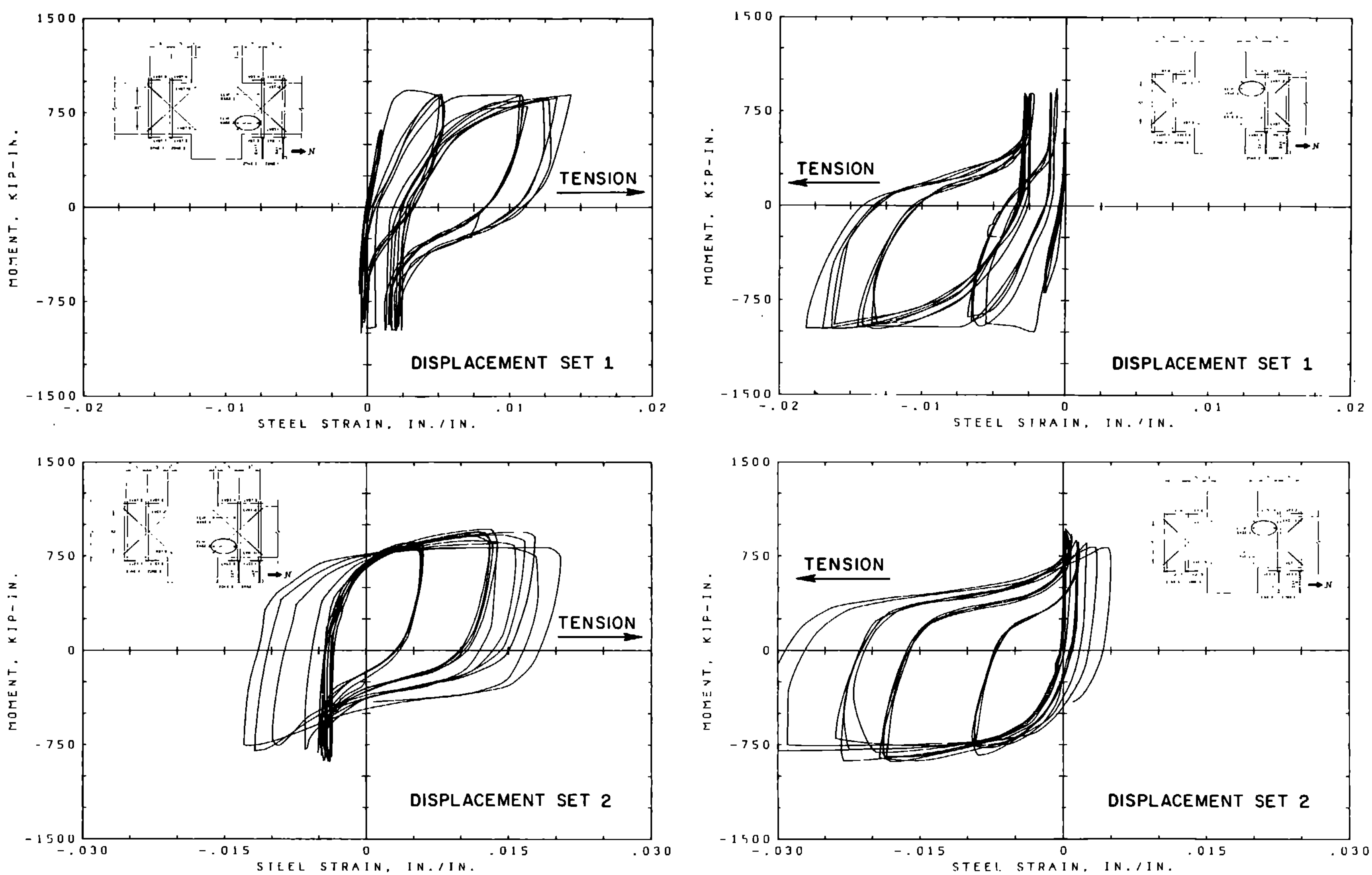

FIG. A.I.a MOMENT–LONGITUDINAL REINFORCEMENT STRAIN DIAGRAMS, SPECIMEN 1

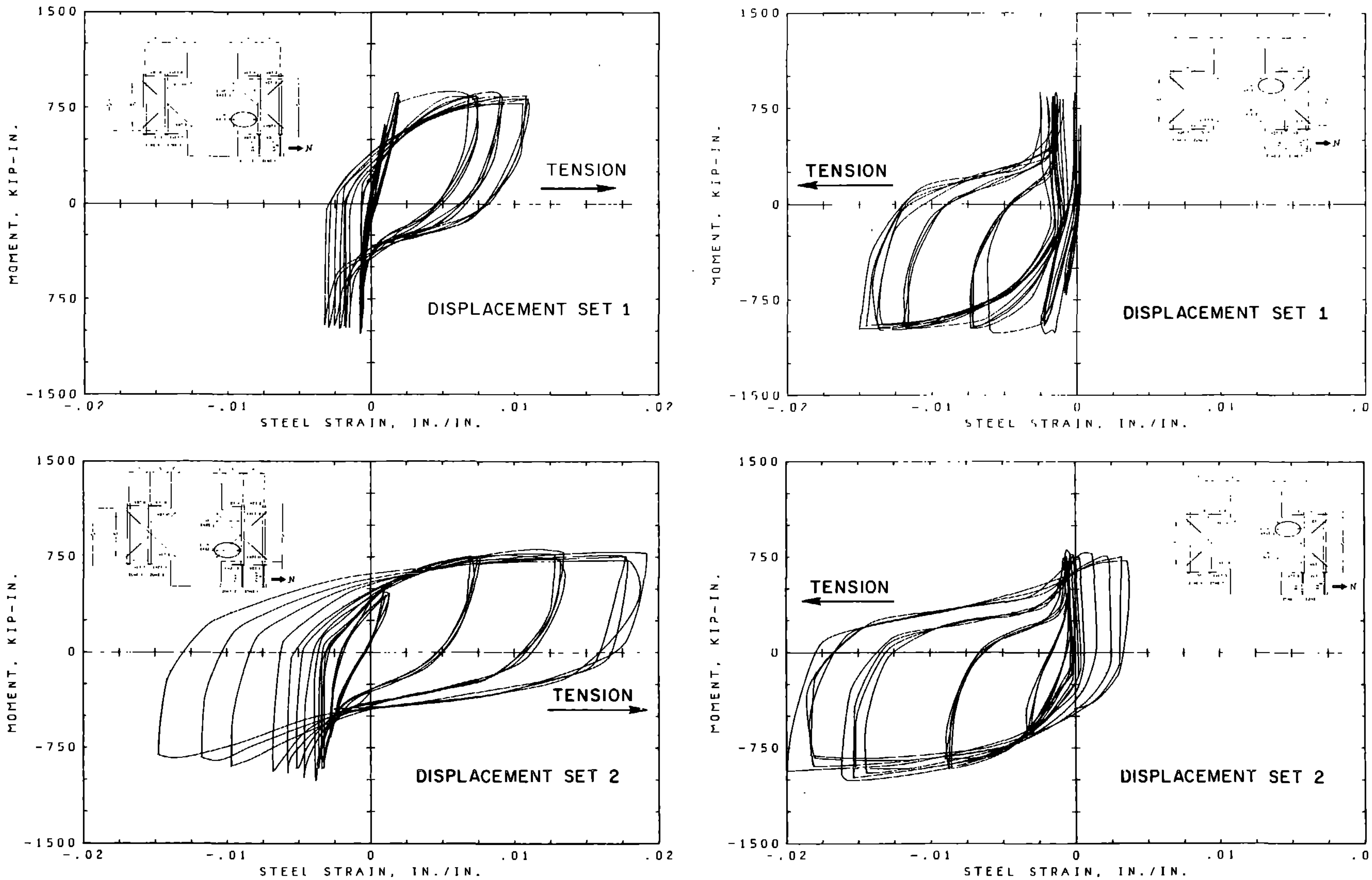

FIG. A.I.b MOMENT – LONGITUDINAL REINFORCEMENT STRAIN DIAGRAMS, SPECIMEN 2

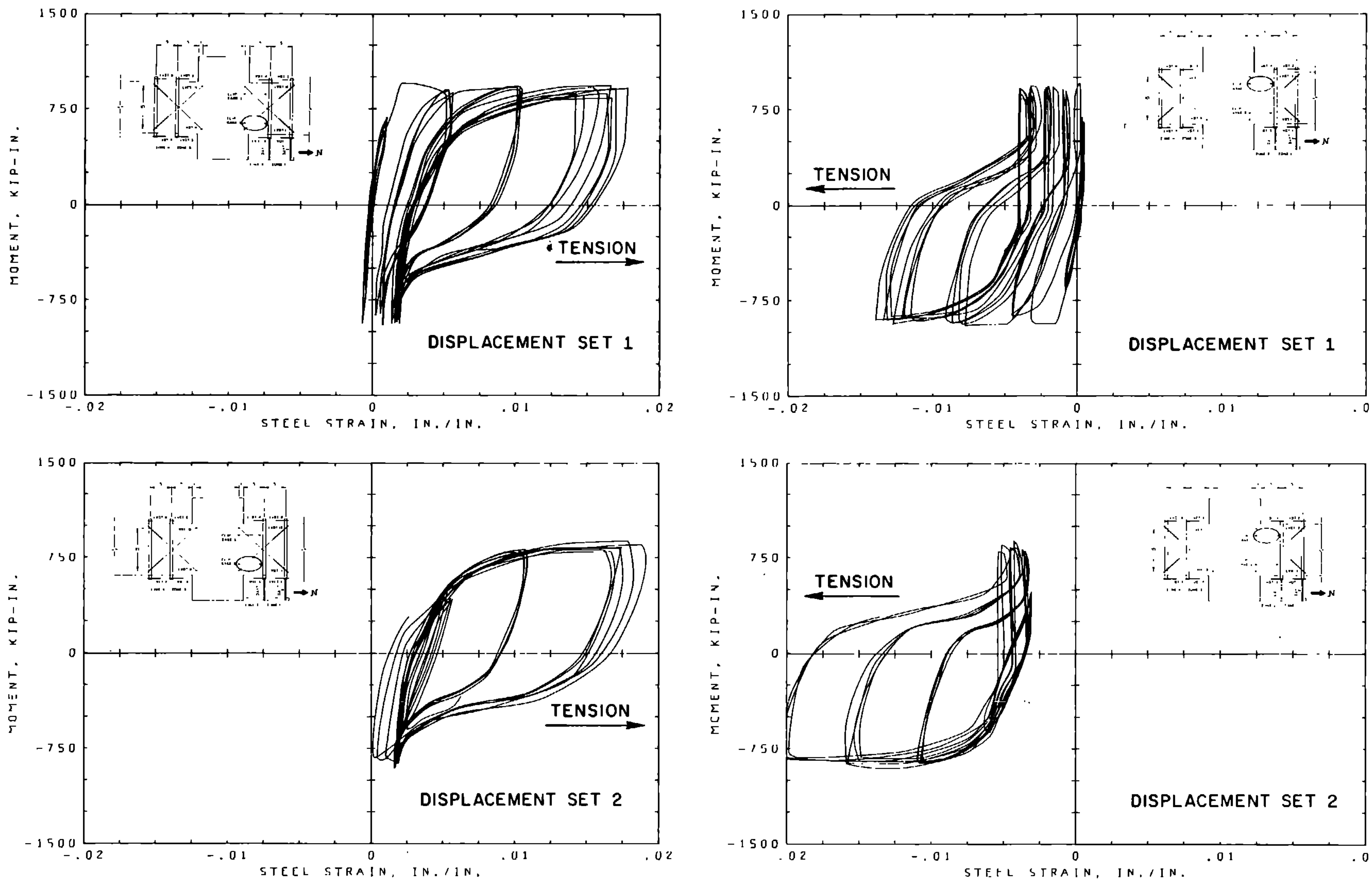

FIG. A.I.c MOMENT-LONGITUDINAL REINFORCEMENT STRAIN DIAGRAMS, SPECIMEN 3

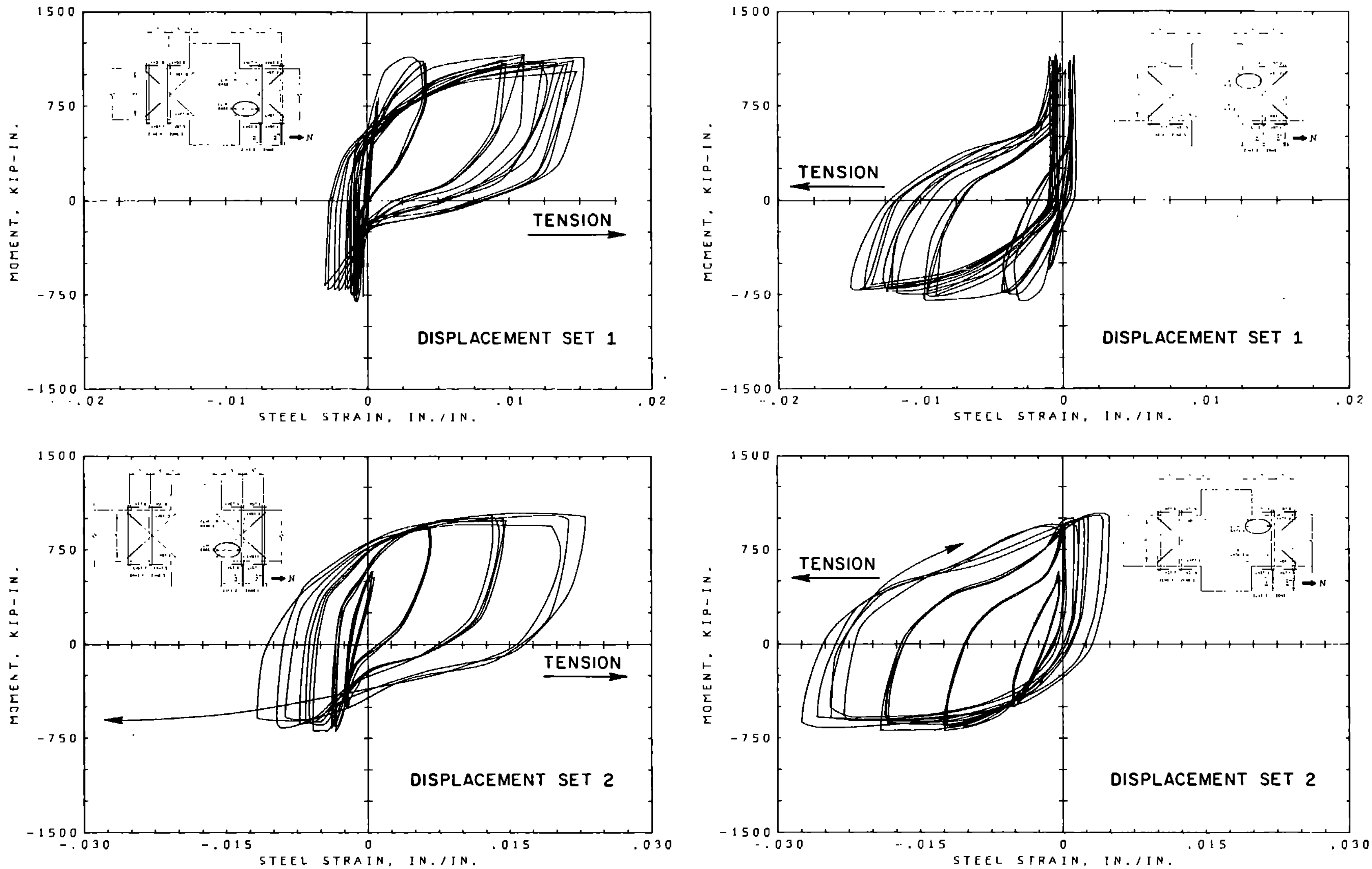

FIG. A.1.d MOMENT - LONGITUDINAL REINFORCEMENT STRAIN DIAGRAMS, SPECIMEN 4

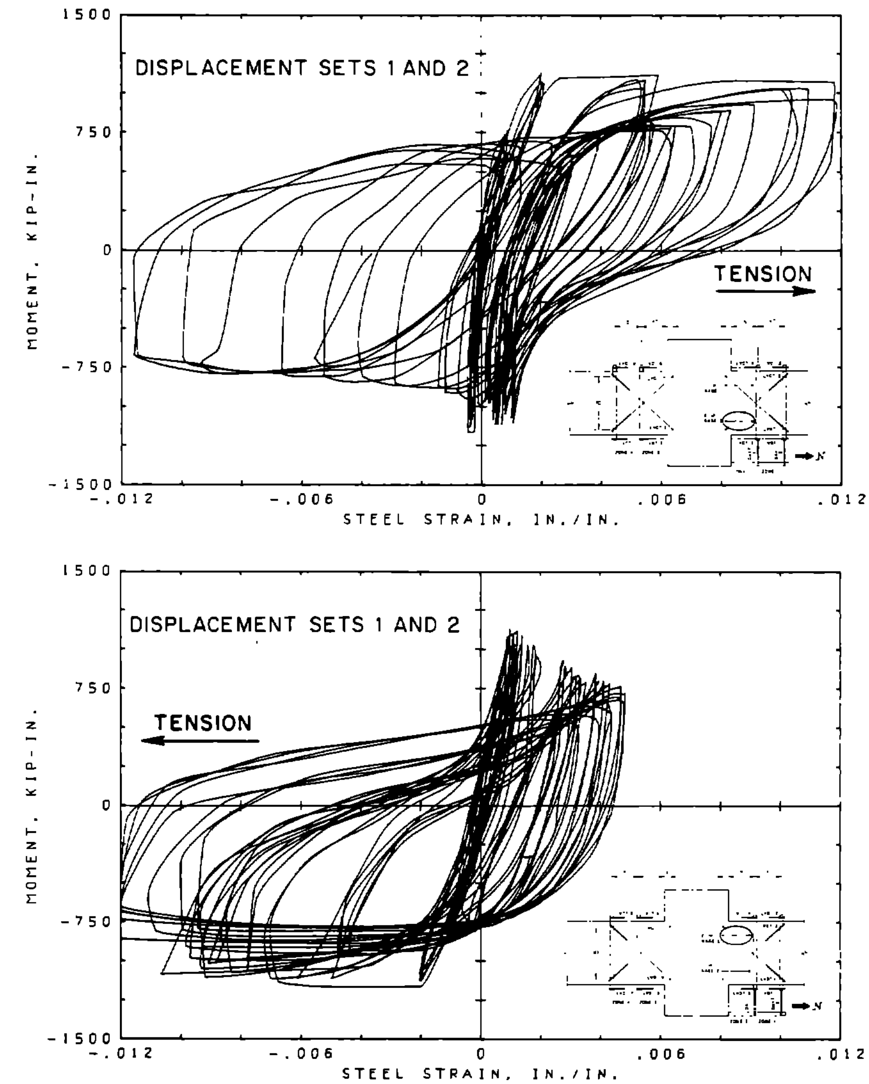

FIG. A.1.e MOMENT-LONGITUDINAL REINFORCEMENT STRAIN DIAGRAMS, SPECIMEN 5

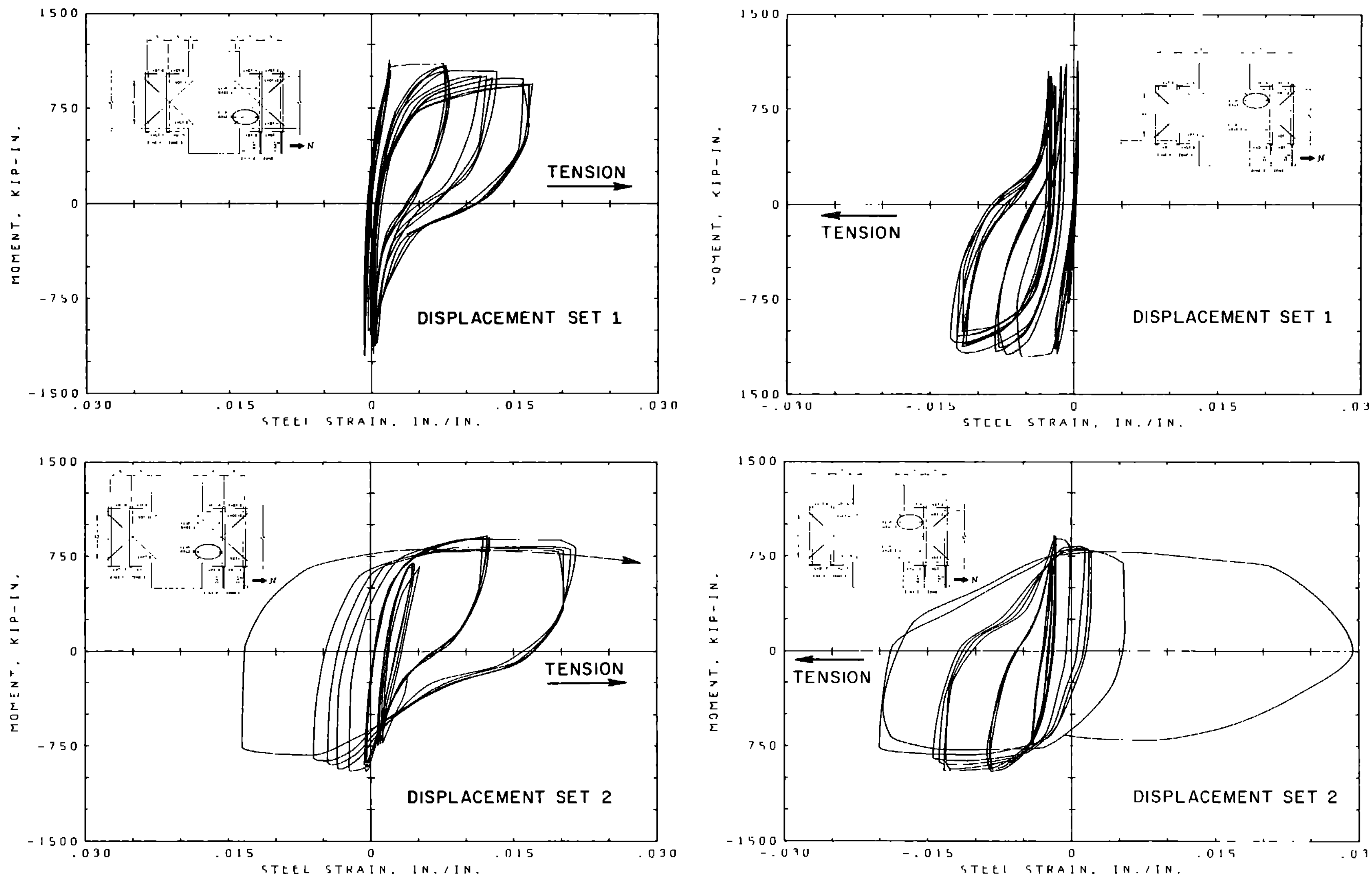

FIG. A.I.f MOMENT-LONGITUDINAL REINFORCEMENT STRAIN DIAGRAMS, SPECIMEN 6

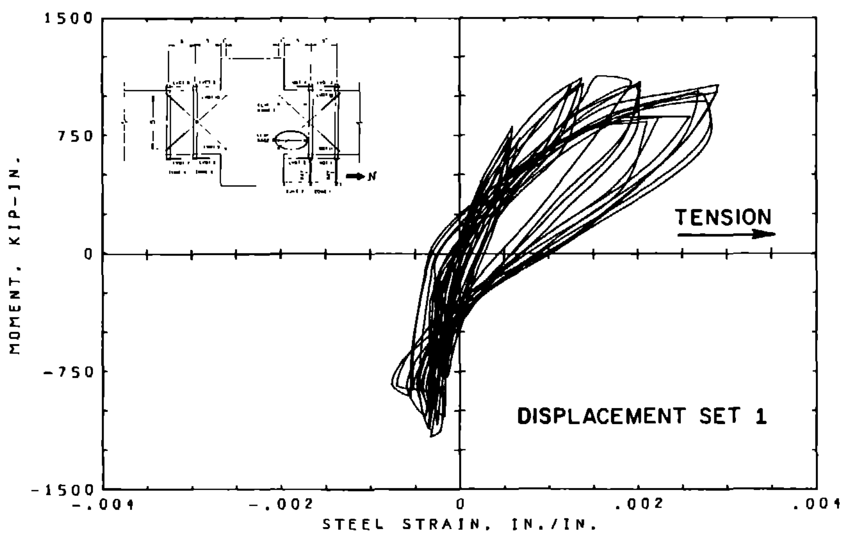

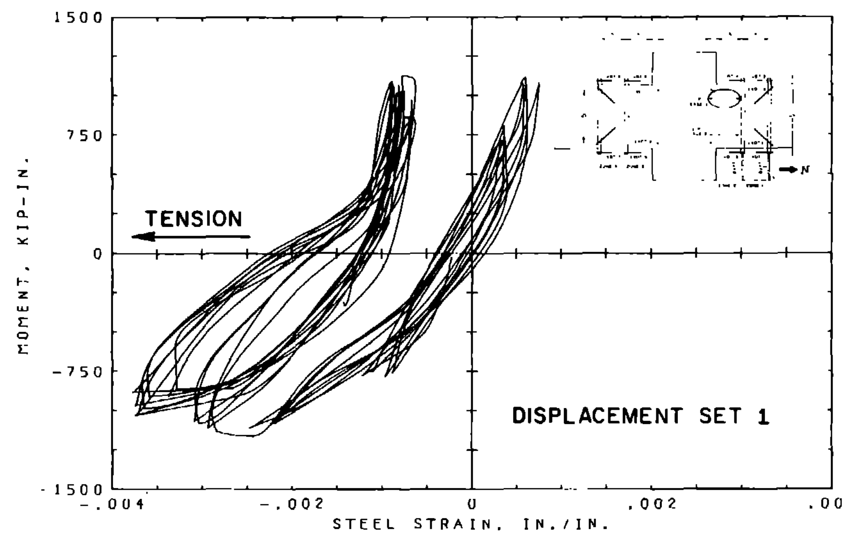

DISPLACEMENT SET 2:
NOT AVAILABLE

DISPLACEMENT SET 2:
NOT AVAILABLE

FIG. A.I.g MOMENT-LONGITUDINAL REINFORCEMENT STRAIN DIAGRAMS, SPECIMEN 7

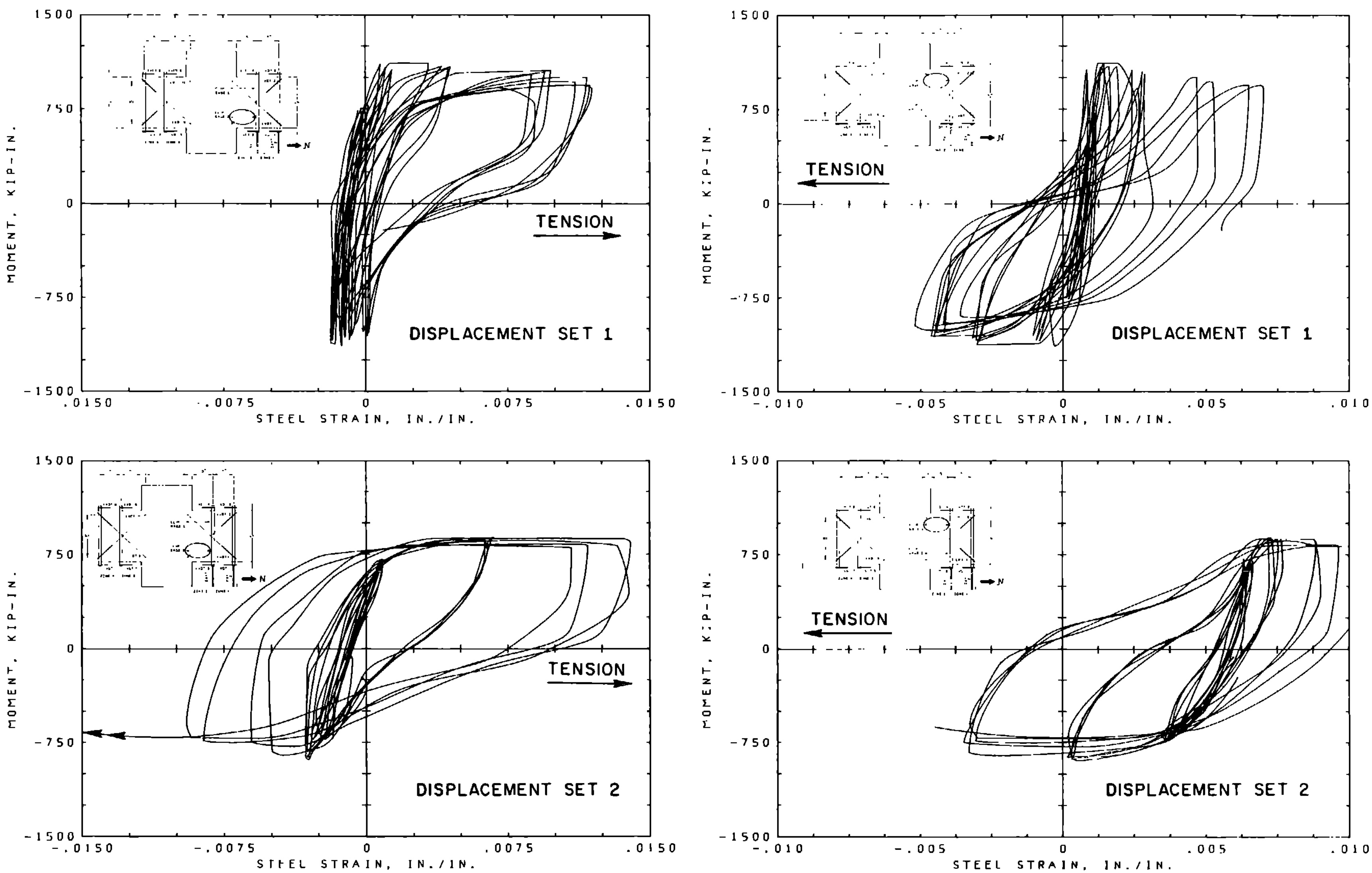

FIG. A.I.h MOMENT-LONGITUDINAL REINFORCEMENT STRAIN DIAGRAMS, SPECIMEN 8

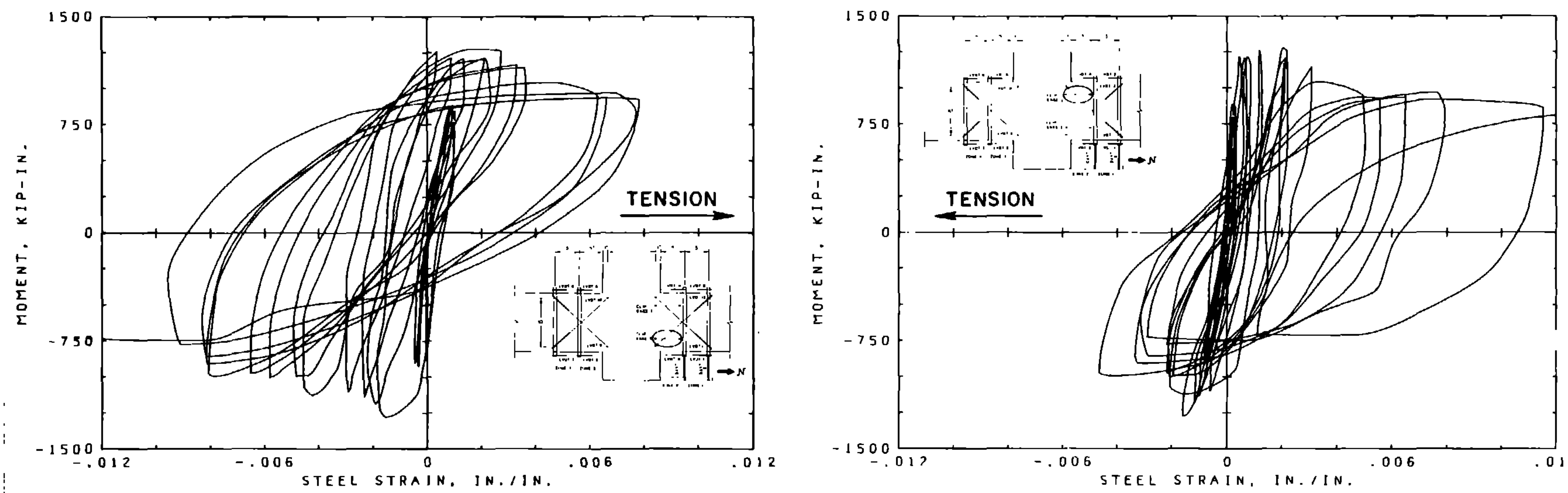

FIG. A.I.i MOMENT-LONGITUDINAL REINFORCEMENT STRAIN DIAGRAMS, SPECIMEN 9

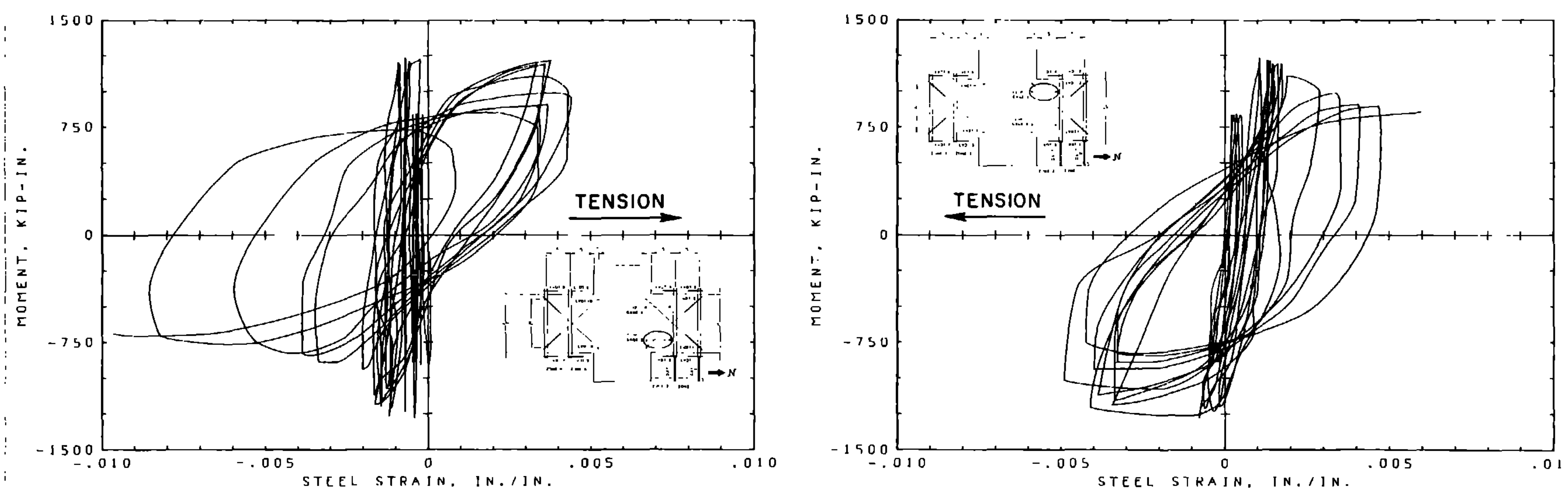

FIG. A.I.j MOMENT-LONGITUDINAL REINFORCEMENT STRAIN DIAGRAMS, SPECIMEN 10

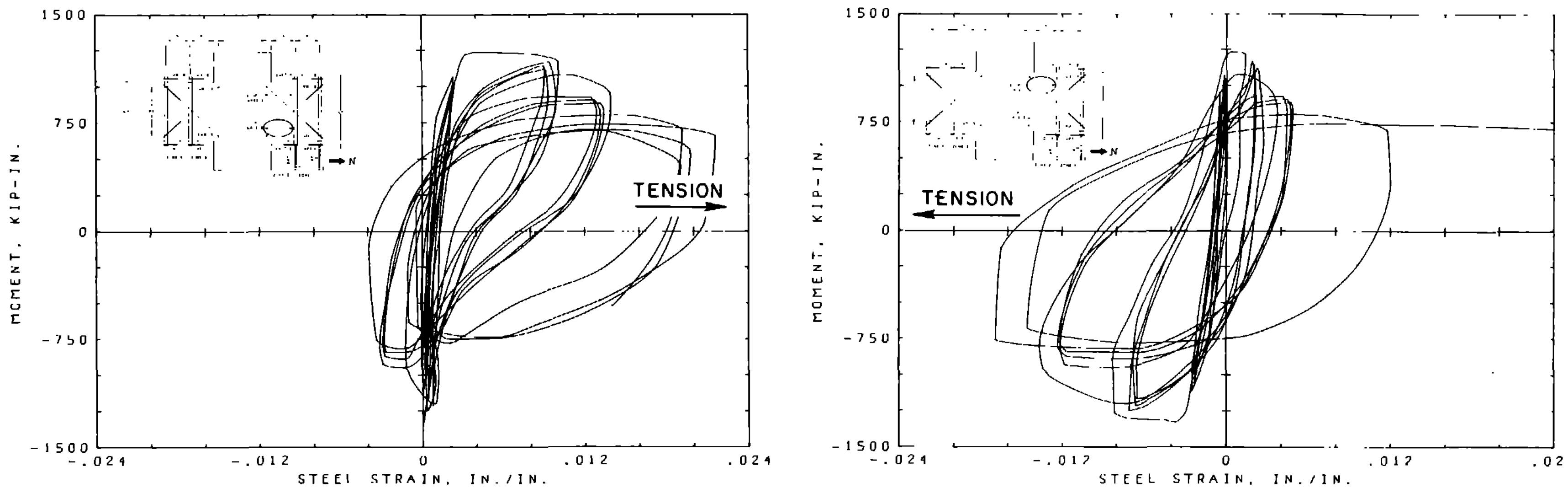

FIG. A.I.k MOMENT-LONGITUDINAL REINFORCEMENT STRAIN DIAGRAMS, SPECIMEN 11

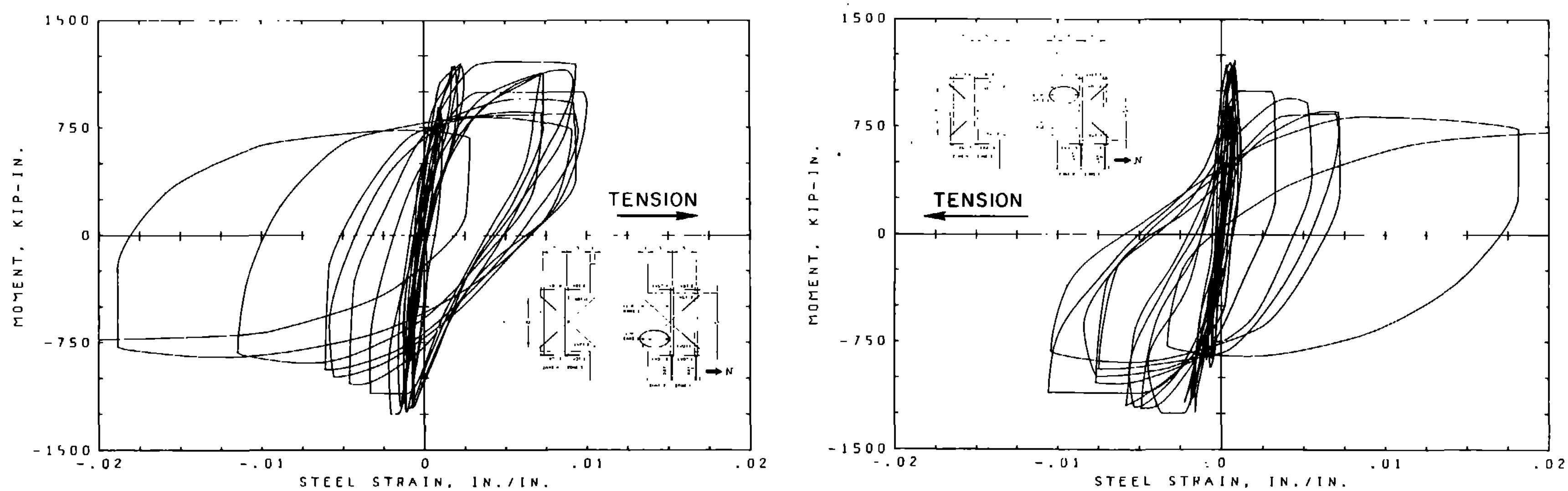

FIG. A.I.ℓ MOMENT-LONGITUDINAL REINFORCEMENT STRAIN DIAGRAMS, SPECIMEN 12

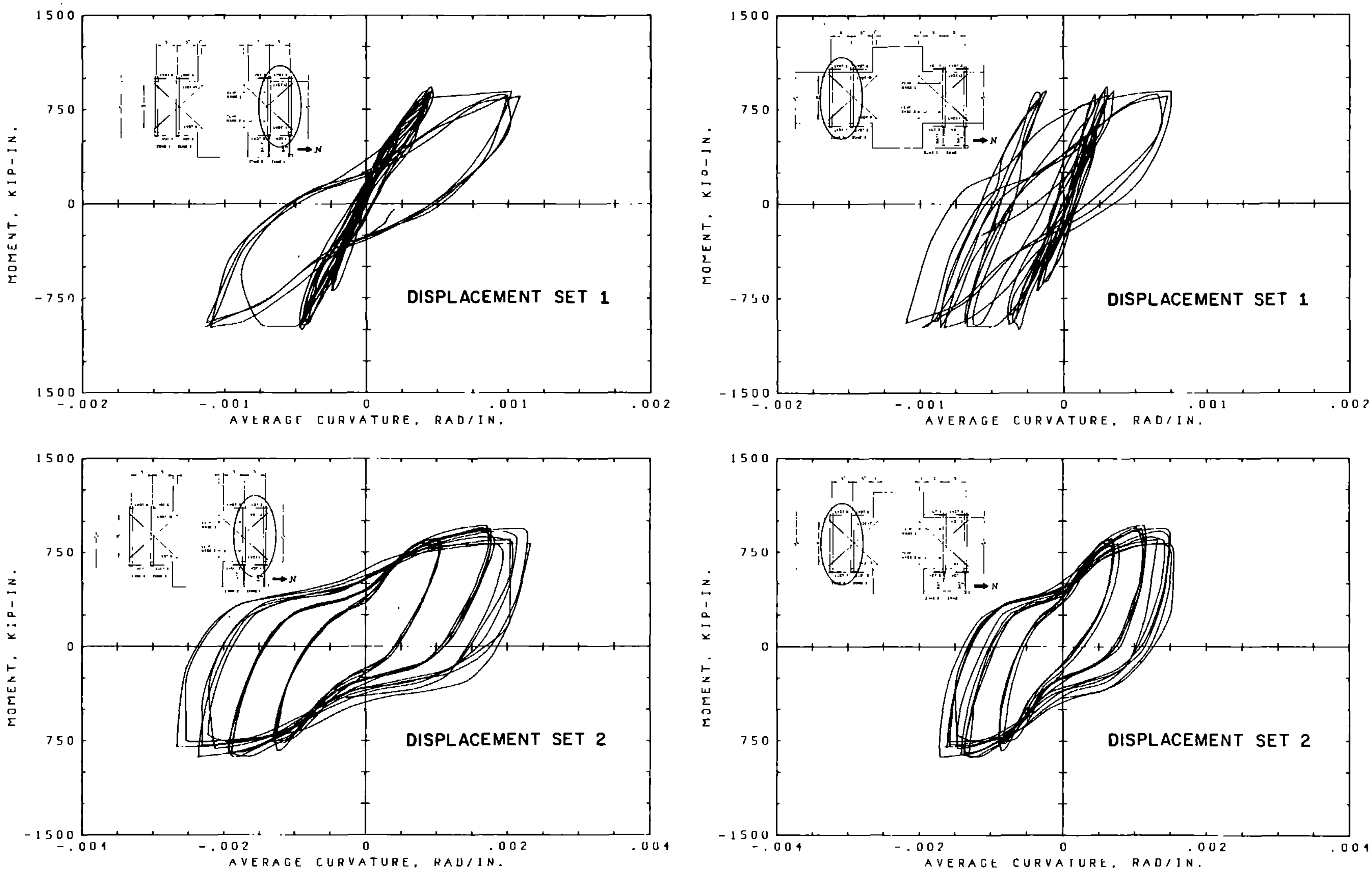

FIG. A.2.a MOMENT-AVERAGE CURVATURE DIAGRAMS, SPECIMEN 1

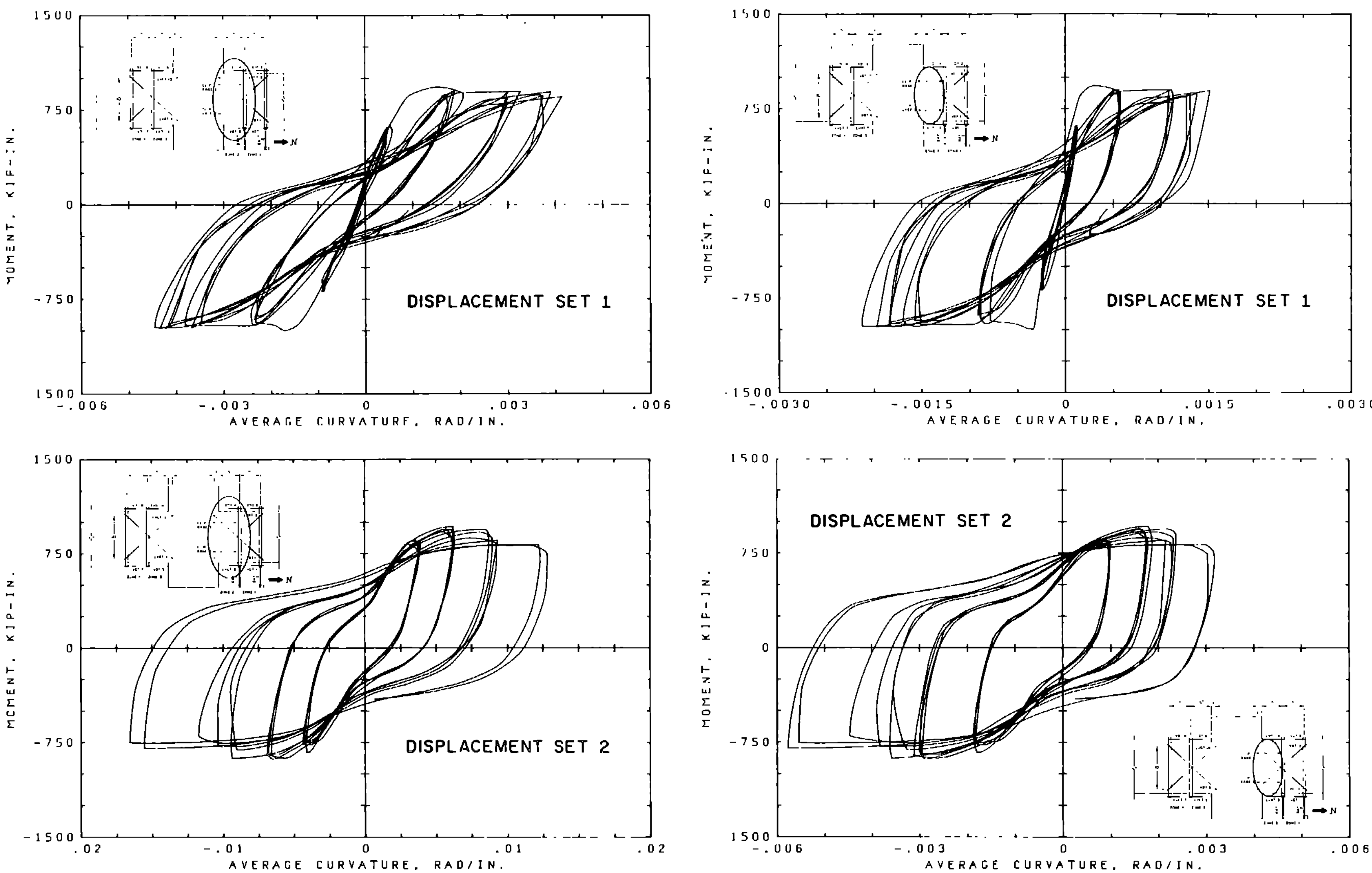

FIG. A.2.a (CONTINUED) MOMENT–LONGITUDINAL REINFORCEMENT STRAIN DIAGRAMS, SPECIMEN 1

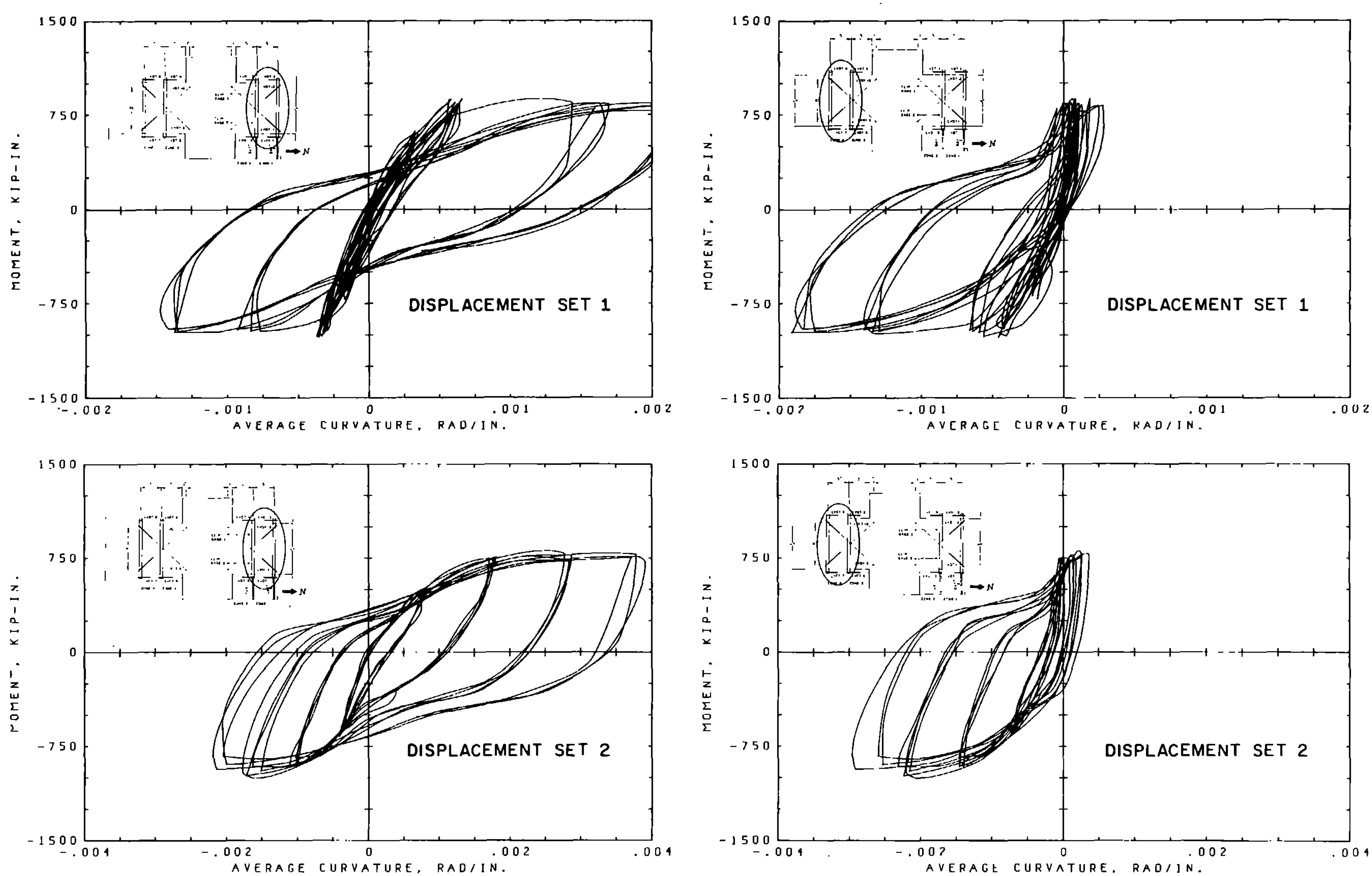

FIG. A.2.b MOMENT-AVERAGE CURVATURE DIAGRAMS, SPECIMEN 2

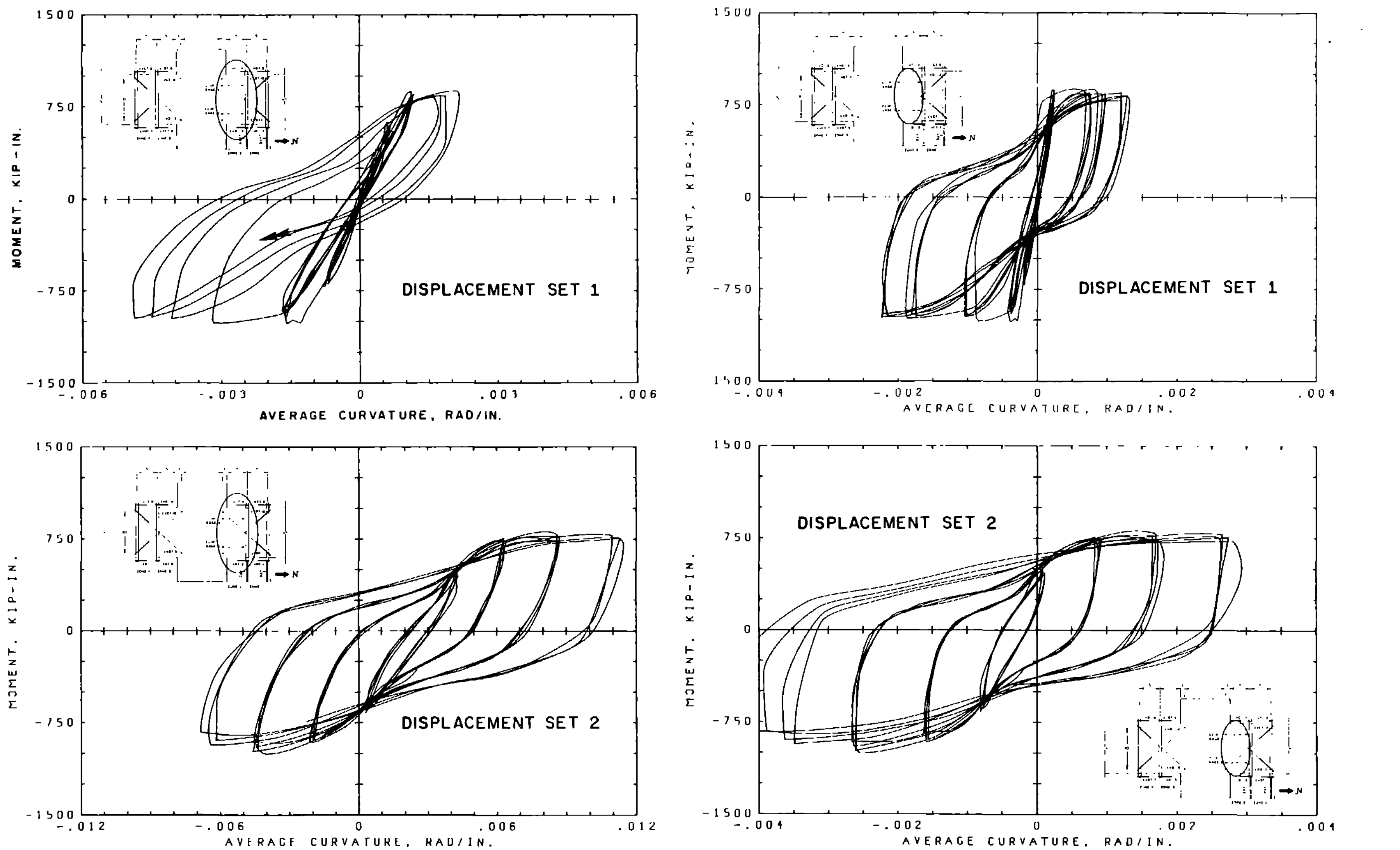

FIG. A.2.b (CONTINUED) MOMENT—LONGITUDINAL REINFORCEMENT STRAIN DIAGRAMS, SPECIMEN 2

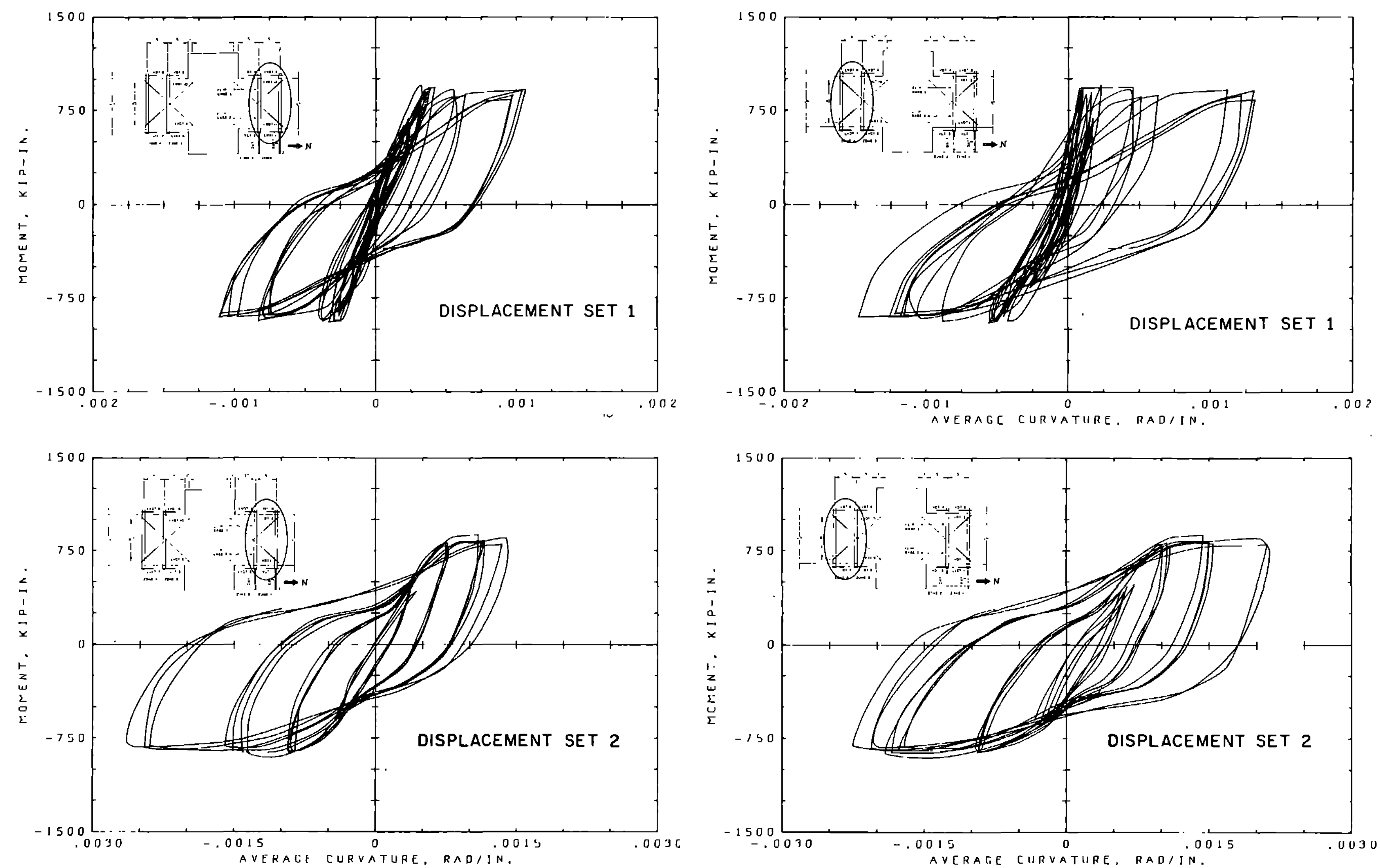

FIG. A.2.c MOMENT-AVERAGE CURVATURE DIAGRAMS, SPECIMEN 3

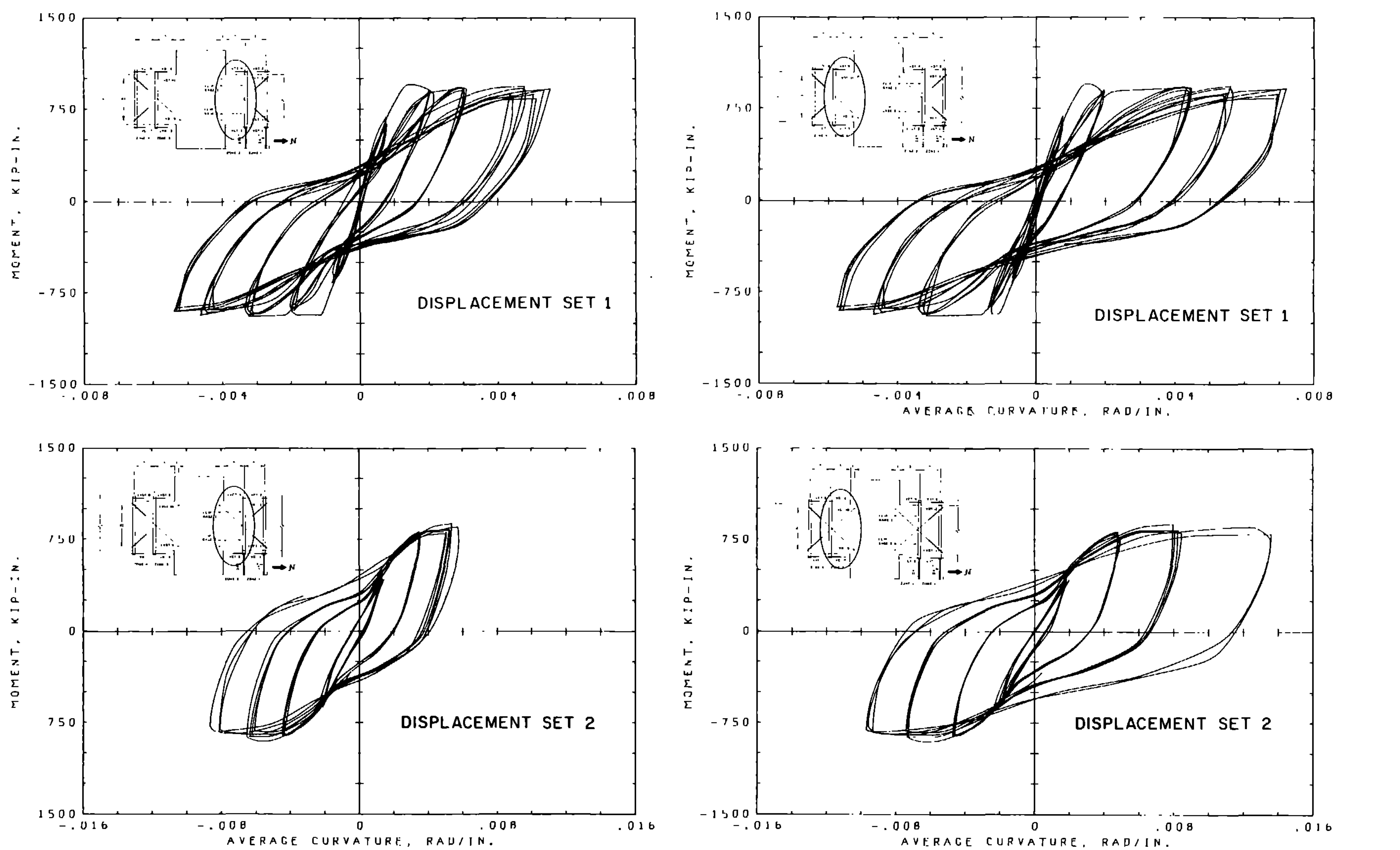

FIG. A.2.c (CONTINUED) MOMENT–LONGITUDINAL REINFORCEMENT STRAIN DIAGRAMS, SPECIMEN 3

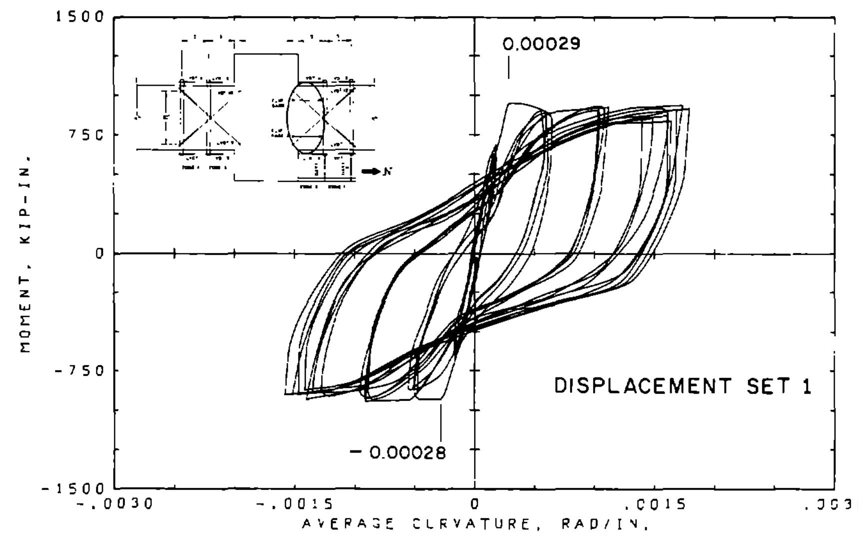

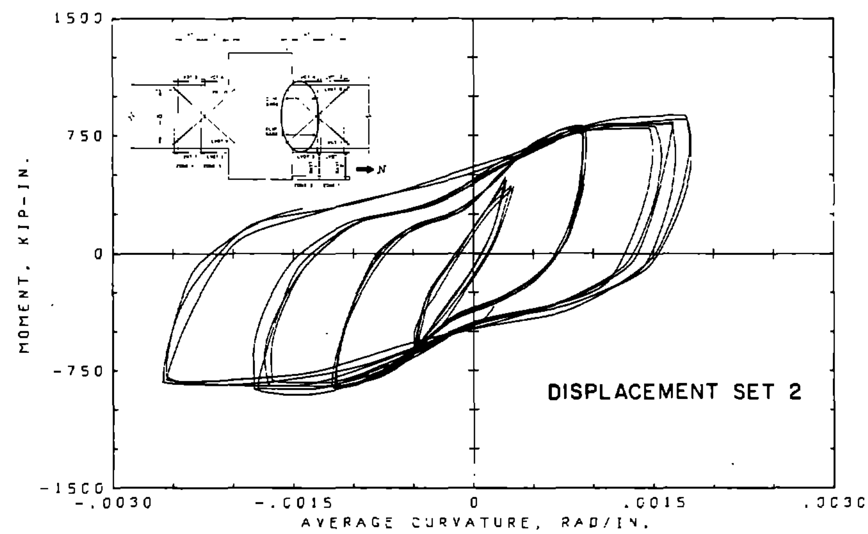

FIG. A.2.c (CONTINUED) MOMENT-LONGITUDINAL REINFORCEMENT STRAIN DIAGRAMS, SPECIMEN 3

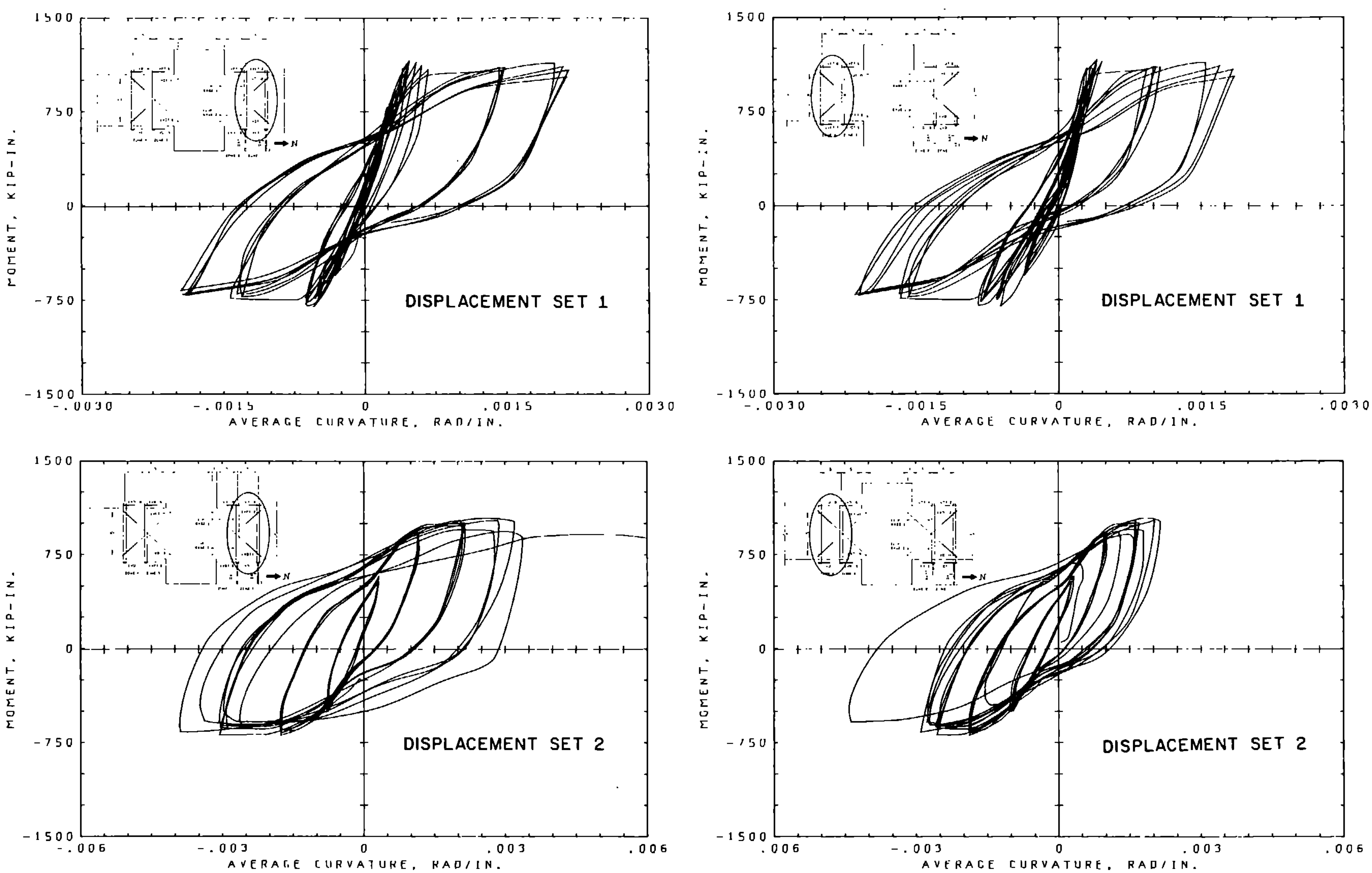

FIG. A.2.d MOMENT-AVERAGE CURVATURE DIAGRAMS, SPECIMEN 4

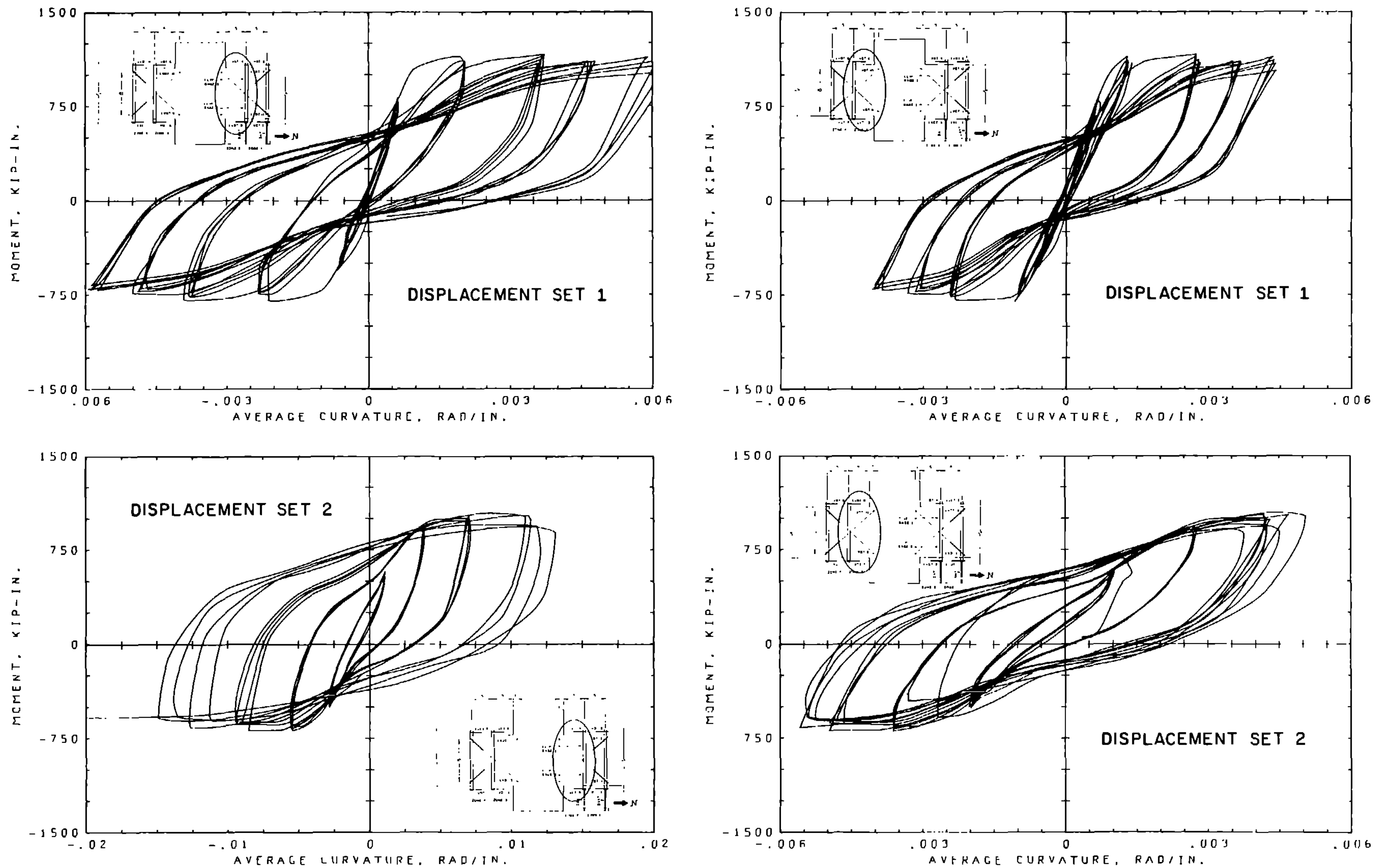

FIG. A.2.d (CONTINUED) MOMENT-LONGITUDINAL REINFORCEMENT STRAIN DIAGRAMS, SPECIMEN 4

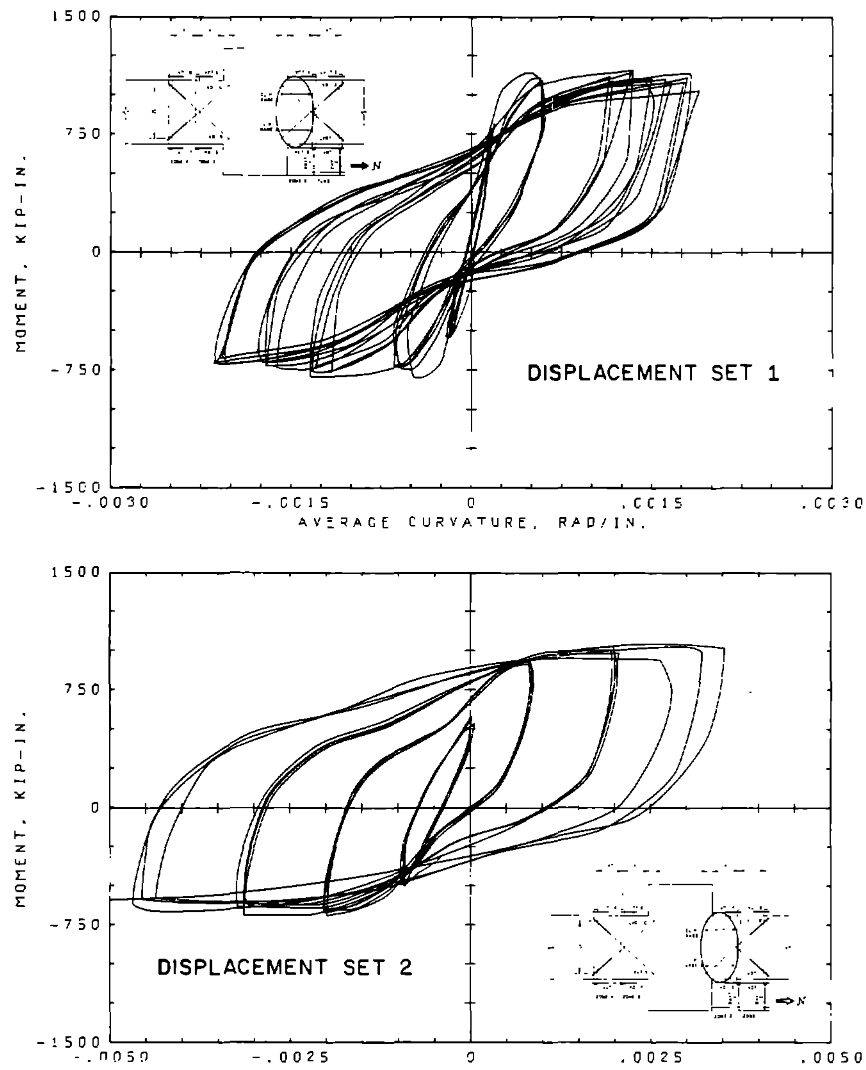

FIG. A.2.d (CONTINUED) MOMENT-LONGITUDINAL REINFORCEMENT STRAIN DIAGRAMS, SPECIMEN 4

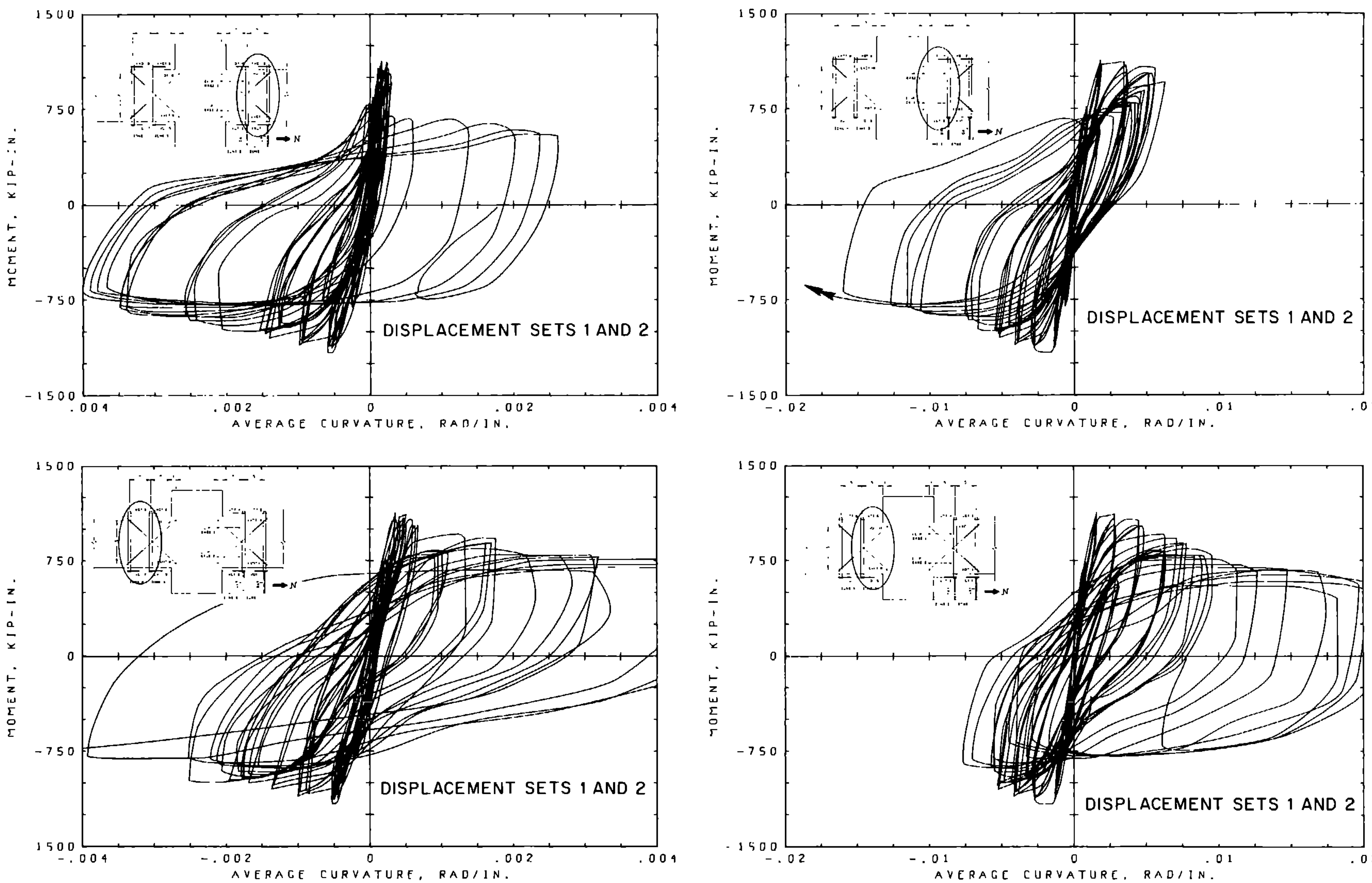

FIG. A.2.e MOMENT-AVERAGE CURVATURE DIAGRAMS, SPECIMEN 5

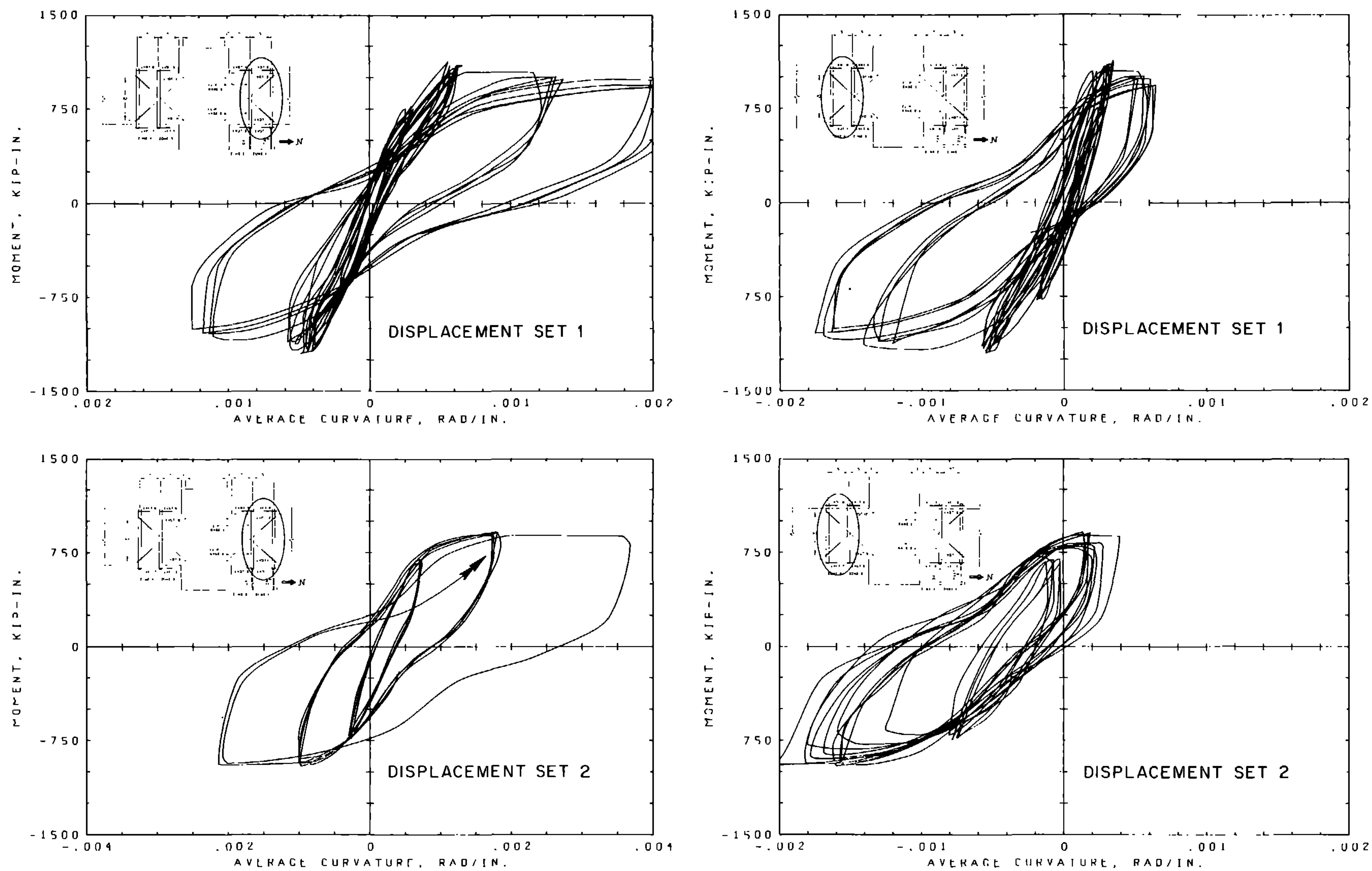

FIG. A.2.f MOMENT-AVERAGE CURVATURE DIAGRAMS, SPECIMEN 6

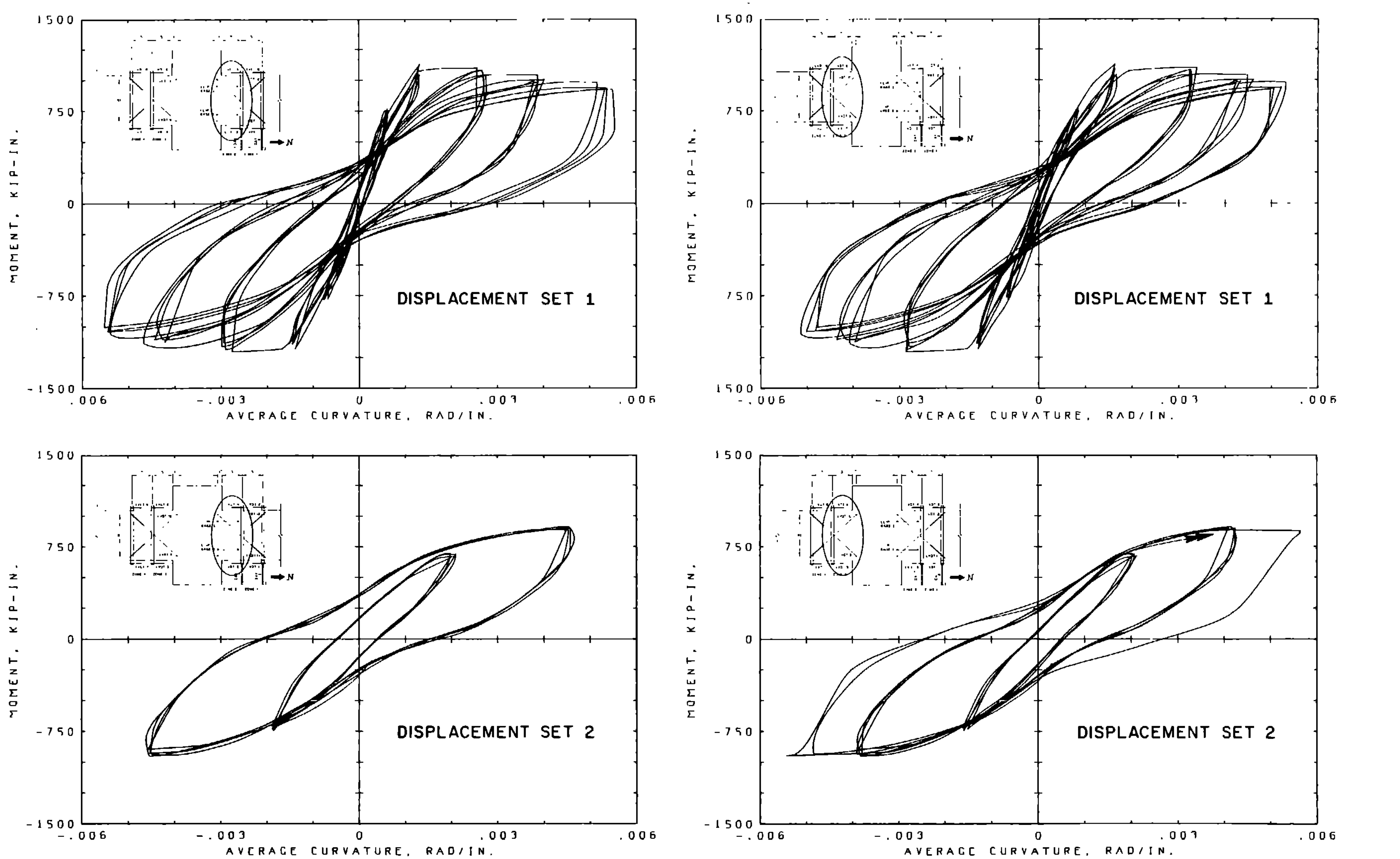

FIG. A.2.f (CONTINUED) MOMENT–LONGITUDINAL REINFORCEMENT STRAIN DIAGRAMS, SPECIMEN 6

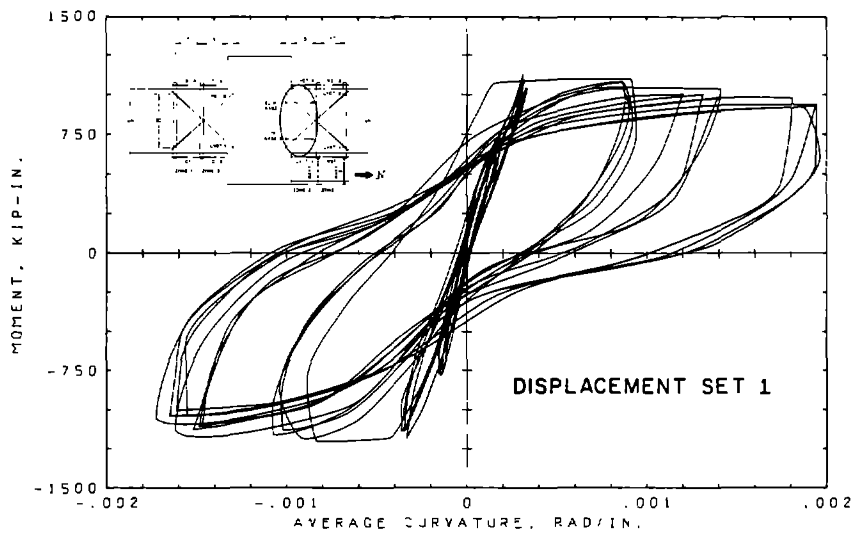

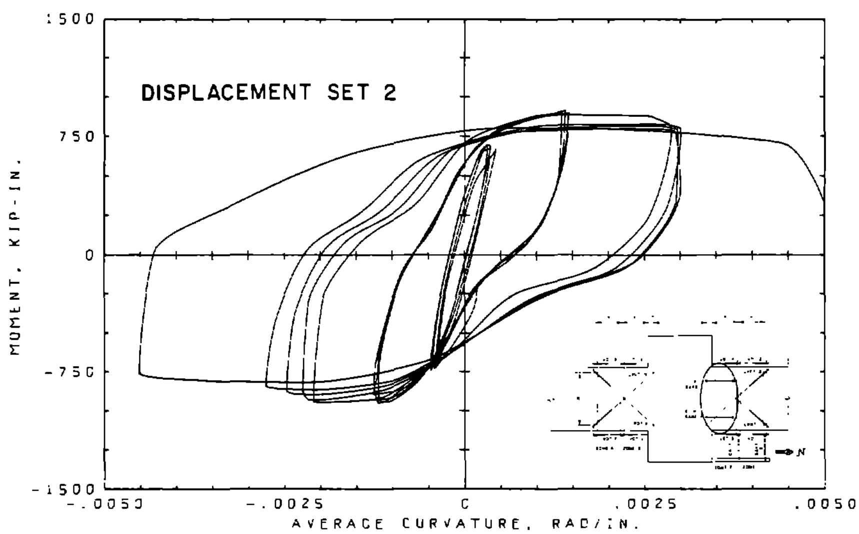

FIG. A.2.f (CONTINUED) MOMENT-LONGITUDINAL REINFORCEMENT STRAIN DIAGRAMS, SPECIMEN 6

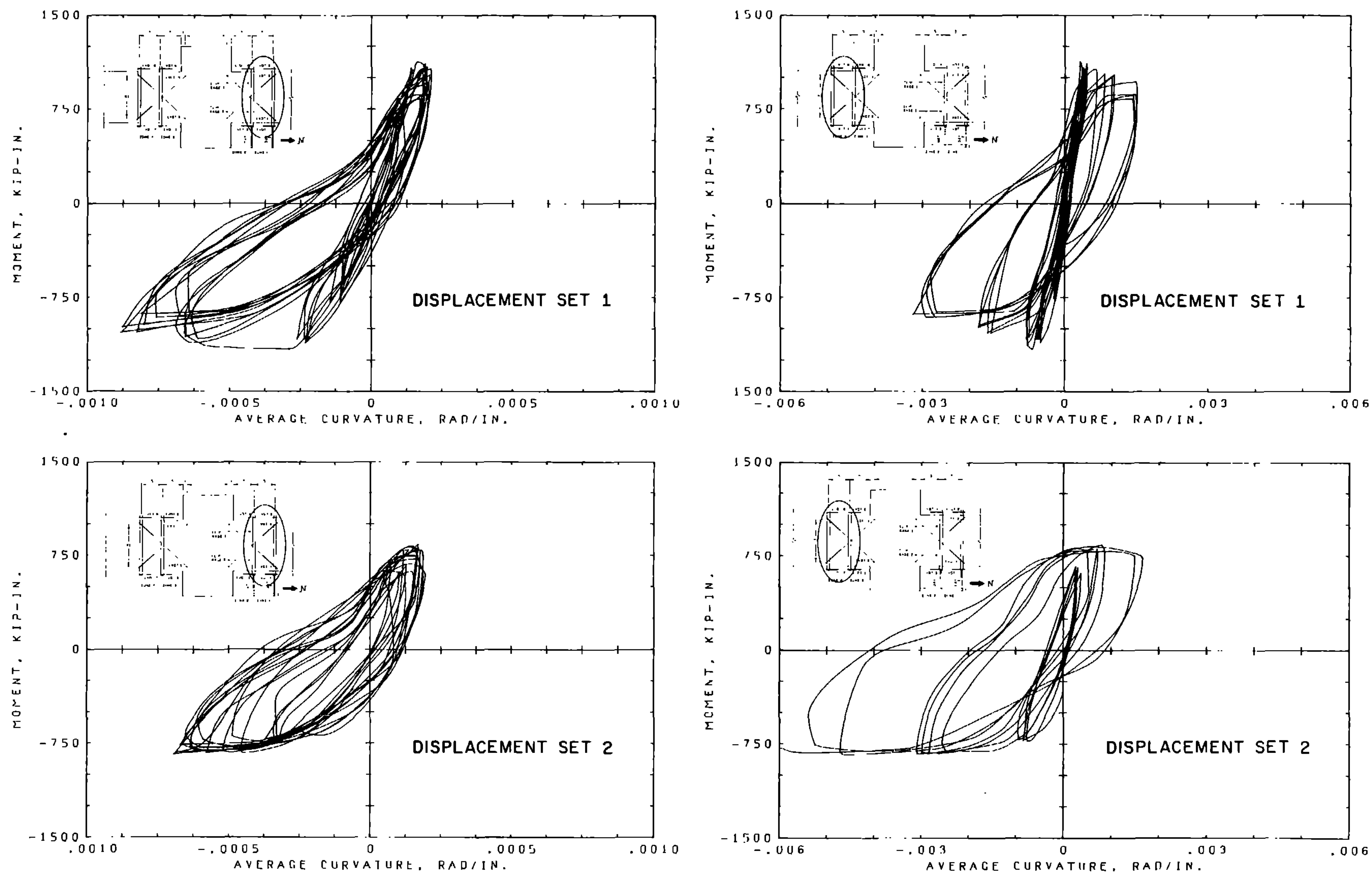

FIG. A.2.g MOMENT-AVERAGE CURVATURE DIAGRAMS, SPECIMEN 7

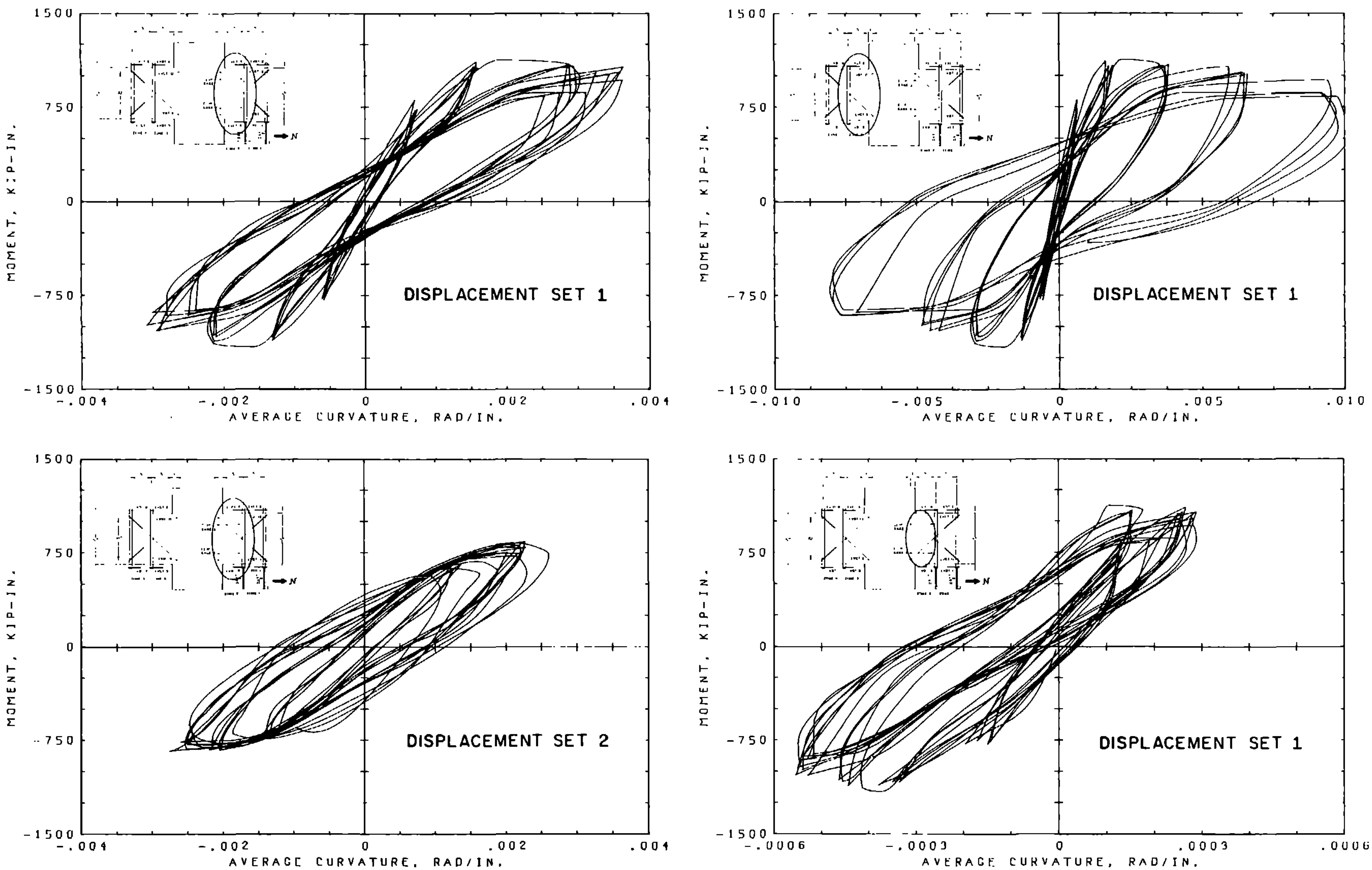

FIG. A.2.g (CONTINUED) MOMENT-LONGITUDINAL REINFORCEMENT STRAIN DIAGRAMS, SPECIMEN 7

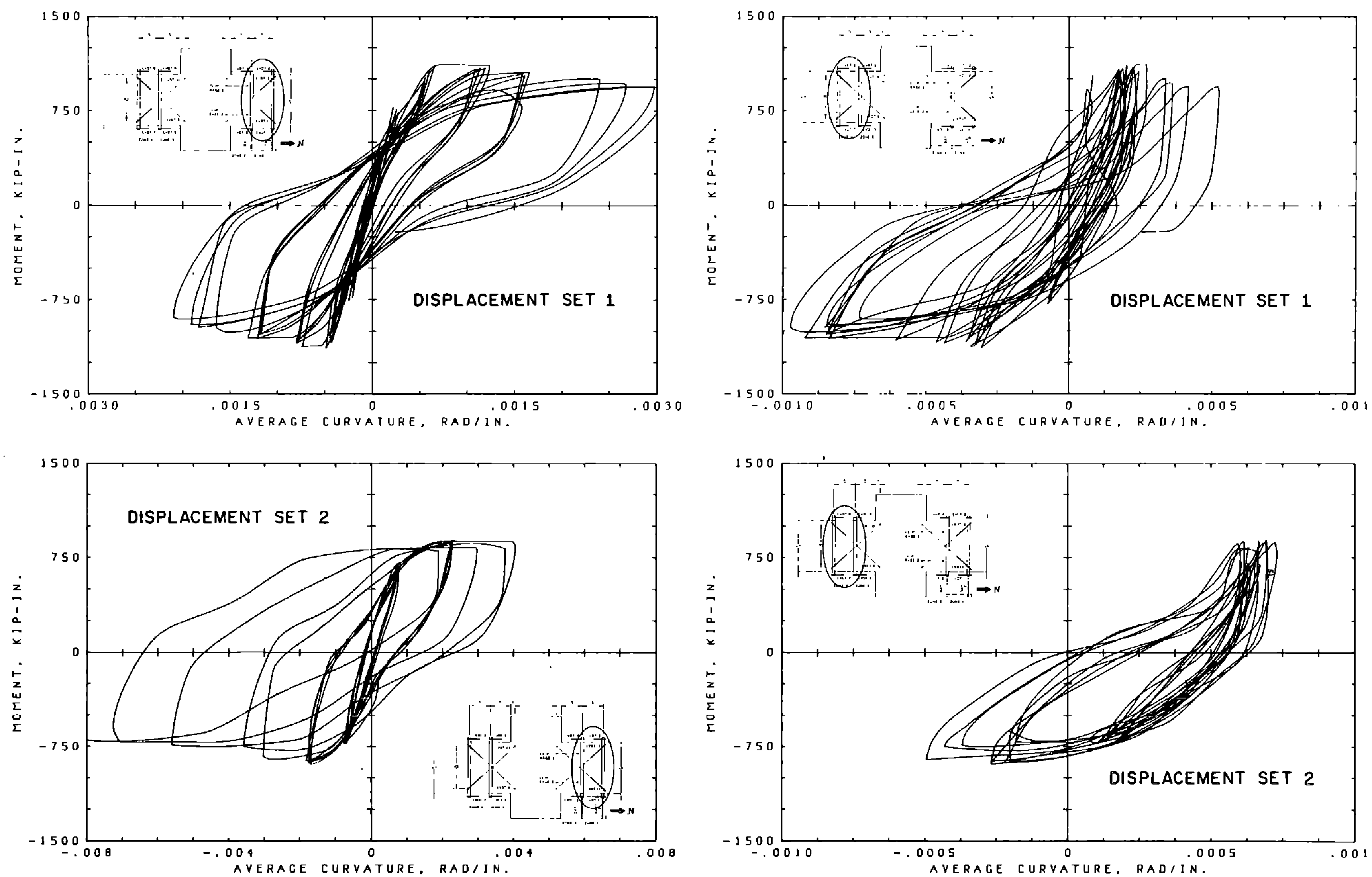

FIG. A.2.h MOMENT-AVERAGE CURVATURE DIAGRAMS, SPECIMEN 8

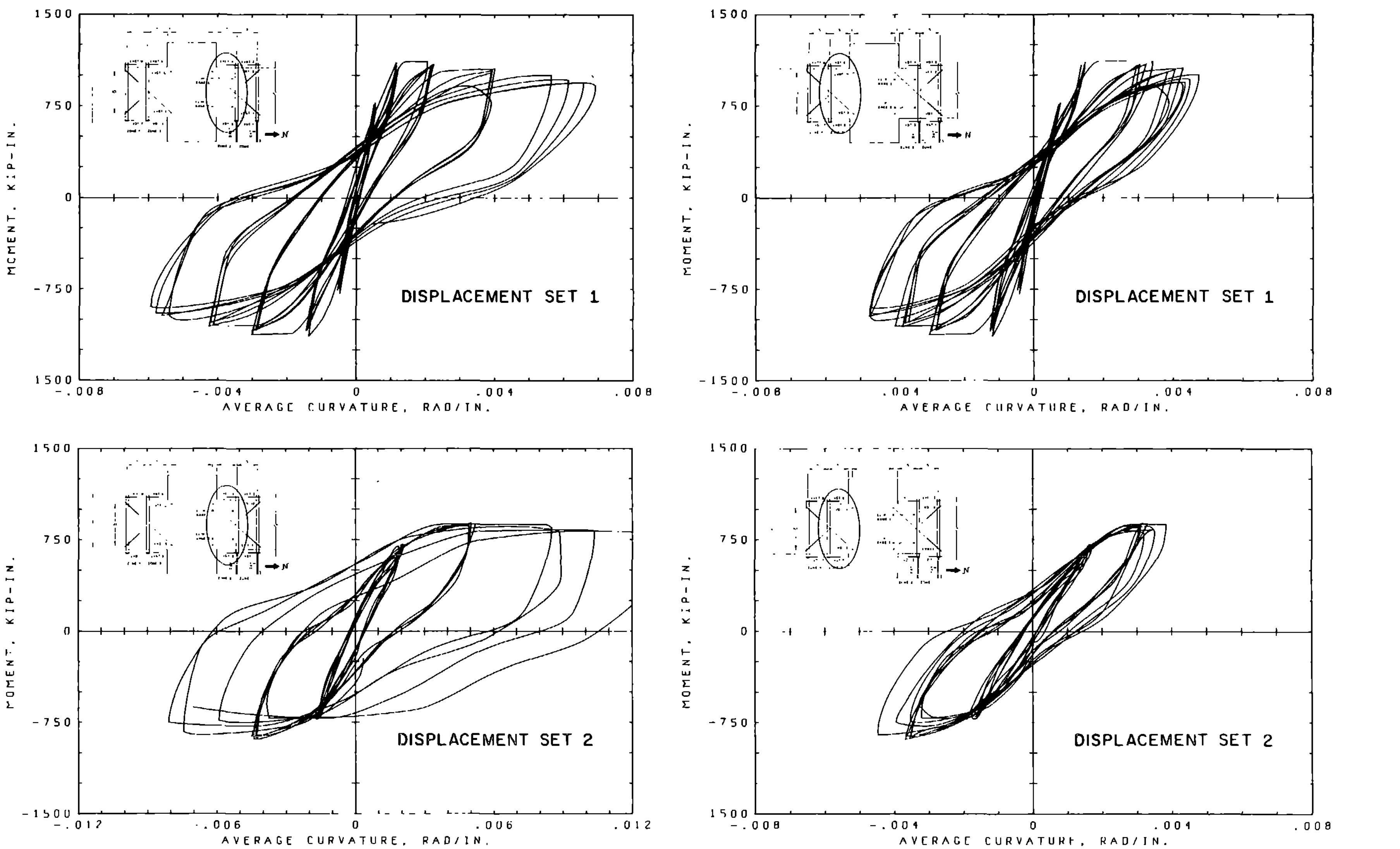

FIG. A.2.h (CONTINUED) MOMENT-LONGITUDINAL REINFORCEMENT STRAIN DIAGRAMS, SPECIMEN 8

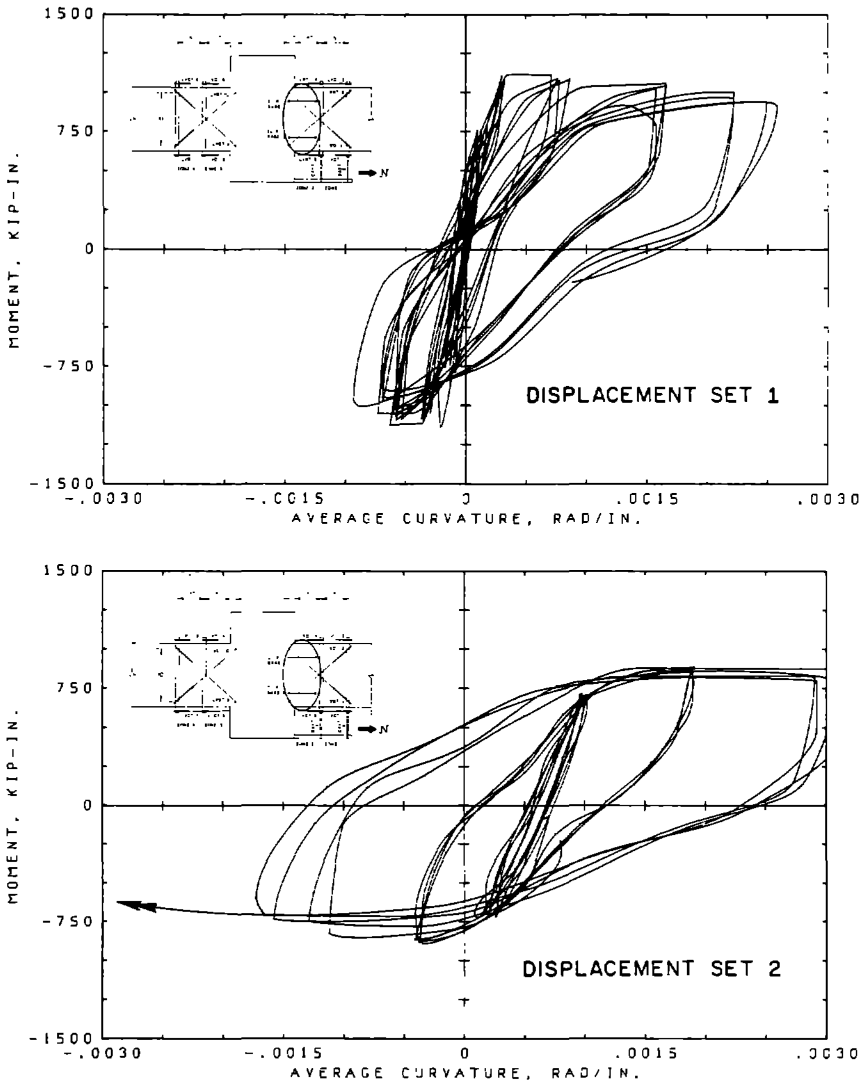

FIG. A.2.h (CONTINUED) MOMENT-LONGITUDINAL REINFORCEMENT STRAIN DIAGRAMS, STRAIN 8

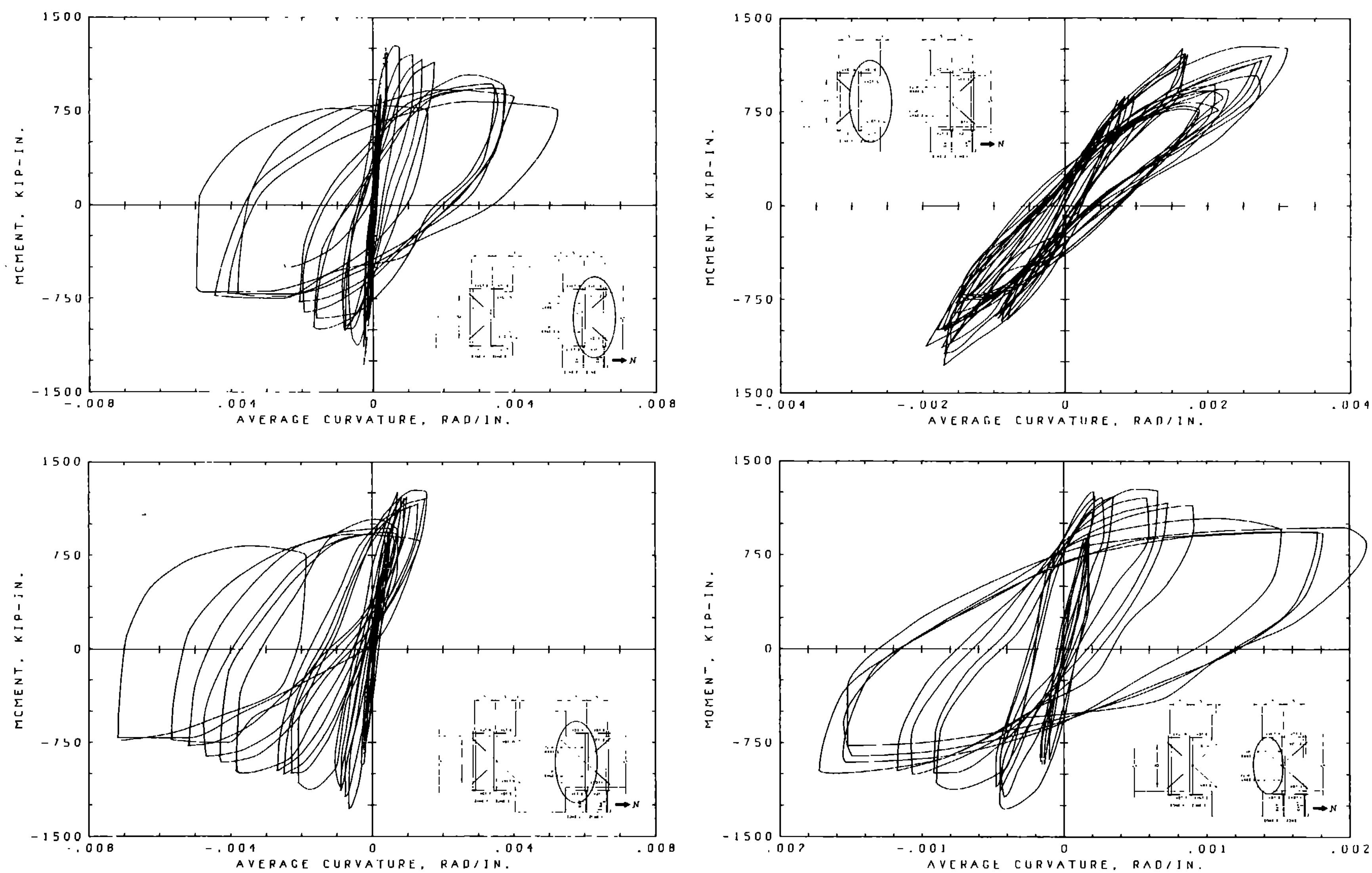

FIG. A.2.i MOMENT-AVERAGE CURVATURE DIAGRAMS, SPECIMEN 9

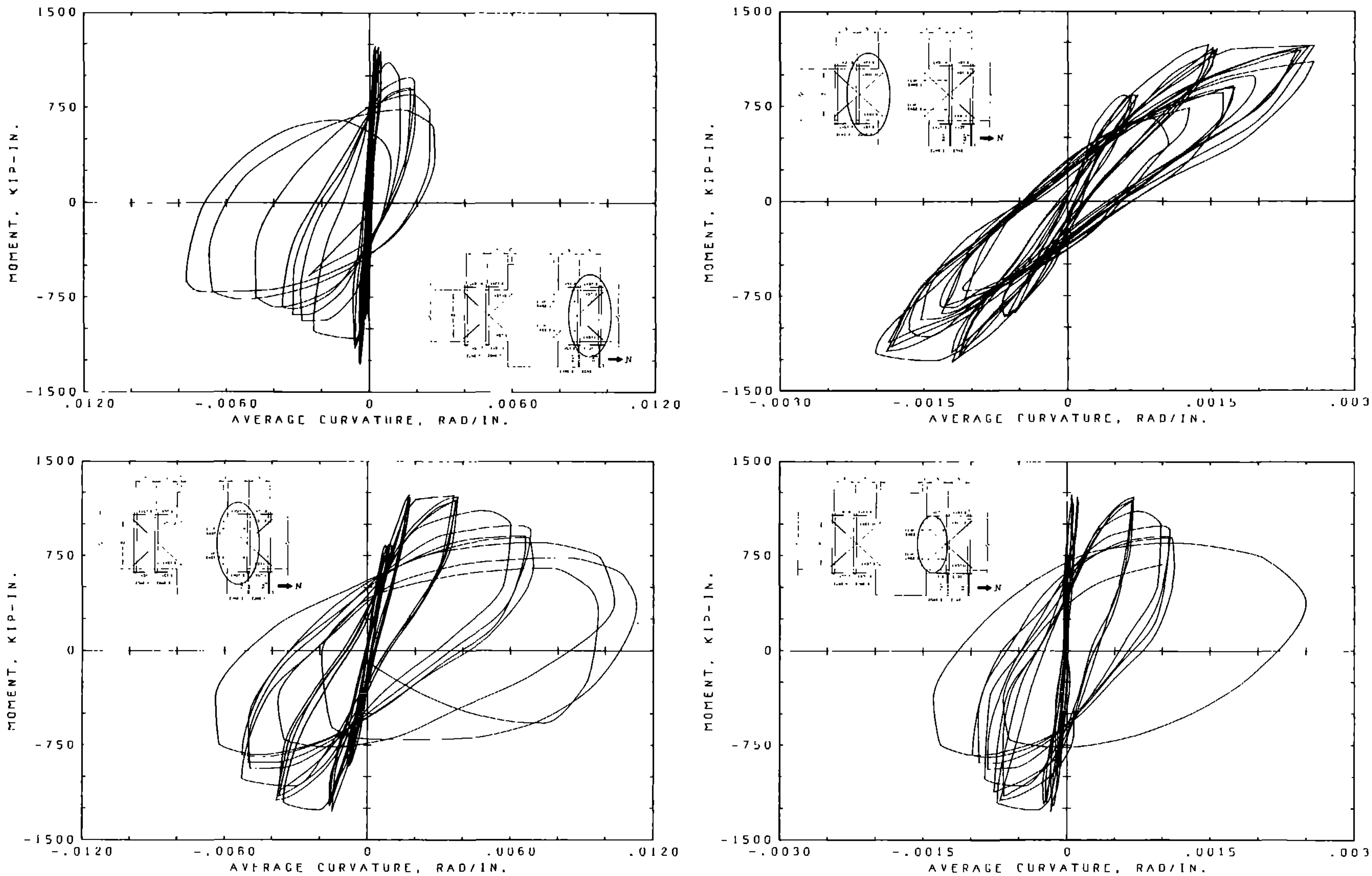

FIG. A.2.j MOMENT-AVERAGE CURVATURE DIAGRAMS, SPECIMEN 10

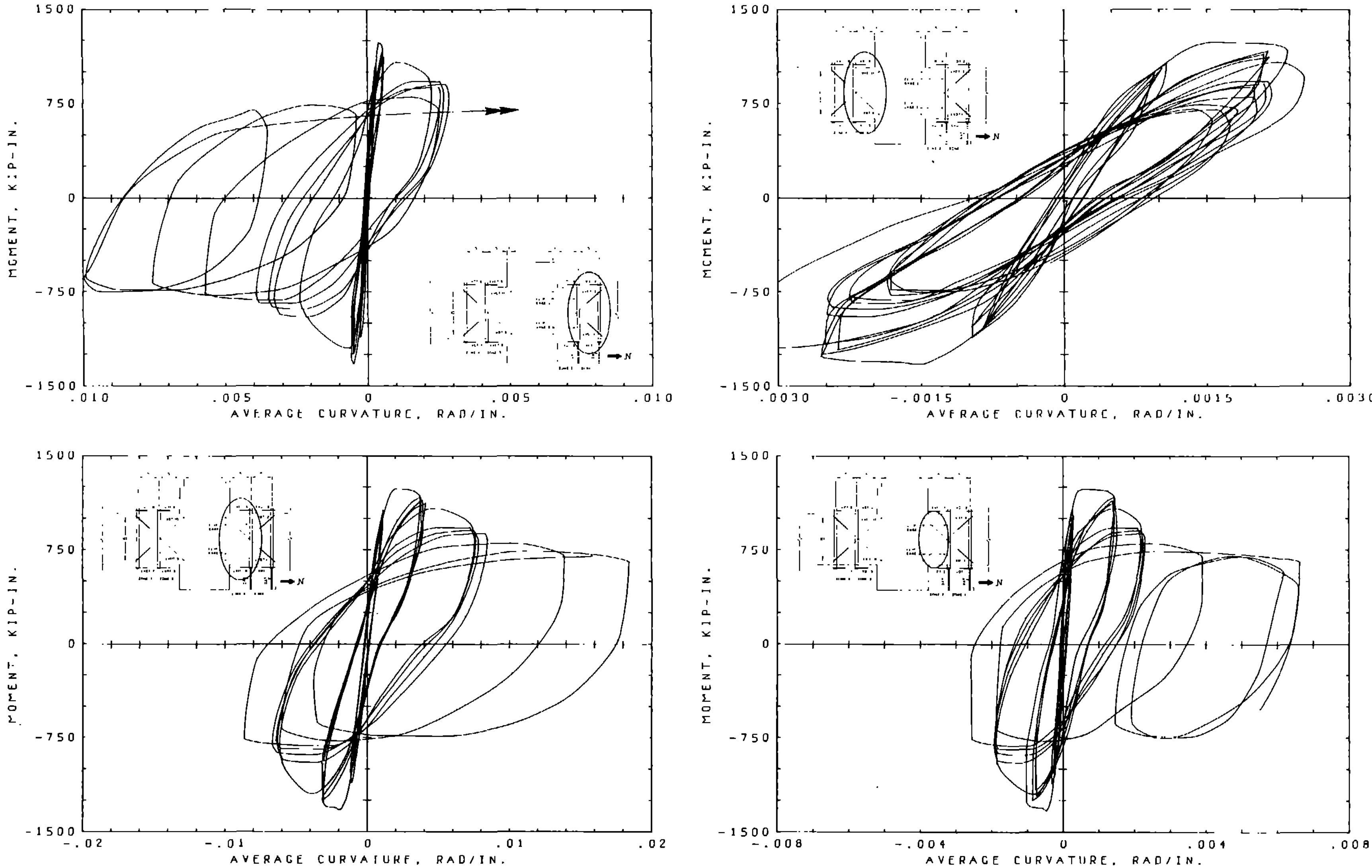

FIG. A.2.k MOMENT-AVERAGE CURVATURE DIAGRAMS, SPECIMEN II

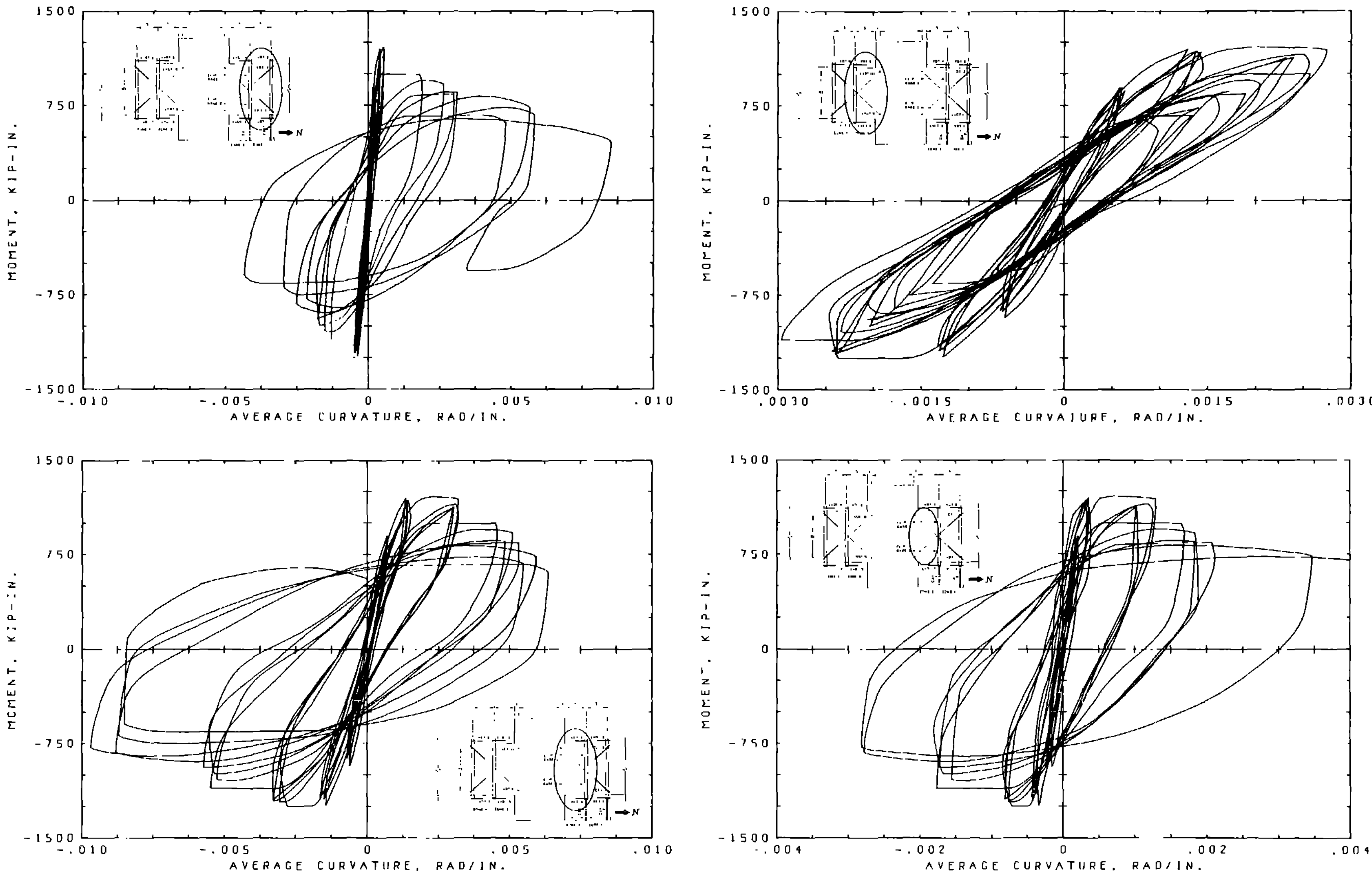

FIG. A.2.ℓ MOMENT-AVERAGE CURVATURE DIAGRAMS, SPECIMEN 12

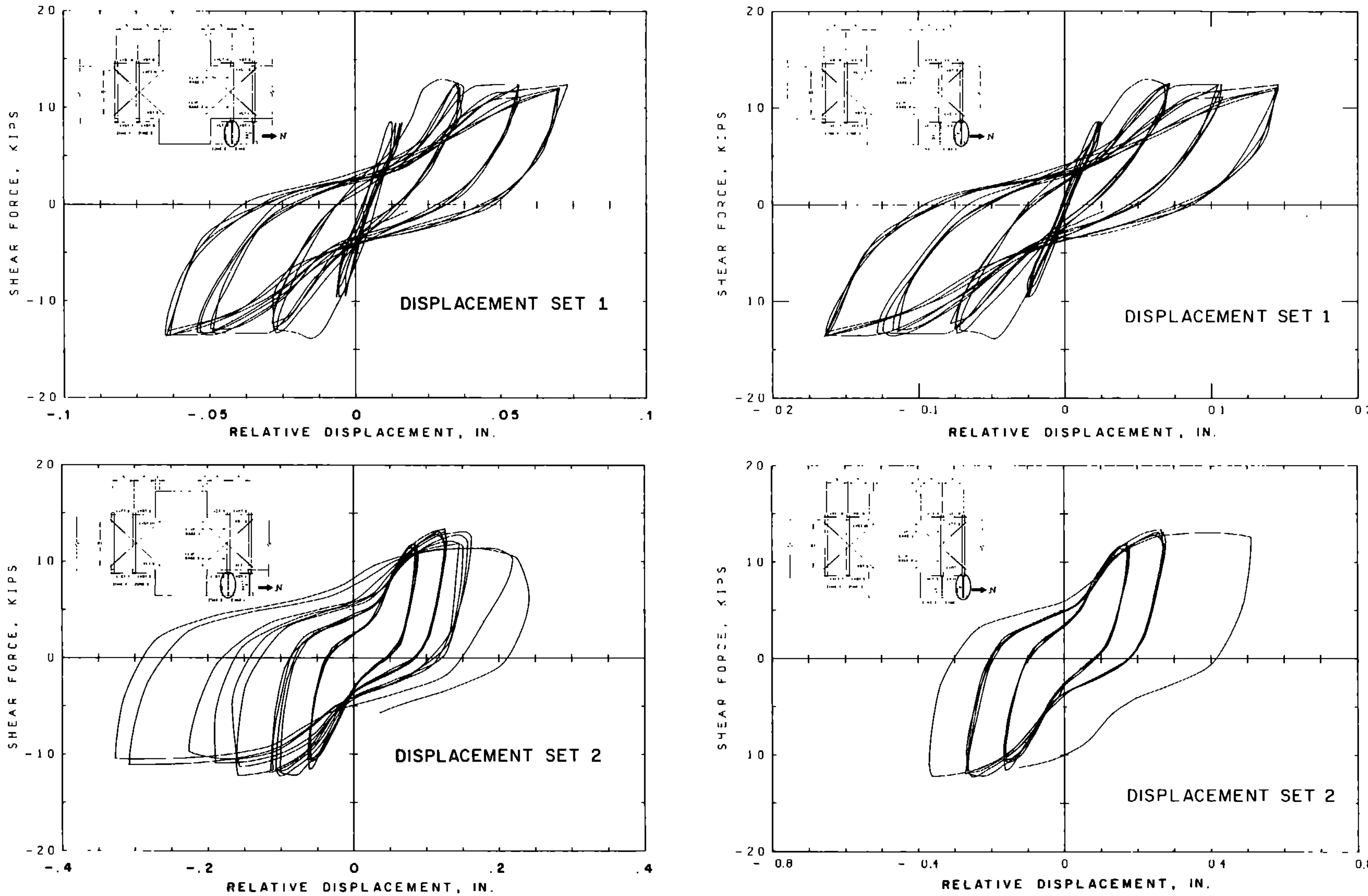

FIG. A.3.a SHEAR FORCE-RELATIVE DISPLACEMENT DIAGRAMS, SPECIMEN 1

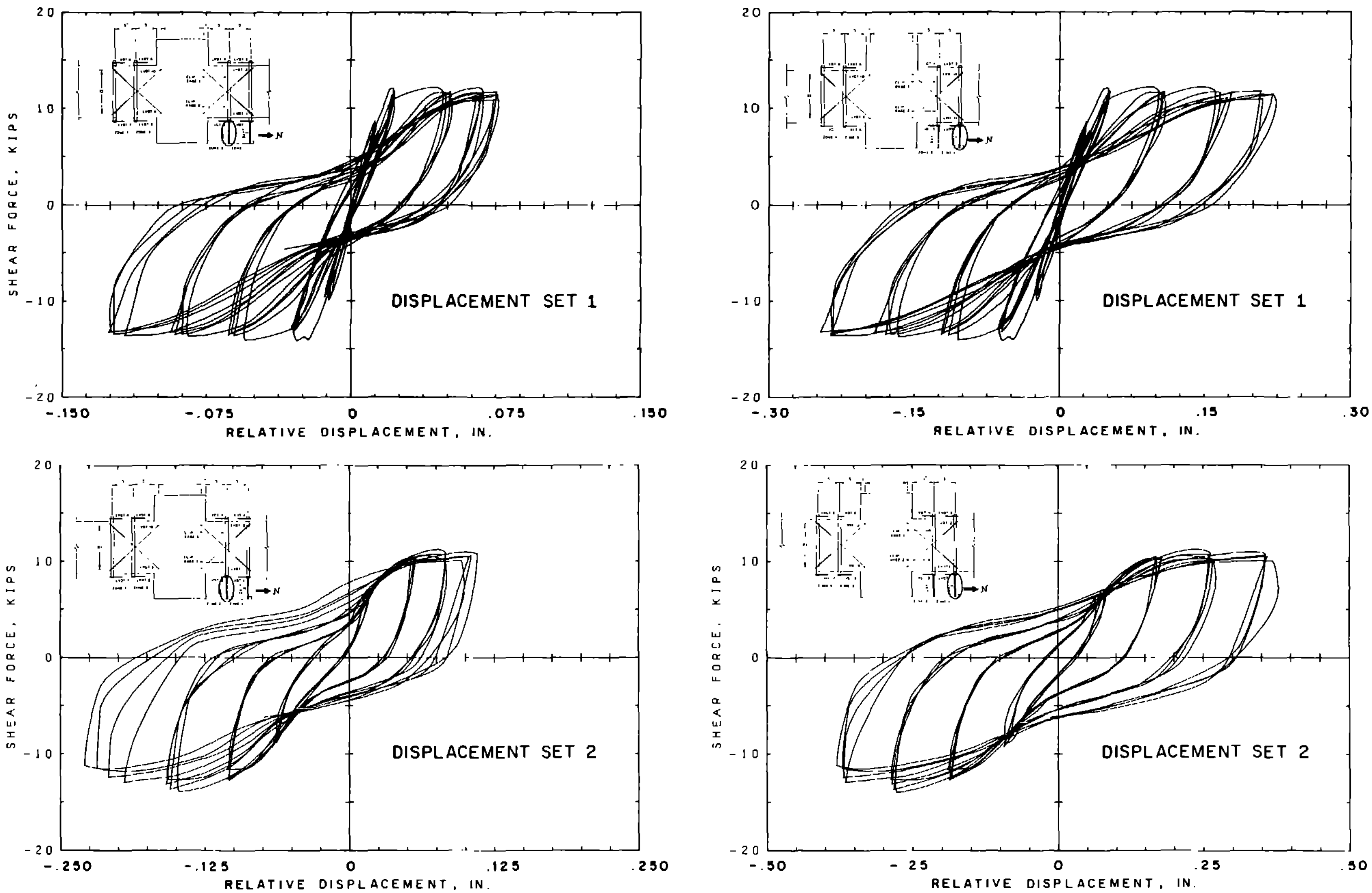

FIG. A.3.b SHEAR FORCE–RELATIVE DISPLACEMENT DIAGRAMS, SPECIMEN 2

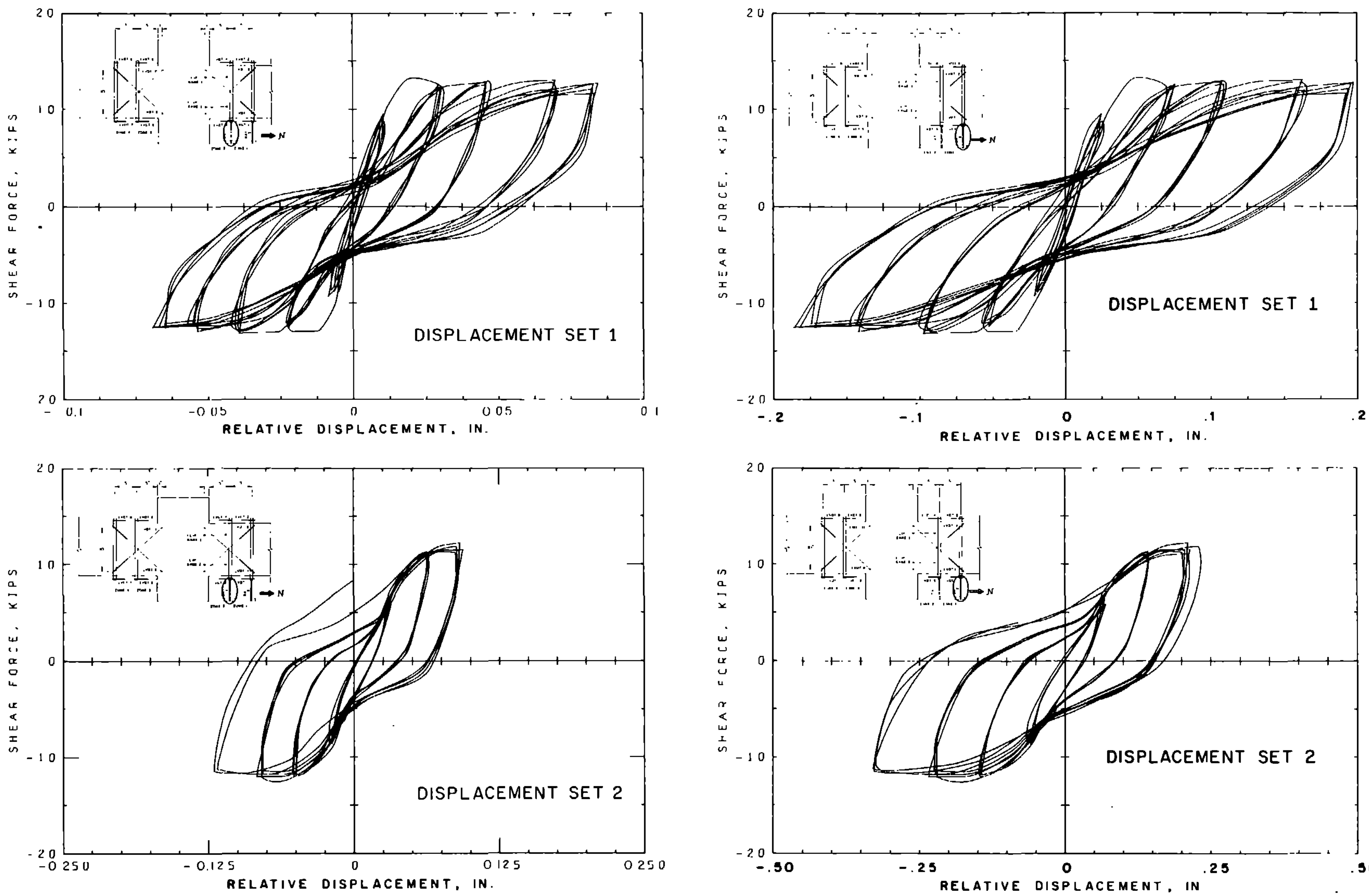

FIG. A.3.c SHEAR FORCE–RELATIVE DISPLACEMENT DIAGRAMS, SPECIMEN 3

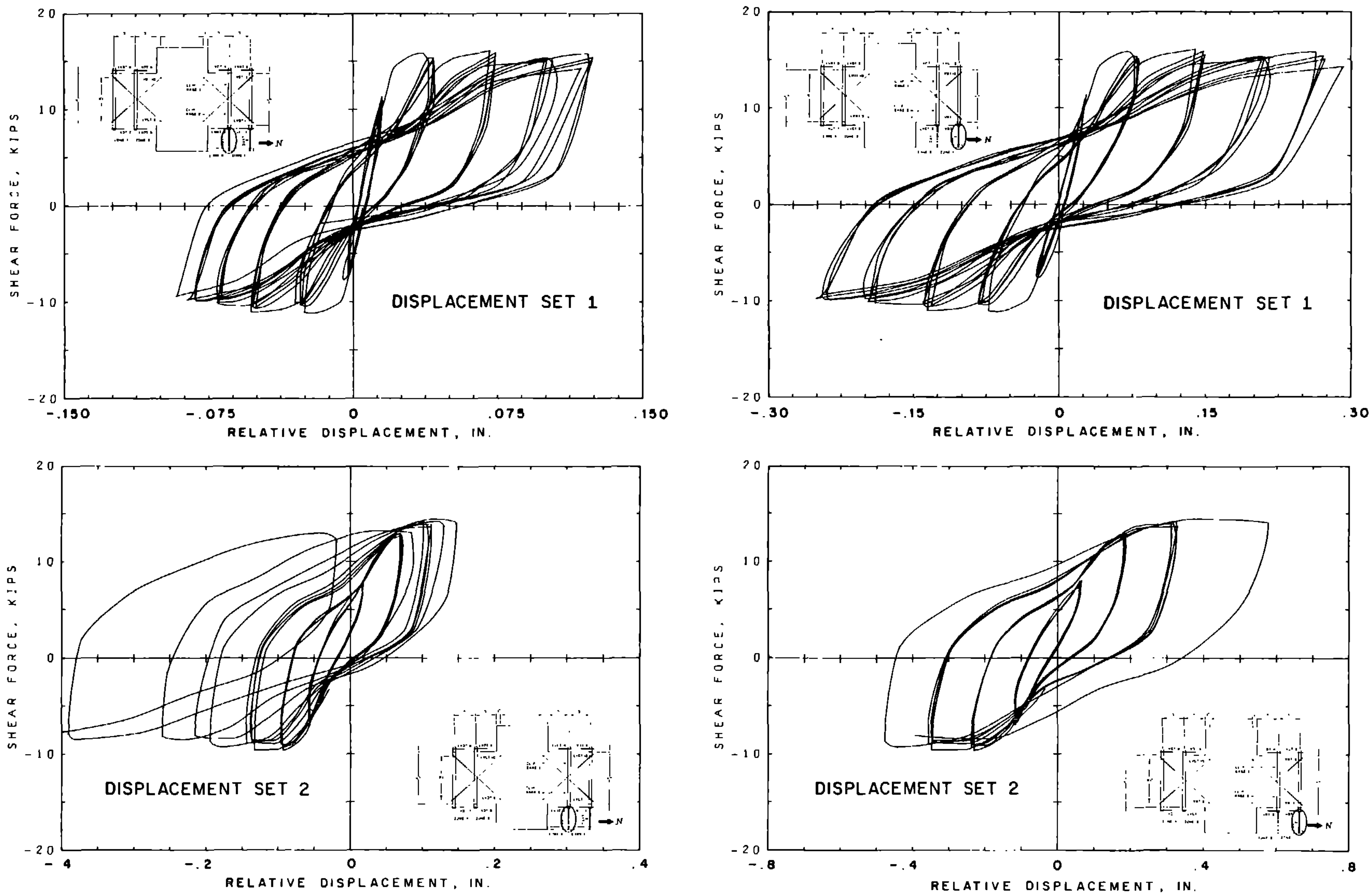

FIG. A.3.d SHEAR FORCE–RELATIVE DISPLACEMENT DIAGRAMS, SPECIMEN 4

DISPLACEMENT SET 1:
NOT AVAILABLE

DISPLACEMENT SET 1:
NOT AVAILABLE

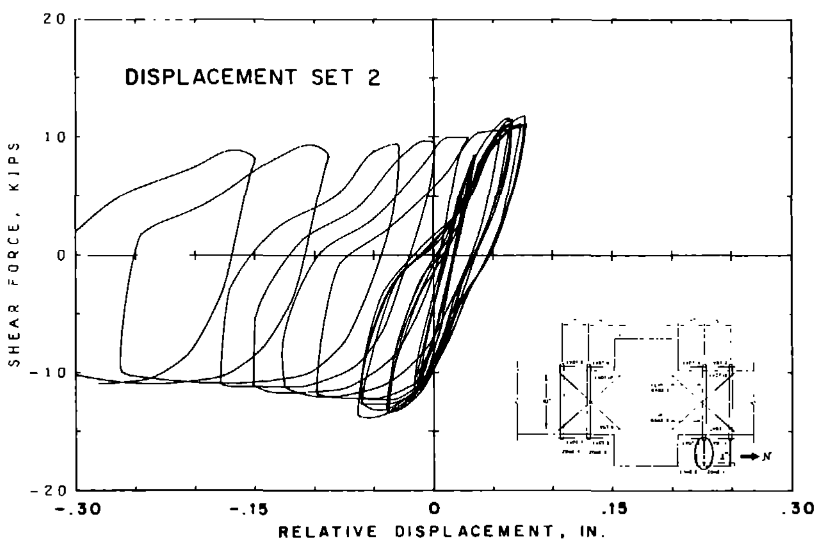

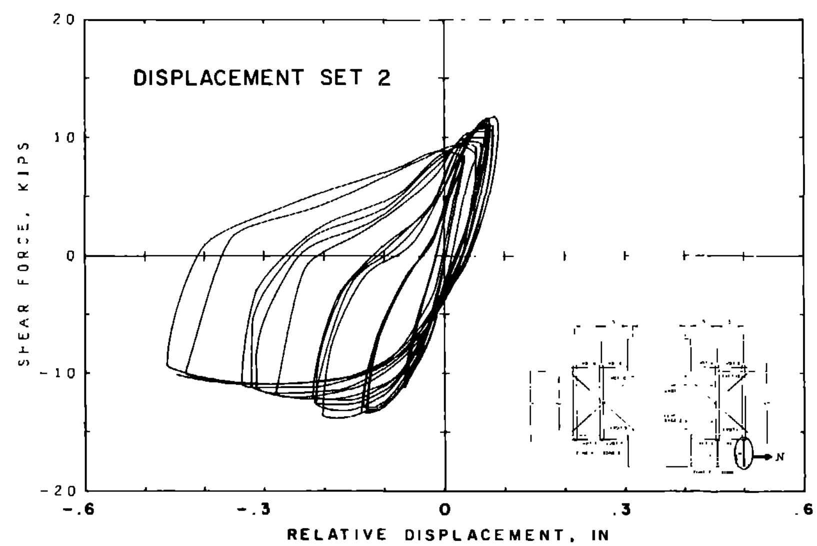

FIG. A.3.e SHEAR FORCE–RELATIVE DISPLACEMENT DIAGRAMS, SPECIMEN 5

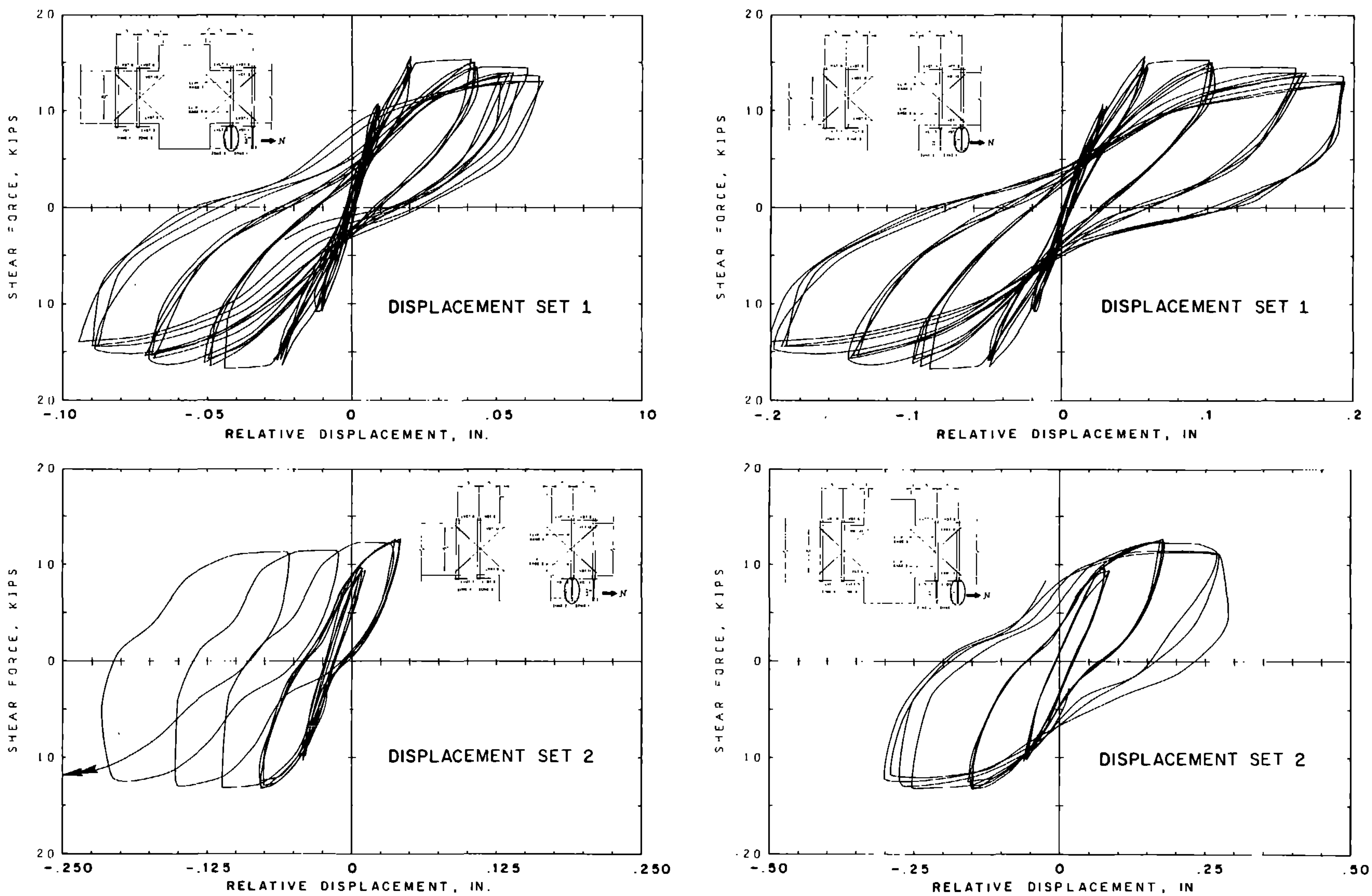

FIG. A.3.f SHEAR FORCE - RELATIVE DISPLACEMENT DIAGRAMS, SPECIMEN 6

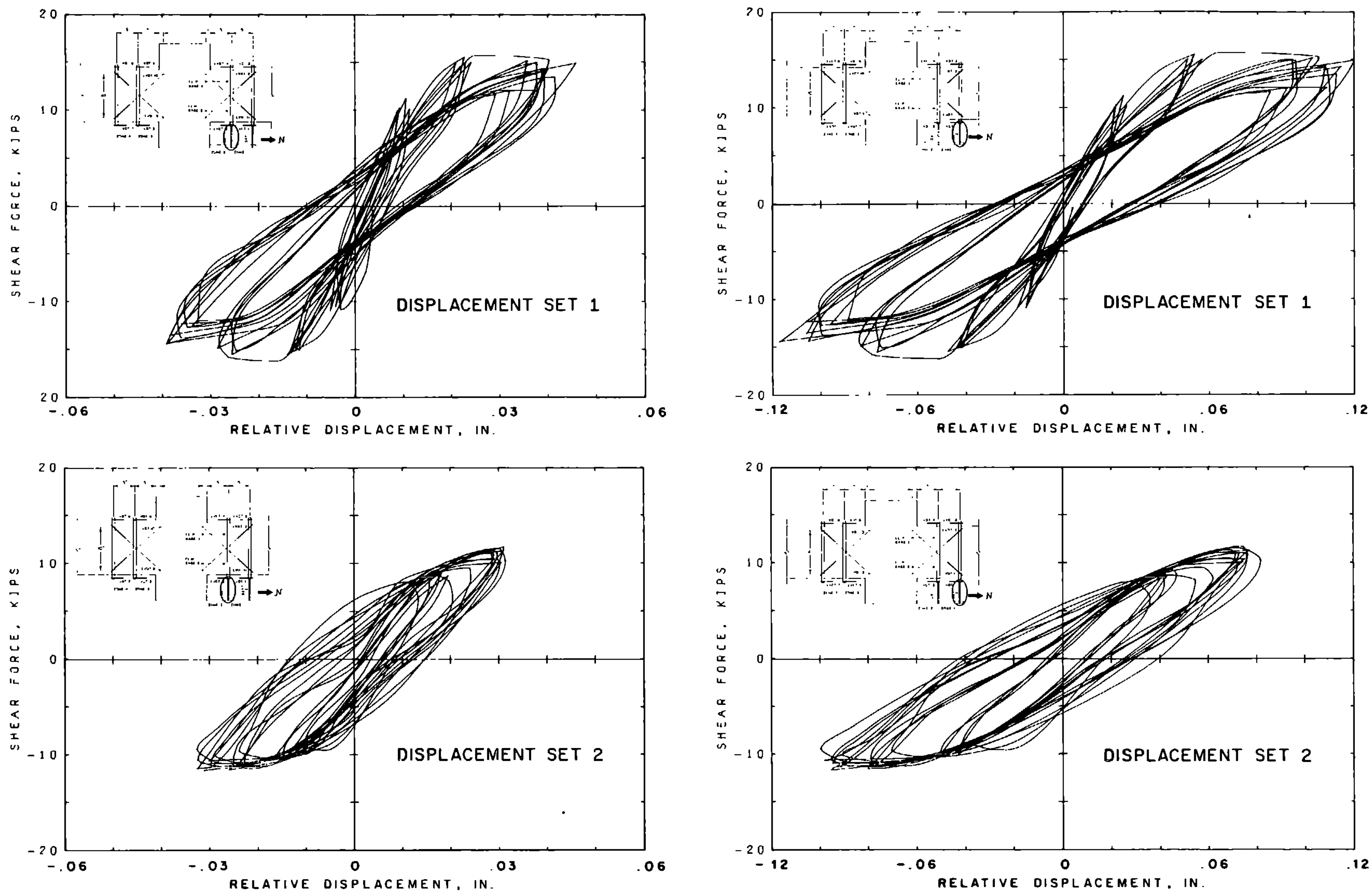

FIG. A.3.g SHEAR FORCE-RELATIVE DISPLACEMENT DIAGRAMS, SPECIMEN 7

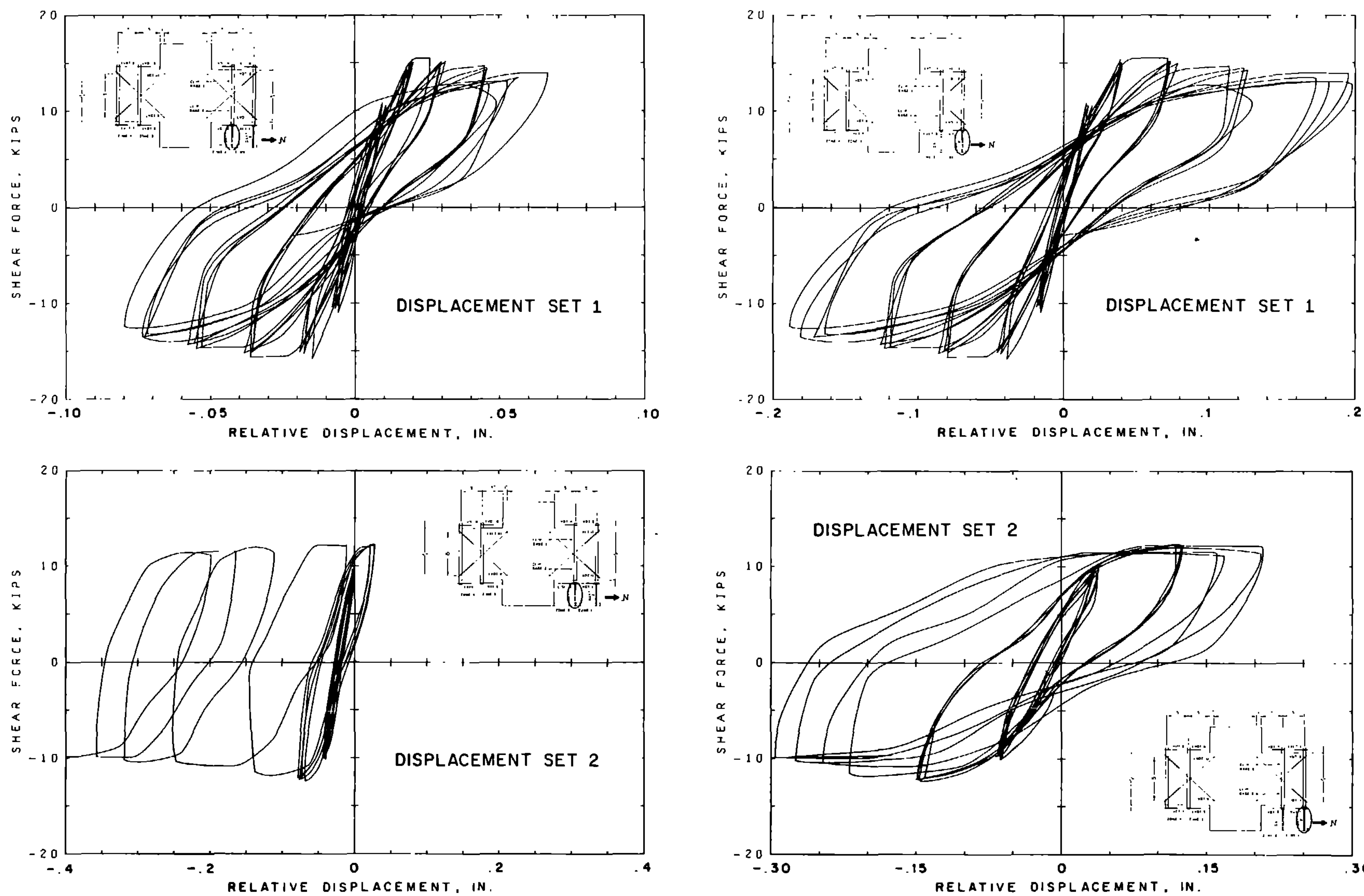

FIG. A.3.h SHEAR FORCE–RELATIVE DISPLACEMENT DIAGRAMS, SPECIMEN 8

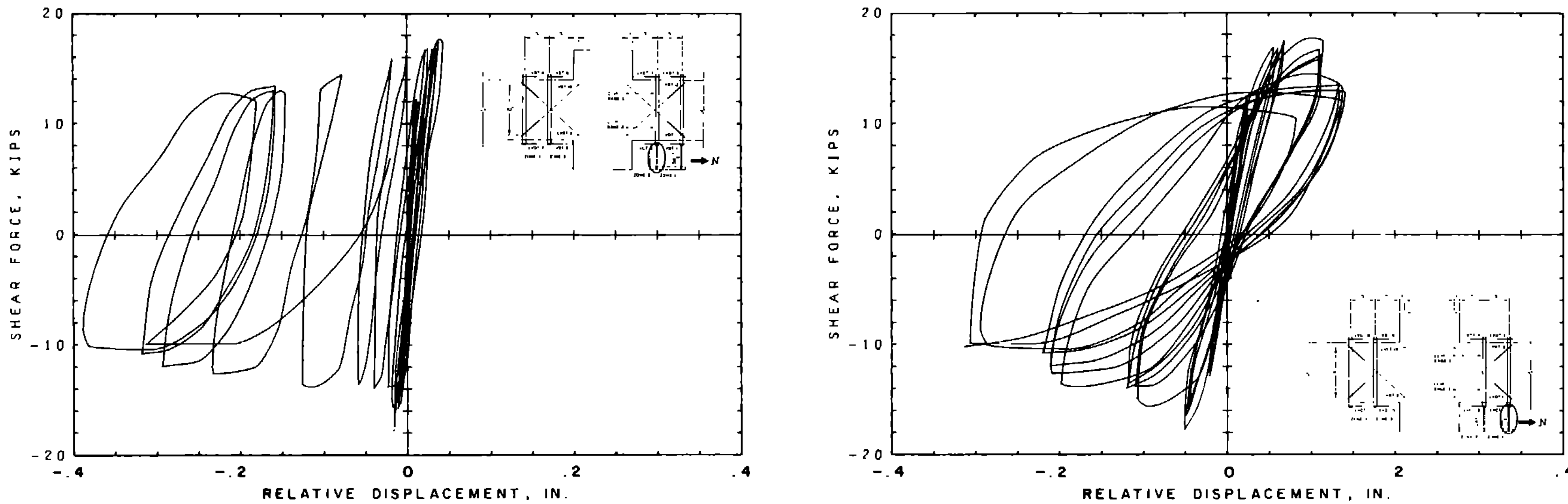

FIG. A.3.i SHEAR FORCE-RELATIVE DISPLACEMENT DIAGRAMS, SPECIMEN 9

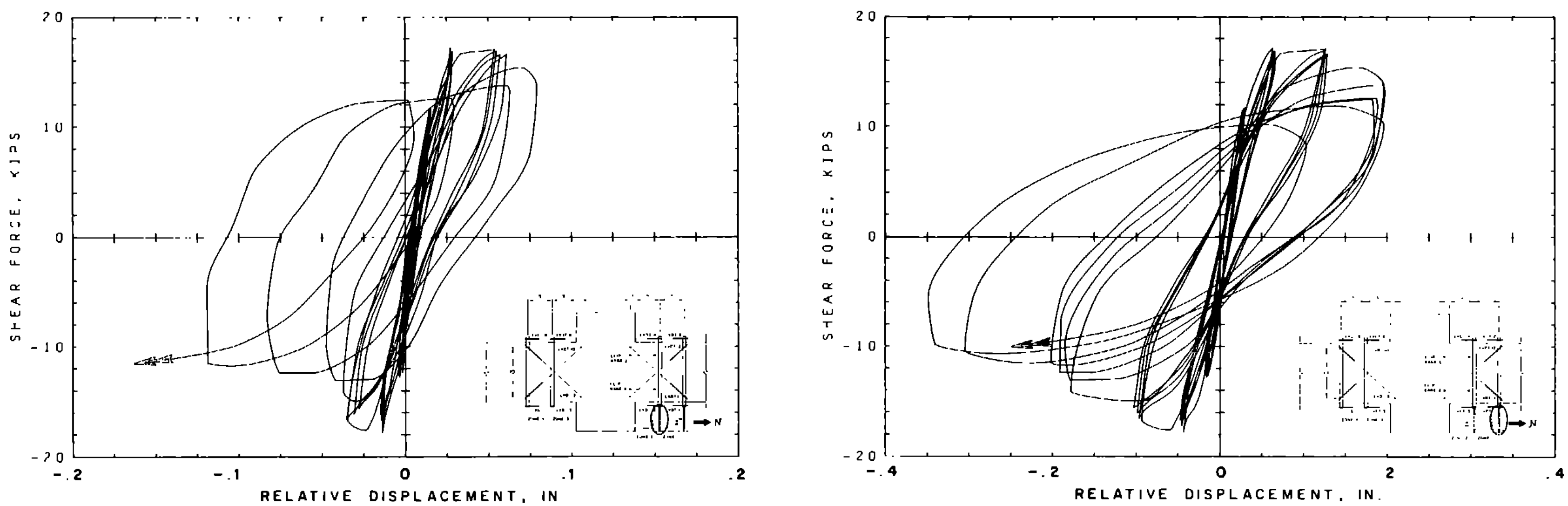

FIG. A.3.j SHEAR FORCE-RELATIVE DISPLACEMENT DIAGRAMS, SPECIMEN 10

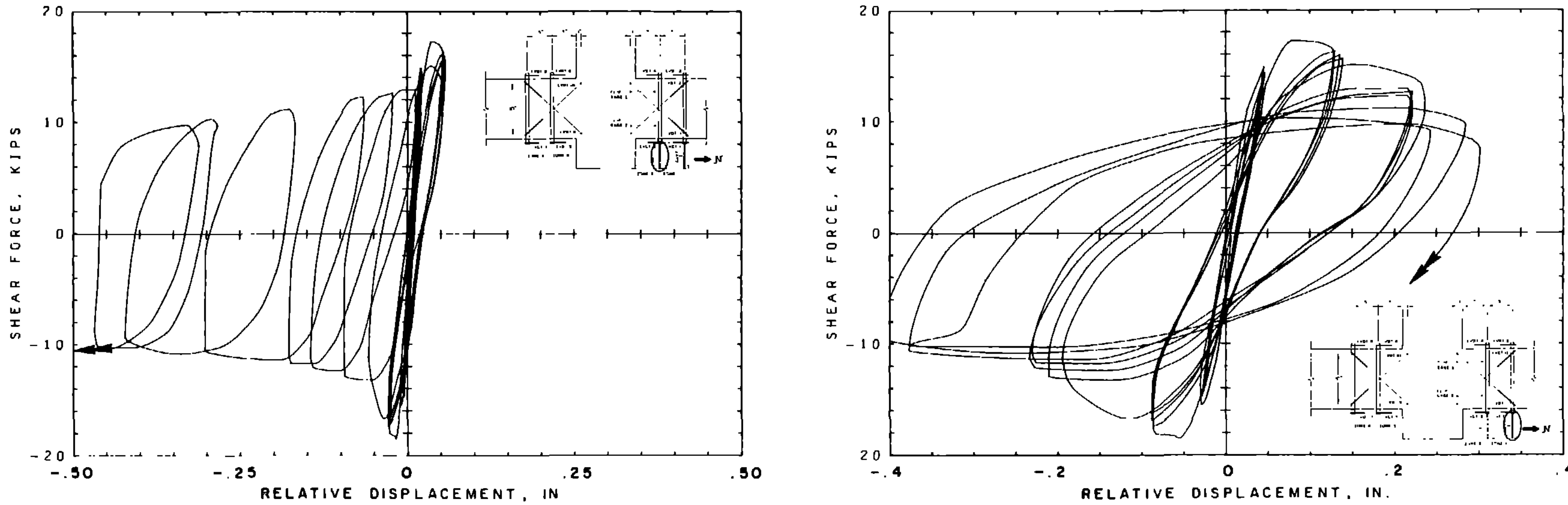

FIG. A.3.k SHEAR FORCE-RELATIVE DISPLACEMENT DIAGRAMS, SPECIMEN 11

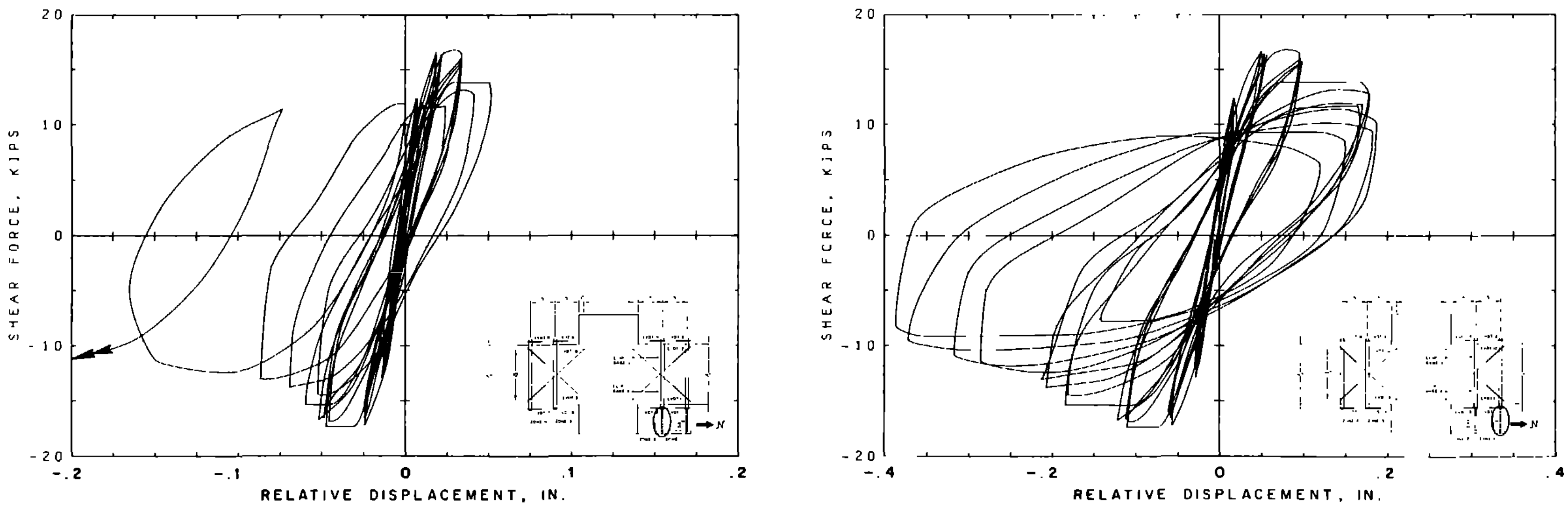

FIG. A.3.ℓ SHEAR FORCE-RELATIVE DISPLACEMENT DIAGRAMS, SPECIMEN 12

V vs. γ NORTH,
DISPLACEMENT SET 1:
NOT AVAILABLE

V vs. γ SOUTH,
DISPLACEMENT SET 1:
NOT AVAILABLE

V vs. γ NORTH,
DISPLACEMENT SET 2:
NOT AVAILABLE

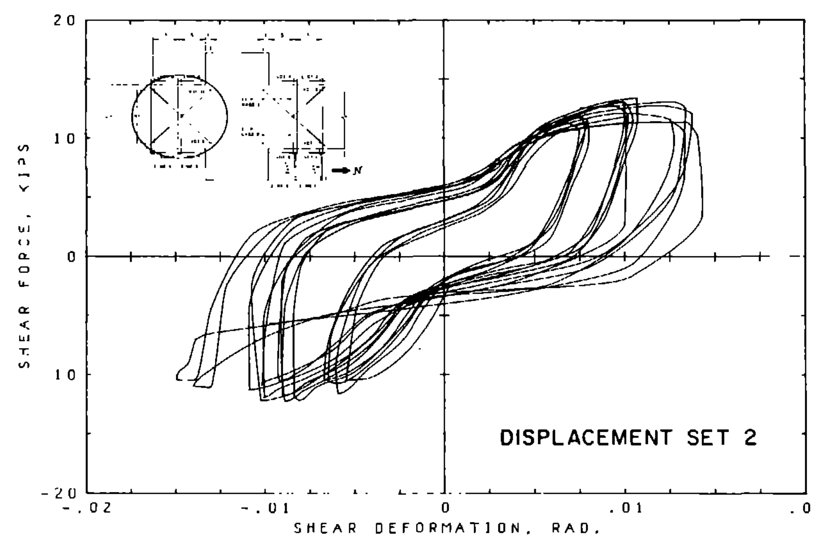

FIG. A.4.a SHEAR FORCE – SHEAR DEFORMATION DIAGRAMS, SPECIMEN 1

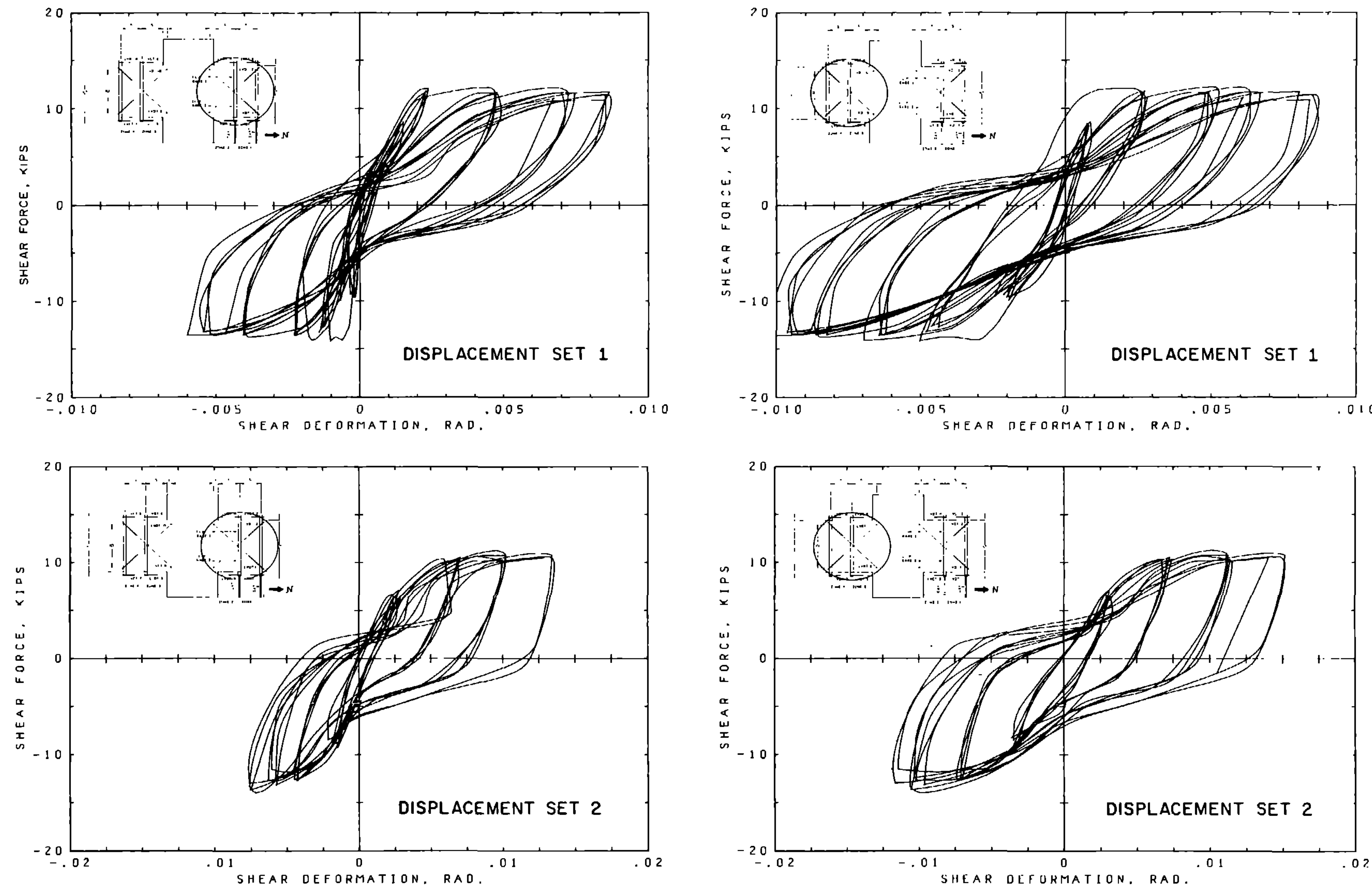

FIG. A.4.b SHEAR FORCE – SHEAR DEFORMATION DIAGRAMS, SPECIMEN 2

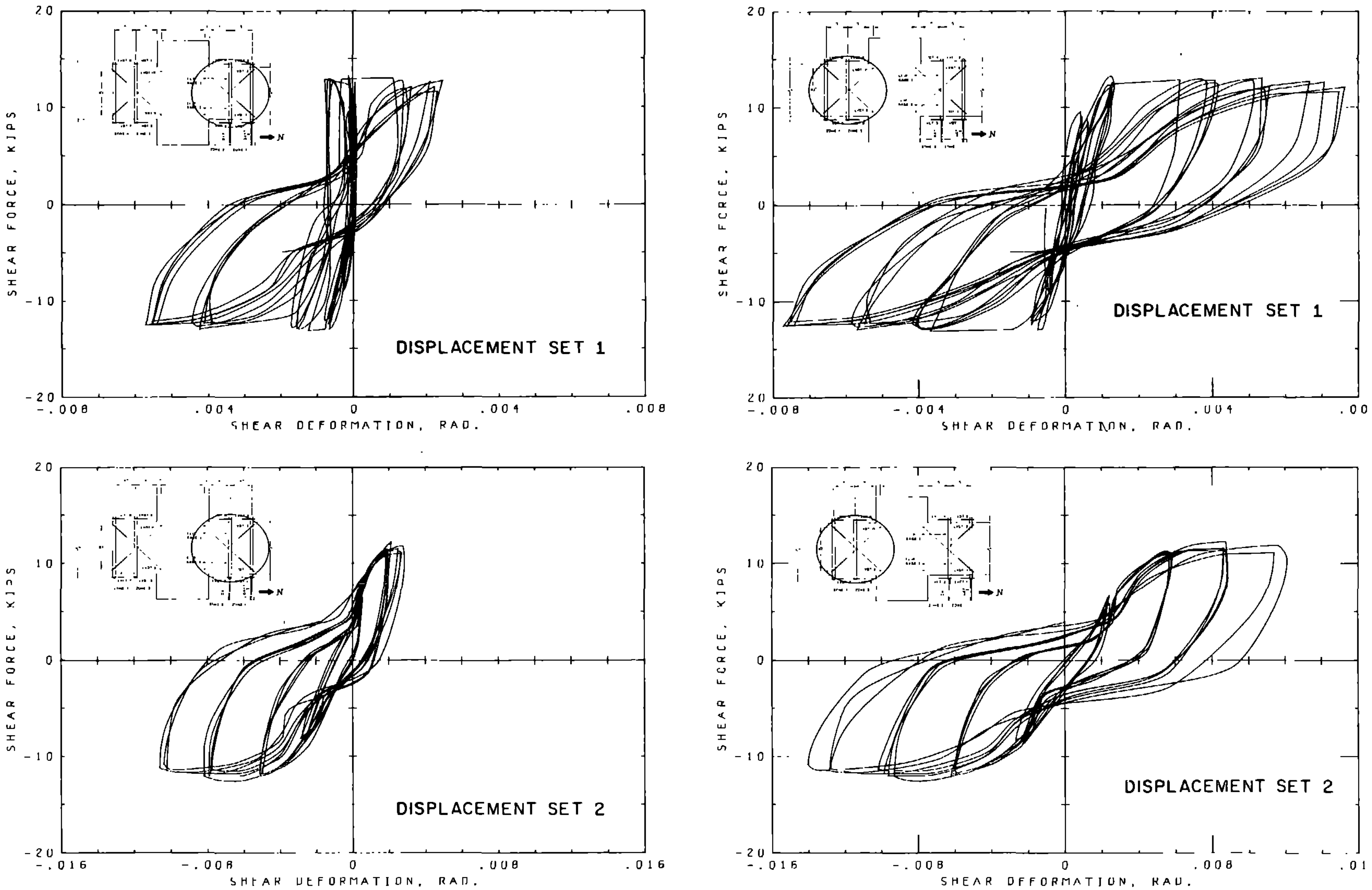

FIG. A.4.c SHEAR FORCE-SHEAR DEFORMATION DIAGRAMS, SPECIMEN 3

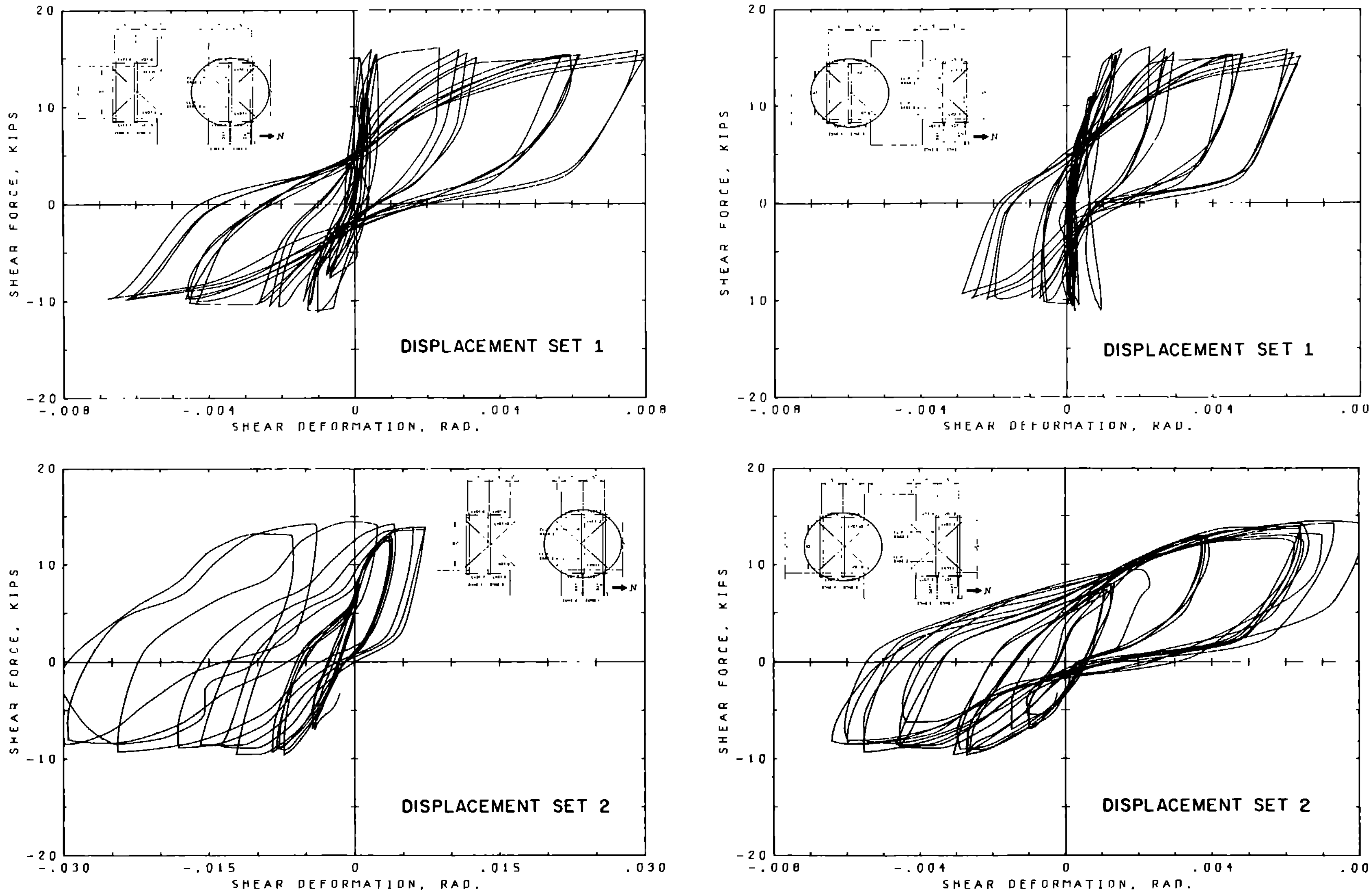

FIG. A.4.d SHEAR FORCE – SHEAR DEFORMATION DIAGRAMS, SPECIMEN 4

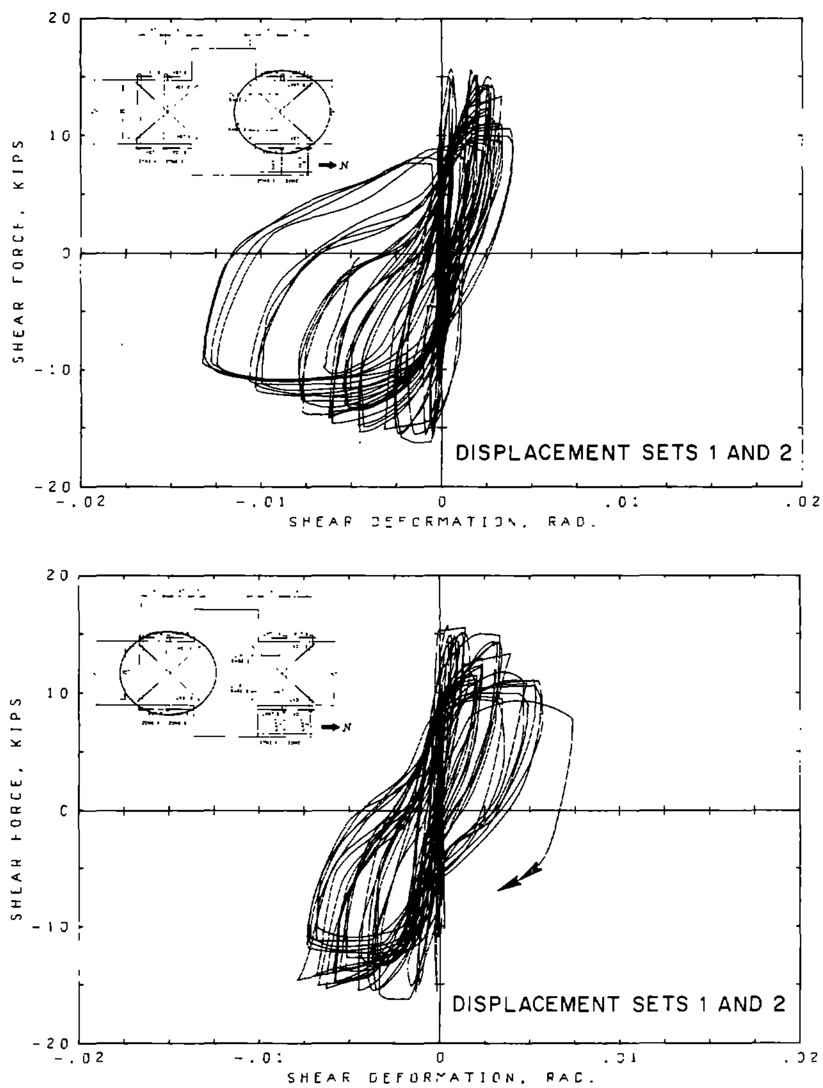

FIG. A.4.e SHEAR FORCE – SHEAR DEFORMATION DIAGRAMS, SPECIMEN 5

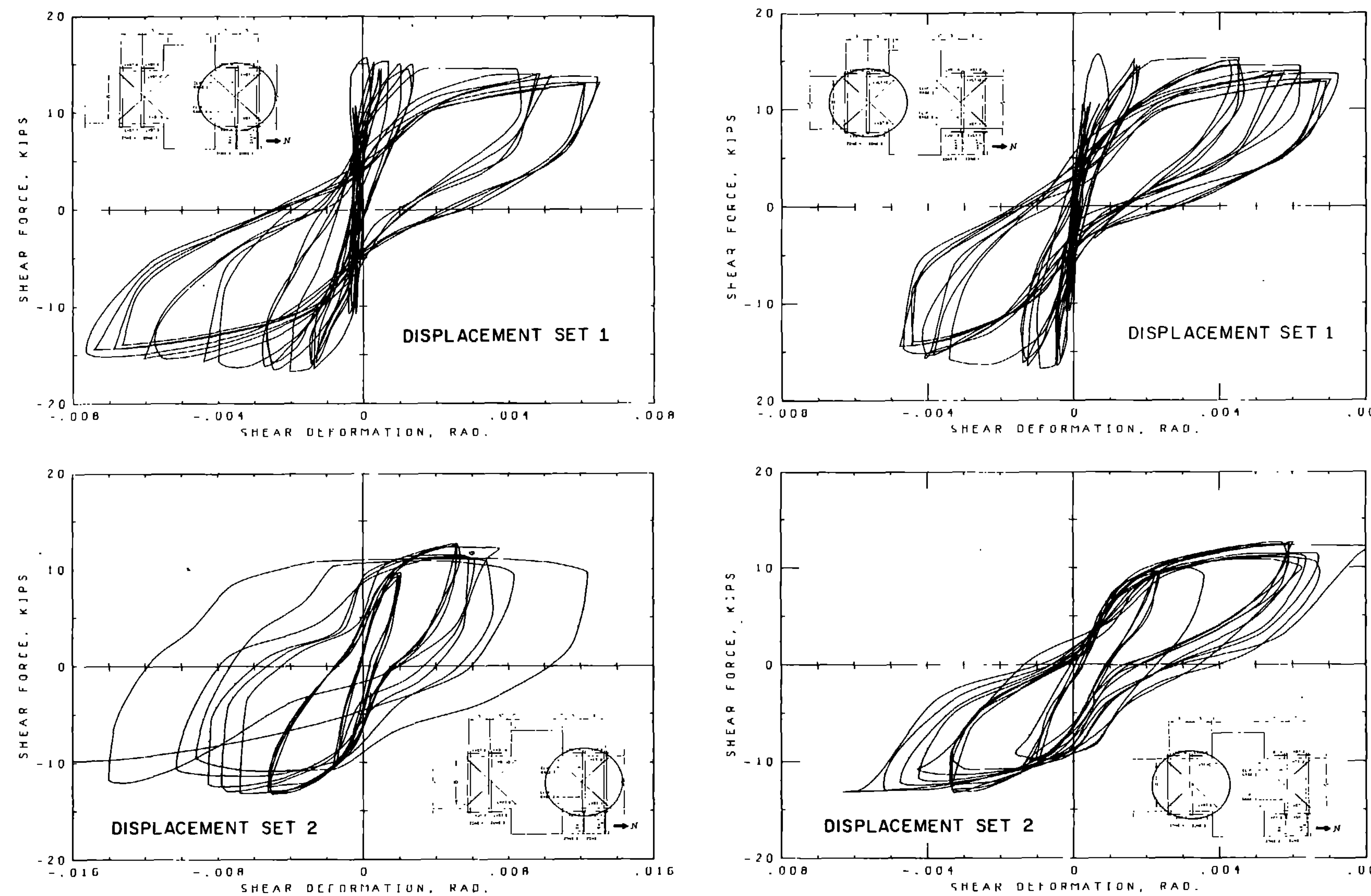

FIG. A.4.f SHEAR FORCE-SHEAR DEFORMATION DIAGRAMS, SPECIMEN 6

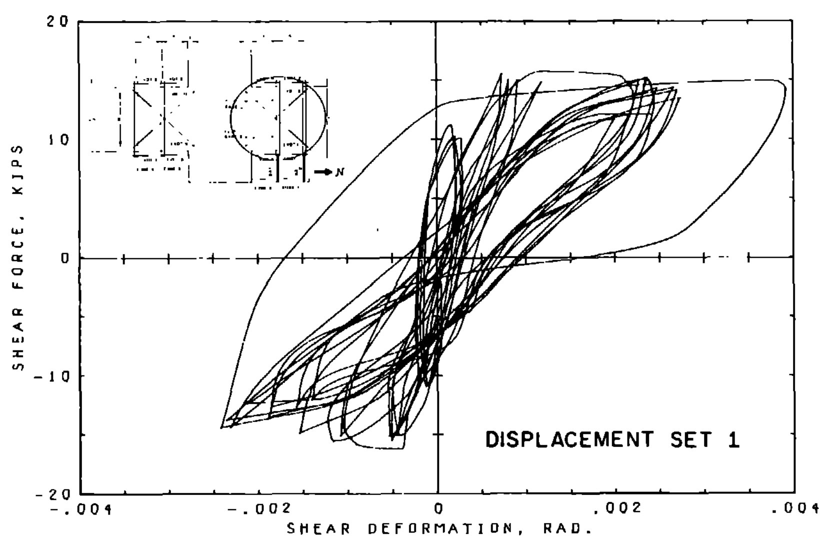

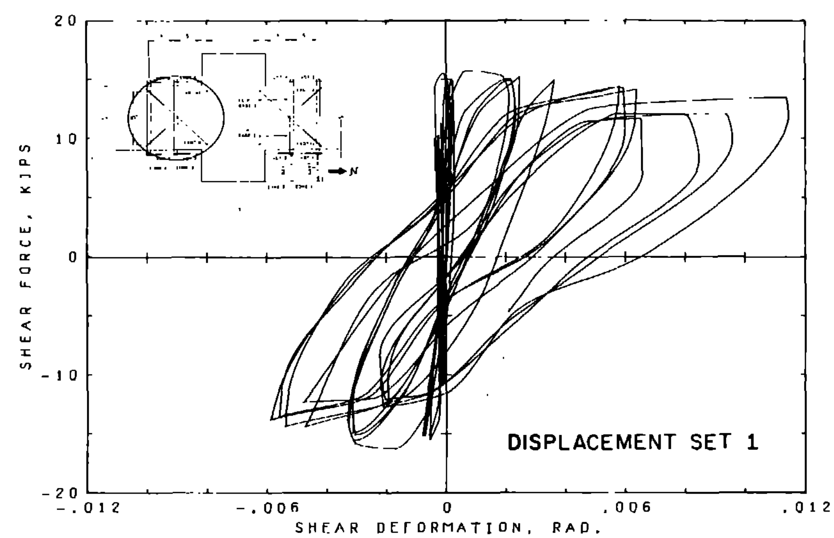

V vs. γ NORTH
DISPLACEMENT SET 2:
NOT AVAILABLE

V vs. γ SOUTH,
DISPLACEMENT SET 2:
NOT AVAILABLE

FIG. A.4.g SHEAR FORCE-SHEAR DEFORMATION DIAGRAMS, SPECIMEN 7

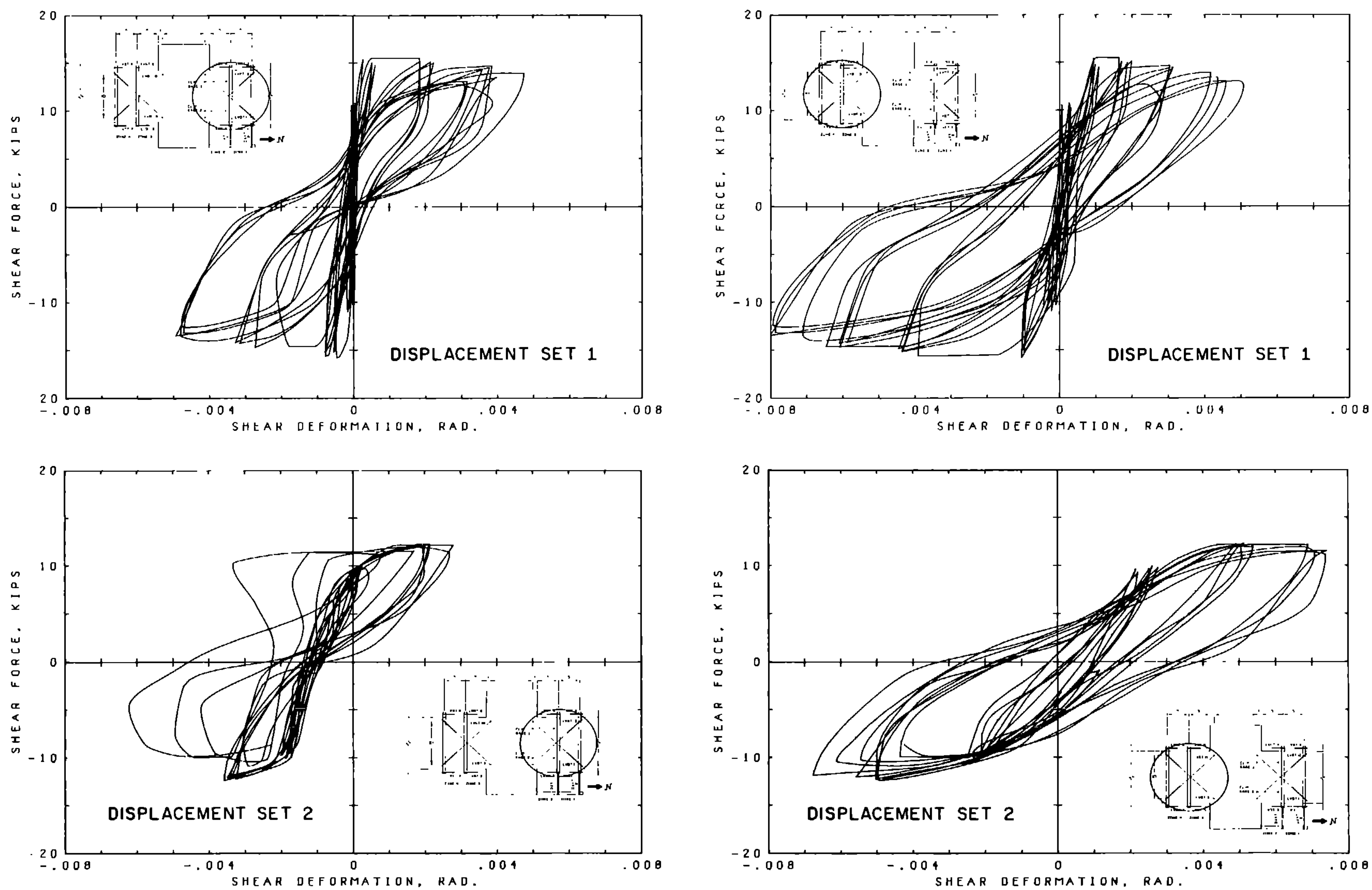

FIG. A.4.h SHEAR FORCE – SHEAR DEFORMATION DIAGRAMS, SPECIMEN 8

V vs. γ NORTH
NOT AVAILABLE

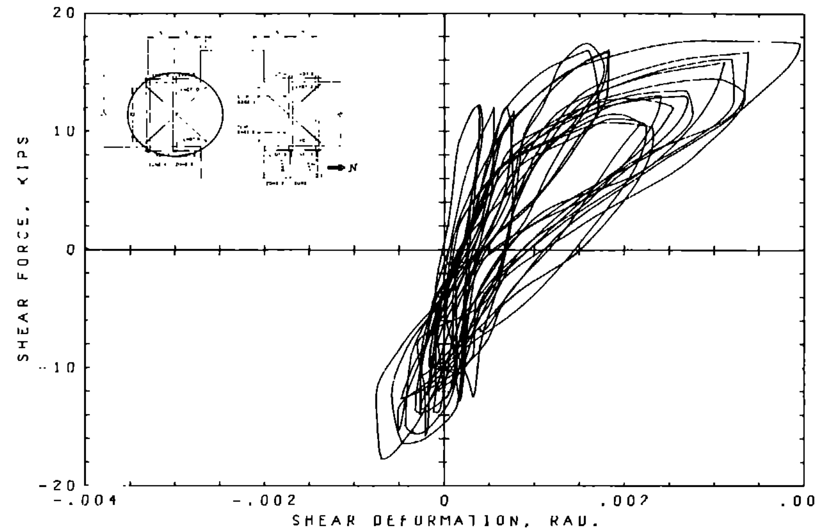

FIG. A.4.i SHEAR FORCE – SHEAR DEFORMATION DIAGRAMS, SPECIMEN 9

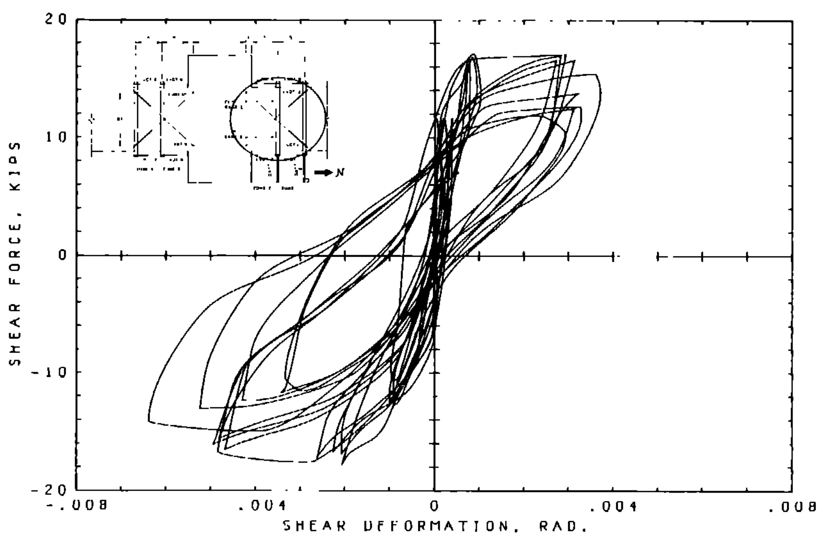

V vs. γ SOUTH
NOT AVAILABLE

FIG. A.4.j SHEAR FORCE – SHEAR DEFORMATION DIAGRAMS, SPECIMEN 10

V vs. γ NORTH
NOT AVAILABLE

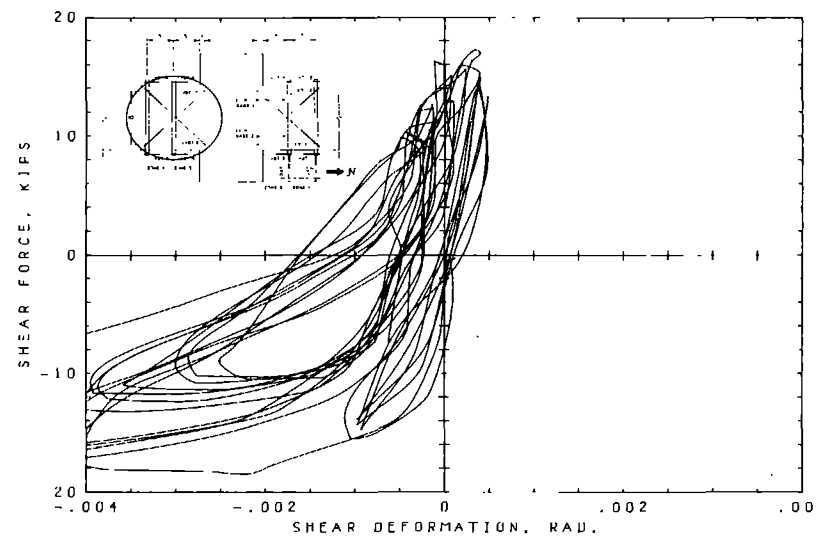

FIG. A.4.k SHEAR FORCE – SHEAR DEFORMATION DIAGRAMS, SPECIMEN 11

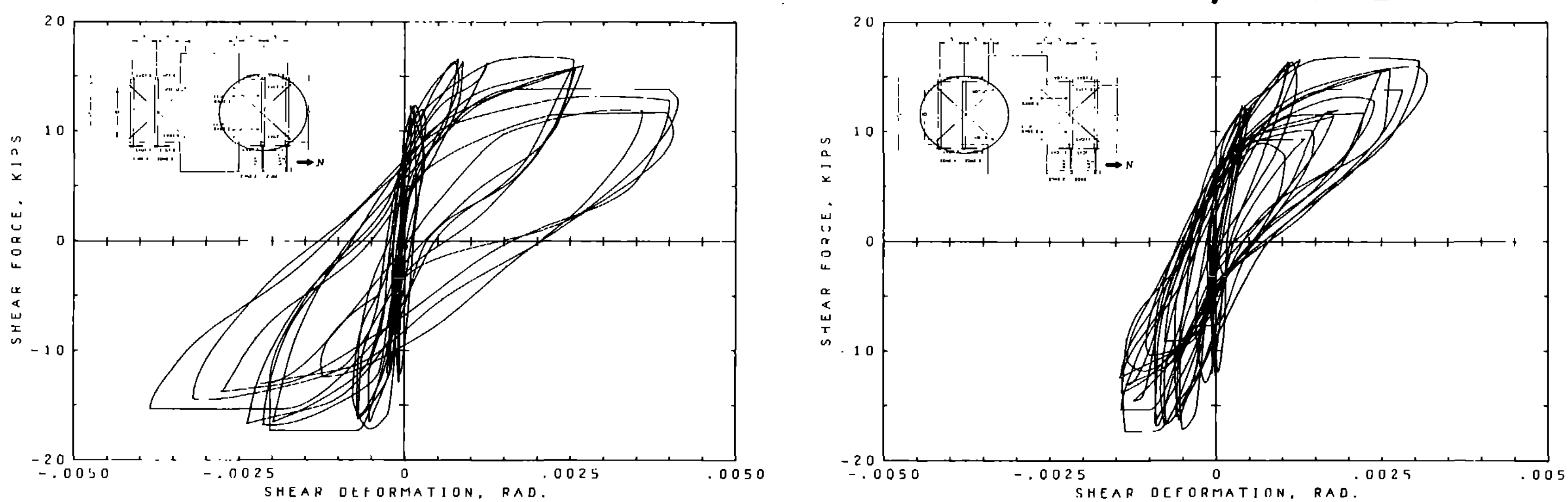

FIG. A.4.ℓ SHEAR FORCE – SHEAR DEFORMATION DIAGRAMS, SPECIMEN 12

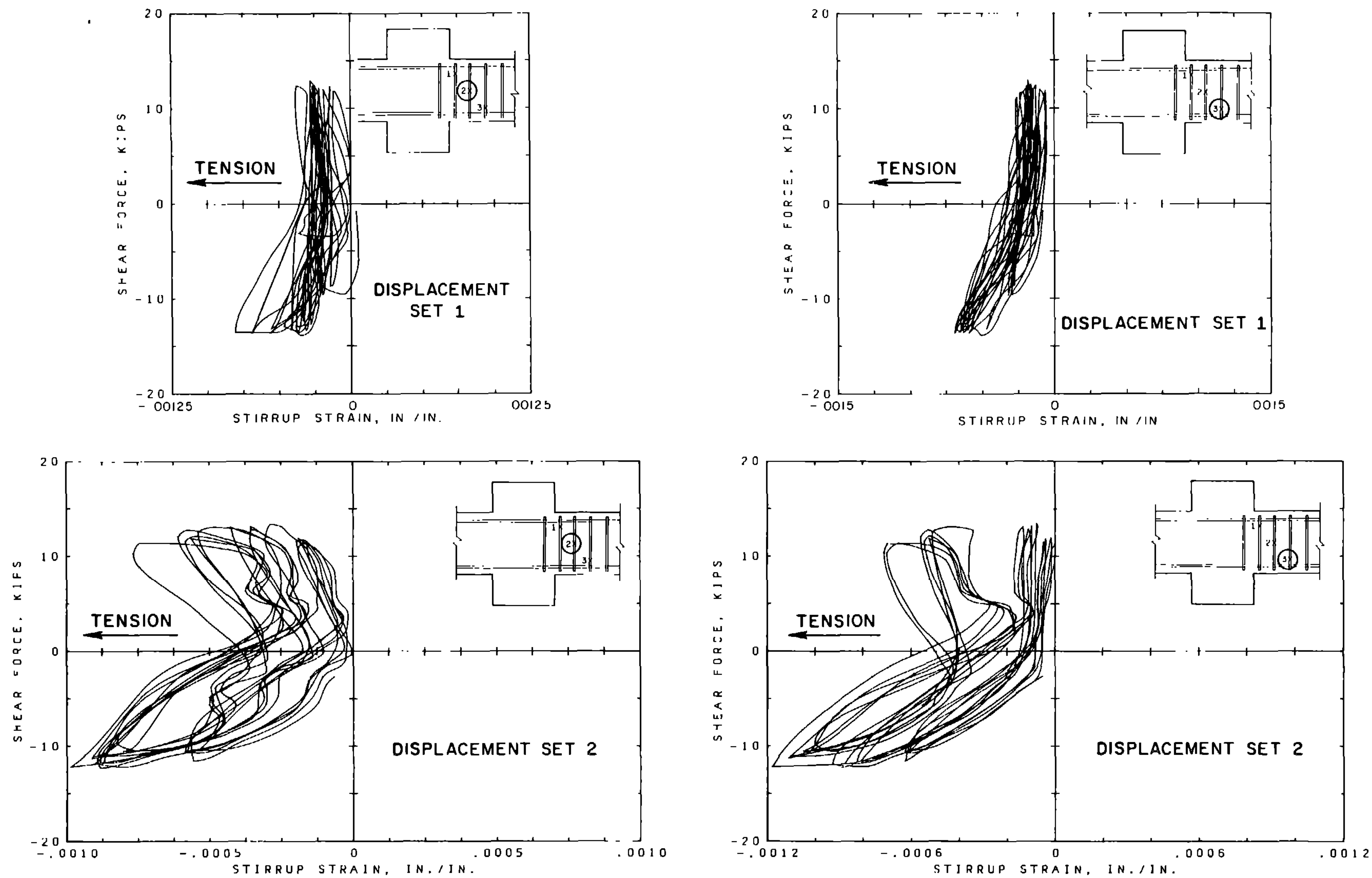

FIG. A.5.a SHEAR FORCE – TRANSVERSE REINFORCEMENT DIAGRAMS, SPECIMEN 1

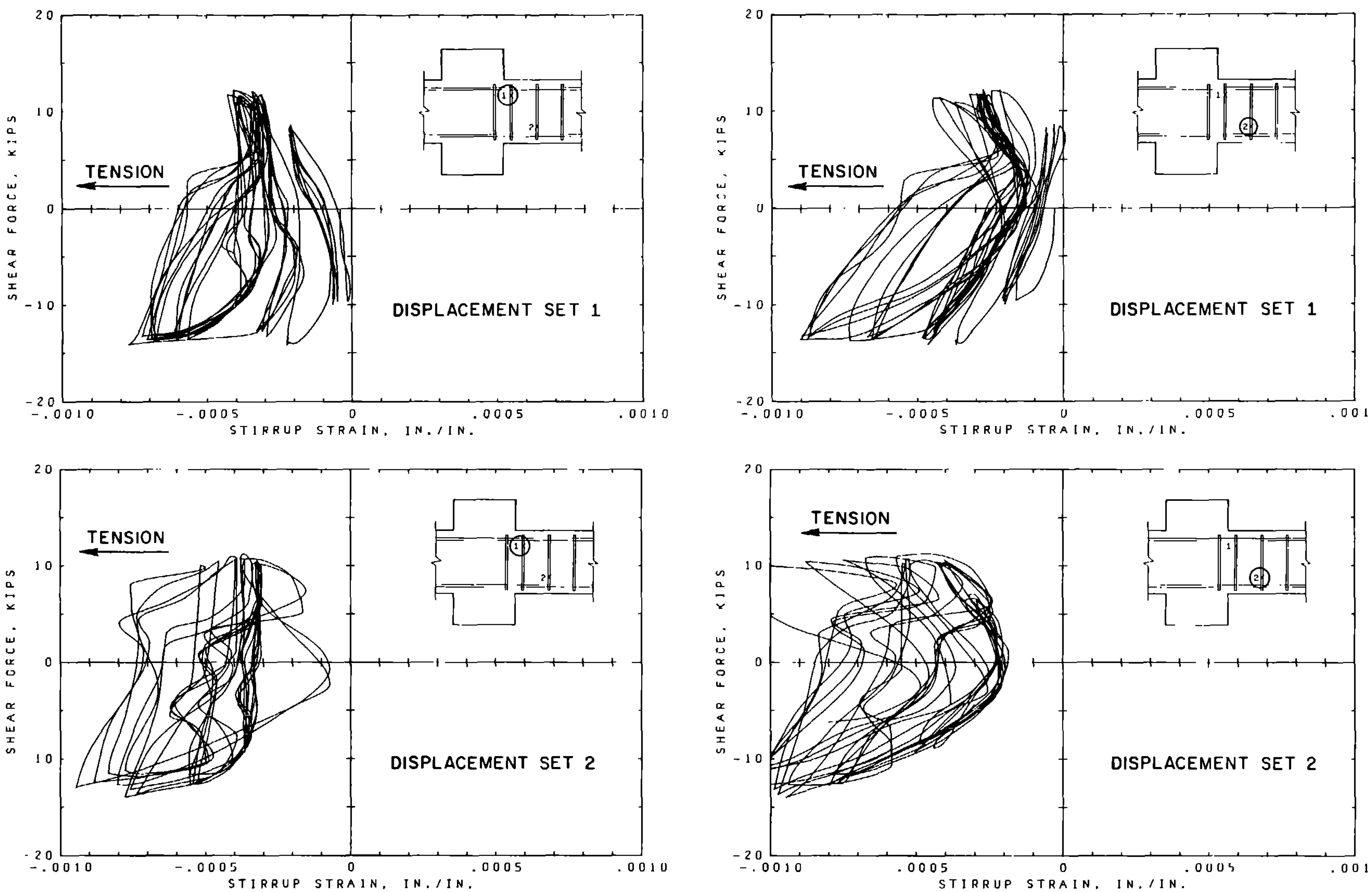

FIG. A.5.b SHEAR FORCE-TRANSVERSE REINFORCEMENT DIAGRAMS, SPECIMEN 2

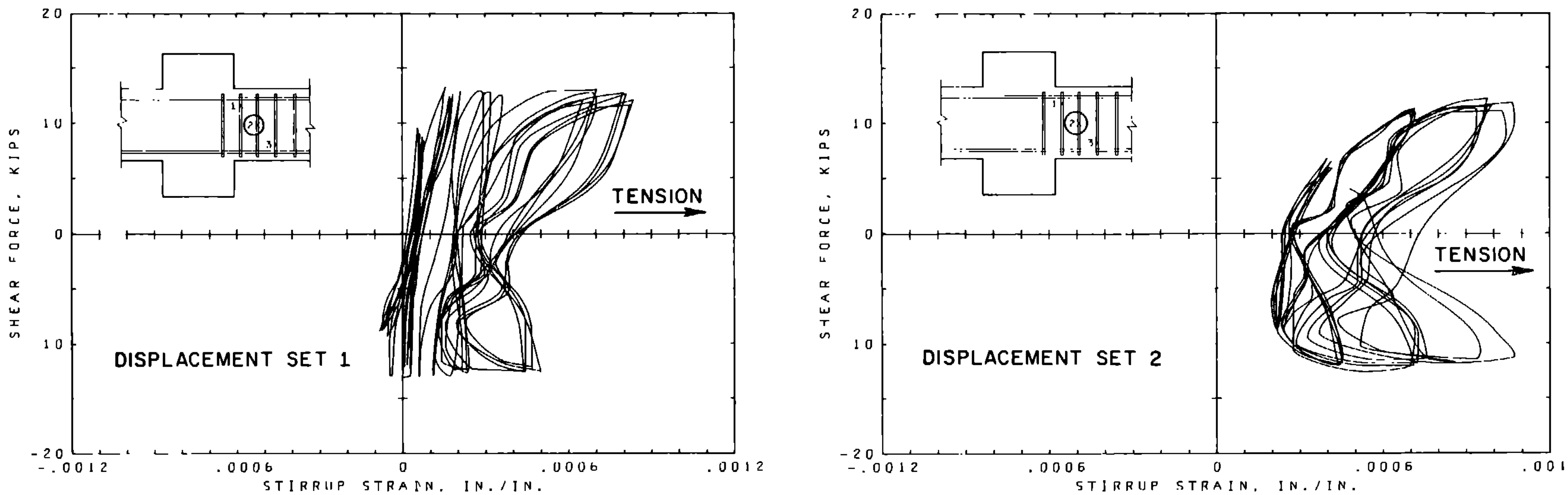

FIG. A.5.c SHEAR FORCE-TRANSVERSE REINFORCEMENT DIAGRAMS, SPECIMEN 3

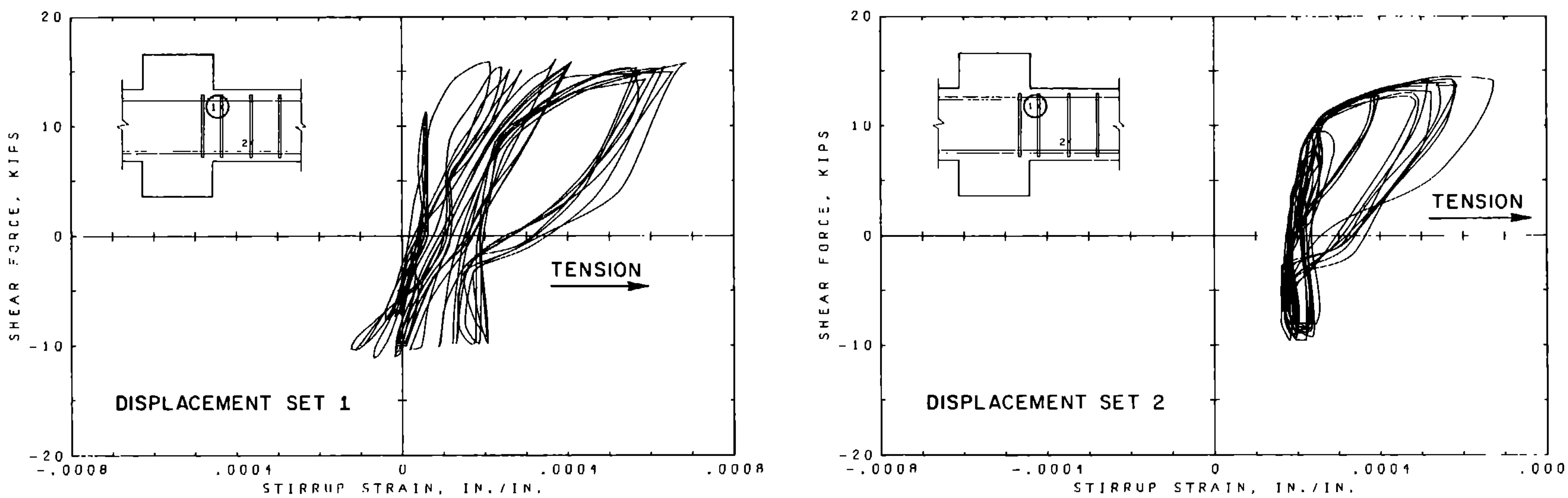

FIG. A.5.d SHEAR FORCE-TRANSVERSE REINFORCEMENT DIAGRAMS, SPECIMEN 4

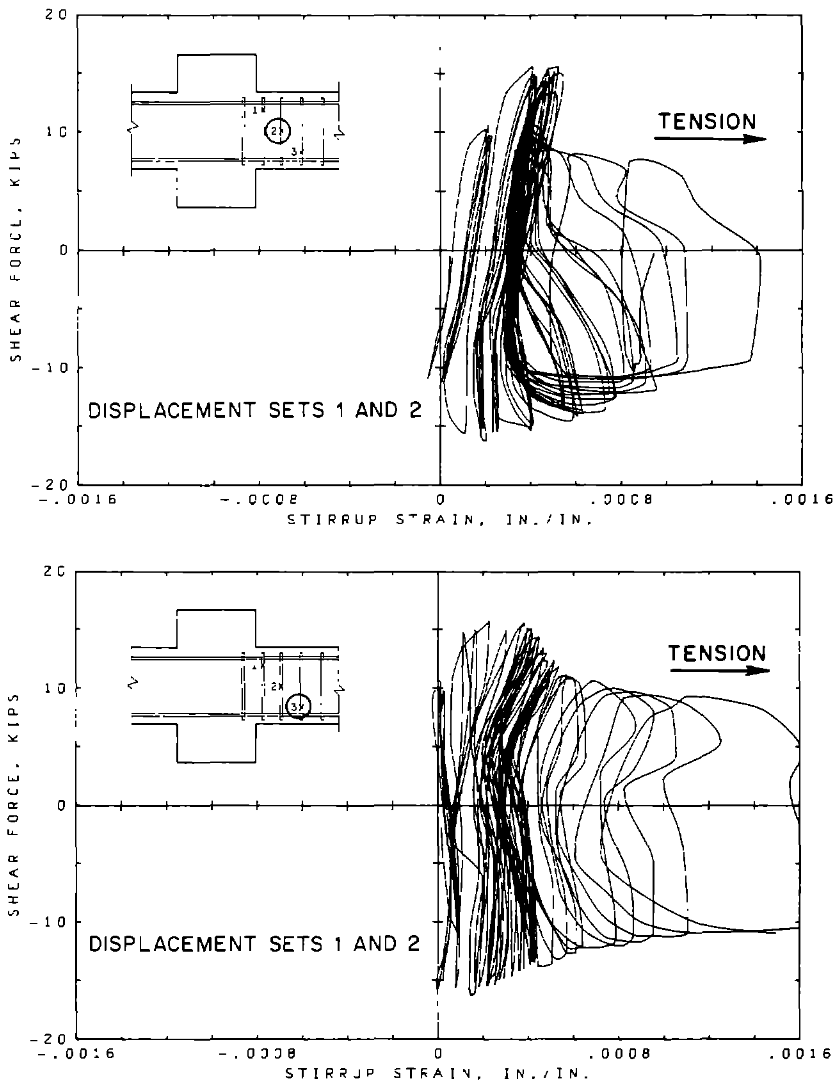

FIG. A.5.e SHEAR FORCE–TRANSVERSE REINFORCEMENT DIAGRAMS, SPECIMEN 5

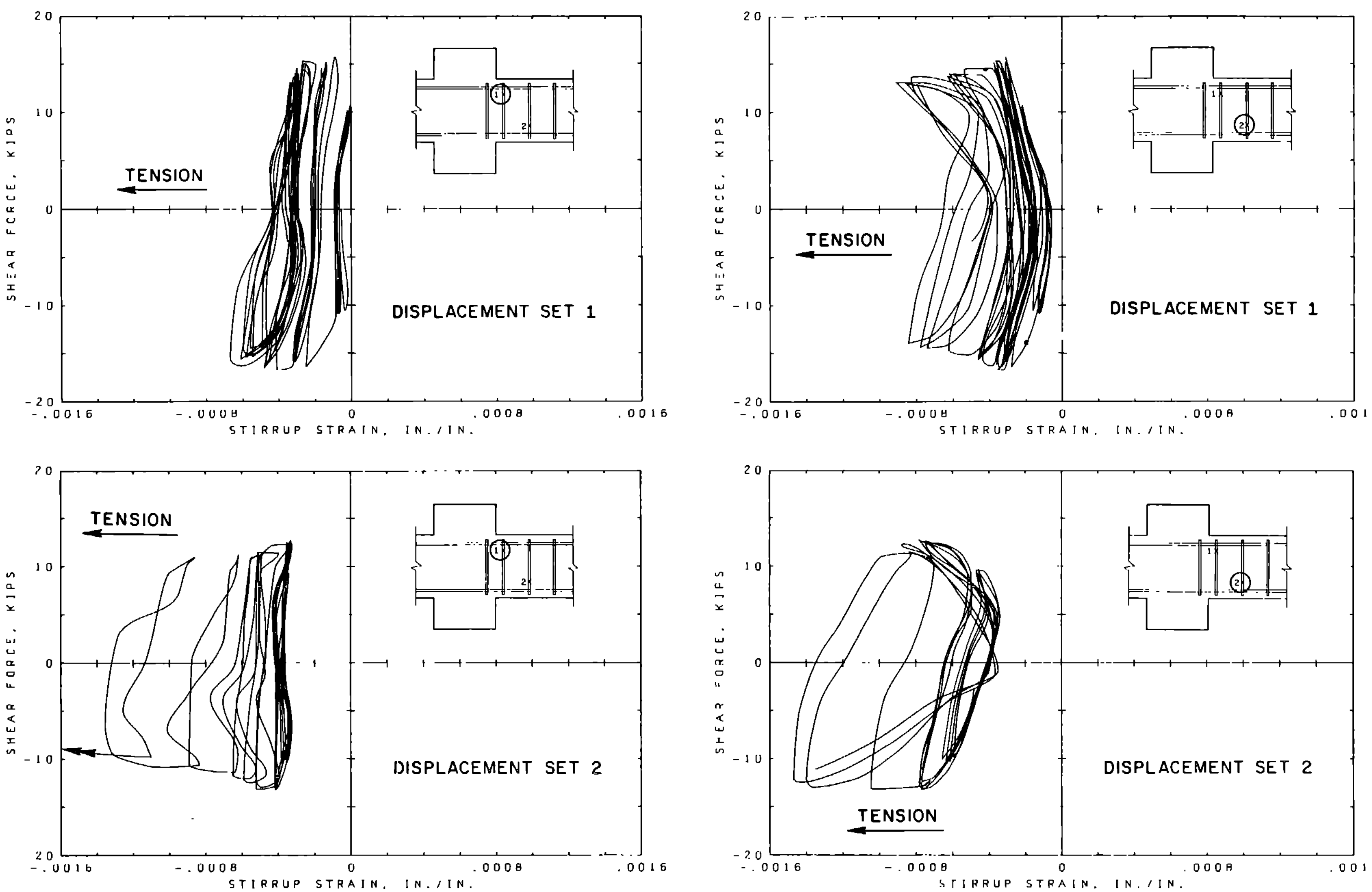

FIG. A.5.f SHEAR FORCE–TRANSVERSE REINFORCEMENT DIAGRAMS, SPECIMEN 6

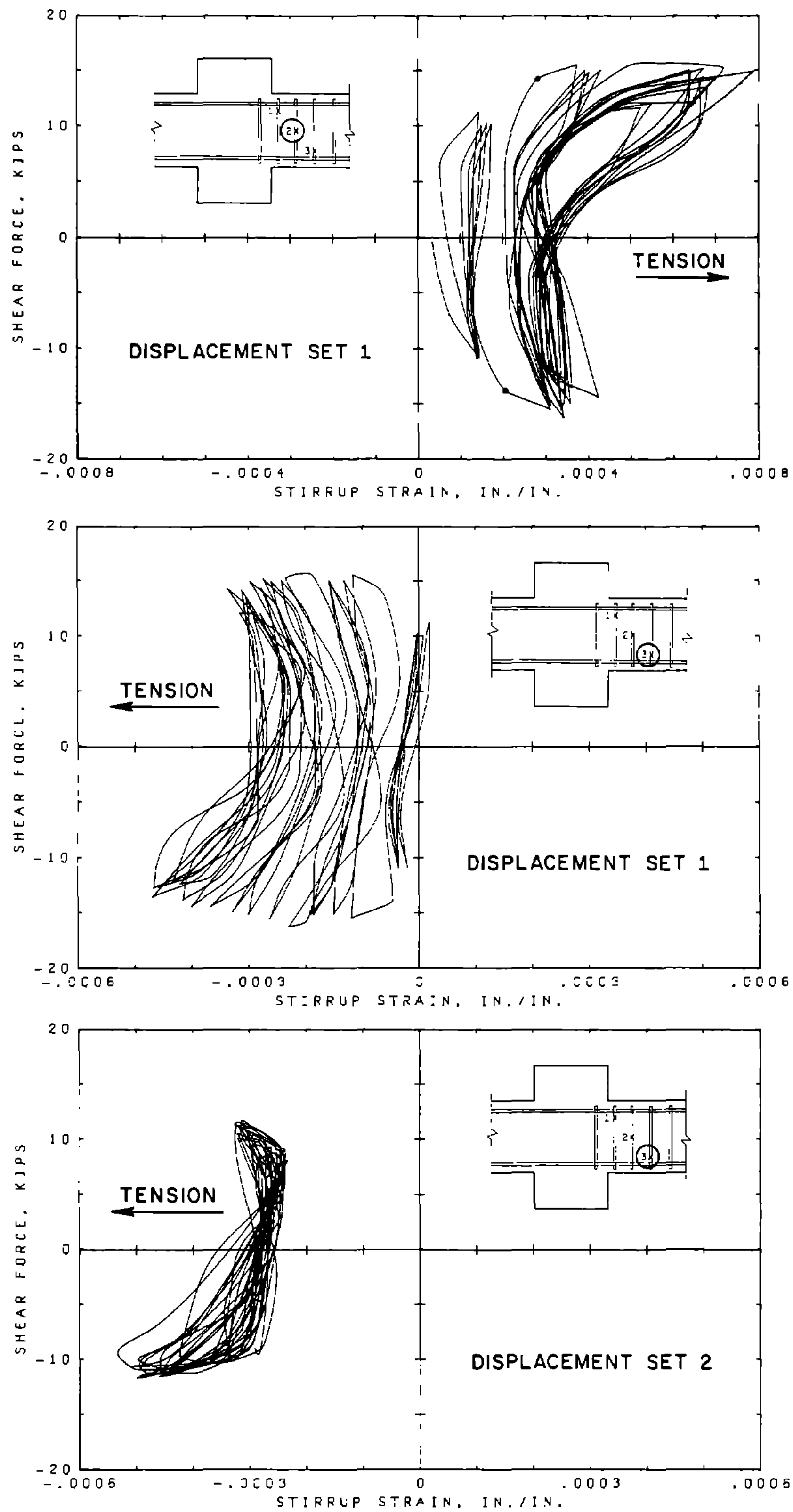

FIG. A.5.g SHEAR FORCE-TRANSVERSE REINFORCEMENT DIAGRAMS, SPECIMEN 7

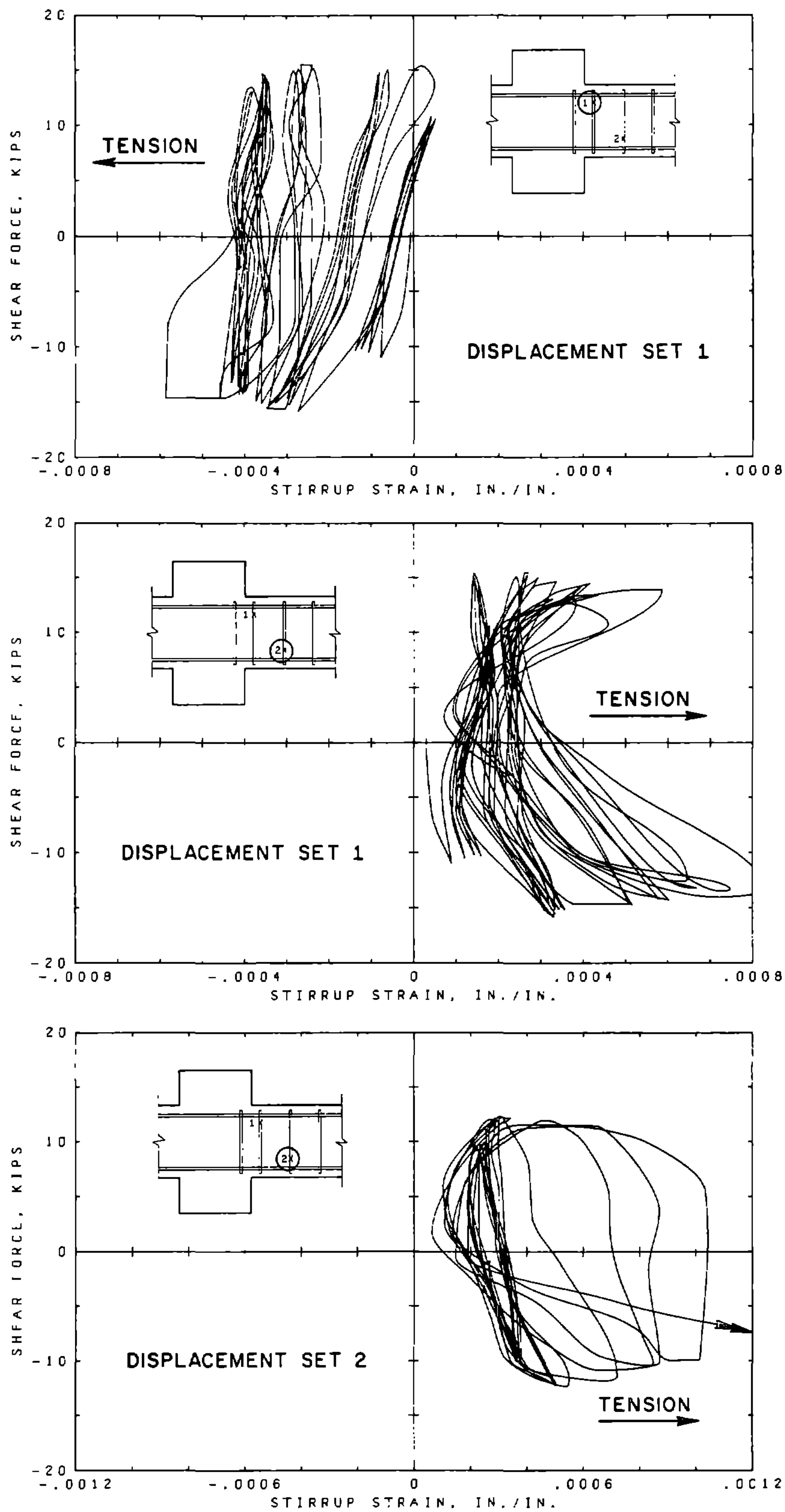

FIG. A.5.h SHEAR FORCE-TRANSVERSE REINFORCEMENT DIAGRAMS, SPECIMEN 8

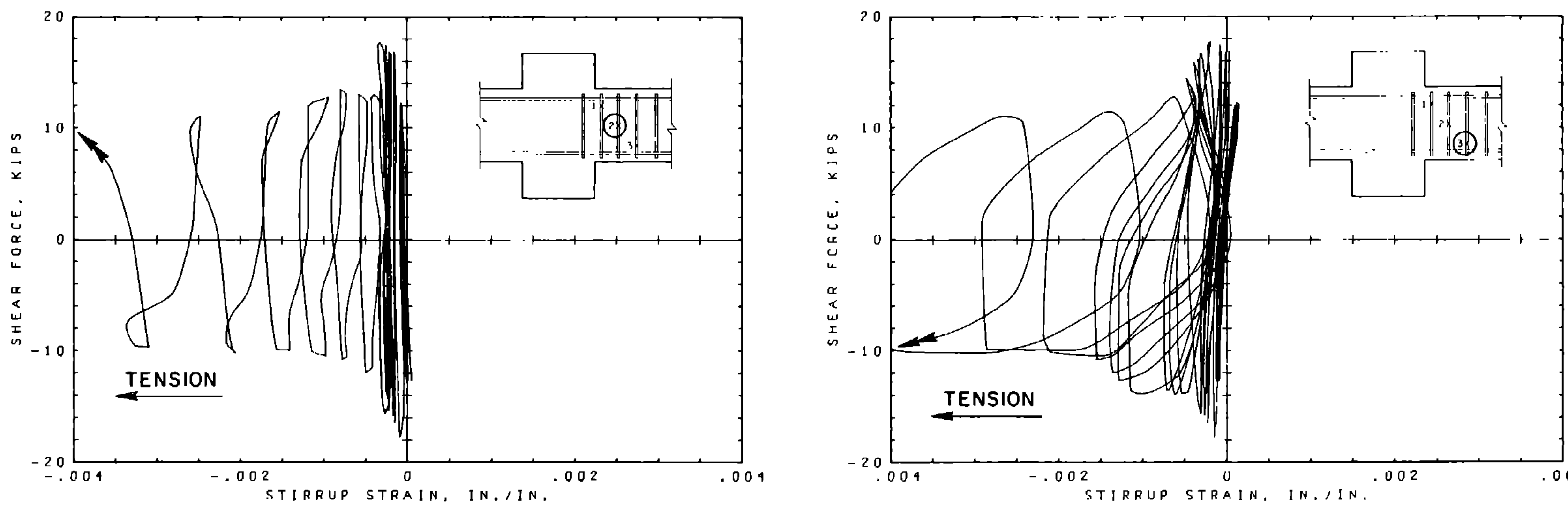

FIG. A.5.i SHEAR FORCE–TRANSVERSE REINFORCEMENT DIAGRAMS, SPECIMEN 9

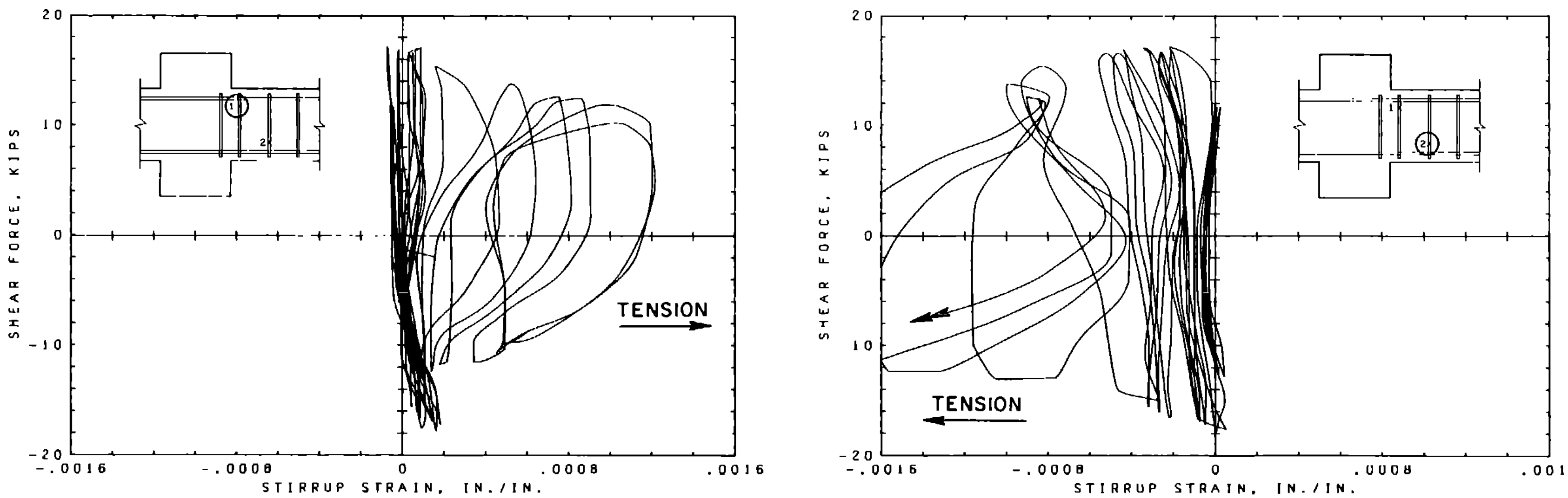

FIG. A.5.j SHEAR FORCE–TRANSVERSE REINFORCEMENT DIAGRAMS, SPECIMEN 10

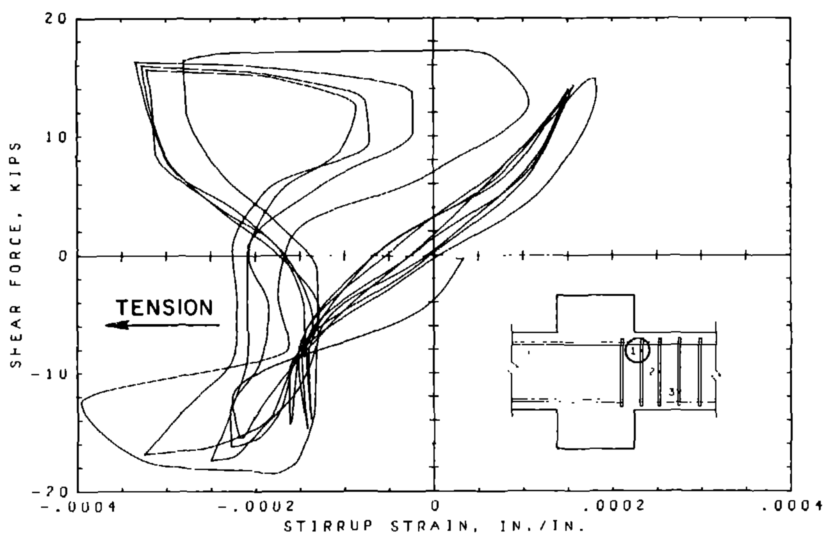

STRAIN GAGES ON TIES NOS. 2 AND 3
NOT OPERATIVE

FIG. A.5.k SHEAR FORCE-TRANSVERSE REINFORCEMENT DIAGRAMS, SPECIMEN 11

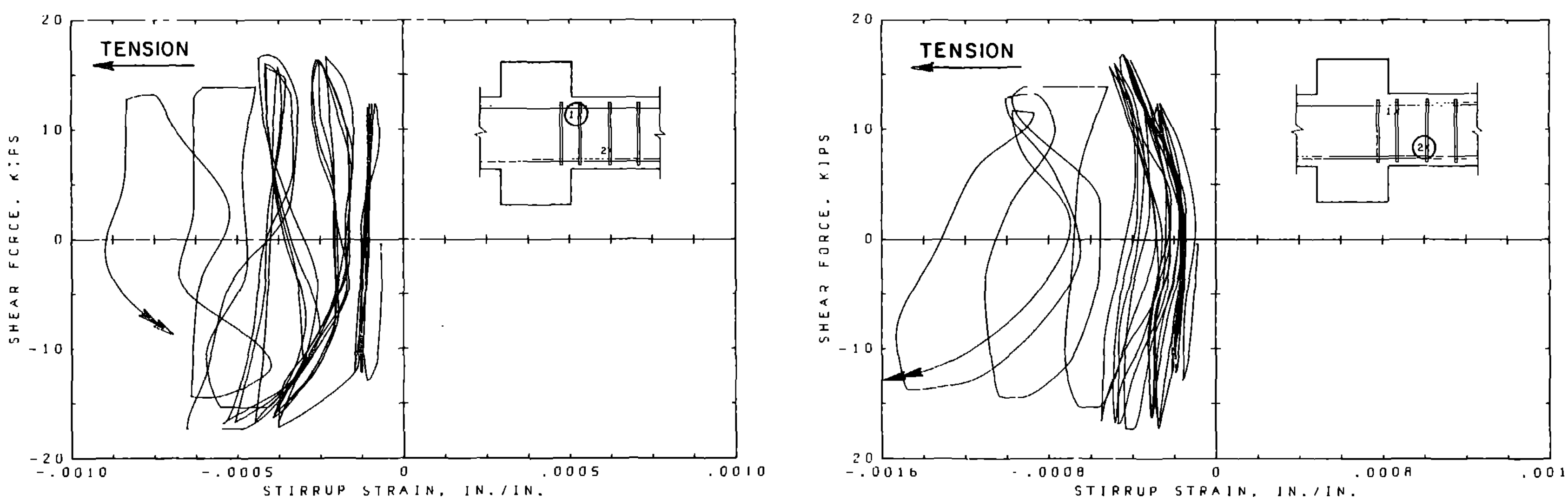

FIG. A.5.ℓ SHEAR FORCE-TRANSVERSE REINFORCEMENT DIAGRAMS, SPECIMEN 12

EARTHQUAKE ENGINEERING RESEARCH CENTER REPORTS

EERC 67-1 "Feasibility Study Large-Scale Earthquake Simulator Facility," by J. Penzien, J. G. Bouwkamp, R. W. Clough and D. Rea - 1967 (PB 187 905)

EERC 68-1 Unassigned

EERC 68-2 "Inelastic Behavior of Beam-to-Column Subassemblages Under Repeated Loading," by V. V. Bertero - 1968 (PB 184 888)

EERC 68-3 "A Graphical Method for Solving the Wave Reflection-Refraction Problem," by H. D. McNiven and Y. Mengi 1968 (PB 187 943)

EERC 68-4 "Dynamic Properties of McKinley School Buildings," by D. Rea, J. G. Bouwkamp and R. W. Clough - 1968 (PB 187 902)

EERC 68-5 "Characteristics of Rock Motions During Earthquakes," by H. B. Seed, I. M. Idriss and F. W. Kiefer - 1968 (PB 188 338)

EERC 69-1 "Earthquake Engineering Research at Berkeley," - 1969 (PB 187 906)

EERC 69-2 "Nonlinear Seismic Response of Earth Structures," by M. Dibaj and J. Penzien - 1969 (PB 187 904)

EERC 69-3 "Probabilistic Study of the Behavior of Structures During Earthquakes," by P. Ruiz and J. Penzien - 1969 (PB 187 886)

EERC 69-4 "Numerical Solution of Boundary Value Problems in Structural Mechanics by Reduction to an Initial Value Formulation," by N. Distefano and J. Schujman - 1969 (PB 187 942)

EERC 69-5 "Dynamic Programming and the Solution of the Biharmonic Equation," by N. Distefano - 1969 (PB 187 941)

Note: Numbers in parenthesis are Accession Numbers assigned by the National Technical Information Service. Copies of these reports may be ordered from the National Technical Information Service, 5285 Port Royal Road, Springfield, Virginia, 22161. Accession Numbers should be quoted on orders for the reports (PB --- ---) and remittance must accompany each order. (Foreign orders, add $2.50 extra for mailing charges.) Those reports without this information listed are not yet available from NTIS. Upon request, EERC will mail inquirers this information when it becomes available to us.

EERC 69-6 "Stochastic Analysis of Offshore Tower Structures," by A. K. Malhotra and J. Penzien - 1969 (PB 187 903)

EERC 69-7 "Rock Motion Accelerograms for High Magnitude Earthquakes," by H. B. Seed and I. M. Idriss - 1969 (PB 187 940)

EERC 69-8 "Structural Dynamics Testing Facilities at the University of California, Berkeley," by R. M. Stephen, J. G. Bouwkamp, R. W. Clough and J. Penzien - 1969 (PB 189 111)

EERC 69-9 "Seismic Response of Soil Deposits Underlain by Sloping Rock Boundaries," by H. Dezfulian and H. B. Seed - 1969 (PB 189 114)

EERC 69-10 "Dynamic Stress Analysis of Axisymmetric Structures under Arbitrary Loading," by S. Ghosh and E. L. Wilson - 1969 (PB 189 026)

EERC 69-11 "Seismic Behavior of Multistory Frames Designed by Different Philosophies," by J. C. Anderson and V. V. Bertero - 1969 (PB 190 662)

EERC 69-12 "Stiffness Degradation of Reinforcing Concrete Structures Subjected to Reversed Actions," by V. V. Bertero, B. Bresler and H. Ming Liao - 1969 (PB 202 942)

EERC 69-13 "Response of Non-Uniform Soil Deposits to Travel Seismic Waves," by H. Dezfulian and H. B. Seed - 1969 (PB 191 023)

EERC 69-14 "Damping Capacity of a Model Steel Structure," by D. Rea, R. W. Clough and J. G. Bouwkamp - 1969 (PB 190 663)

EERC 69-15 "Influence of Local Soil Conditions on Building Damage Potential during Earthquakes," by H. B. Seed and I. M. Idriss - 1969 (PB 191 036)

EERC 69-16 "The Behavior of Sands under Seismic Loading Conditions," by M. L. Silver and H. B. Seed - 1969 (AD 714 982)

EERC 70-1 "Earthquake Response of Concrete Gravity Dams," by A. K. Chopra - 1970 (AD 709 640)

EERC 70-2 "Relationships between Soil Conditions and Building Damage in the Caracas Earthquake of July 29, 1967," by H. B. Seed, I. M. Idriss and H. Dezfulian - 1970 (PB 195 762)

EERC 70-3 "Cyclic Loading of Full Size Steel Connections," by E. P. Popov and R. M. Stephen - 1970 (PB 213 545)

EERC 70-4 "Seismic Analysis of the Charaima Building, Caraballeda, Venezuela," by Subcommittee of the SEAONC Research Committee: V. V. Bertero, P. F. Fratessa, S. A. Mahin, J. H. Sexton, A. C. Scordelis, E. L. Wilson, L. A. Wyllie, H. B. Seed and J. Penzien, Chairman - 1970 (PB 201 455)

EERC 70-5 "A Computer Program for Earthquake Analysis of Dams," by A. K. Chopra and P. Chakrabarti - 1970 (AD 723 994)

EERC 70-6 "The Propagation of Love Waves across Non-Horizontally Layered Structures," by J. Lysmer and L. A. Drake - 1970 (PB 197 896)

EERC 70-7 "Influence of Base Rock Characteristics on Ground Response," by J. Lysmer, H. B. Seed and P. B. Schnabel - 1970 (PB 197 897)

EERC 70-8 "Applicability of Laboratory Test Procedures for Measuring Soil Liquefaction Characteristics under Cyclic Loading," by H. B. Seed and W. H. Peacock - 1970 (PB 198 016)

EERC 70-9 "A Simplified Procedure for Evaluating Soil Liquefaction Potential," by H. B. Seed and I. M. Idriss - 1970 (PB 198 009)

EERC 70-10 "Soil Moduli and Damping Factors for Dynamic Response Analysis," by H. B. Seed and I. M. Idriss - 1970 (PB 197 869)

EERC 71-1 "Koyna Earthquake and the Performance of Koyna Dam," by A. K. Chopra and P. Chakrabarti - 1971 (AD 731 496)

EERC 71-2 "Preliminary In-Situ Measurements of Anelastic Absorption in Soils Using a Prototype Earthquake Simulator," by R. D. Borcherdt and P. W. Rodgers - 1971 (PB 201 454)

EERC 71-3 "Static and Dynamic Analysis of Inelastic Frame Structures," by F. L. Porter and G. H. Powell - 1971 (PB 210 135)

EERC 71-4 "Research Needs in Limit Design of Reinforced Concrete Structures," by V. V. Bertero - 1971 (PB 202 943)

EERC 71-5 "Dynamic Behavior of a High-Rise Diagonally Braced Steel Building," by D. Rea, A. A. Shah and J. G. Bouwkamp - 1971 (PB 203 584)

EERC 71-6 "Dynamic Stress Analysis of Porous Elastic Solids Saturated with Compressible Fluids," by J. Ghaboussi and E. L. Wilson - 1971 (PB 211 396)

EERC 71-7 "Inelastic Behavior of Steel Beam-to-Column Subassemblages," by H. Krawinkler, V. V. Bertero and E. P. Popov - 1971 (PB 211 335)

EERC 71-8 "Modification of Seismograph Records for Effects of Local Soil Conditions," by P. Schnabel, H. B. Seed and J. Lysmer - 1971 (PB 214 450)

EERC 72-1 "Static and Earthquake Analysis of Three Dimensional Frame and Shear Wall Buildings," by E. L. Wilson and H. H. Dovey - 1972 (PB 212 904)

EERC 72-2 "Accelerations in Rock for Earthquakes in the Western United States," by P. B. Schnabel and H. B. Seed - 1972 (PB 213 100)

EERC 72-3 "Elastic-Plastic Earthquake Response of Soil-Building Systems," by T. Minami - 1972 (PB 214 868)

EERC 72-4 "Stochastic Inelastic Response of Offshore Towers to Strong Motion Earthquakes," by M. K. Kaul - 1972 (PB 215 713)

EERC 72-5 "Cyclic Behavior of Three Reinforced Concrete Flexural Members with High Shear," by E. P. Popov, V. V. Bertero and H. Krawinkler - 1972 (PB 214 555)

EERC 72-6 "Earthquake Response of Gravity Dams Including Reservoir Interaction Effects," by P. Chakrabarti and A. K. Chopra - 1972 (AD 762 330)

EERC 72-7 "Dynamic Properties on Pine Flat Dam," by D. Rea, C. Y. Liaw and A. K. Chopra - 1972 (AD 763 928)

EERC 72-8 "Three Dimensional Analysis of Building Systems," by E. L. Wilson and H. H. Dovey - 1972 (PB 222 438)

EERC 72-9 "Rate of Loading Effects on Uncracked and Repaired Reinforced Concrete Members," by S. Mahin, V. V. Bertero, D. Rea and M. Atalay - 1972 (PB 224 520)

EERC 72-10 "Computer Program for Static and Dynamic Analysis of Linear Structural Systems," by E. L. Wilson, K.-J. Bathe, J. E. Peterson and H. H. Dovey - 1972 (PB 220 437)

EERC 72-11 "Literature Survey - Seismic Effects on Highway Bridges," by T. Iwasaki, J. Penzien and R. W. Clough - 1972 (PB 215 613)

EERC 72-12 "SHAKE-A Computer Program for Earthquake Response Analysis of Horizontally Layered Sites," by P. B. Schnabel and J. Lysmer - 1972 (PB 220 207)

EERC 73-1 "Optimal Seismic Design of Multistory Frames," by V. V. Bertero and H. Kamil - 1973

EERC 73-2 "Analysis of the Slides in the San Fernando Dams during the Earthquake of February 9, 1971," by H. B. Seed, K. L. Lee, I. M. Idriss and F. Makdisi - 1973 (PB 223 402)

EERC 73-3 "Computer Aided Ultimate Load Design of Unbraced Multistory Steel Frames," by M. B. El-Hafez and G. H. Powell - 1973

EERC 73-4 "Experimental Investigation into the Seismic Behavior of Critical Regions of Reinforced Concrete Components as Influenced by Moment and Shear," by M. Celebi and J. Penzien - 1973 (PB 215 884)

EERC 73-5 "Hysteretic Behavior of Epoxy-Repaired Reinforced Concrete Beams," by M. Celebi and J. Penzien - 1973

EERC 73-6 "General Purpose Computer Program for Inelastic Dynamic Response of Plane Structures," by A. Kanaan and G. H. Powell - 1973 (PB 221 260)

EERC 73-7 "A Computer Program for Earthquake Analysis of Gravity Dams Including Reservoir Interaction," by P. Chakrabarti and A. K. Chopra - 1973 (AD 766 271)

EERC 73-8 "Behavior of Reinforced Concrete Deep Beam-Column Subassemblages under Cyclic Loads," by O. Kustu and J. G. Bouwkamp - 1973

EERC 73-9 "Earthquake Analysis of Structure-Foundation Systems," by A. K. Vaish and A. K. Chopra - 1973 (AD 766 272)

EERC 73-10 "Deconvolution of Seismic Response for Linear Systems," by R. B. Reimer - 1973 (PB 227 179)

EERC 73-11 "SAP IV: A Structural Analysis Program for Static and Dynamic Response of Linear Systems," by K.-J. Bathe, E. L. Wilson and F. E. Peterson - 1973 (PB 221 967)

EERC 73-12 "Analytical Investigations of the Seismic Response of Long, Multiple Span Highway Bridges," by W. S. Tseng and J. Penzien - 1973 (PB 227 816)

EERC 73-13 "Earthquake Analysis of Multi-Story Buildings Including Foundation Interaction," by A. K. Chopra and J. A. Gutierrez - 1973 (PB 222 970)

EERC 73-14 "ADAP: A Computer Program for Static and Dynamic Analysis of Arch Dams," by R. W. Clough, J. M. Raphael and S. Majtahedi - 1973 (PB 223 763)

EERC 73-15 "Cyclic Plastic Analysis of Structural Steel Joints," by R. B. Pinkney and R. W. Clough - 1973 (PB 226 843)

EERC 73-16 "QUAD-4: A Computer Program for Evaluating the Seismic Response of Soil Structures by Variable Damping Finite Element Procedures," by I. M. Idriss, J. Lysmer, R. Hwang and H. B. Seed - 1973 (PB 229 424)

EERC 73-17 "Dynamic Behavior of a Multi-Story Pyramid Shaped Building," by R. M. Stephen and J. G. Bouwkamp - 1973

EERC 73-18 "Effect of Different Types of Reinforcing on Seismic Behavior of Short Concrete Columns," by V. V. Bertero, J. Hollings, O. Kustu, R. M. Stephen and J. G. Bouwkamp - 1973

EERC 73-19 "Olive View Medical Center Material Studies, Phase I," by B. Bresler and V. V. Bertero - 1973 (PB 235 986)

EERC 73-20 "Linear and Nonlinear Seismic Analysis Computer Programs for Long Multiple-Span Highway Bridges," by W. S. Tseng and J. Penzien - 1973

EERC 73-21 "Constitutive Models for Cyclic Plastic Deformation of Engineering Materials," by J. M. Kelly and P. P. Gillis - 1973 (PB 226 024)

EERC 73-22 "DRAIN - 2D User's Guide," by G. H. Powell - 1973 (PB 227 016)

EERC 73-23 "Earthquake Engineering at Berkeley - 1973" - 1973 (PB 226 033)

EERC 73-24 Unassigned

EERC 73-25 "Earthquake Response of Axisymmetric Tower Structures Surrounded by Water," by C. Y. Liaw and A. K. Chopra - 1973 (AD 773 052)

EERC 73-26 "Investigation of the Failures of the Olive View Stairtowers during the San Fernando Earthquake and Their Implications in Seismic Design," by V. V. Bertero and R. G. Collins - 1973 (PB 235 106)

EERC 73-27 "Further Studies on Seismic Behavior of Steel Beam-Column Subassemblages," by V. V. Bertero, H. Krawinkler and E. P. Popov - 1973 (PB 234 172)

EERC 74-1 "Seismic Risk Analysis," by C. S. Oliveira - 1974 (PB 235 920)

EERC 74-2 "Settlement and Liquefaction of Sands under Multi-Directional Shaking," by R. Pyke, C. K. Chan and H. B. Seed - 1974

EERC 74-3 "Optimum Design of Earthquake Resistant Shear Buildings," by D. Ray, K. S. Pister and A. K. Chopra - 1974 (PB 231 172)

EERC 74-4 "LUSH - A Computer Program for Complex Response Analysis of Soil-Structure Systems," by J. Lysmer, T. Udaka, H. B. Seed and R. Hwang - 1974 (PB 236 796)

EERC 74-5 "Sensitivity Analysis for Hysteretic Dynamic Systems: Applications to Earthquake Engineering," by D. Ray - 1974 (PB 233 213)

EERC 74-6 "Soil-Structure Interaction Analyses for Evaluating Seismic Response," by H. B. Seed, J. Lysmer and R. Hwang - 1974 (PB 236 519)

EERC 74-7 Unassigned

EERC 74-8 "Shaking Table Tests of a Steel Frame - A Progress Report," by R. W. Clough and D. Tang - 1974

EERC 74-9 "Hysteretic Behavior of Reinforced Concrete Flexural Members with Special Web Reinforcement," by V. V. Bertero, E. P. Popov and T. Y. Wang - 1974 (PB 236 797)

EERC 74-10 "Applications of Reliability-Based, Global Cost Optimization to Design of Earthquake Resistant Structures," by E. Vitiello and K. S. Pister - 1974 (PB 237 231)

EERC 74-11 "Liquefaction of Gravelly Soils under Cyclic Loading Conditions," by R. T. Wong, H. B. Seed and C. K. Chan - 1974

EERC 74-12 "Site-Dependent Spectra for Earthquake-Resistant Design," by H. B. Seed, C. Ugas and J. Lysmer - 1974

EERC 74-13 "Earthquake Simulator Study of a Reinforced Concrete Frame," by P. Hidalgo and R. W. Clough - 1974 (PB 241 944)

EERC 74-14 "Nonlinear Earthquake Response of Concrete Gravity Dams," by N. Pal - 1974 (AD/A006583)

EERC 74-15 "Modeling and Identification in Nonlinear Structural Dynamics, I - One Degree of Freedom Models," by N. Distefano and A. Rath - 1974 (PB 241 548)

EERC 75-1 "Determination of Seismic Design Criteria for the Dumbarton Bridge Replacement Structure, Vol. I: Description, Theory and Analytical Modeling of Bridge and Parameters," by F. Baron and S.-H. Pang - 1975

EERC 75-2 "Determination of Seismic Design Criteria for the Dumbarton Bridge Replacement Structure, Vol. 2: Numerical Studies and Establishment of Seismic Design Criteria," by F. Baron and S.-H. Pang - 1975

EERC 75-3 "Seismic Risk Analysis for a Site and a Metropolitan Area," by C. S. Oliveira - 1975

EERC 75-4 "Analytical Investigations of Seismic Response of Short, Single or Multiple-Span Highway Bridges," by Ma-chi Chen and J. Penzien - 1975 (PB 241 454)

EERC 75-5 "An Evaluation of Some Methods for Predicting Seismic Behavior of Reinforced Concrete Buildings," by Stephen A. Mahin and V. V. Bertero - 1975

EERC 75-6 "Earthquake Simulator Study of a Steel Frame Structure, Vol. I: Experimental Results," by R. W. Clough and David T. Tang - 1975 (PB 243 981)

EERC 75-7 "Dynamic Properties of San Bernardino Intake Tower," by Dixon Rea, C.-Y. Liaw, and Anil K. Chopra - 1975 (AD/A008406)

EERC 75-8 "Seismic Studies of the Articulation for the Dumbarton Bridge Replacement Structure, Vol. I: Description, Theory and Analytical Modeling of Bridge Components," by F. Baron and R. E. Hamati - 1975

EERC 75-9 "Seismic Studies of the Articulation for the Dumbarton Bridge Replacement Structure, Vol. 2: Numerical Studies of Steel and Concrete Girder Alternates," by F. Baron and R. E. Hamati - 1975

EERC 75-10 "Static and Dynamic Analysis of Nonlinear Structures," by Digambar P. Mondkar and Graham H. Powell - 1975 (PB 242 434)

EERC 75-11 "Hysteretic Behavior of Steel Columns," by E. P. Popov, V. V. Bertero and S. Chandramouli - 1975

EERC 75-12 "Earthquake Engineering Research Center Library Printed Catalog" - 1975 (PB 243 711)

EERC 75-13 "Three Dimensional Analysis of Building Systems," Extended Version, by E. L. Wilson, J. P. Hollings and H. H. Dovey - 1975 (PB 243 989)

EERC 75-14 "Determination of Soil Liquefaction Characteristics by Large-Scale Laboratory Tests," by Pedro De Alba, Clarence K. Chan and H. Bolton Seed - 1975

EERC 75-15 "A Literature Survey - Compressive, Tensile, Bond and Shear Strength of Masonry," by Ronald L. Mayes and Ray W. Clough - 1975

EERC 75-16 "Hysteretic Behavior of Ductile Moment Resisting Reinforced Concrete Frame Components," by V. V. Bertero and E. P. Popov - 1975

EERC 75-17 "Relationships Between Maximum Acceleration, Maximum Velocity, Distance from Source, Local Site Conditions for Moderately Strong Earthquakes," by H. Bolton Seed, Ramesh Murarka, John Lysmer and I. M. Idriss - 1975

EERC 75-18 "The Effects of Method of Sample Preparation on the Cyclic Stress-Strain Behavior of Sands," by J. Paul Mulilis, Clarence K. Chan and H. Bolton Seed - 1975

EERC 75-19 "The Seismic Behavior of Critical Regions of Reinforced Concrete Components as Influenced by Moment, Shear and Axial Force," by B. Atalay and J. Penzien - 1975